LWI Report no. 988

Hydraulic Performance, Wave Loading and Response of Elastocoast Revetments and their Foundation - A Large Scale Model Study -

(Final Report)

Prof. Dr.-Ing. H. Oumeraci
Dipl.-Ing. T. Staal
Dipl.-Ing. S. Pfoertner
Dipl.-Ing. G. Ludwigs
Dipl.-Ing. M. Kudella

Braunschweig, 8th January 2010

Abstract

ELASTOCOAST revetments are highly porous structures made of crushed stones which are durably and elastically bonded by Polyurethane (PU). To improve the understanding of the physical processes involved in the wave-structure-foundation interaction and to develop prediction formulae for both hydraulic performance and wave loading more than 75 large-scale model tests using both regular and irregular waves were performed. Three *ELASTOCOAST* revetment alternatives with the same slope (1:3) and the same revetment thickness (0.20 m) but with different thicknesses of the underlying filter layer (0.00 m, 0.10 m and 0.20 m for *Model Alternatives* A, B and C, respectively) were tested. More than 85 measuring devices synchronously connected to two video cameras were used.

Prediction formulae are developed for wave reflection, wave run-up and run-down as a function of the surf similarity parameter which illustrate the advantage of *ELASTOCOAST* revetments as compared to conventional revetments. For instance, more than 25% less wave run-up may result on comparison to smooth impermeable revetments.

Using a surf similarity-based wave load classification as well as a systematic parametrization in both time and space, prediction formulae are also developed for both impact loads on and just beneath the revetment. These include the peak pressure p_{max}, its location in relation to still water level z_{pmax}, the spatial pressure distribution and the time related parameters (rise time and total load duration).

Prediction formulae for the wave-induced pore pressure in the sand core beneath the revetment are also provided, including the maximum pressure at the upper boundary of the sand layer and its development in deeper layers.

Formulae are also proposed for the flexural displacement δ of the *ELASTOCOAST* revetment, showing that for impact load much smaller displacements would result than for non-impact load and that δ linearly increases with peak pressure p_{max} for a given revetment thickness.

Finally, a stability analysis of *Model Alternative* A is performed on basis of the results of the measurements and the simultaneously recorded videos. The results illustrate why *Model Alternative* A failed due to local transient soil liquefaction while *Model Alternative* B tested synchronously under the same wave conditions did not fail.

Contents

List of figures

List of tables

List of symbols

Parameter	Dimension	Description
B_{crest}	[m]	crest width of the revetment
C_r	[-]	reflection coefficient
c_0/c	[-]	relative wave speed
D_{10}	[m]	diameter of particles which exceed the 10% value of sieve curve
D_{50}	[m]	50% value of sieve curve (mean particle size)
D_{60}	[m]	60% value of sieve curve
d	[m]	thickness of *ELASTOCOAST* revetment
Δd	[m]	distance of sensors of layer thickness gauge
f	[Hz]	frequency
H	[m]	wave height
H_{m0}	[m]	"significant wave height" (frequency domain)
H_{nom}	[m]	nominal wave height
H_s	[m]	significant wave height (time domain)
h_s	[m]	water depth (here: in the wave flume)
$h(x)$	[m]	local water depth
K_s	[-]	shoeling coefficient
k	[m/s]	hydraulic permeability
L	[m]	wave length
L_0	[m]	wavelength in deepwater
$L_{m-1,0}$	[m]	wave length corresponding to wave period $T_{m-1,0}$
m_0, m_{-1}	[-]	zeroth and minus 1 moment of the energy density spectrum
n	[-]	number of waves
O_{90}	[µm]	characteristic hole width of the geotextile
p_+	[Pa]	excess pressure
p_-	[Pa]	under pressure
p_0	[Pa]	initial pore pressure at z'=0
$p_0(x)$	[Pa]	hydrostatic pressure at local water depth h(x)
p_{hydro}	[Pa]	hydrostatic pressure
p_{max}	[Pa]	maximum (peak) pressure at layer 1
$p_{2,max}$	[Pa]	maximum pressure at layer 2
$p_{3,max}$	[Pa]	maximum pressure at layer 3
$p_{4,max}$	[Pa]	maximum pressure at layer 4
$p_{5,max}$	[Pa]	maximum pressure at layer 5
p_i	[Pa]	wave pressure at point i on the revetment
p_i'	[Pa]	wave pressure at point i beneath the revetment
p_{stat}	[Pa]	quasi-static pressure
$p_{imp,stat}$	[Pa]	quasi-static component of impact load
R_u	[m]	wave run-up height
$R_{u2\%}$	[m]	wave run-up height exceeded by 2% of the incoming waves
$R_{u,max}$	[m]	maximum wave run-up
R_d	[m]	wave run-down height

$R_{d2\%}$	[m]	wave run-down height exceeded by 2% of the incoming waves
T	[s]	wave period
T_m	[s]	mean wave period
$T_{m-1,0}$	[s]	mean wave period ($= m_{-1}/m_0$)
T_{nom}	[s]	nominal wave period
T_p	[s]	peak period of the wave spectrum
t_A	[s]	rise time
t_D	[s]	impact duration
$t_{stat,1}$, $t_{stat,2}$	[s]	Parameters of temporal abstraction
$t_{stat,imp}$	[s]	rise time for quasi-static component and non-impact load
$t_{u0,max}$		time of occurance of $u_{0,max}$
U	[−]	uniformity coefficient (D_{60}/D_{10})
u_0	[Pa]	initial pore pressure at the surface (= wave pressure)
$u_{0,max}$	[Pa]	maximal initial pore pressure at the surface (= wave pressure)
u_t	[Pa]	transient pore pressure
$u_{t,i,layerj}$	[Pa]	negative pore pressure at point i and layer j
u_r	[Pa]	residual pore pressure
$u_{r,4}$	[Pa]	residual pore pressure at layer 4
$u_{r,5}$	[Pa]	residual pore pressure at layer 5
x_{mi}	[-]	input parameter for model
y_m	[-]	measured output parameter
z	[m]	characteristic depth
z'	[m]	characteristic depth normal to the slope
z_i	[m]	location at point I on the revetment
$z_i{}'$	[m]	location at point I beneath the revetment
z_{-98}	[m]	wave run-down exceeded by 2% of the incoming waves
$z_{2,pmax}$	[m]	impct point of the wave beneath the revetment
z_{pmax}	[m]	impact point of the wave on the revetment

α	[°]	angle of slope
γ_f	[-]	coefficient for friction influence
$\Delta\bar{u}$	[-]	dimensionless difference of negative pore pressure
δ	[m]	Flexural displacement of the *ELASTOCOAST* revetment
σ'	[-]	coefficient of variation
ξ_0	[-]	surf similarity parameter based on L_0
$\xi_{m-1,0}$	[-]	surf similarity parameter based on $L_{m-1,0}$

1 Framework and Objectives

1.1 Motivation, Framework and Agreements

ELASTOCOAST is a new type of bounded porous revetment developed by the Elastogran GmbH. The material consists of a highly porous gravel medium which is stuck together by a two-component plastic polyurethane (PU).

The basic material and hydraulic properties have already been investigated by Gu, 2007b and Evertz, 2009. Tentative structural analysis and design based on several assumptions related to wave loading and resistance parameters have also been conducted within the framework of the more recent master thesis of Bijlsma, 2008, including Gu, 2007a. However, reliable methods for the design wave loads and the structure response based on wave flume experiments are not yet available. This was recently confirmed by the master thesis of Davidse, 2009 who reviewed the formulae available for wave impact loads. In fact, particularly the response of the structure due to breaking wave impact load under realistic wave conditions is not yet known. This also holds true for the interaction between the wave load and the responses of the *ELASTOCOAST* structure together with its filter layer and the subsoil foundation which must be considered as an integrated system.

In order to improve the understanding of all relevant processes and, as a result, to come up with reliable and practical formulae/diagrams which may be applied for design purposes, large scale experiments have been performed from May to June 2009 in the Large Wave Flume (Grosser Wellenkanal, GWK) in Hanover, Germany. These experiments were defined in the proposal dated 2008-03-13 (FZK, 2008b) and specified in more detail according to the report describing the pre-design and preparatory works (Oumeraci et al., 2009b). The latter addresses the pre-design of the model setup by making use of empirical models, the numerical simulations performed as part of a master thesis (Staal, 2008) and the experimental measurements previously performed on a dike in GWK (Geisenhainer et al., 2008).

As agreed in the FZK-BASF meeting on 2009-01-23, the present study first covers the model setup as specified in the aforementioned proposal (FZK, 2008b) and report (Oumeraci et al., 2009b). This does not include the introduction of an initial gap beneath *Model Alternative* A of the *ELASTOCOAST* revetment. This second model setup as suggested in the proposal dated 2008-06-02 (FZK, 2008a) was planned to be discussed at a later stage as it had to be based on the results of the tests to be performed for the first model set-up.

The model setup in the present study initially consisted of two revetment alternatives having the same thickness (0.15 m) and the same slope steepness (1:3): In *Model Alternative A* the revetment lies directly on the geotextile/sand slope while in *Model Alternative B* a filter layer

using the same crushed rock material as for the *ELASTOCOAST* revetment is inserted between the *ELASTOCOAST* layer and the geotextile/sand slope (Fig. 1.1). The crushed stone material consists of limestone with a grading 20/40 mm. The two *Models Alternatives A and B* are built side by side, each covering half of the wave flume width (2 x 2.5 m) and tested simultaneously using the same incident wave conditions. These were fixed at the FZK-BASF-Meeting mentioned above.
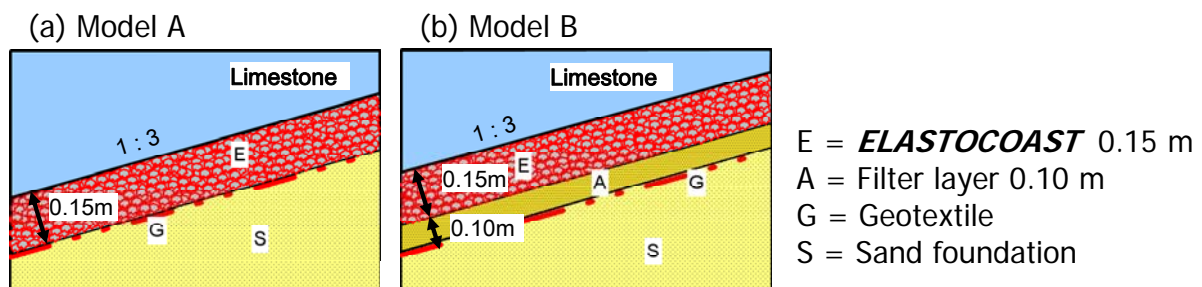
Fig. 1.1:   Detailed cross section of the two alternatives *Model A* (a) and *Model B* (b) (FZK, 2008b)

Further agreements which were achieved in the aforementioned and further meetings are summarized in the introductory chapter of the pre-design report (Oumeraci et al., 2009b). This report has served as the main guidance for the realization of the model set-up, the deployed measuring and observation techniques as well as for the testing conditions, programme and procedure.

After the damage of *Model Alternative A* which occurred at an unexpectedly early stage (Monday 18th May 2009 for regular wave tests with nominal wave height of 1.3 m and period of 5.0 s), the decision was taken, together with BASF at a meeting in FZK on the next day (Tuesday 19th May 2009), to replace the damaged *Model Alternative A* by *Model Alternative C* using crushed granite stones instead of crushed limestones with a grading of 16/36 mm as shown in Fig. 1.2. Some selected tests performed for *Model Alternative A* before damage were repeated for both *Model Alternatives B* and *C* before proceeding with the test programme as initially planned for *Model Alternatives A* and *B*. Therefore, the present study will address the results related to all three model alternatives (Fig. 1.1 and Fig. 1.2) including the analysis of the damage experienced by *Model Alternative A*.
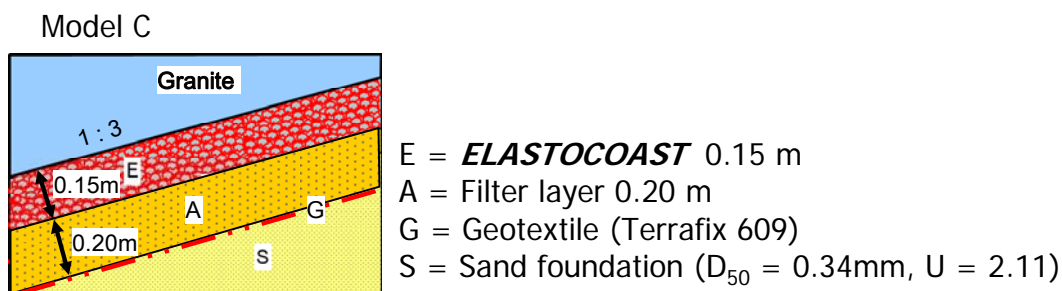
Fig. 1.2:   *Model Alternative* C

1.2 Objectives

As specified in the proposal (FZK, 2008b) and the pre-design report (Oumeraci et al., 2009b), the objective of this study is to achieve a better understanding of the physical processes associated with the wave loading and response of the *ELASTOCOAST* revetment and its foundation. Based on this improved understanding the development of empirical formulae and diagrams are developed to predict:

i)   the reflection performance of the *ELASTOCOAST* revetment which is important for instance to assess the effect on sea bed scour and on navigation;

ii)   the wave run-up and run-down which are important to assess the extent of the revetment up- and downwards and thus the required height of the structure;

iii)   the pressure distribution induced by both breaking and non breaking waves on the surface of the revetment and just beneath the revetment;

iv)   the pore pressure distribution induced by both breaking and non breaking waves at different depths in the soil beneath the revetment.

Moreover, further analysis of the severe failure experienced by *Model Alternative A* based on the preliminary analysis provided just after the occurrence of the damage (Oumeraci et al., 2009a) will be performed, comparing the measurements of the same tests for *Model Alternative B* and the measurements of the previous test with a shorter period for *Model Alternative A*.

2 Model set-up, measuring techniques, and test programme

2.1 Model set-up

The experiments were performed in the Large Wave Flume (GWK) of Hannover, Germany. It is about 300 m long and 5 m wide. The depth of 7 m allows water levels up to 5 m, where regular waves with wave heights up to 2 m and wave spectra with significant wave heights up to 1.3 m can be generated (non-breaking waves). Moreover, solitary waves up to about 1.0 m and "freak" waves (wave focussing) up to 2.5 m can also be generated. The wave generator has an active absorption control, thus providing constant input wave parameters over longer test durations.

A cross section and a section along the flume with the *ELASTOCOAST* revetment (slope 1:3) are given in Fig. 2.1, also showing the x-y coordinate system used for the model construction and the location of the measuring devices. The zero x-position corresponds to the middle position of the wave paddle and the zero y-position to the bottom of the flume.

Fig. 2.1: *ELASTOCOAST* revetment in GWK and location of wave gauges

(a) SAND EMBANKMENT

The embankment was built of sand with a mean grain size of about 0.34 mm. The grain size distribution is given in Fig. 2.2, also showing that $D_{10}=0.18$ mm and $U= D_{60}/D_{10}= 2.11$.

Fig. 2.2:   Grain size distribution of the sand material for the embankment built in GWK

The sand was used to build a 1:3 slope. It was carefully compacted to achieve a uniformly distributed compaction (Fig. 2.3).
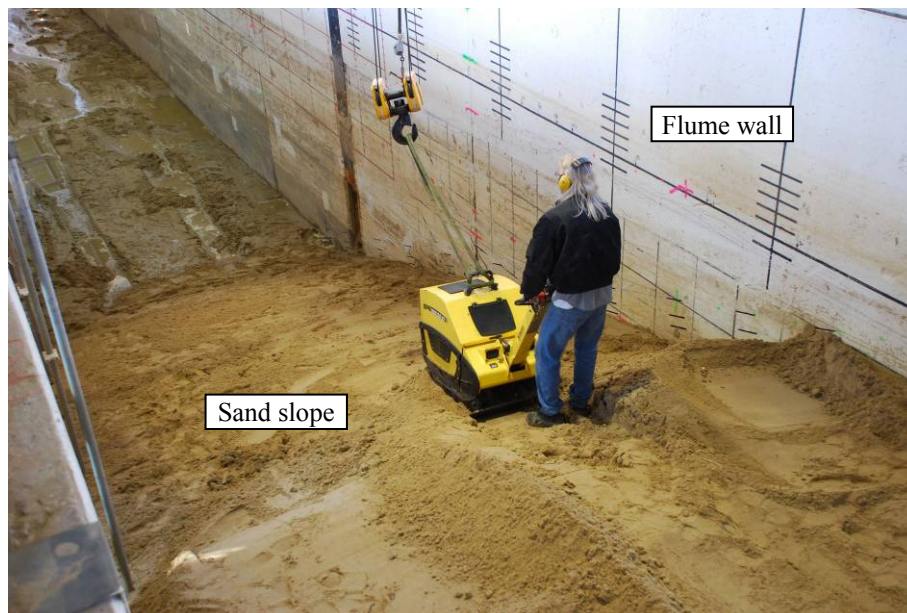
Fig. 2.3:   Compaction of the 1:3 sand slope

(b) LOWER AND UPPER BOUNDARY OF *ELASTOCOAST* REVETMENT

The foreshore of the *ELASTOCOAST* revetment (slope of 1:3) is a sand bed with a slope of 1:20. The toe of the revetment is located 1.0 m above the flume bottom while the crest of the revetment is extended up to 6.70 m near the top edge of the flume which is at 7.00 m (Fig. 2.4).
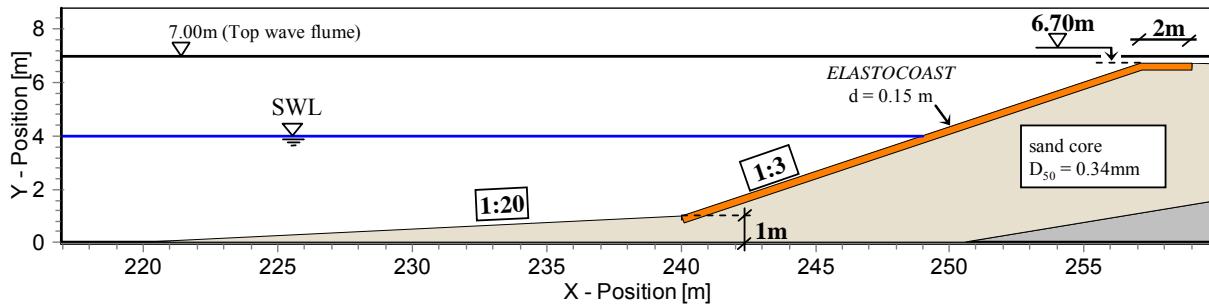
Fig. 2.4: Lower and upper boundary of *ELASTOCOAST* revetment

Following an agreement between BASF and FZK the toe construction as exemplarily shown in Fig. 2.5 for *Model Alternative* B and also depicted during construction in Fig. 2.6 was adopted which corresponds to a design commonly applied in the field.
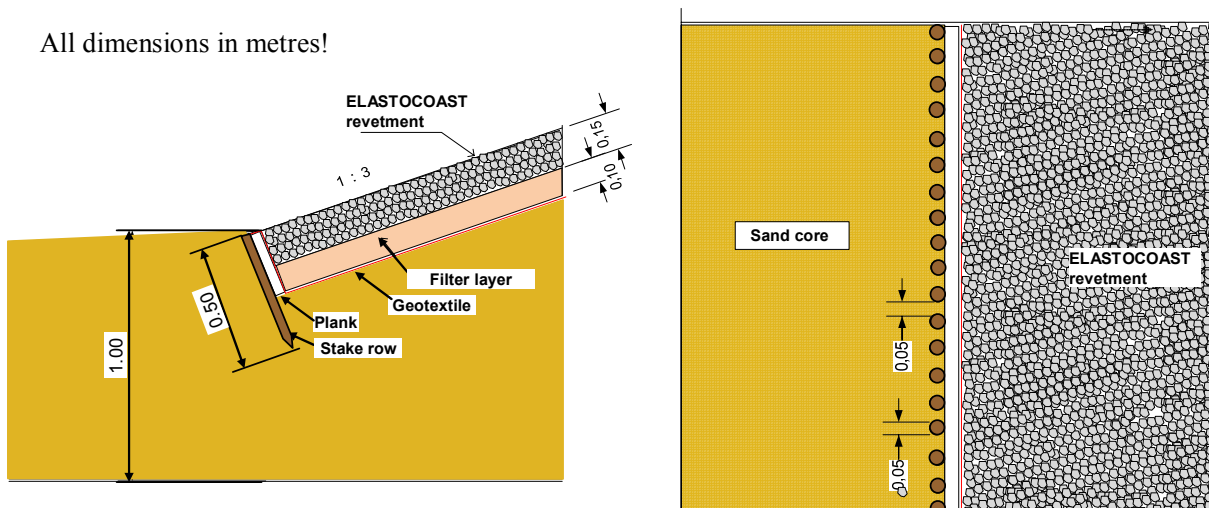
Fig. 2.5: Toe protection of the revetment (exemplarily for Alternative B)
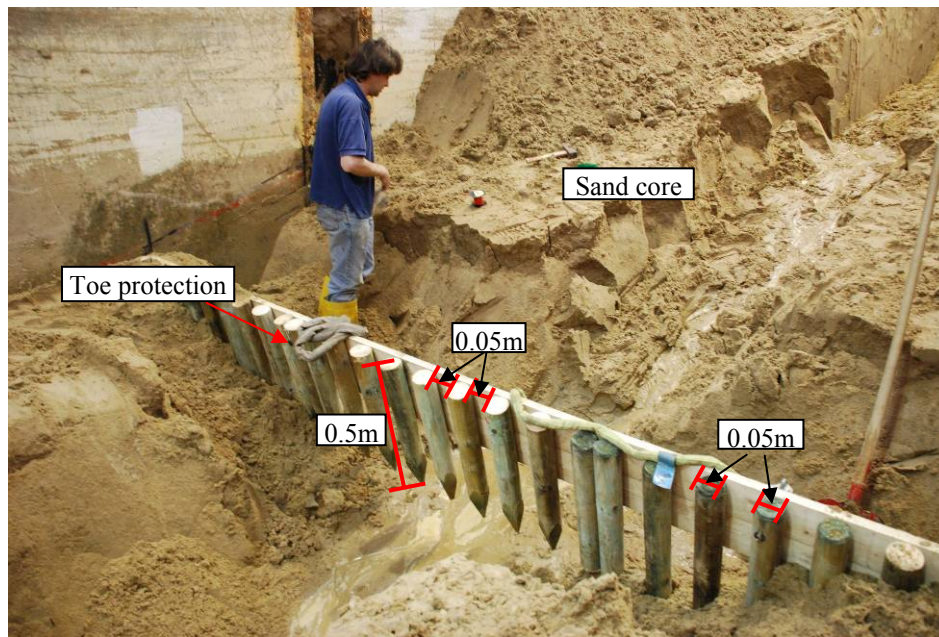
Fig. 2.6:   Toe protection of the revetment during construction

The upper edge of the revetment is located 6.7 m above the flume bottom, thus providing a minimum freeboard of 0.3 m for a better control of the discharge of overtopping water. In order to stabilize the crest of the sand embankment, the *ELASTOCOAST* layer is extended at the crest 2 m in horizontal direction. The sand surface behind the *ELASTOCOAST* crest is stabilized by a geotextile mattress (Fig. 2.7).
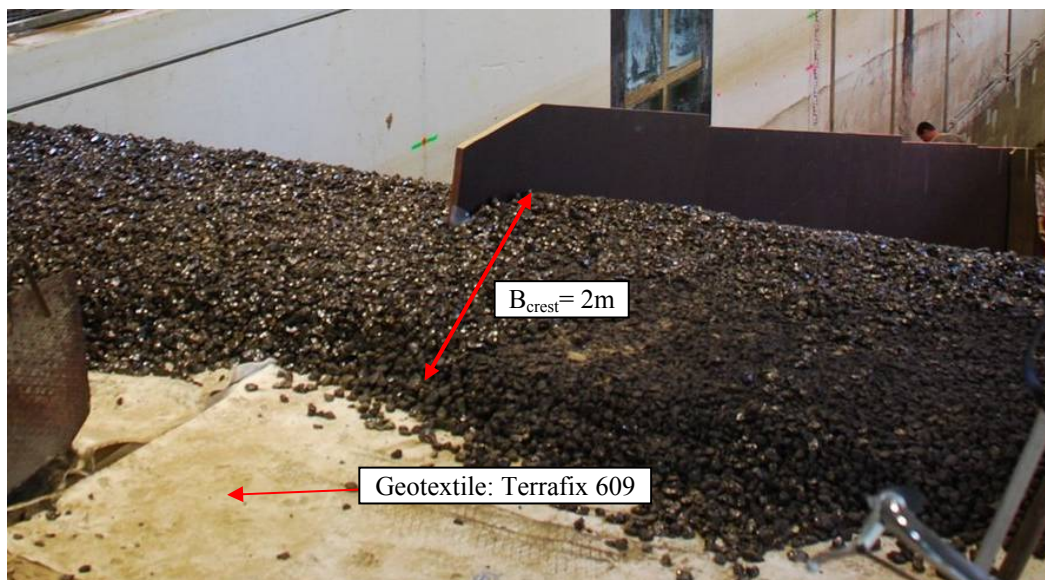
Fig. 2.7:   Crest of the revetment (see also Fig. 2.4)

(c) REVETMENT ALTERNATIVES, GEOTEXTILE AND SEPARATION WALL

In a first phase, the model set-up consists of two alternative revetments. The two *Model Alternatives* A and B were built together side by side, each covering half of the wave flume width (2 x 2.5 m) and tested simultaneously using the same incident wave conditions.

Both model alternatives had an *ELASTOCOAST* layer of the same thickness (d = 0.15 m) made of the same crushed limestones (20/40 mm) bonded together by the same Polyurethane. The difference between the two models consists only in the layer beneath the *ELASTOCOAST* revetment (Fig. 2.8 a, b).

(a) Model A   (b) Model B

E = **ELASTOCOAST** 0.15 m
(crushed Limestone 20/40 mm)
A = Filter layer 0.10 m
(crushed Limestone 20/40 mm)
G = Geotextile (Terrafix 609)
S = Sand foundation
(D_{50} = 0.34mm, U=D_{60}/D_{10}=2.11)
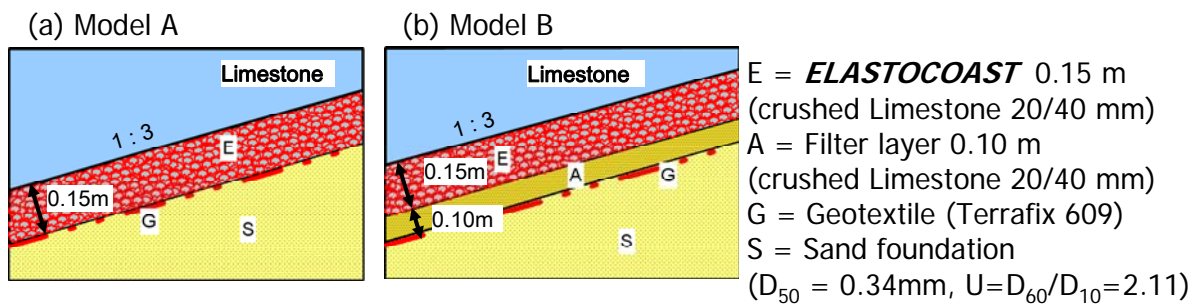
Fig. 2.8:   *Model Alternatives* A and B

In *Model Alternative A* the *ELASTOCOAST* revetment lies directly on a geotextile which was selected to fulfil two requirements: i) capacity to retain the finer fractions of the sand and ii) much higher hydraulic permeability than the sand underneath. Both requirements are fulfilled best by using a non-woven geotextile. Therefore "Terrafix 609" from "Naue Gmbh" is selected. The characteristic hole width O_{90} = 79.9 μm fulfils the first requirement. The hydraulic permeability k (measured at 10°C) is given with $4.7*10^{-3}$ m/s, which is much higher than the permeability of the sand with about k = $1*10^{-4}$ m/s. The detailed specification of the selected type "Terrafix 609" can be found in the test report of Federal Waterways Engineering and Research Institute (BAW, 2005). The selected geotextile is also used to provide a separation between the *ELASTOCOAST* revetment, the sidewalls of the flume and the separation wall (Fig. 2.9).

Fig. 2.9:   Geotextile placed beneath the revetment and extended at the side walls and the separation wall

In *Model Alternative B* a filter layer with a thickness of 0.10 m using the same crushed lime-stone material (20/40 mm) as for the *ELASTOCOAST* revetment is inserted between the *ELASTOCOAST* layer and the geotextile lying on the sand slope (Fig. 2.8b).

The two alternatives are separated by a thin wall made of water resistant plywood. Its extension along the slope from toe to crest underneath the *ELASTOCOAST* surface covers the length of the whole revetment construction, as shown in Fig. 2.10.
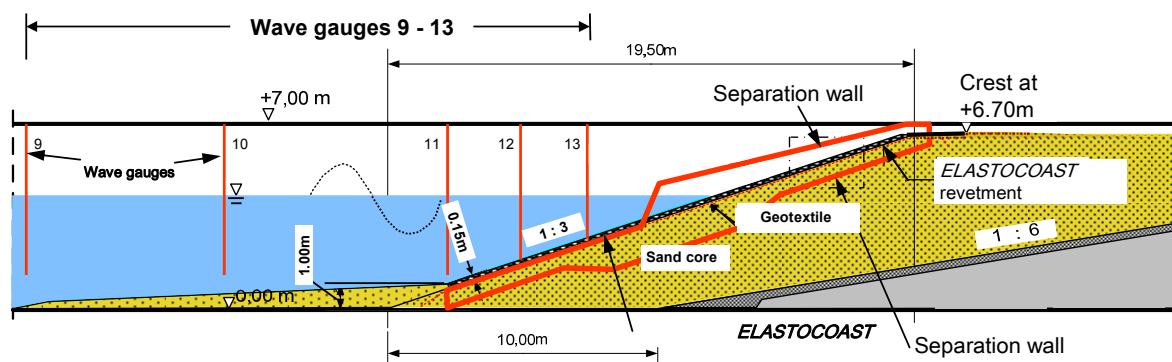
Fig. 2.10: Cross section of model with separation wall

The extent in normal direction to the slope is adapted to the hydraulic boundary conditions which were assessed in the pre-design report (Oumeraci et al., 2009b). The extension above the surface of the slope revetment corresponds to the development of the layer thickness assessed in the same report. At the point of maximum wave run up (pre-assessed with $z_{98} = 0.64$ m) a height of at least 0.76 m corresponding to the maximum water layer thickness

expected during run-up must be provided. The overhang is assumed to decrease linearly in direction to the crest (remaining overhang at the crest =0.3 m, corresponding to the minimum freeboard of 0.3 m). Below the run-down point, the wave kinematics for the different model alternatives can be considered to be similar, therefore no overhang is necessary below the run-down point and it can be reduced to zero.

The embedding depth inside the subsoil in the area of the impact point is derived from the pore pressure development in the subsoil as estimated in the pre-design report (Oumeraci et al., 2009b). At least three times the characteristic length had to be used (3*0.6 m = 1.8 m). Underneath that depth the pore pressure differences between the two model alternatives were assumed to be negligible. Underneath and above the impact area the embedding depth is reduced due to the reduced transmission depth of dynamic pore pressure.

The separation wall must be thin enough to avoid affecting the incident waves and stiff enough to withstand any transversal load due to different hydraulic conditions at the two model alternatives and to minimise the unfavourable effects on the soil parameter due to transversal motions of the wall. Therefore, a vertical stabilization beam is installed near the seaward edge of the wall. The bonding length inside the sand corresponds to the length of the separation wall. The top is fixed at a crossbeam spanning the flume. The different construction phases of the separation wall are illustrated in Fig. 2.11.

The completed separation wall with both *Model Alternatives* A and B are documented in Fig. 2.12b as an overview from the toe of the revetment. All tests were performed with a metal nose on the lower end of the separation wall (Fig. 2.12a).

(a) Positioning the wall

(b) Embedding the wall by sand on both sides

(c) Installed wall with toe

Fig. 2.11: Placement of the separation wall in the sand embankment
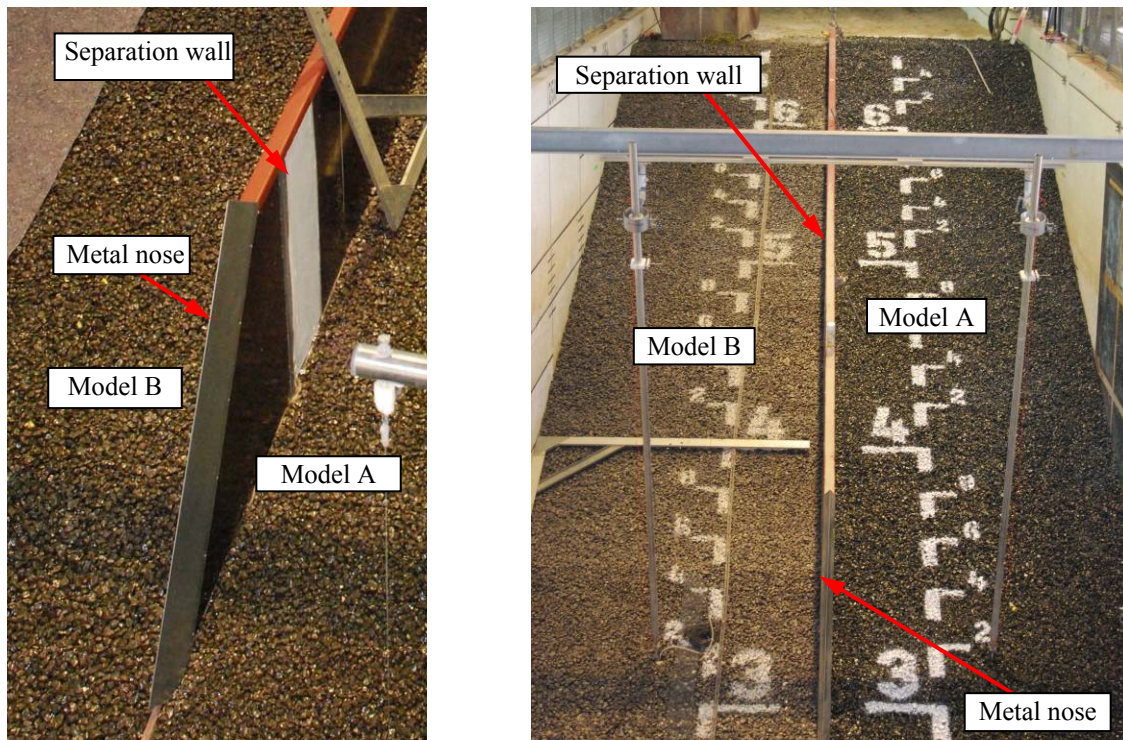
(a) Front view from the toe with metal nose   (b) Front view on revetment A and B with separation wall

Fig. 2.12. Installed separation wall between the two *Model Alternatives* A and B

After the damage of *Model Alternative A* which was built over one half width of the flume (see Annex A), the damaged revetment was completely removed and replaced by a third *Model Alternative C* (Fig. 2.13). This alternative is similar to *Model Alternative A* and *B* but the *ELASTOCOAST* layer consists of crushed granite stones (Grading 16/36 mm) and the thickness of the under layer made of the same stones is with 0.20 m twice as large as *Model Alternative B*.

E = ***ELASTOCOAST*** 0.15 m (crushed Granite 16/36 mm)
A = Filter layer 0.20 m (crushed Granite 16/36 mm)
G = Geotextile (Terrafix 609)
S = Sand foundation ($D_{50}=0.34$mm, $U=D_{60}/D_{10}=2.11$)
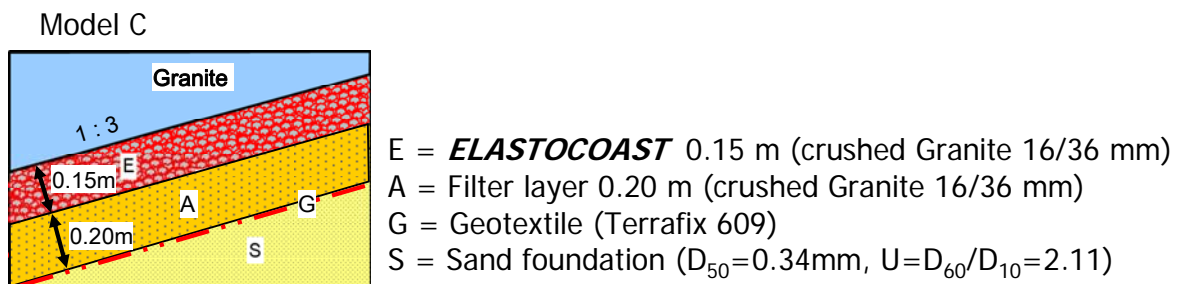
Fig. 2.13: *Model Alternative* C (built after failure of *Model Alternative* A)

Hydraulic properties of the crushed stone material used for the *ELASTOCOAST* and the under layer can be approximately estimated from data earlier provided (Muttray, 2000) where similar crushed stones with $D_{50}=34$ mm in the core of rubble mound breakwater tested in GWK

were used. The porosity n was estimated to n = 0.388 and the FORCHHEIMER coefficients a and b were determined to a = 0.89 and b = 23.0, including inertia coefficient c = 0.41 if the extended Forchheimer equation is used (for similar wave heights and periods as used in the present study).

2.2 Measuring and observation techniques

2.2.1 Overview, synchronisation and data acquisition system

The type, number, and optimal location of the measuring devices and observation techniques were determined on the basis of a desk study performed for this purpose by using existing analytical, semi-empirical, and numerical models to assess wave run-up and run down processes, wave pressure distributions on and just beneath the *ELASTOCOAST* revetment as well as the wave-induced pressure distribution at different depths in the sand beneath the revetment (Oumeraci et al., 2009b). Based on the results of this study, a total of 86 measuring devices and two digital video cameras connected to a data acquisition system have been installed (Fig. 2.14). As a result a total of 88 measuring channels are obtained consisting of 15 wave gauges, 4 wave run-up gauges, 10 gauges together with two ultrasonic devices for the water layer thickness in the swash zone, 3 velocity propellers for the velocity of the waves running up the slope, 48 pressure transducers, 2 inductive displacement meters, 2 accelerometers and 2 control signals. As illustrated in Fig. 2.14, the same devices are placed at the same location for both model alternatives built side by side in the wave flume.

All measuring devices and the two video cameras are synchronised. The position of the measuring and observation devices is displayed in Fig. 2.14. The coordinates of the measuring devices are listed in Annex A.
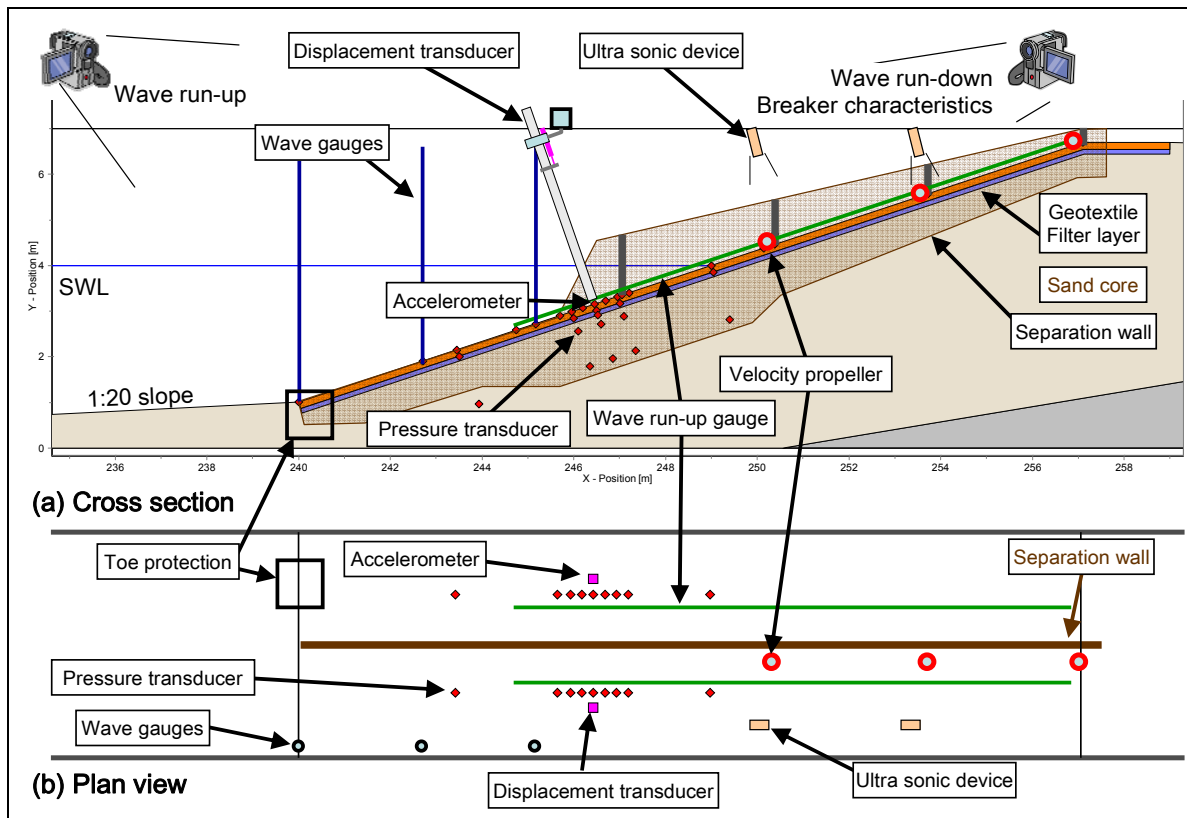
Fig. 2.14: Measuring and observation devices at and beneath the revetment – Overview

The data acquisition system, shown in Fig. 2.15, consists of 11 amplifiers, 2 analogue digital converters, each of them converting the signals of all 88 channels in a redundant array and sending the data respectively to one of the 2 data acquisition computers where the signals are recorded.
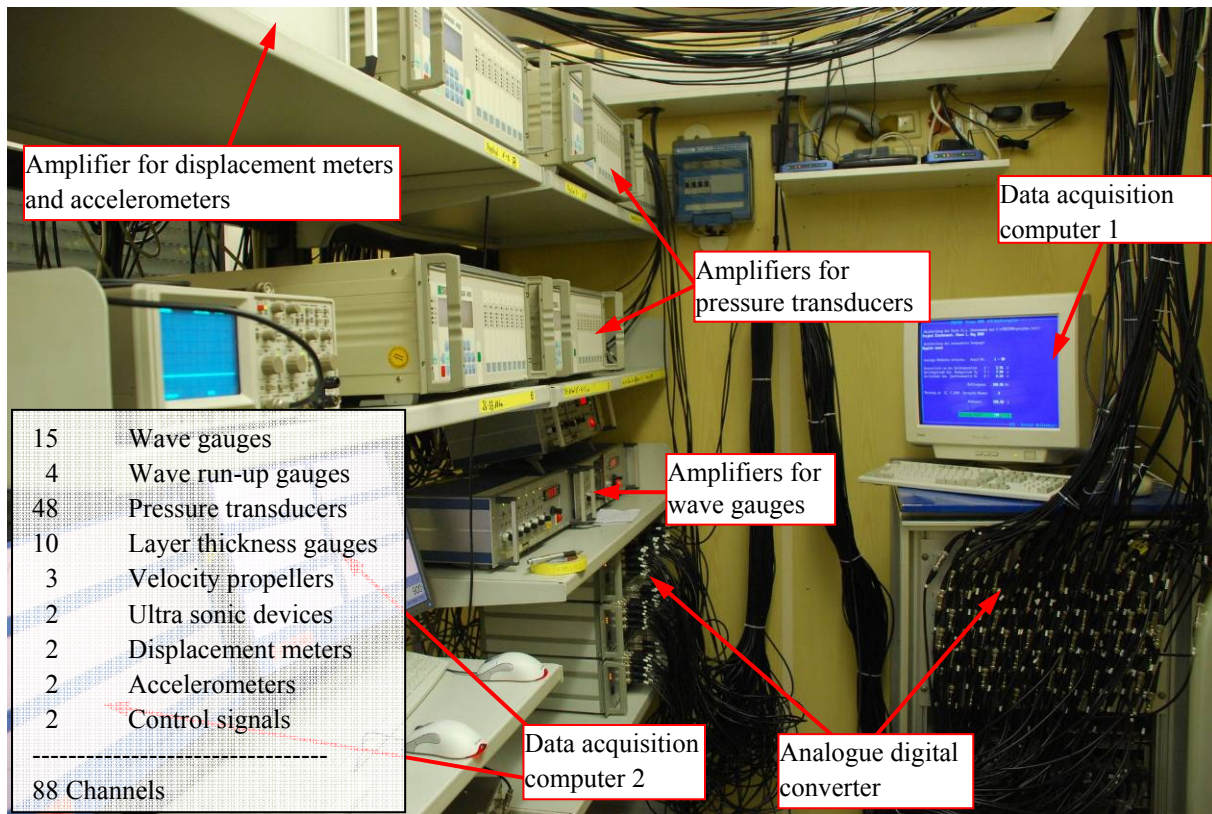
Fig. 2.15: Data acquisition system

2.2.2 Pressure transducers

A total of 48 pressure transducers are installed for both model alternatives to measure on one hand the wave load and especially the impact load on the surface of the slope revetment, underneath the *ELASTOCOAST* layer, and at the bottom of the filter layer, and on the other hand the wave-induced pore pressure inside the embankment and the fluctuation of the internal water level.

Pressure transducers on the surface of the revetment

According to the results of the numerical simulations performed in the pre-design report (Oumeraci et al., 2009b), the area of large pressure gradients during impact spreads over about 1 m (horizontally) around the impact point. Therefore, seven pressure transducers (PT02 - PT08 for *Model Alternatives A* and *C*, PT27 - PT33 for *Model Alternative B*) with a distance of $\Delta x = 0.25$ m cover the impact area. The corresponding locations are shown in Fig. 2.16 for *Model Alternative A* (without filter layer); in Fig. 2.17 for *Model Alternative B* (with filter layer of 0.10 m), and in Fig. 2.18 for *Model Alternative C* (filter layer of 0.20 m). One further transducer (PT09, PT39) is located near the still water level in order to better define an upper boundary for the impact pressure measurement and to measure the quasi-

hydrostatic load during run-up. A corresponding transducer (PT01 for Models A and C; PT26 for Model B) is located 3 m seaward of the impact point (in x-direction) for the measurement of the quasi-hydrostatic wave pressure.
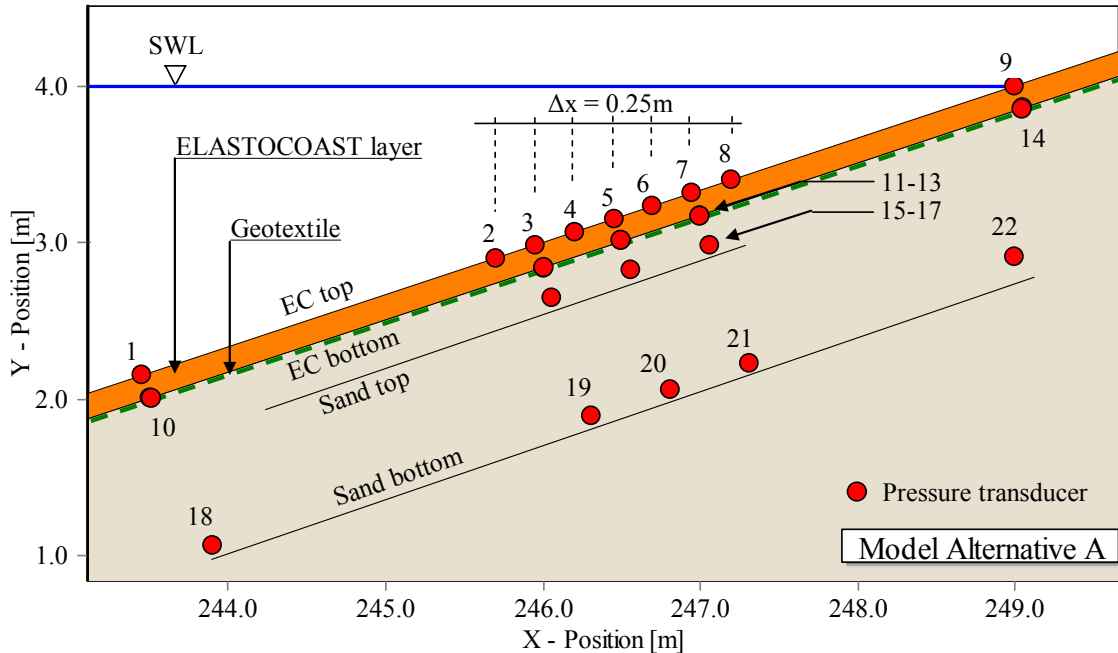
Fig. 2.16: Locations of pressure transducers in *Model Alternative* A
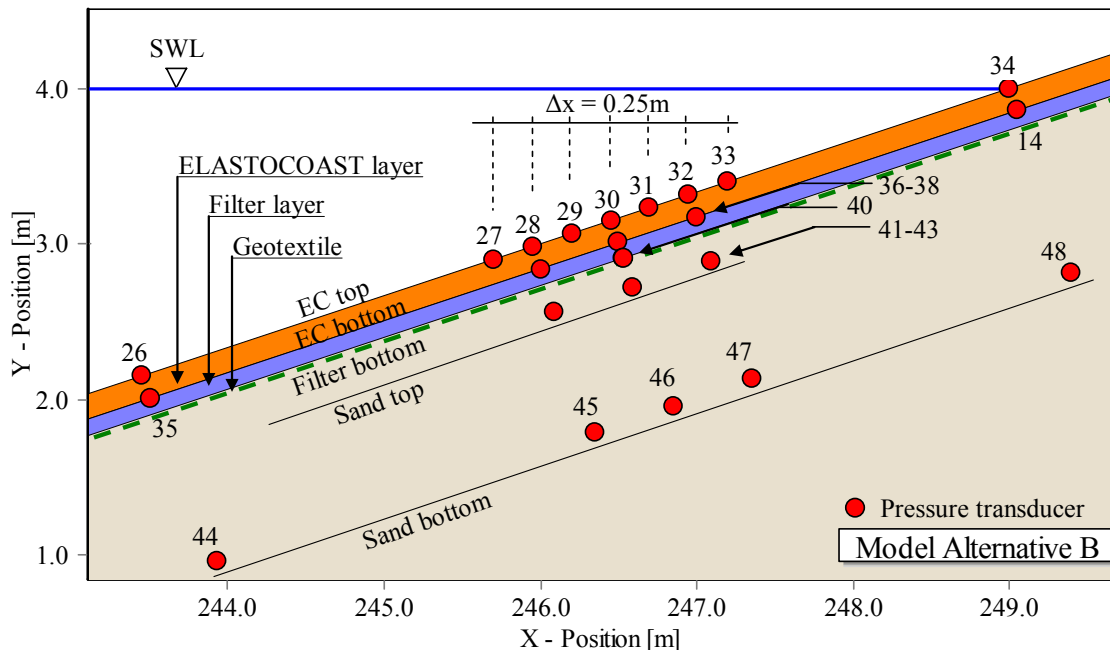
Fig. 2.17: Location of pressure transducer in *Model Alternative* B
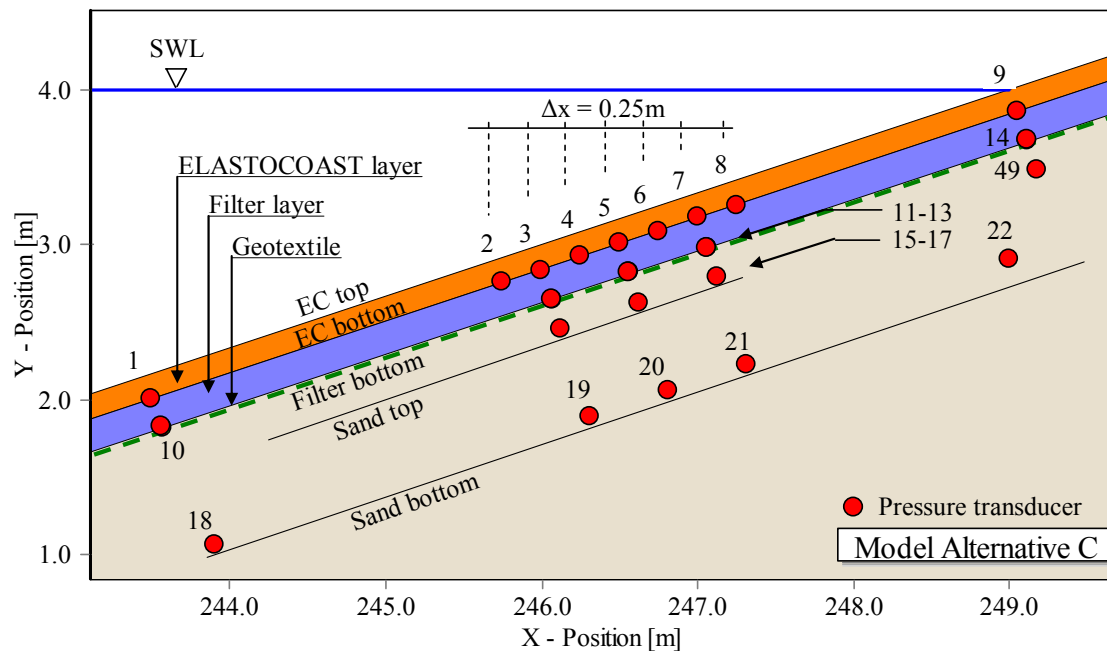
Fig. 2.18: Location of pressure transducers in *Model Alternative* C

Pressure transducers beneath *ELASTOCOAST* revetment:

Based on the results of the pre-design report (Oumeraci et al., 2009b) the number of transducers required within the impact area just beneath the revetment has been reduced to three transducers (PT11-PT13 for Models A and C, and PT36-PT38 for Model B). Two transducers (PT10, PT14 exemplary for Model A) at the outer boundaries complete the transducer distribution in the plane just beneath the *ELASTOCOAST* layer (see Fig. 2.14-Fig. 2.18).

Since the total thickness of the revetment including the filter layer differs for the three model alternatives, this implies some differences in the installation of the pressure transducers in *Model Alternatives* A, B, and C.

In *Model Alternative A* without any gravel filter layer, a total of 22 pressure transducers are installed distributed over four layers: one on the surface of the revetment slope (PT01-PT09), one just beneath the *ELASOTOCOAST* layer (PT10-PT14) and two in different depth within the sand embankment (PT15-PT17 and PT18-PT22), see Fig. 2.16.

In *Model Alternative B* with a gravel filter layer of 0.10 m (Fig. 2.17) a total of 23 pressure transducers are installed in a similar manner as in *Model Alternative A,* but an extra transducer (PT40) has been added just above the geotextile in order to measure the pressure damping in the filter layer. No further transducers are necessary because the damping is expected to be similar along the slope.

In *Model Alternative C* with a gravel filter layer of 0.20 m which was built to replace the damaged and removed *Model Alternative A,* a total of 23 pressure transducers were installed

in a similar manner as for *Model Alternative A* with the exception (i) that the two upper layers of the transducers (on the surface and just beneath the 0.15 m thick *ELASTOCOAST* layer) are shifted to the surface of the filter layer and just beneath and (ii) that one additional pressure transducer (PT49) was placed in the sand top layer.

To record the fluctuation of the internal water table three pressure transducers were added on the side of *Model Alternative A* and *Model C* in x-positions of 251.1 m, 253.6 m and 255.6 m at a distance of 2.91 m apart from the flume bottom (Fig. 2.19).
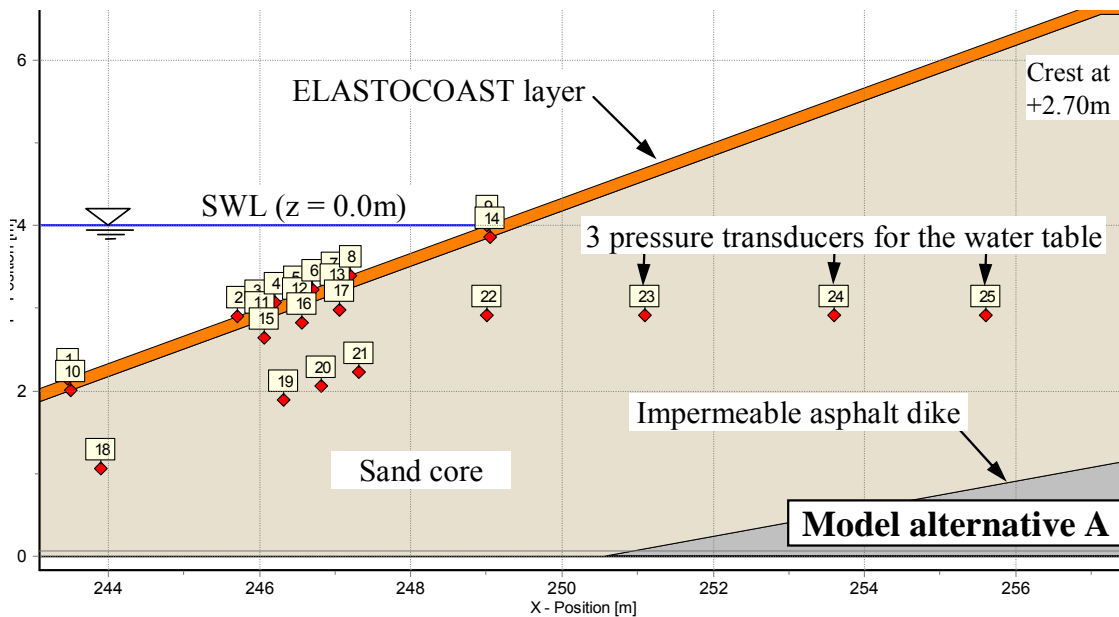
Fig. 2.19: Location of additional pressure transducers to record the internal water table

To ensure an accurate position of the pressure transducers they were mounted on a rigid frame which could be embedded in the sand core precisely. To protect them from damage during construction as well as during the testing phase they were coated by geotextile (Fig. 2.20).
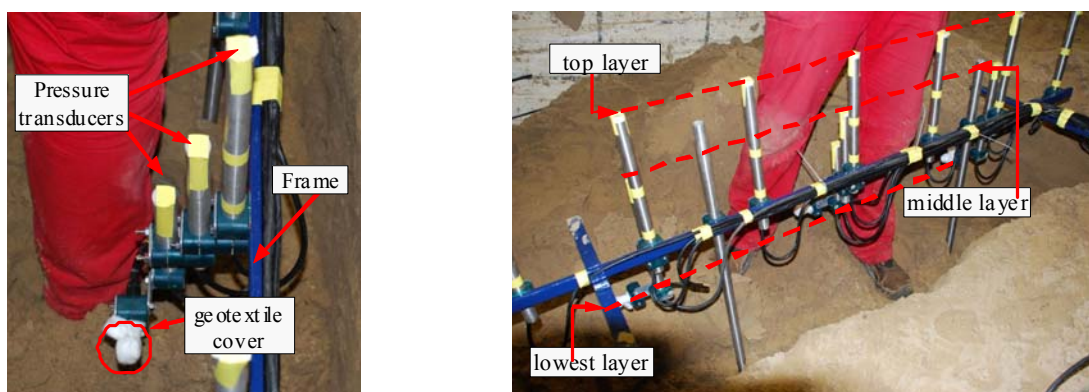
(a) Holding frame with pressure transducers

(b) Detail of holding frame

Fig. 2.20: Installation of pore pressure transducers

2.2.3 Wave gauges

To record the waves along the wave flume up to the *ELASTOCOAST* model, 13 resistive wire gauges are installed on the side wall of the flume (Fig. 2.10 and Fig. 2.21). The locations of the wave gauges along the flume are defined in Annex A and indicated in Fig. 2.1, showing (i) one array with four gauges in the far field (WG 1-4), and (ii) one array with four gauges in the near field (WG 5-8) to perform a reflection analysis as well as (iii) five wave gauges well-distributed over the sloped foreshore (WG 9-13), three of which (WG 11-13) being also depicted in Fig. 2.22.

(a) WG 10 in the flume   (b) Principle sketch
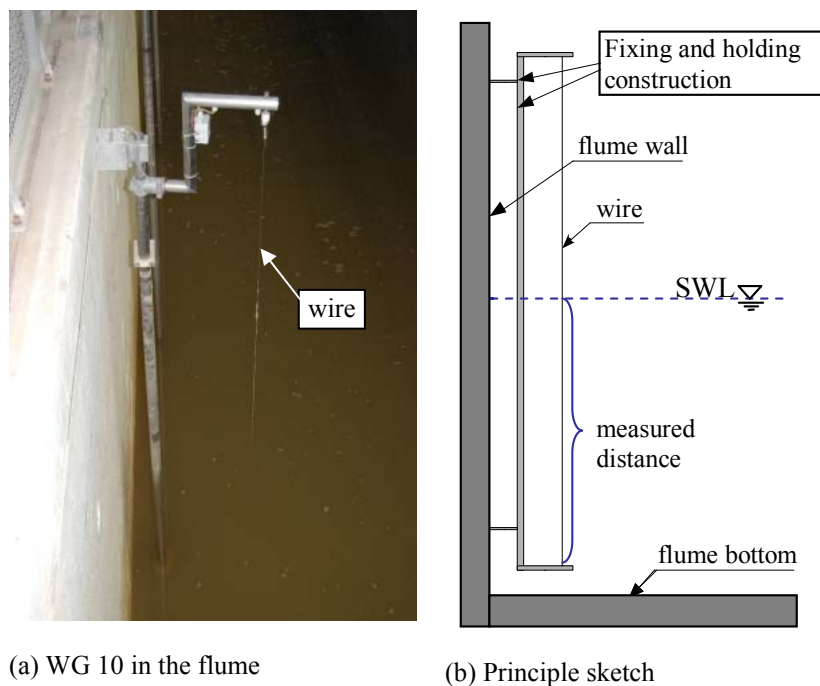
Fig. 2.21: Resistive wave gauges fixed at the side wall of the wave flume
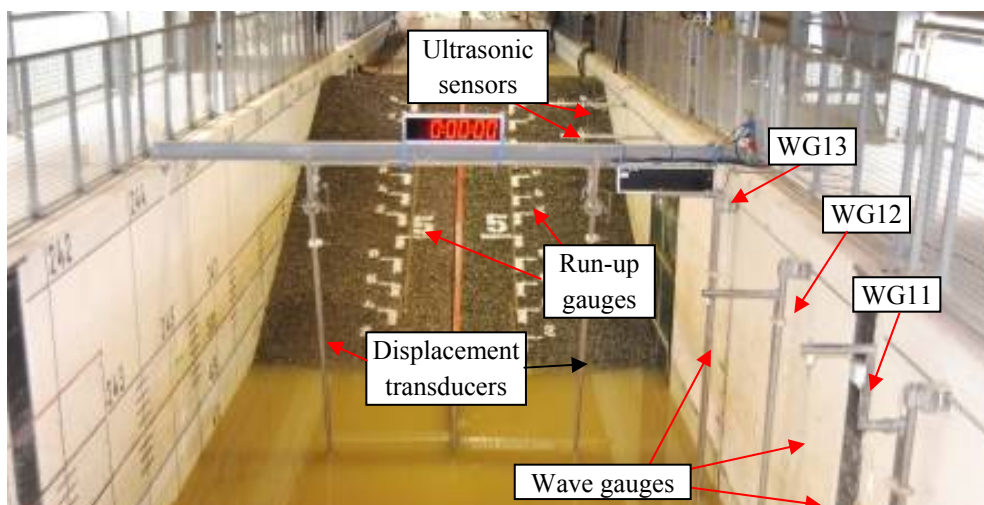
Fig. 2.22: Wave gauges over the sloped seabed

2.2.4 Wave run-up gauges, water layer thickness gauges and velocimeters

(a) Run-up gauges

Wave run-up gauges were fixed on each of the revetment alternatives along the slope and are based on the same principle (resistive wire) as the wave gauges described above. Due to the large length of the slope two gauges are mounted together on each side to cover the entire wave run- up and run-down area (Fig. 2.22). The measuring area covered along the slope is indicated in Fig. 2.23 while the location on the slope is shown in Fig. 2.24a and the connection between the two gauges in Fig. 2.24b. The white painting on the slope is to record the wave run up by video for comparison (see Section 2.2.6).
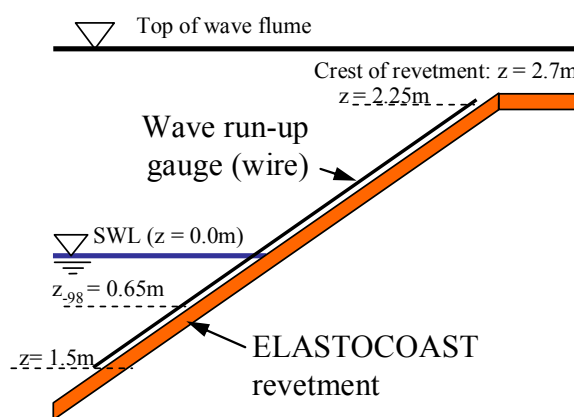
Fig. 2.23: Principle sketch of the wave run-up gauges
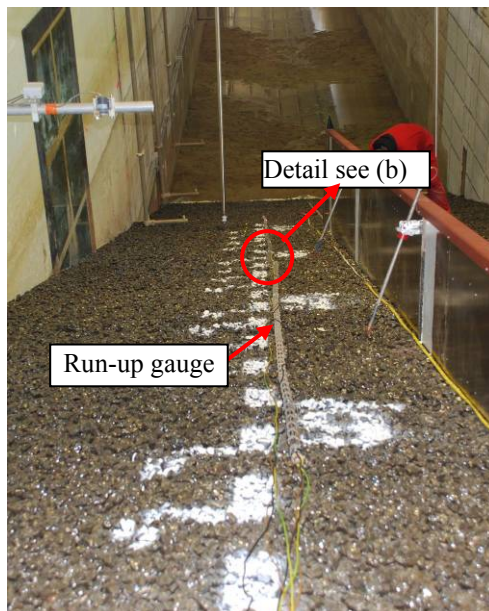
(a) Run-up gauge in Model A   (b) Connection of the two run-up gauges
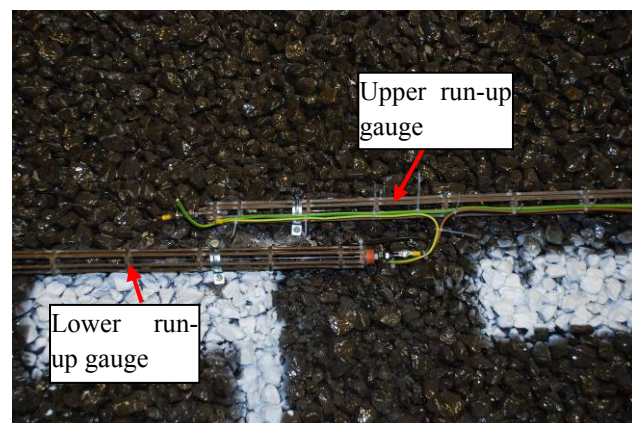
Fig. 2.24: Run-up gauges installed in the wave flume

(b) Layer thickness gauges

On each side of the separation wall five step gauges are installed to record the layer thickness of the water running up and down the slope of Model A/C (LTG 1-5) and Model B (LTG 6-10). The step gauges consist of electrodes at distances of 1, 2 or 5 cm which define the measuring increment (Fig. 2.25a), i.e. in contrast to the aforementioned resistive wave gauges the record is discontinuous (stepwise) and the measurement accuracy therefore depends on the selected distance between the electrodes.

The step gauges are placed at different locations along the separation wall which are defined in Annex A. The three upper locations are indicated in Fig. 2.25b. At the location just above the impact zone two step gauges with 1 cm (LTG 2 and LTG 7) and 2 cm (LTG 3 and LTG 8) electrode distances are installed above each other. The two upper step gauges have 1 cm (LTG 5 and LTG 10) and 2 cm (LTG 4 and LTG 9) electrode distances. The lowest step gauges are located just next to the nose of the separation wall (LTG 1 and LTG 6) with electrode distances of 5 cm.

(a) Layer thickness gauge

(b) Location Model A
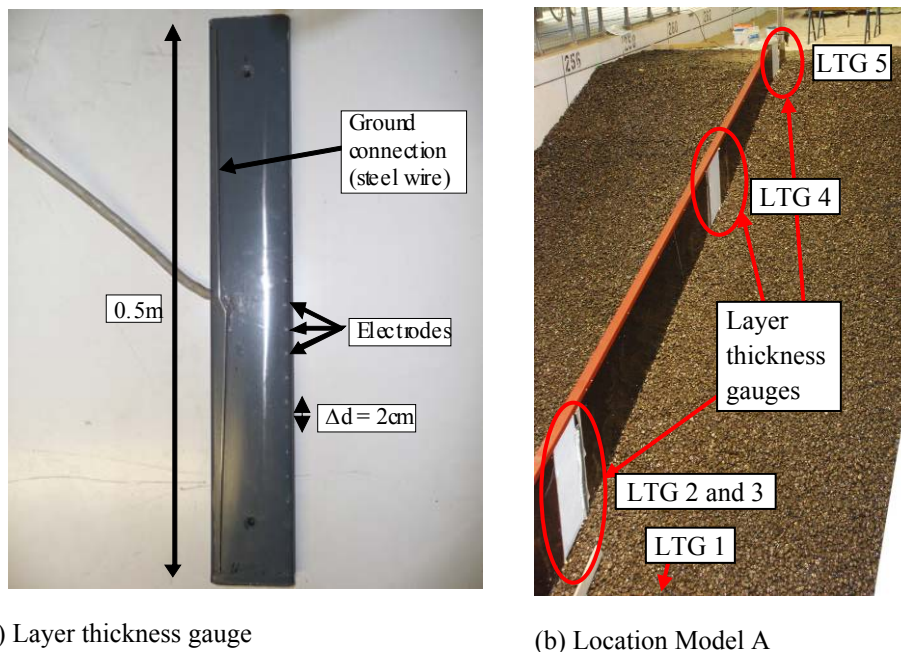
Fig. 2.25: Layer thickness gauges installed in the wave flume

(c) Ultrasonic sensors

Over the slope of Model A and later also Model C two ultrasonic sensor M300/95 (MASSA) are installed to tentatively record the layer thickness of the water running up the slope (Fig. 2.26). High frequency ultrasonic signals are emitted within an angle of 8° and reflected by the target object which is in this case the surface of the water layer. The distance to the target is obtained from the time for the reflected echo to return to the sensor and the speed of sound which is also provided by the sensor as a function of the temperature. During the instal-

lation it is also possible to define the minimum and maximum distance which is measured (Fig. 2.26b). This can be important for minimizing problems which may occur for instance through splashing water (for more details on the capabilities and limitations of the M-300/95 sensor see report by Oumeraci & Staal, 2009). Both sensors are installed at the same locations along the slope as step gauges (LTG 2 and LTG 4) in order to compare the results.
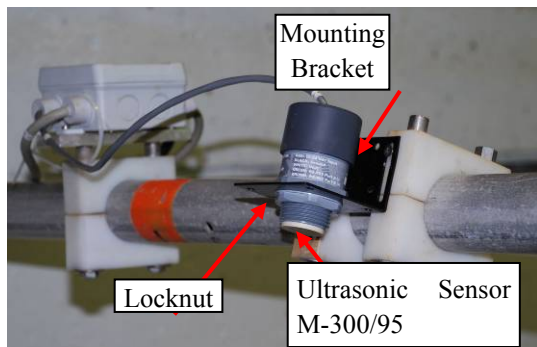
(a) Installation system
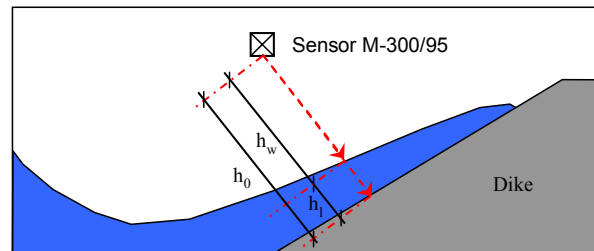
(b) Principle of layer thickness measurements
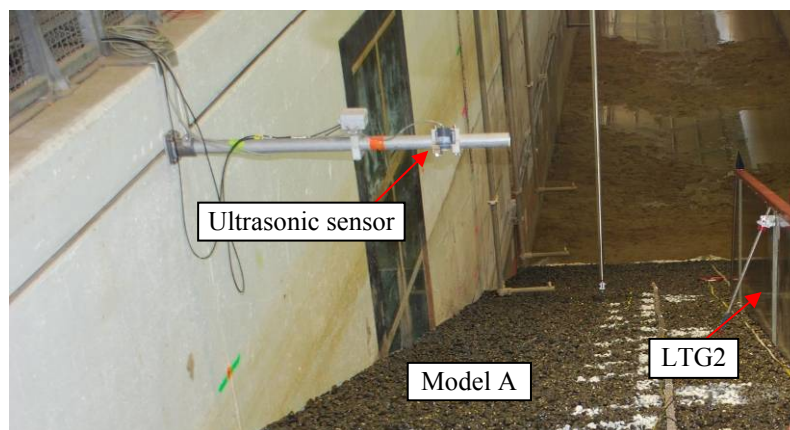
(c) Installed ultrasonic sensor for *Model Alternative* A

Fig. 2.26: Ultrasonic sensors to tentatively record the water layer thickness on the slope

(d) Velocity meters

To measure the velocity of the water layer running up the slope three micro-propellers (D = 11 x 15 mm, Type C-43921 from Schiltknecht Messtechnik AG) are installed at the same location as the three upper layer thickness gauges (LTG 2, 4 and 5). They are fixed at the separation wall on the side of Model A/C as shown in Fig. 2.27.
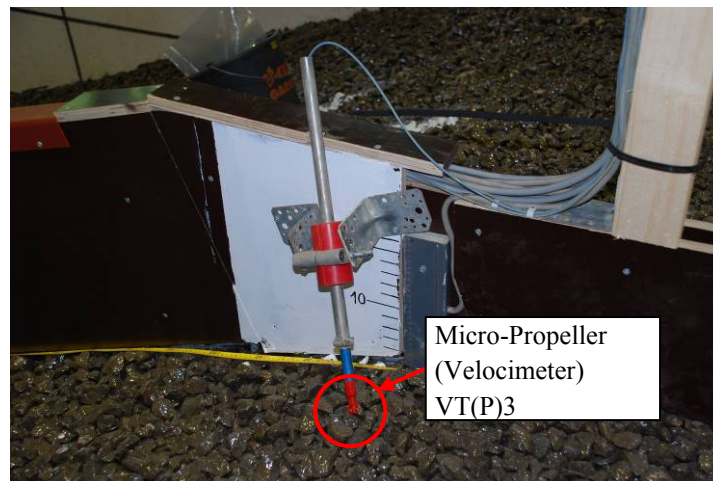
Fig. 2.27: Micro-propeller at the separation wall near the revetment crest

2.2.5 Displacement meters and accelerometers

The dynamic response of the *ELASTOCOAST* revetment to the wave load essentially consists in flexural motions normal to the slope. To record these motions on Models A, B, and C, inductive displacement transducers (Plunger type "Wal" from Hottinger Baldwin Messtechnik) were installed in the impact zone. As the measurement device is very sensitive to high water pressures and sediments, the device is located in a certain distance to the surface of the *ELASTOCOAST* revetment. The motions are transferred by a very stiff light aluminium tube from the surface to the transducer, which is fixed at a crossbeam spanning the flume. The location of the devices and the set-up of the displacement meter are shown in Fig. 2.28a.

The aluminium tube is fixed with a hinge bearing (anchor) at the revetment (Fig. 2.28c) while the upper edge passes a sliding sleeve thus enabling only axial motions. The sliding sleeve is fixed at the crossbeam (Fig. 2.28b). The axial motions, which correspond to the revetment motions normal to the slope, are thus recorded by the displacement meter.

In addition, accelerometers (Type ARH-100A from Tokyo Sokki Kenkyujo Co. Ltd.) were fixed to the revetment at the same location as the displacement meter (Fig. 2.28c) to tentatively record the accelerations of the revetment normal to the slope (Fig. 2.29)
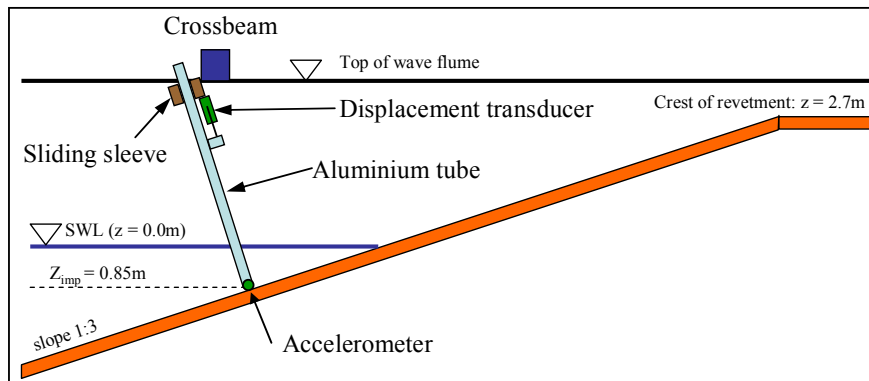
(a) Setup and location of displacement meter and accelerometer
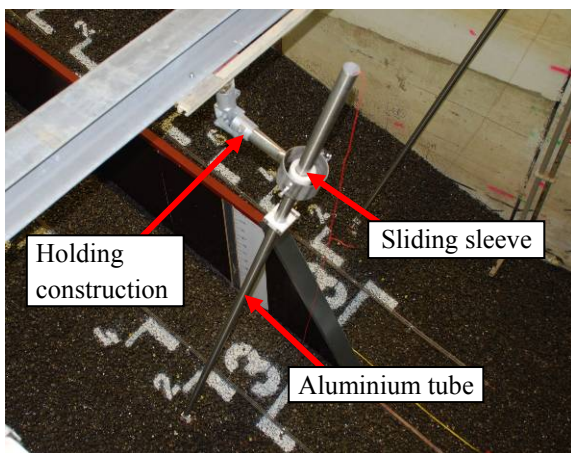
(b) Sliding sleeve and holding construction
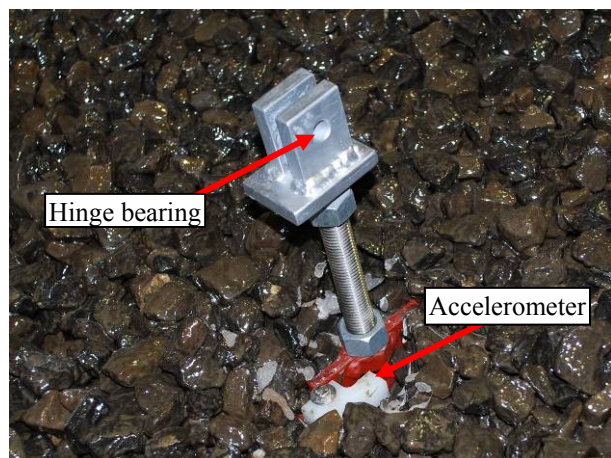
(c) Hinge bearing (anchor) and accelerometer

Fig. 2.28: Set-up of the inductive displacement meter and accelerometer

Fig. 2.29: Accelerometer before the installation on the *ELASTOCOAST* revetment

2.2.6 Observation techniques

For a better interpretation and verification of the signals recorded by most of the installed transducers several observation methods were used. As indicated in Fig. 2.14, two fixed video cameras were deployed during each test where one essentially focussed on the breaking impact zone, and the other one on the entire run-up and run-down zone (swash zone). To enable and facilitate the comparison of the video observations with the measurements from the transducers further supporting means were used, including:

- Two video clocks controlled by the same trigger signal as the 88 measuring channels which were synchronised together (Fig. 2.30a, b),

- Labelling on the revetment and on the side wall of the flume (Fig. 2.30a) as well as on the separation wall (Fig. 2.30c),

- An additional mobile camera was also used to check the layer thickness gauges and to record further possible events.
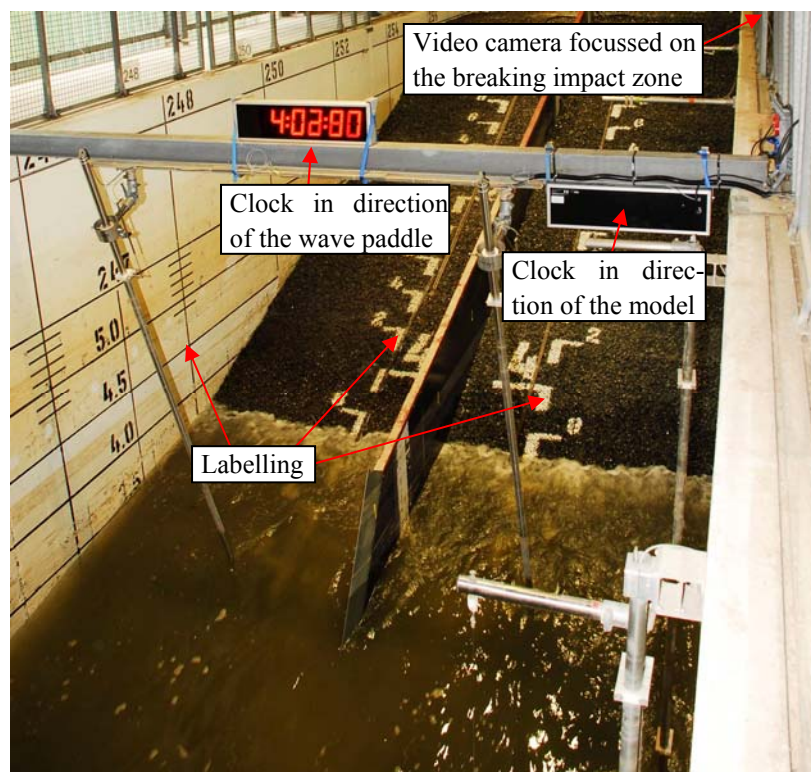
(a) Labelling on the *ELASTOCOAST* revetment
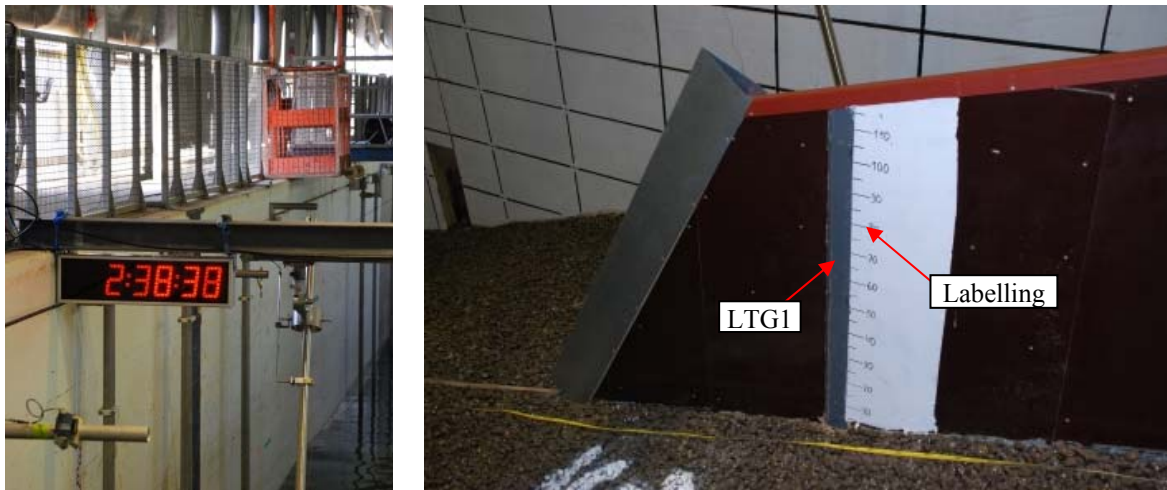
(b) Clock in wave direction   (c) Labelling and Layer thickness gauge at separation wall

Fig. 2.30: Deployed observation techniques

2.3 Test conditions, programme and procedure

Since the measurement and observations are intended to provide a better understanding of the processes involved and the determination of empirical design formulae for wave reflection, wave run-up and run-down, location of impact point, wave pressure distribution on and beneath the slope as well as pore pressure distribution in the soil beneath the revetment, the focus is put on a systematic variation of the wave parameters using both regular waves (process understanding) and wave spectra (design). In addition, the effect of solitary wave and "freak waves" were also briefly examined. The still water level was varied among the tests to direct the impact point of the breaking waves to the densely arranged pressure transducers of the impact area.

2.3.1 Test conditions and test programme

This section describes the test conditions and the test programme for all configurations used for the three structures described in section 2.1. In Tab. 2.3 and Tab. 2.4 the combination of wave heights and wave periods are summarised. The desired (nominal) values, indicated by the suffix "nom", are given regardless to the analysed values later in this report.

Since the main goal of the study is to come up with empirical formulae/diagrams which can be used for design purposes, the main focus was put on the experiments with *wave spectra*. A variation of the wave parameters over a range relevant for common design conditions will allow obtaining more generic results. As the majority of application cases are expected at the shoreline around the Northern Sea, JONSWAP spectra are used for the generation of irregular

waves. The number of irregular waves generated per test initially was at least 1000. The spectra generated for the tests with irregular waves and large wave parameters at the end of the testing phase comprised of at least 500 waves because of the capability limits of the wave generator. But tests showed that the reduction of the number of waves from 1000 to 500 did not affect noticeably the results of the statistical analysis. The characteristics of the JONSWAP spectrum used are the Peak factor $\gamma = 3.3$ and the Groupiness factor GF = 0.7 – 0.8.

Regular waves are necessary for a better understanding of the associated processes at and beneath the revetment. However, the variation of wave parameters can be restricted without loosing any valuable information. For most of the tests with regular waves the number of waves per test was at least 100. In the end of the testing phase the number of waves was reduced to 50 and then to 30 waves.

These considerations have initially led to the wave parameter matrix compiled in Tab. 2.1. Regular waves (indicated by "R") and wave spectra (indicated by "S" and highlighted in green) are considered. Tab. 2.1 includes wave heights larger than the maximum wave height ($H_{max} = 1.5$ m) used for the calculation of the hydraulic boundary conditions in the pre-design report (Oumeraci et al., 2009b). The irregular wave tests highlighted in yellow (Tab. 2.1) were planned to be performed only when there is still time available in the testing phase of the project.

> *Remark:*
>
> *The model setup and the locations of the pressure transducers were adjusted for large impact loads due to breaking waves. In case of waves with smaller wave heights, the impact point was expected to shift shoreward outside the area covered with pressure transducers. For these wave conditions the water level in the flume was therefore adjusted in order to move the impact zone back to the area covered by the pressure transducers. The necessary change in water level was determined during the test phase.*

The limiting wave steepness is calculated by the Miche-formula (Eq. (2.1)):

$$\left(\frac{H}{L}\right)_{max} = 0.142 \tanh \frac{2\pi h_s}{L} \tag{2.1}$$

with:

L   [m]   wave length for water depth $h_s = 4.0$m

Tab. 2.1: Initially planned test programme matrix with wave parameters for water depth h_s=4.0m

Wave Period T or Tp [s]		Wave Height H or H$_s$ [m]														
		0.2	0.3	0.4	0.5	0.6	0.7	0.8	0.9	1.0	1.1	1.2	1.3	1.4	1.5	1.7
3.0	R	R				R				R		Breaking due to wave steepness				
	S	S	S	S	S											
4.0	R	R				R				R			R			
	S	S	S	S	S	S	S									
5.0	R	R				R				R			R		R	
	S	S	S	S	S	S	S	S	S	S						
6.0	R	R				R				R			R		R	R
	S	S	S	S	S	S	S	S	S	S	S					
7.0	R	R				R				R			R		R	R
	S	S	S	S	S	S	S	S	S	S	S					
8.0	R	R				R				R			R		R	R
	S	S	S	S	S	S	S	S	S	S	S	S				
Water depth h$_s$=4.0m																

Optional Wave spectra Not generable

Information about the expected breaker types is given in Tab. 2.2. The wave steepness H/L (or H_s/L) is calculated by the Fenton/McKee equation for the local wave length in the flume (h_s = 4.0m) by using linear wave theory:

$$L = L_0 \left(\tanh \left(\frac{2\pi h_s}{L_0} \right)^{3/4} \right)^{2/3} \tag{2.2}$$

with:

L_0 [m]   wavelength in deepwater $L_0 = \dfrac{g \cdot T}{2\pi}$ (2.3)

h_s [m]   water depth
T   [s]   wave period

The surf similarity parameter ξ_d (= $\xi_{m-1,0\,f}$ for wave spectra) relates the slope angle α to the wave steepness H/L_0 (=$H/L_{m-1,0}$ for wave spectra) calculated by the wavelength L_0 in deep water according to Eq. (2.4):

$$\xi_{m-1,0} = \frac{\tan \alpha}{\sqrt{H/L_{m-1,0}}} \tag{2.4}$$

with:

$L_{m-1,0}$ [m]   wave length corresponding to wave period $T_{m-1,0}$
$T_{m-1,0}$ [s] m_{-1}/m_0 mean wave period
m_0, m_{-1} [-]   zeroth and negative first moment of the energy density spectrum S(f) with
         $m_n = \int S(f) f^n df$

f   [Hz]   frequency in the wave energy spectrum

Model set-up, measuring techniques, and test programme

Depending on the value of the surf similarity parameter, surging breakers ($\xi_d > 3.3$), collapsing breakers ($2.6 < \xi_d < 3.3$), and plunging breakers ($\xi_d < 2.6$) are indicated in Table 2.3 by different colours. The dispersion parameter h_s/L (relative water depth) for all tests varies between 0.083 ($T = 8$ s) and 0.298 ($T = 3$ s), corresponding to the transition zone between deepwater and shallow water conditions.

The plunging breakers are preferably used for the investigation of the impact load at the *ELASTOCOAST* revetment, while the surging breakers are more relevant for the wave run-up and the development of residual pore pressure in the sand. Like in Tab. 2.1, the optional tests are also highlighted in yellow in Tab. 2.2.

Tab. 2.2: Initially planned surf similarity parameter, wave steepness and breaker types

		Wave Height H or H_s [m]															
		0,2	0,3	0,4	0,5	0,6	0,7	0,8	0,9	1,0	1,1	1,2	1,3	1,4	1,5	1,7	
	3,0	2,79	2,28	1,98	1,77	1,61	1,49	1,40	1,32	1,25	1,19	Breaking due to wave steepness					ξ
		0,015	0,023	0,030	0,038	0,045	0,053	0,060	0,068	0,076	0,083						H/L
	4,0	3,73	3,04	2,63	2,36	2,15	1,99	1,86	1,76	1,67	1,59	1,52	1,46	1,41		1,28	ξ
		0,010	0,014	0,019	0,024	0,029	0,034	0,038	0,043	0,048	0,053	0,058	0,062	0,067		0,081	H/L
	5,0	4,66	3,80	3,29	2,95	2,69	2,49	2,33	2,20	2,08	1,99	1,90	1,83	1,76	1,70	1,60	ξ
		0,007	0,011	0,014	0,018	0,021	0,025	0,028	0,032	0,035	0,039	0,042	0,046	0,050	0,053	0,060	H/L
	6,0	5,59	4,56	3,95	3,53	3,23	2,99	2,97	2,63	2,50	2,38	2,28	2,19	2,11	2,04	1,92	ξ
		0,006	0,008	0,011	0,014	0,017	0,020	0,023	0,025	0,028	0,031	0,034	0,037	0,040	0,042	0,048	H/L
	7,0	6,52	5,32	4,61	4,12	3,76	3,49	3,26	3,07	2,92	2,78	2,66	2,56	2,46	2,38	2,24	ξ
		0,005	0,007	0,009	0,012	0,014	0,017	0,019	0,021	0,024	0,026	0,028	0,031	0,033	0,036	0,040	H/L
	8,0	7,45	6,08	5,27	4,71	4,30	3,98	3,73	3,51	3,33	3,18	3,04	2,92	2,82	2,72	2,56	ξ
		0,004	0,006	0,008	0,010	0,012	0,014	0,016	0,018	0,021	0,023	0,025	0,027	0,029	0,031	0,035	H/L
		Water depth h_s=4.0m															

(Wave Period T or Tp [s] labels the rows: 3,0 / 4,0 / 5,0 / 6,0 / 7,0 / 8,0)

Legend:
- Surging breaker
- Collapsing breaker
- Plunging breaker
- Optional
- Not generable

Due to the damage of *Model Alternative A* which occurred at an unexpectedly early stage with regular waves (Oumeraci et al., 2009a) and further constraints, including the introduction of *Model Alternative C*, the test programme has been (slightly) modified as shown in Tab. 2.3 and Tab. 2.4 for *Model Alternatives A, B* and *C*, respectively. A complete overview of the tests performed can be found in Annex B, including the nominal and actual incident wave parameters wave parameters, the water depth in the wave flume as well as the corresponding surf similarity parameter and reflection coefficient for both regular wave tests (B.1.1) and irregular wave tests (B.1.2). An overview of the test results is given in Annex C for both regular waves (C.1.1) and irregular waves (C.1.2 and C.1.3), including wave run-up, run-down and the wave-induced pressure recorded at different pressure transducer layers 1-5 for all tested *Model Alternatives A, B* and *C*.

Tab. 2.3: Final test programme for *Model Alternatives* A and B

Model A B	Test Phase 1											
H / T	0,2	0,3	0,4	0,5	0,6	0,7	0,8	0,9	1	1,1	1,2	1,3
3 ξ	RW 2,79				RW 1,61				RW 1,25			
4 ξ	RW 3,73				RW 2,15				RW 1,67			RW 1,46
5 ξ	RW 4,66				RW 2,69							RW 1,83
6 ξ	RW 5,59				RW 3,23							
7 ξ	RW 6,52				RW 3,76							
8 ξ	RW 7,45				RW 4,30							

RW regular waves   WS irregular waves

Tab. 2.4: Final test programme for *Model Alternatives* B and C

Model C B	Test Phase 2											
H / T	0,2	0,3	0,4	0,5	0,6	0,7	0,8	0,9	1	1,1	1,2	1,3
3 ξ	WS 2,79	WS 2,28	RW WS 1,98	RW WS 1,77	RW WS 1,61	RW 1,49	RW 1,40	RW 1,32	RW 1,25			
4 ξ	WS 3,73	WS 3,04	WS 2,63	WS 2,36	WS 2,15							
5 ξ	RW 4,66	WS 3,80		WS 2,95	WS 2,69		WS 2,33	WS 2,20	RW WS 2,08			
6 ξ	WS 5,59	WS 4,56	WS 3,95	WS 3,53	RW WS 3,23	WS 2,99	WS 2,79	WS 2,63	RW WS 2,50	WS 2,38		RW RW 2,19
7 ξ	WS 6,52	WS 5,32	WS 4,61	RW WS 4,12	RW WS 3,76	WS 3,48	WS 3,26		RW WS 2,92			
8 ξ	RW WS 7,45		RW WS 5,27	WS 4,71	WS 4,30		WS 3,73		RW WS 3,33			

RW regular waves   WS irregular waves

2.3.2   Test procedure

Initially it was planned to start the testing programme first with regular waves (at least 100 waves per test), followed by JONSWAP wave spectra (at least 1000 waves per test) and few additional tests using solitary waves and "freak waves", adjusting the still water level for each test in order to shift the impact point in the area covered with pressure transducers. Because of the long time it takes to change the water level in the large wave flume (about 1 minute per cm) it was necessary to minimise the number of time-consuming water level changes. Thus, before the aforementioned damage occurred, *Model Alternatives A* and *B* were first subject to a series of regular wave tests with increasing wave height (H = 0.2 m to H = 1.3 m) starting with the tests performed at a still water level of 3.40 m. Within each test series the wave period was increased for each test from T = 3 s to T = 8 s (Tab. 2.1). The damage of *Model Alternative A* occurred for a wave with nominal wave height H = 1.3 m and wave period

T = 5 s. After the damage, *Model Alternative A* was replaced by *Model Alternative C*. Subsequently, the test procedure for *Model Alternatives B* and *C* was adapted to the new situation by starting first with the tests with small wave heights up to H = 0.6 m, including tests with regular waves as well as tests with irregular waves. Only when all required tests up to a wave height of 0.6 m were successfully performed the wave height was increased up to H = 1.3 m, to avoid another unexpected early failure of the new revetment.

Regular wave tests

The wave parameter combinations for the regular wave tests are listed in Tab. 2.3 with water depths ranging form h_s = 3.40 m to 4.20 m, wave periods from T = 3 s to 8 s and wave heights from H = 0.2 m to 1.3 m. All tests were run with activated absorption system. The test phase begun with regular wave tests comprising of 100 waves, starting with a nominal wave height of 0.2 m and a nominal wave period of 3 s. To direct the impact point of the breaking waves to the pressure transducers at the middle of the impact area (y = 3.15 m), the water level had to be adjusted to 3.40 m. After all tests were performed, which were estimated to be run at this water depth, the water level was raised to h_s = 3.6 m to fulfil the requirements of the next few tests. At each water level the tests were performed starting with the lowest wave height and wave period, increasing the wave parameters until the water level had to be adjusted for the next tests. For the last few tests with regular waves the number of generated waves was reduced to first 50 and then 30 in order to save time. This reduction did not decrease the statistical use of the obtained data.

Model Alternative A and *B* were subject to a series of tests (summarized in Tab. 2.3), following the above described procedure until *Model Alternative A* failed during a test with wave parameters H = 1.3 m and T = 5 s. After replacing the damaged revetment by a new revetment, defined as *Model Alternative C*, the tests were resumed by repeating some of the already performed tests, for now skipping the tests with wave heights above H = 0.6 m. It was discussed to perform first all tests with low wave heights including the tests with irregular waves before increasing the wave height above 0.6 m up to 1.3 m in order to gain as much data as possible before another unexpected failure would recur.

The preformed tests, including the incidend wave parameters and the reflection coefficient are given in Annex B.1.1. The results are summarized in Annex C.1.1, providing the run-up, the run-down and the wave-induced pressure.

Irregular wave tests

Tests with irregular waves were only performed for *Model Alternative B* and *C* and were also started with a wave height of H = 0.2 m and a wave period of T = 3 s, following the same procedure as during the tests with regular waves, in order to minimize the number of water level adjustments. For these tests, wave periods from T = 3 s up to 8 s and wave heights from H = 0.2 m to 1.1 m were used (Tab. 2.4). All tests were run with 1000 waves and activated

absorption system, except for the last few tests with large wave heights which were run with only 500 waves, because of the limitations of the wave generator.

The performed tests, including incidend wave parameters and thereflection coefficient are given in Annex B.1.2. The results are summarized in Annex C.1.2 and C.1.3, providing the run-up, the run-down and the wave-induced pressure at the different transducer layers.

Solitary wave and freak wave tests (additional tests).

At the end of the test phase, after all required test with regular and irregular waves were performed, some additional tests were run, generating solitary waves and so called "freak waves" (wave focussing). The solitary wave tests comprise parameter combinations for water level $h_s = 4.0$ m with wave heights ranging from H = 0.25 m up to 1.20 m.

For the tests with "freak waves", wave heights from H = 0.8 m to 1.4 m were used. The focus point of the wave group was adjusted to direct the impact point of the breaking wave to the array of pressure transducers of the impact area.

The analysis of these additional tests is not part of this report, but the measurements will be analysed at a later stage (outside this project).

3   Incident wave parameters and wave reflection analysis

The analysis is performed separately for regular and irregular waves. As mentioned in section 2.3.1, the focus is on the analysis of the irregular wave tests, since they are more relevant for design purposes. In order to make the report more easily readable, the results of the analysis of regular wave tests are given separately in an Annex D1. Reference to these results may however be made where appropriate (e.g. for comparison or a better understanding) in the main text related to the results of irregular wave tests.

Since *Model Alternative A* was tested only for regular waves before it failed, the analysis of the irregular wave tests is related only to *Model Alternatives B and C* (nevertheless, Model A is also considered in the analysis of regular wave tests in the aforementioned Annex.)

3.1   Incident wave parameters

The water surface elevation measured in the wave flume is the result of the superposition of incident and reflected waves. In order to determine the incident wave height for each test, a reflection analysis using a least square method (Mansard & Funke, 1980) was performed. Four wave gauges, which were arranged within "gauges array 1" about 85 m in front of the wave maker (s. Fig. 3.1 and Annex D1), were used for reflection analysis.
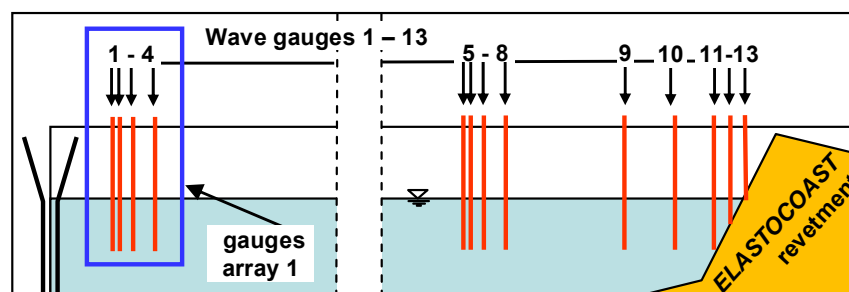
Fig. 3.1:   Position of wave" gauges array 1" in the large wave flume (GWK)

For each wave gauges array the combinations of 3 of 4 wave gauges within one gauges array were used for the analysis. As a result incident wave heights H_{m0} and characteristic wave period $T_{m-1,0}$ as well as the reflection coefficient C_r were obtained. Example time series of incident and reflected irregular waves are shown in Fig. 3.2.
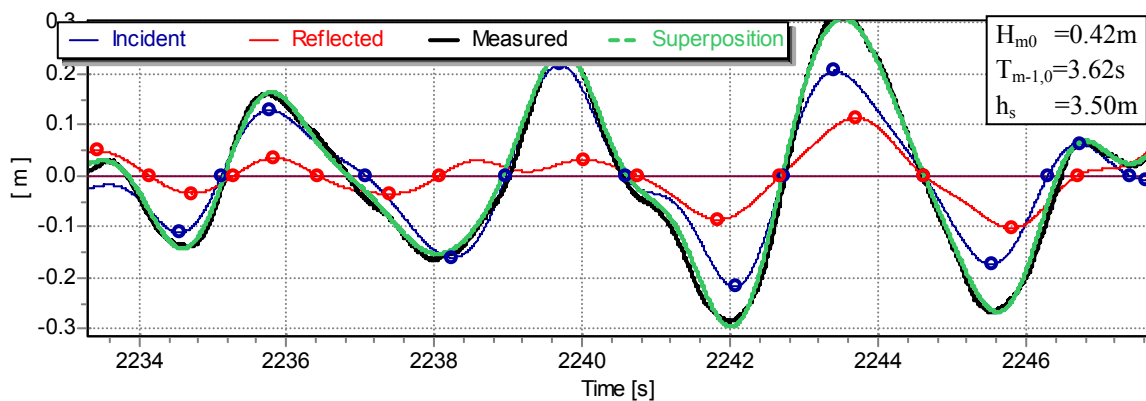
Fig. 3.2: Time series of incident and reflected waves (wave gauge arrays 1, s. Fig. 3.1)

Fig. 3.2 shows that the superposition (coloured green) of incident (coloured blue) and reflected (coloured red) waves obtained from the reflection analysis have the same height as the measured waves (coloured black).

The mean values of the 4 possible combinations were then used and compared to the desired (nominal) parameters. Accordingly, the relation between the nominal wave height H_{nom} and the actual incident wave height H_{m0} for all tests with wave spectra for different water level is shown in Fig. 3.3. The dashed lines indicate the range of scatter observed in the measurements.
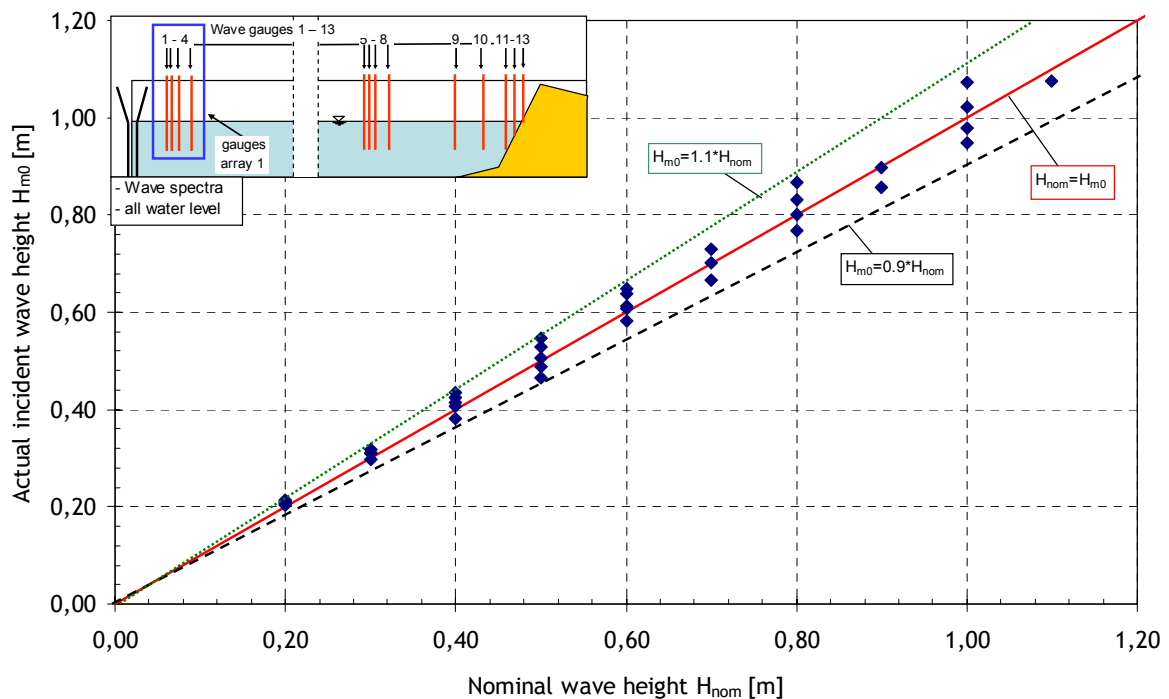
Fig. 3.3: Comparison of incident wave height H_{m0} and nominal wave height H_{nom} for all irregular wave tests with different water levels

It can be seen from Fig. 3.3 that for most values H_{nom} the maximum spreading of the incident wave height H_{m0} ranged from -10% to +10 %.

> *Remark:*
>
> *For regular waves (mean wave height H_m) the scatter is larger ranging from -14% to +18 % (s. Annex D.1, Fig. D.1.2).*

These differences are quite normal under lab conditions and indicate that measured and nominal wave heights are of the same order of magnitude. However, due to the observed differences, further analysis always refers to the actually measured incident wave height related to deep water conditions which corresponds approximately to those measured in the far field (average wave gauge array 1). The deep water wave height was calculated using the shoaling coefficient (EAK, 2002):

$$\frac{H}{H_0} = K_s = \sqrt{\frac{1}{2n} \cdot \frac{c_0}{c}} \tag{3.1}$$

with:

H	[m]	wave height
H_0	[m]	deep water wave height
K_s	[-]	Shoaling coefficient
n	[-]	ratio of wave speed and group speed
c_0/c	[-]	relative wave speed

As shown in Fig. 3.4 the difference between deep water wave height and incident wave height H_{m0} obtained at wave gauges array 1 is negligible (less than 4%). Therefore, a characteristic deep water wave height H_{0m0} (in the following simply called H_{m0}) and wave period $T_{m-1,0}$ were used which lead to the corresponding surf similarity parameter $\xi_{m-1,0}$ and wave steepness H_{m0}/L_0 for irregular waves.

> *Remark:*
>
> *For the regular waves, the deep water wave height H_0 (in the following H_m) and length L_0 were used which lead to the corresponding surf similarity parameter ξ_m and wave steepness H_m/L_0 for regular waves.*

In Fig. 3.5 incident wave period $T_{m-1,0}$ is plotted against nominal wave period T_{nom}. The dashed lines indicate the maximum range of scatter observed in the measurements.
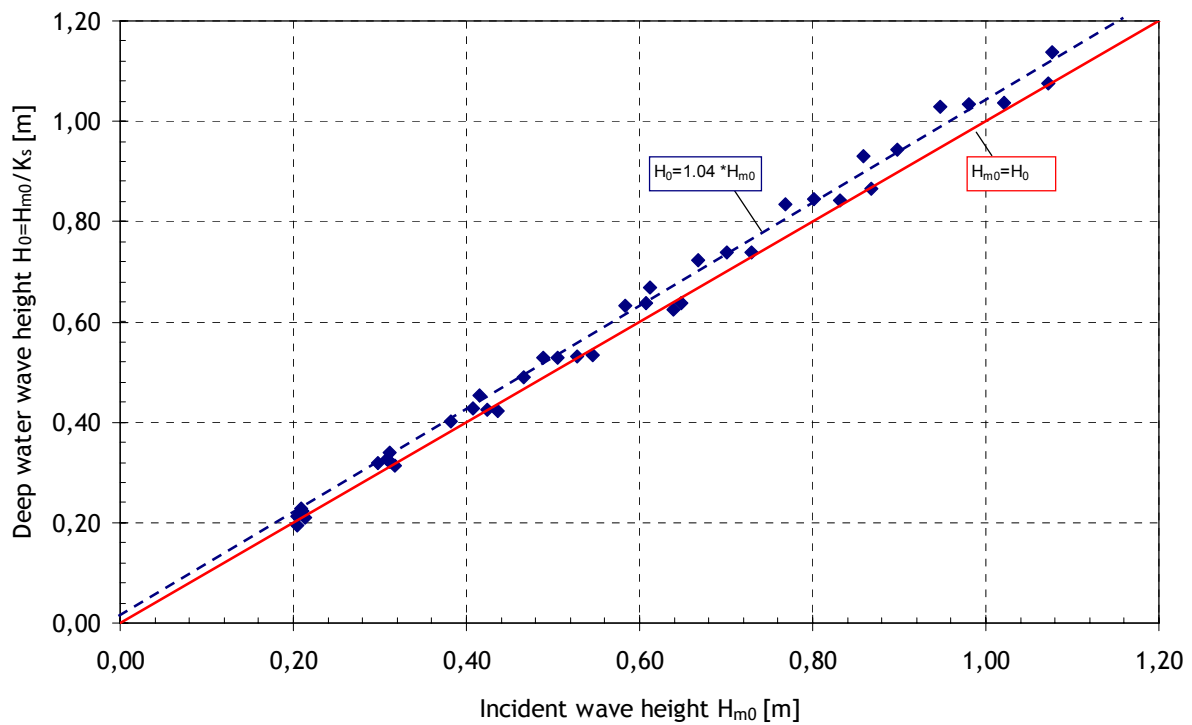
Fig. 3.4: Comparison of incident wave height H_{m0} (wave gauge array 1) and deep water wave height H_0 calculated using the shoaling coefficient K_s
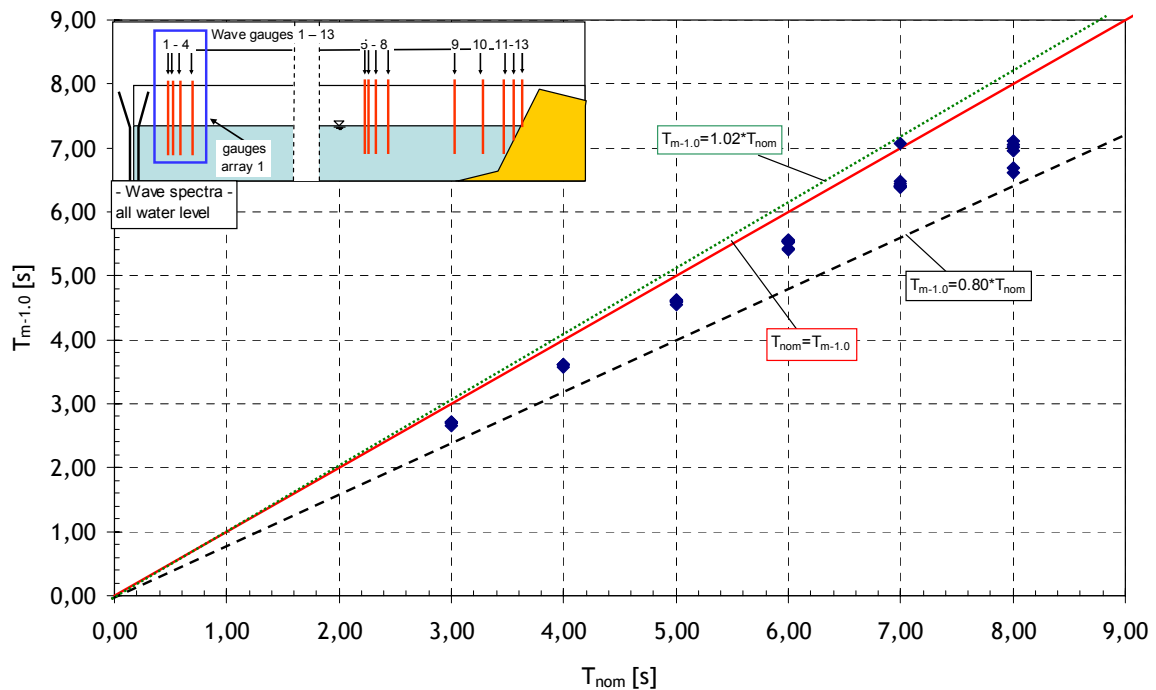
Fig. 3.5: Comparison of $T_{m-1.0}$ and T_{nom} for all tests with for all tests with wave spectra for different water levels

Fig. 3.5 shows that the scatter of wave period $T_{m-1,0}$ was in the range of +2% and -20% which is higher than for the wave heights H_{m0}. Most of the values of incident mean wave periods $T_{m-1,0}$ are lower than the related nominal wave periods T_{nom}.

> *Remark:*
>
> *For regular waves (mean wave period T_m) the range of scatter was only ± 1% (s. Annex D.1). The measured wave periods will be used for further analysis.*

3.2 Wave reflection performance

Wave reflection from coastal structures may severely affect the structure stability by increasing sea bed scour. It may also increase the erosion of the foreshore and of the neighbouring coastal stretches. The reflection coefficient, obtained from the analysis of the tests, ranged from $C_r = 0.26$ (minimum) to $C_r = 0.75$ (maximum) (for regular waves: $C_r = 0.09$ (minimum), $C_r = 0.86$ (maximum)). In Fig. 3.6 the reflection coefficient C_r for irregular waves is plotted against mean wave period $T_{m-1,0}$ to illustrate the influence of the wave period for the *ELASTOCOAST* revetment, sorted after incident deep water wave height H_{m0}. As expected, there is a clear increase of the wave reflection C_r with increasing wave periods. Furthermore, it can be seen that with smaller waves the reflection coefficient C_r increases.

> *Remark:*
>
> *A similar behaviour has also been found for regular wave tests (Fig. D.1.4 in Annex D.1)*
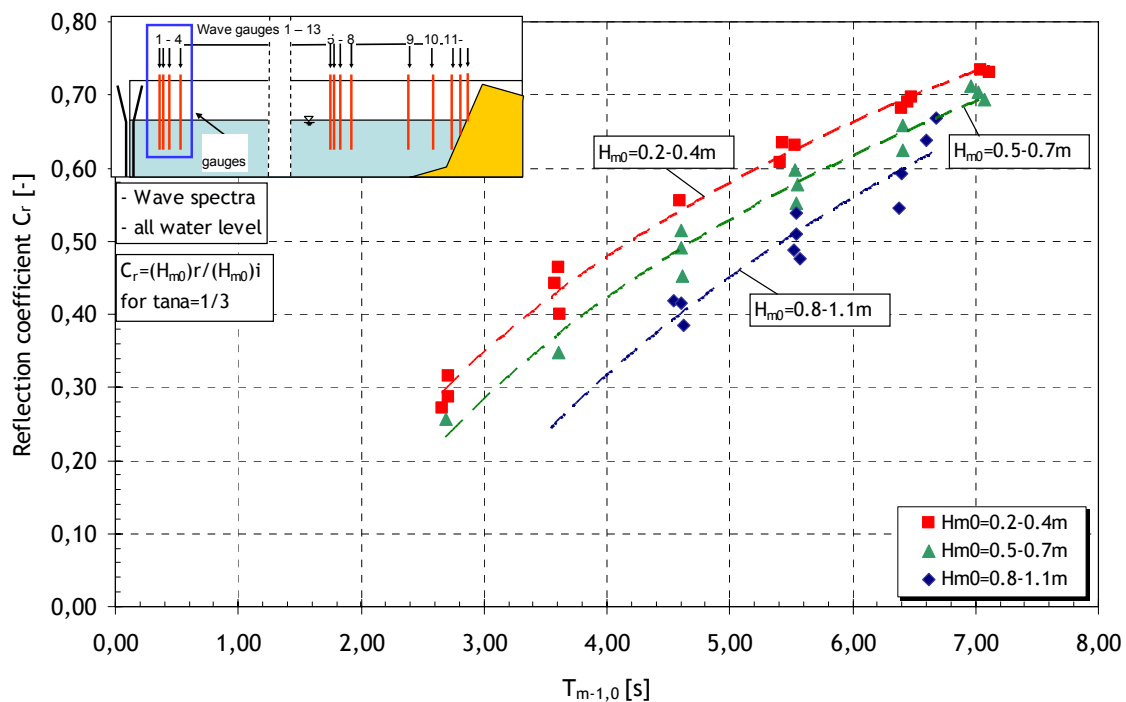
Fig. 3.6:   Reflection coefficient C_r plotted against the wave period $T_{m-1,0}$ ordered by incident wave heights H_{m0}

Several prediction formulae for the reflection coefficient have been proposed in the past (see Oumeraci et al., 2007; Oumeraci & Muttray, 2001; Zanuttigh & Van der Meer, 2006). A comparative analysis of the uncertainties associated with 12 prediction formulae were performed previously (Muttray, 2001), showing coefficients of variation from 10 to 140 %. Amongst the existing formulae, the following one (Seelig, 1983) was found to be most widely used and associated with the lowest uncertainties:

$$C_r = \frac{a \cdot \xi_0^2}{b + \xi_0^2}$$ (3.2)

with:

ξ_0 [-]   surf similarity parameter $\xi_0 = \dfrac{\tan \alpha}{\sqrt{H_0 / L_0}}$ (3.3)

a, b   [-]   structure parameter, depending on the permeability, roughness, geometry and water depth conditions

As a measure of uncertainty in the statistical analysis the *coefficient of variation* is used. It is calculated as follows (Kortenhaus & Oumeraci, 2002):

$$\sigma' = \sqrt{\frac{1}{n-1} \cdot \sum_{i=1}^{n} \left(\frac{y_m}{f(x_{mi})} - 1 \right)^2}$$ (3.4)

with:

σ' [-]   coefficient of variation
n   [-]   number of values
x_{mi} [-]   input parameter for model
y_m [-]   measured output parameters
$f(x_{mi})$ [-]   model output parameter

Plotting the reflection coefficient C_r against surf similarity parameter $\xi_{m-1,0}$, calculated using characteristic wave period $T_{m-1,0}$ and characteristic wave height H_{m0} the result in Fig. 3.7 is obtained. The resulting curve for the tested *ELASTOCOAST* revetment is plotted in comparison with the curves for a smooth impermeable slope and for a sloped structure with two layer rock armour after Allsop & McConnell (as proposed in Herbich, 1999). In the investigations of Allsop and McConnelthe size of the rocks is not given. Since also for the construction of the *ELASTOCOAST* revetment only one size of gravel was used, the effect of the grain size on wave reflexion could not be investigated.
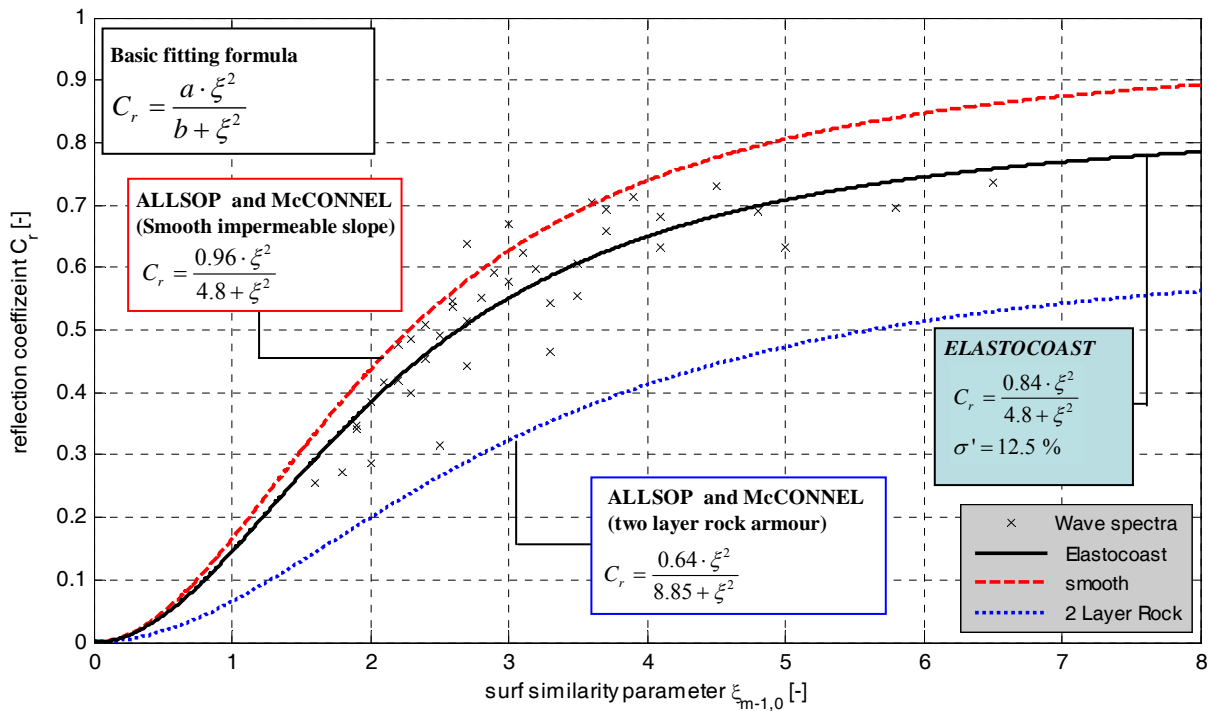
Fig. 3.7:   Reflection coefficient C_r plotted against surf similarity parameter $\xi_{m-1,0}$

The reflection coefficient of the *ELASTOCOAST* revetment remains smaller than that of a smooth impermeable slope. The curve for a two layer rock armour is as expected much smaller than the reflection coefficient for the *ELASTOCOAST* revetment. Hence, the reflection coefficient C_r for the *ELASTOCOAST* revetment investigated in this study can be estimated with Eq. (3.5), associated with a coefficient of variation $\sigma' = 12.5\ \%$:

$$C_r = \frac{0.84 \cdot \xi^2}{4.8 + \xi^2} \qquad (3.5).$$

Further analysis has shown that the reflection coefficient is dependant of the wave period. Fig. 3.8 again depicts reflection coefficient C_r against surf similarity parameter $\xi_{m-1,0}$ but now the data is ordered by the wave period $T_{m-1,0}$. It can be seen that the highest wave period leads to the largest reflection coefficient. These results shown that the effect of the wave period is much more important than considered in surf similarity parameter $\xi_{m-1,0}$. In fact, considering $\xi_{m-1,0}$, C_r is proportional $T_{m-1,0}$ only. Therefore, further analysis should be directed to identify a governing parameter as a substitute for $\xi_{m-1,0}$ which better account for the effect of wave period $T_{m-1,0}$.
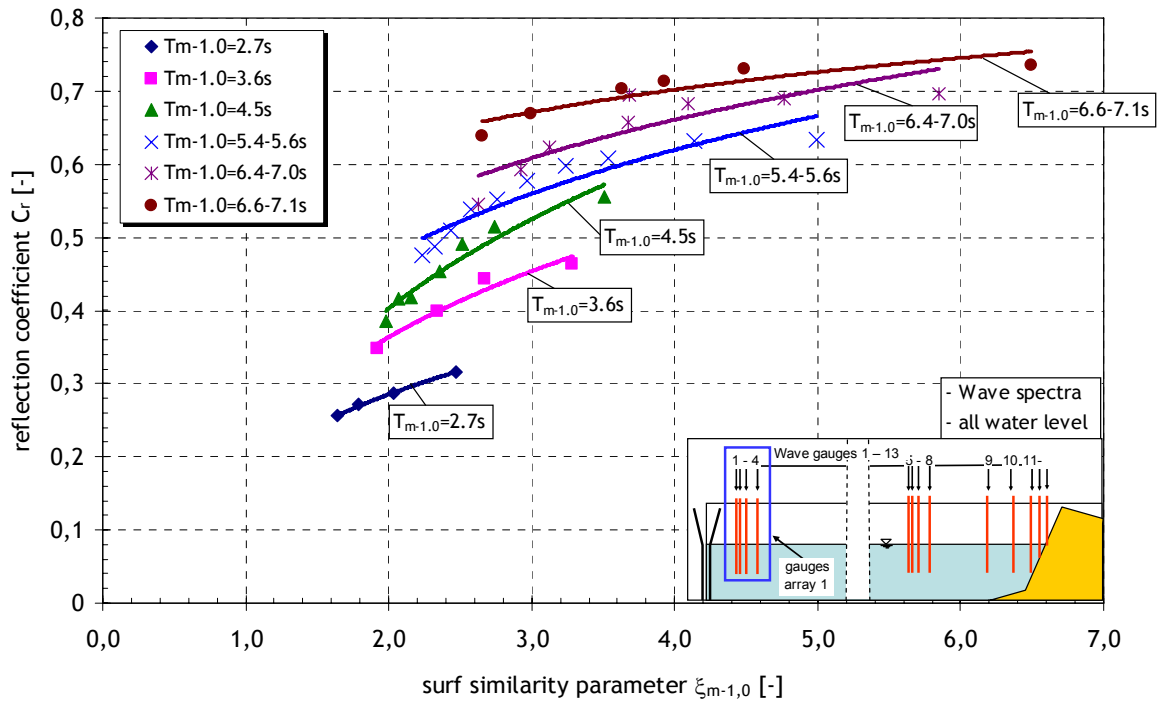
Fig. 3.8:   Reflection coefficient C_r plotted against surf similarity parameter $\xi_{m-1,0}$ ordered by wave periods $T_{m-1,0}$

Remark:

A similar result as in Fig. 3.8 is also found for regular wave tests as shown in Fig. D.1.5 in Annex D.1)

4 Wave run-up and run-down

4.1 Wave run-up

The wave run-up R_u is defined as the maximum elevation from still water level (SWL) to the point to which the water surface rises on the seaward face of the revetment (see Fig. 4.1). R_u is important in defining the required height of the structure. Generally, the run-up level exceeded by 2% of the incident waves ($R_{u2\%}$) is commonly used for design purposes. $R_{u2\%}$ generally depends on the wave height, the surf similarity parameter, the geometry and surface roughness of the slope as well as on the permeability of the structure. For less impermeable structures with a rough slope such as the *ELASTOCOAST* revetment, most of the energy dissipation takes place at the structure face and within the revetment.
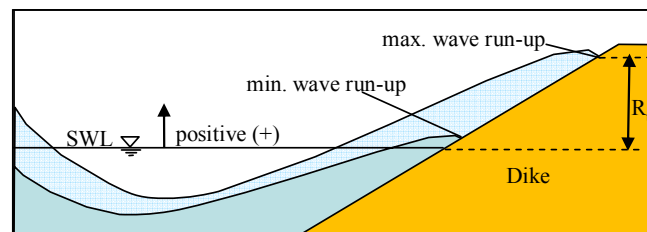
Fig. 4.1:   Definition of wave run-up

The wave run-up was measured with wave run-up gauges (s. section 2.2.4) and compared to the video recordings. This verification was very time consuming, but necessary since it has shown how to analyse the records from the wave run-up gauges properly. It has shown that the results of the wave run-up gauges are indeed reliable when properly analyzed. An example time series for a wave run-up gauge is shown in Fig. 4.2. The indicated point shows the maximum run-up for this test ($R_{umax} = 0.94$ m). Hence, the run-up gauge was used to measure wave run-up and run-down, the maximum amplitudes of each test were defined as wave run-up and the minimum amplitudes of each test were defined as wave run-down.
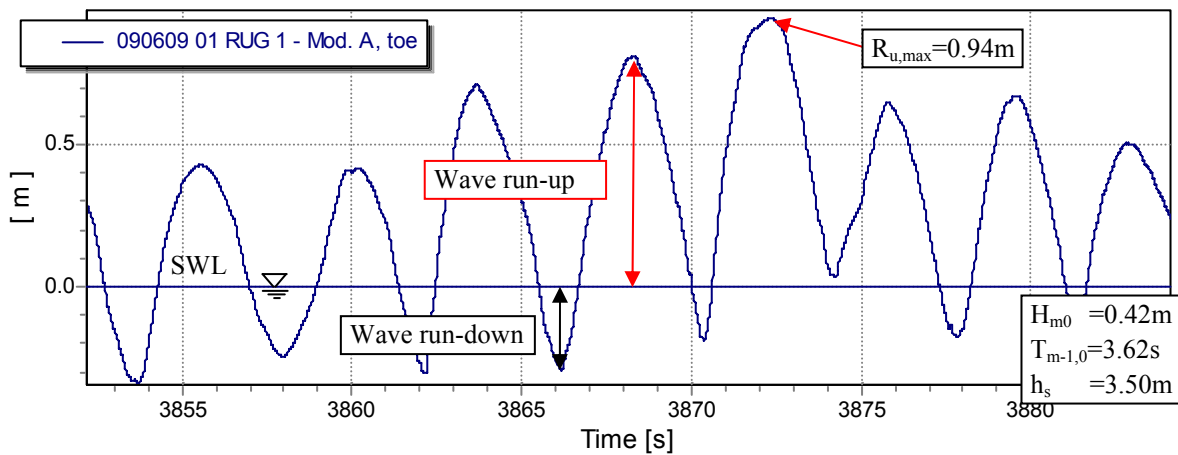
Fig. 4.2: Time series for wave run-up

In Fig. 4.3 the relative wave run-up $R_{u2\%}/H_{m0}$ is plotted for *Model Alternatives B* and *C* against surf similarity parameter $\xi_{m-1,0}$ to show the effect of the surf similarity parameter for the run-up on the *ELASTOCOAST* revetment.
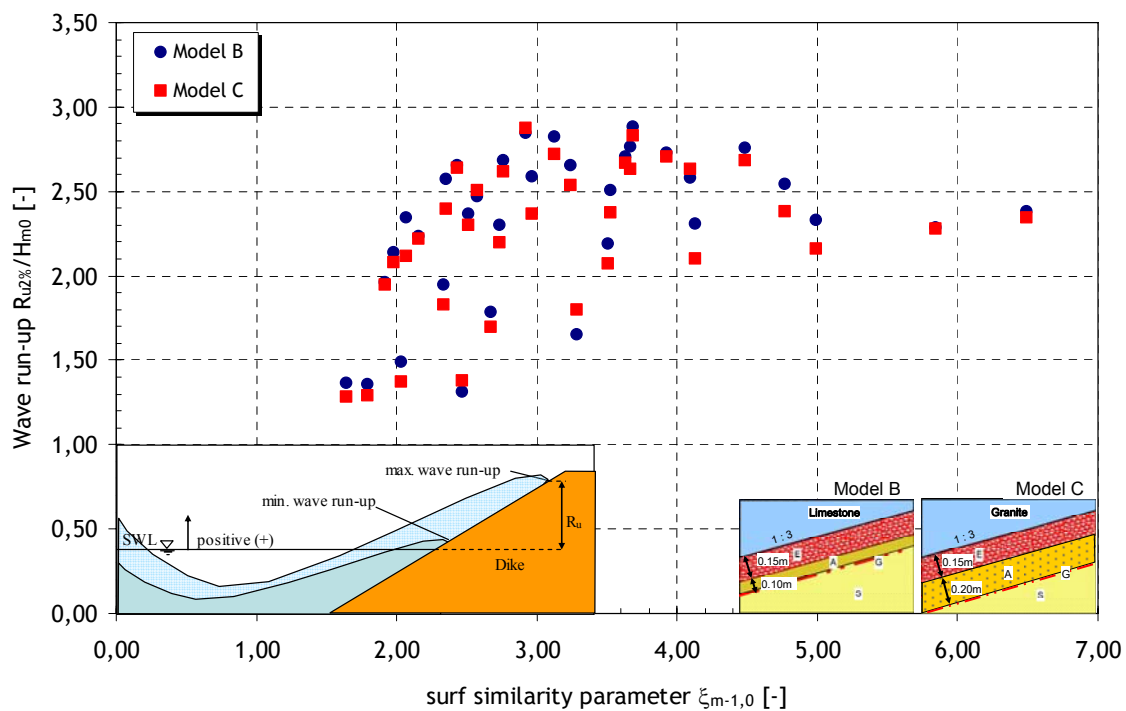
Fig. 4.3: Comparison of relative wave run-up $R_{u2\%}$ for *Model Alternatives* B and C for irregular waves

The measured relative wave run-up for all irregular wave tests ranges from $R_{u2\%}/H_{m0} = 1.28$ for $\xi_{m-1,0} = 1.64$ to $R_{u2\%}/H_{m0} = 2.88$ for $\xi_{m-1,0} = 2.92$. As shown in Fig. 4.3 there is no signifi-

cant difference between *Model Alternatives B* and *C*, although the latter expectedly depicts slightly smaller run-up values.

> *Remark:*
>
> *Comparatively, the measured run-up for regular wave tests is lower ranging from $R_{u2\%}/H_m = 0.89$ for $\xi_m = 1.28$ to $R_{u2\%}/H_m = 2.28$ for $\xi_m = 3.57$ (see Annex D.2 in Fig. D.2.1)*

A literature study has shown that the run-up models for the *ELASTOCOAST* revetment for which the best fit is obtained with the measured data is those proposed by the EurOtop manual (EurOtop, 2007).

$$\frac{R_{u2\%}}{H_{m0}} = \gamma_f \cdot \left[1.65 \cdot \xi_{m-1,0}\right] \quad \text{with } \gamma_f = 1.0 \text{ for smooth impermeable slope} \qquad (4.1)$$

with a maximum of

$$\frac{R_{u2\%}}{H_{m0}} = \gamma_f \cdot \left[4.0 - \frac{1.5}{\sqrt{\xi_{m-1,0}}}\right] \quad \text{with } \gamma_f = 1.0 \text{ for smooth impermeable slope} \qquad (4.2)$$

Based on Eq. (4.1) and Eq. (4.2) for the smooth impermeable slope, the following run-up formula was determined for the *ELASTOCOAST* revetment *Model Alternative B* (Fig. 4.4):

$$\frac{R_{u2\%}}{H_{m0}} = 0.54 \cdot \left[1.65 \cdot \xi_{m-1,0}\right] \quad \text{for } \xi < 2.7 \qquad (4.3)$$

with a maximum of

$$\frac{R_{u2\%}}{H_{m0}} = 0.78 \cdot \left[4.0 - \frac{1.5}{\sqrt{\xi_{m-1,0}}}\right] \quad \text{for } \xi \geq 2.7 \qquad (4.4)$$

while for *Model Alternative C* the following formula was obtained:

$$\frac{R_{u2\%}}{H_{m0}} = 0.52 \cdot \left[1.65 \cdot \xi_{m-1,0}\right] \quad \text{for } \xi < 2.7 \qquad (4.5)$$

with a maximum of

$$\frac{R_{u2\%}}{H_{m0}} = 0.76 \cdot \left[4.0 - \frac{1.5}{\sqrt{\xi_{m-1,0}}}\right] \quad \text{for } \xi \geq 2.7 \qquad (4.6)$$

The wave run-up resulting for the model proposed in EurOtop, 2007 for the smooth imperme-able slope is much higher than the run-up on the *ELASTOCOAST* revetment. The difference is about 25 % for larger $\xi_{m-1,0}$-values while it is up to 50 % for smaller $\xi_{m-1,0}$-values. The difference between *Model Alternatives B* and *C* is negligibly small. The wave run-up for *Model Alternative B* is slightly higher than for *Model Alternative C*.
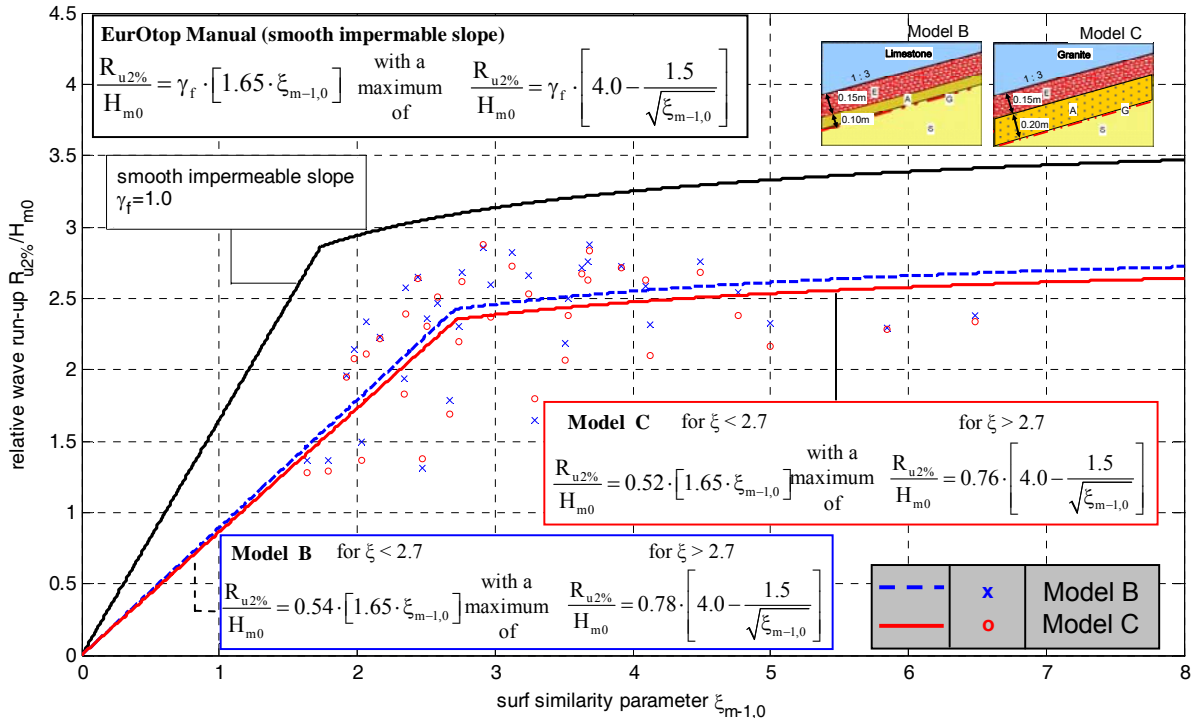
Fig. 4.4:   Wave run-up $R_{u2\%}$ for irregular waves, separated after *Model Alternatives* B and C

Therefore, only one prediction formula for both *Model Alternatives B and C* is proposed for design purpose (see Fig. 4.5):

$$\frac{R_{u2\%}}{H_{m0}} = 0.54 \cdot \left[1.65 \cdot \xi_{m-1,0} \right] \quad \text{for } \xi < 2.7 \tag{4.7}$$

with a maximum of

$$\frac{R_{u2\%}}{H_{m0}} = 0.77 \cdot \left[4.0 - \frac{1.5}{\sqrt{\xi_{m-1,0}}} \right] \quad \text{for } \xi \geq 2.7 \tag{4.8}$$

and a coefficient of variation σ' of about 16 %.
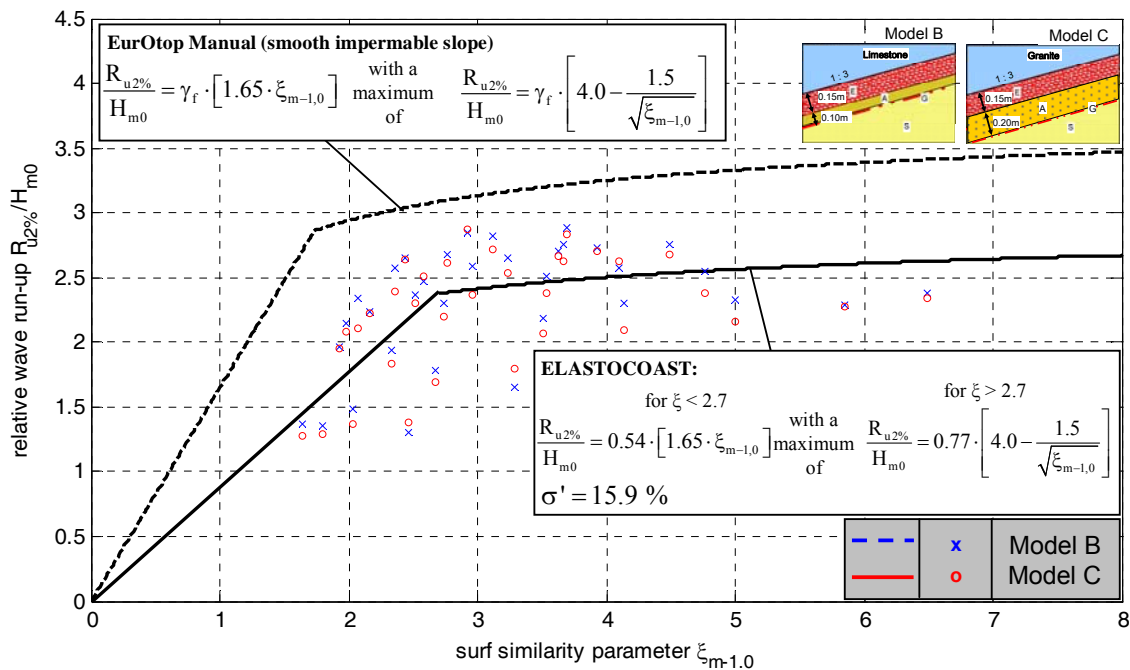
Fig. 4.5: Wave run-up $R_{u2\%}$ for irregular waves

Remark:

Comparatively the wave run-up formulae obtained for regular waves are given in Fig. D.2.2, Annex D.2, showing that lower run-up values are obtained than for regular waves. Moreover, the run-up for Model Alternative A is also considered.

4.2 Wave run-down

The wave run-down R_d is defined as the minimum elevation from still water level (SWL) to the point to which the water surface falls on the seaward face of the revetment (Fig. 4.6). R_d is important in defining the required elevation of the revetment under SWL. It is also important for the uplift pressure on the revetment as a result of the internal water level which is generally higher than the external water level during the down rush process. The run-down level exceeded by 2% of the incident waves ($R_{d2\%}$) is commonly used for design purpose. $R_{d2\%}$ generally depends on the wave height, the surf similarity parameter, the geometry and surface roughness of the slope as well as on the permeability of the structure. As for wave run-up, the run-up gauges were used to measure the wave run-down (Fig. 4.2), including a verification of video recordings.
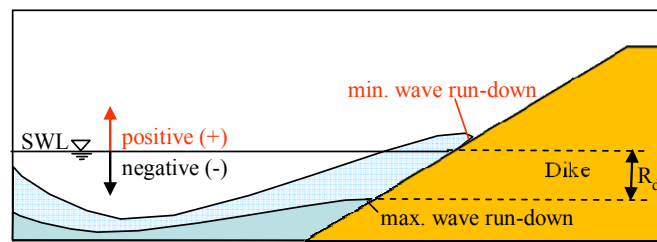
Fig. 4.6: Definition of wave run-down

In Fig. 4.7 the relative wave run-down $R_{d2\%}/H_{m0}$ is plotted for both *Model Alternatives B* and *C* against the surf similarity parameter $\xi_{m-1,0}$ to show the influence of the surf similarity parameter for the run-down on the *ELASTOCOAST* revetment.
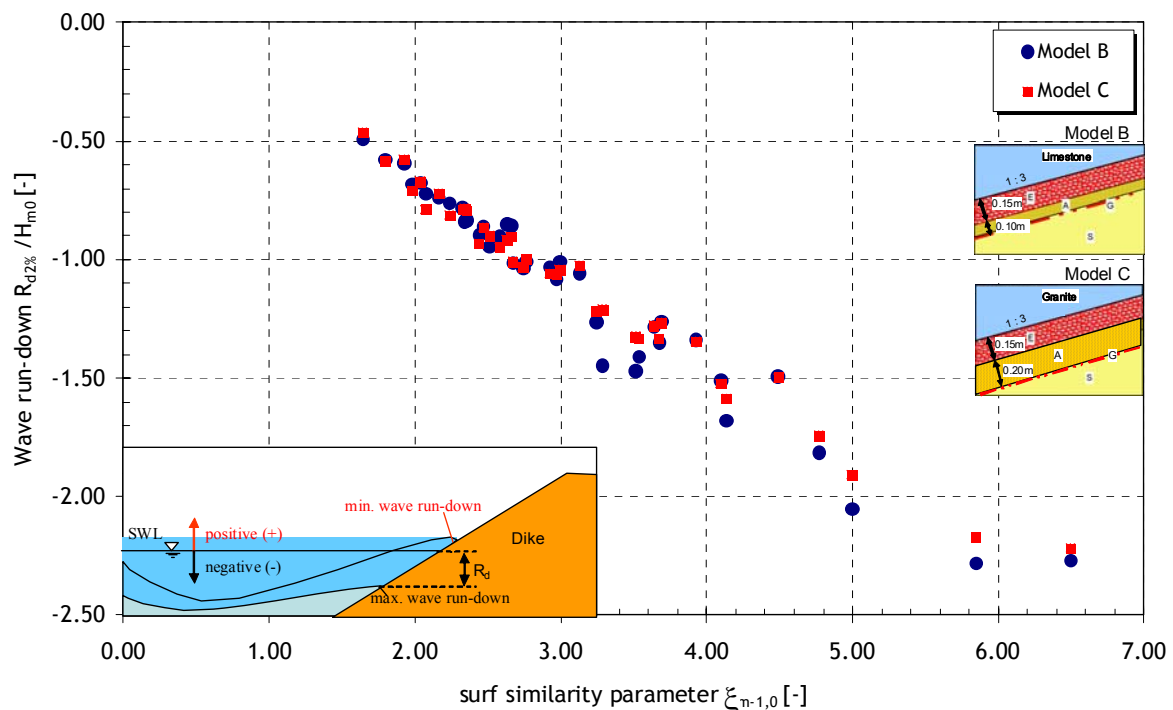
Fig. 4.7: Comparison of relative wave run-down $R_{d2\%}$ for *Model Alternatives* B and C for irregular waves

The measured relative run-down for all irregular wave tests ranges from $R_{d2\%}/H_{m0} = -0.46$ for $\xi_{m-1,0} = 1.64$ to $R_{d2\%}/H_{m0} = -2.27$ for $\xi_{m-1,0} = 6.49$. Comparatively, no difference is depicted between *Model Alternatives B and C* for smaller $\xi_{m-1,0}$-values while for larger $\xi_{m-1,0}$-values ($\xi_{m-1,0} > 3.3$) the run-down for *Model Alternative B* is slightly larger than for *Model Alternative C*. However, the difference is within the range of scatter of the data, so that no discrimination between the data of the two models B and C will be made for the derivation of the wave run-down formula.

> *Remark*
>
> *Comparatively, for regular wave tests also including Model Alternative A the range of scatter of the data is much larger and the relative wave run-down ranges from $R_{d2\%}/H_m = 0.41$ for $\xi = 1.50$ to $R_{d2\%}/H_m = -1.85$ for $\xi = 7.68$ (see Annex D.2, Fig. D.2.3). The positive $R_{d2\%}/H_m$-values for lower ξ-values mean that the lowest water surface elevation at the outer slope remains above still water level. This has also been observed in the results of many experimental studies on wave run-down using regular waves (e.g. Schüttrumpf, 2001, Pilarczyk et al., 1995,Bruun & Grünback, 1977).*

A literature study has shown that the run-down models for the *ELASTOCOAST* revetment for which the best fit is obtained with the measured data are (i) those proposed by the CEM (USACE, 2002) (Part-VI) for a smooth revetment of placed concrete block (Eq. (4.9))

$$\frac{R_{d2\%}}{H_{m0}} = -0.5 \cdot \xi_{0p} + 0.2 \tag{4.9}$$

and (ii) the model developed for smooth impermeable slopes (Pilarczyk et al., 1995) (Eq. (4.10)).

$$\frac{R_{d2\%}}{H_{m0}} = -0.33 \cdot \xi_{0p} \quad \text{for } \xi_{m-1.0} < 4.5$$

$$\frac{R_{d2\%}}{H_{m0}} = -1.5 \quad \text{for } \xi_{0p} \geq 4.5 \tag{4.10}$$

Based on these models the following run-down formula was determined for the *ELASTO-COAST* revetment *Model Alternatives B* and *C* (Fig. 4.8):

$$\frac{R_{d2\%}}{H_{m0}} = -0.42 \cdot \xi_{m-1.0} + 0.17 \quad \text{for } \xi_{m-1.0} < 5.7 \tag{4.11}$$

with a maximum of

$$\frac{R_{d2\%}}{H_{m0}} = -2.25 \quad \text{for } \xi_{m-1.0} \geq 5.7 \tag{4.12}$$

and a coefficient of variation σ' of 6.1 %.

Larger $R_{d2\%}/H_{m0}$-values than for a smooth impermeable slope are obtained for the *ELASTO-COAST* revetment. The difference is particularly large (up to 66%) for large $\xi_{m-1,0}$-values ($\xi_{m-1,0} > 6$) while smaller run-down values than for a smooth revetment of placed concrete blocks as reported in CEM (USACE, 2002) will result (Fig. 4.8).
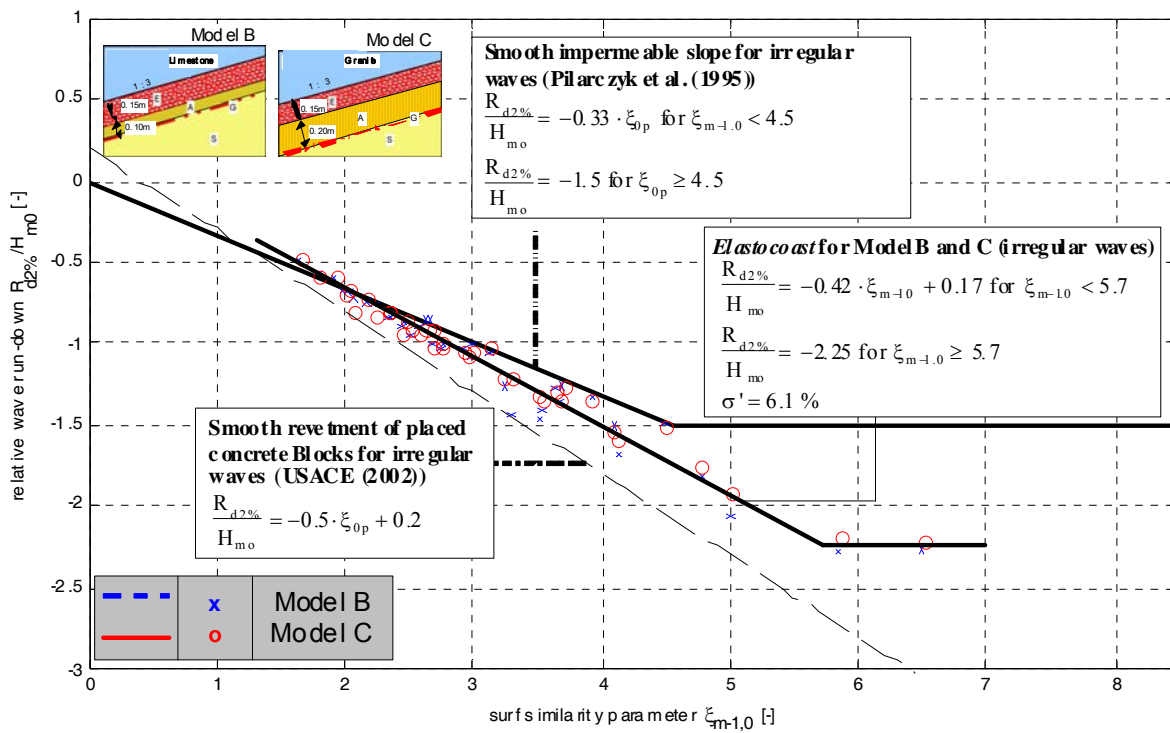
Fig. 4.8:   Wave run-down $R_{d2\%}$ for irregular waves

Remark

Comparatively, the results for regular wave tests, also including Model Alternative A, are given in Fig. D.2.4 Annex D.2, showing a similar relationship but providing lower run-down values than for irregular waves.

5 Wave pressure on and just beneath the revetment

The main objective of this chapter is to analyse the data related to the wave-induced pressure on the surface of the *ELASTOCOAST* revetment and just beneath the revetment. Based on this analysis prediction formulae for the maximum pressure induced by waves, the spatial pressure distribution, including the time parameters required for the dynamic (impact) loading will be developed. In the same way as for the analysis of the hydraulic performance (sections 3.1 - 3.2), the deep water parameters for incident waves are also considered in this analysis. Like in sections 3.1 - 3.2 only irregular wave tests are considered below, while the results of regular wave tests are provided in Annex D. Nevertheless, remarks related to the comparison with regular waves with reference to Annex D will also be made were appropriate. As already mentioned in the introduction of Chapter 3, due to the failure of *Model Alternative A* for regular waves, no irregular wave tests were performed for *Model Alternative A*, so that only *Model Alternatives B* and *C* are considered for irregular wave tests.

First, the parameterisation in both space and time of the wave-induced pressures on and just beneath the revetment is described, including the definition of the notation of the most important parameters in both spatial and time domains. Discrimination between quasi-static wave loads and impact loads will be made through the entire analysis within this chapter. This applies for the pressure on and just beneath the revetment.

Second, the maximum pressure induced by the waves on and just beneath the revetment (peak pressure p_{max}) will be analysed and formulae for its prediction will be developed.

Third, the location z_{pmax} of the maximum wave-induced pressure (peak pressure p_{max}) as related to still water level (SWL) will be analysed and prediction formulae will be proposed.

Forth, the spatial distribution of wave-induced pressure on and beneath the revetment will be analysed and formulae for their prediction will be derived.

Fifth, the rise time of the pressure and the load derivation as related to the period of the incident waves in deep water will be analysed and formulae for their prediction will be derived.

Finally, a summary of all proposed prediction formulae will be given, including a critical discussion of the results.

5.1 Definitions, wave load classification and parameterisation

(a)   Reference pressure for pressure measurements

All measured pressures refer to the pressure induced by wave motion only, excluding hydrostatic pressure resulting from water depth h at still water level (SWL); i.e. before each test

(still water level and no waves!) all pressure transducers are set to p=0. Although, hydrostatic pressure $p_0(x)$ depends on the local water depth $h(x)$ (see Fig. 5.1).

$$p_0(x) = \rho \cdot g \cdot h(x) \tag{5.1}$$

According to Eq. (5.1), $p_0(x < 0) = 0$ at the waterline $(x = 0)$, and above $(z<0)$ and shoreward of the waterline $(x < 0)$. Thus, the reference pressure for all measured pressure values is $p_0(x)$ according to Eq. (5.1). This applies for all pressure transducers on the slope surface, just beneath the revetment and in the sand beneath the revetment.
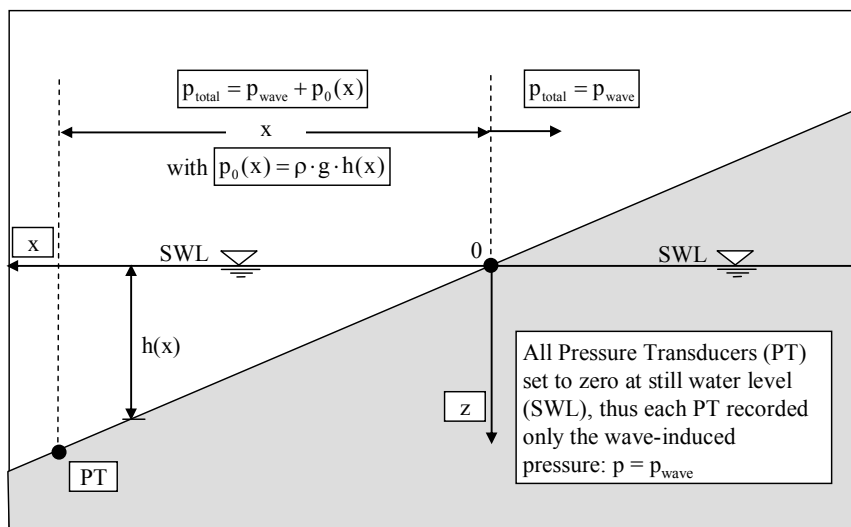
Fig. 5.1: Reference pressure $p_0(x)$ for pressure measured at each PT

(b)   Wave load classification

For the range of surf similarity parameters ξ tested (ξ = 1.6 to 6.5 for irregular waves) two loading cases were determined which are separated by a transition zone (Fig. 5.2):

- Impact load for $\xi < 2.5$

- Transition zone for ξ = 2.5-2.9

- Non-impact loads for $\xi > 2.9$

The surf similarity parameter ξ is related to the incident deep water wave parameters H_{m0} and L_0 calculated with $T_{m-1,0}$ (see Chapter 3, Eq. (3.3)).

$$\xi = \xi_{m-1,0} = \frac{\tan \alpha}{\sqrt{H_{m0} / L_0}}$$
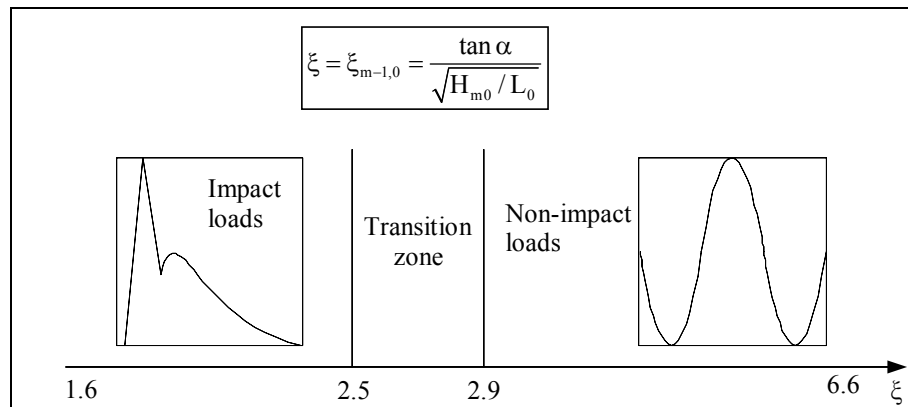
Fig. 5.2:   Wave load classification for waves at the *ELASTOCOAST* revetment

Remark:

For regular waves (range of surf similarity parameters: $\xi = 1.7$ to about 8), the transition zone is wider ($\xi = 1.6$-2.6) than for irregular wave tests (see Annex D.3.1).

Due to the highly transient character of the transition zone and since the recorded pressure values in this zone are generally between the values recorded in the two other zones, prediction formulae will explicitly be developed for impact load and non-impact load, so that an interpolation can be made for the transition zone.

(c)   Parameterisation of impact load

The impact load induced by waves plunging on the slope is characterised by a pressure peak of short duration (impact component) which is super-imposed by a quasi-static component varying cyclicly with the wave motion on the slope (wave period T). This is shown in Fig. 5.3 which also depicts the definition of the maximum pressure p_{max} for the impact load component and $p_{stat,imp}$ for the quasi static load component.
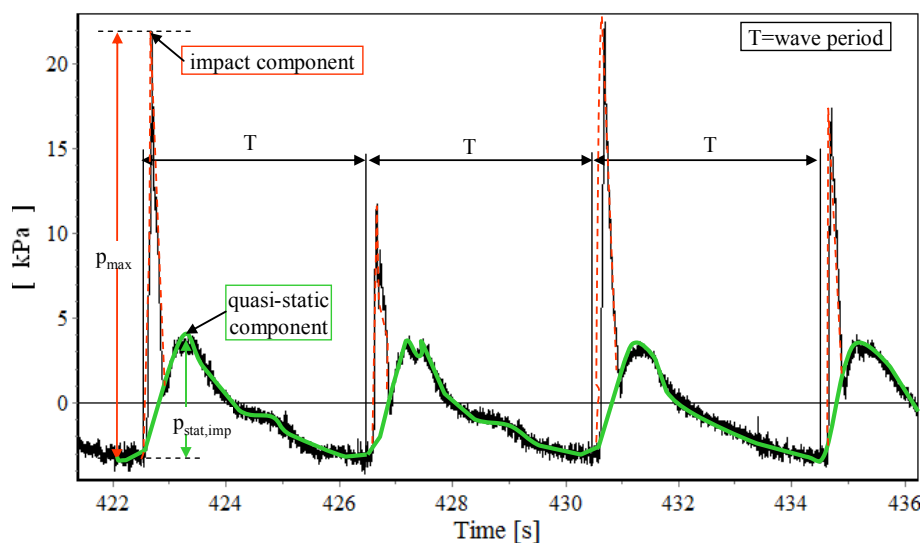
Fig. 5.3:   Definition of impact pressure and quasi-static component for breaking wave impact load

The parameterisation of the impact load in the time domain is illustrated in Fig. 5.4. The different pressures and the time related parameters are defined separately for the impact load component and the quasi-static load component in Fig. 5.4a. Both load components are idealised by two triangles (Fig. 5.4b), so that the entire pressure history for impact load can be parameterized as illustrated by Fig. 5.4c:

- The impact component is described by three parameters: peak pressure p_{max}, rise time t_A and impact duration t_D.

- The quasi-static component is also described by three parameters: peak pressure $p_{stat,imp}$, rise time $t_{stat,imp}$ and load duration T which corresponds to the period of the incident waves.

The same parameterization applies for the impact load beneath the revetment. The parameterization of the impact load in space is illustrated in Fig. 5.5 for pressure on and beneath the revetment.

(a) Time history of an impact pressure

(b) Simplified time history

(c) Parameterized time history
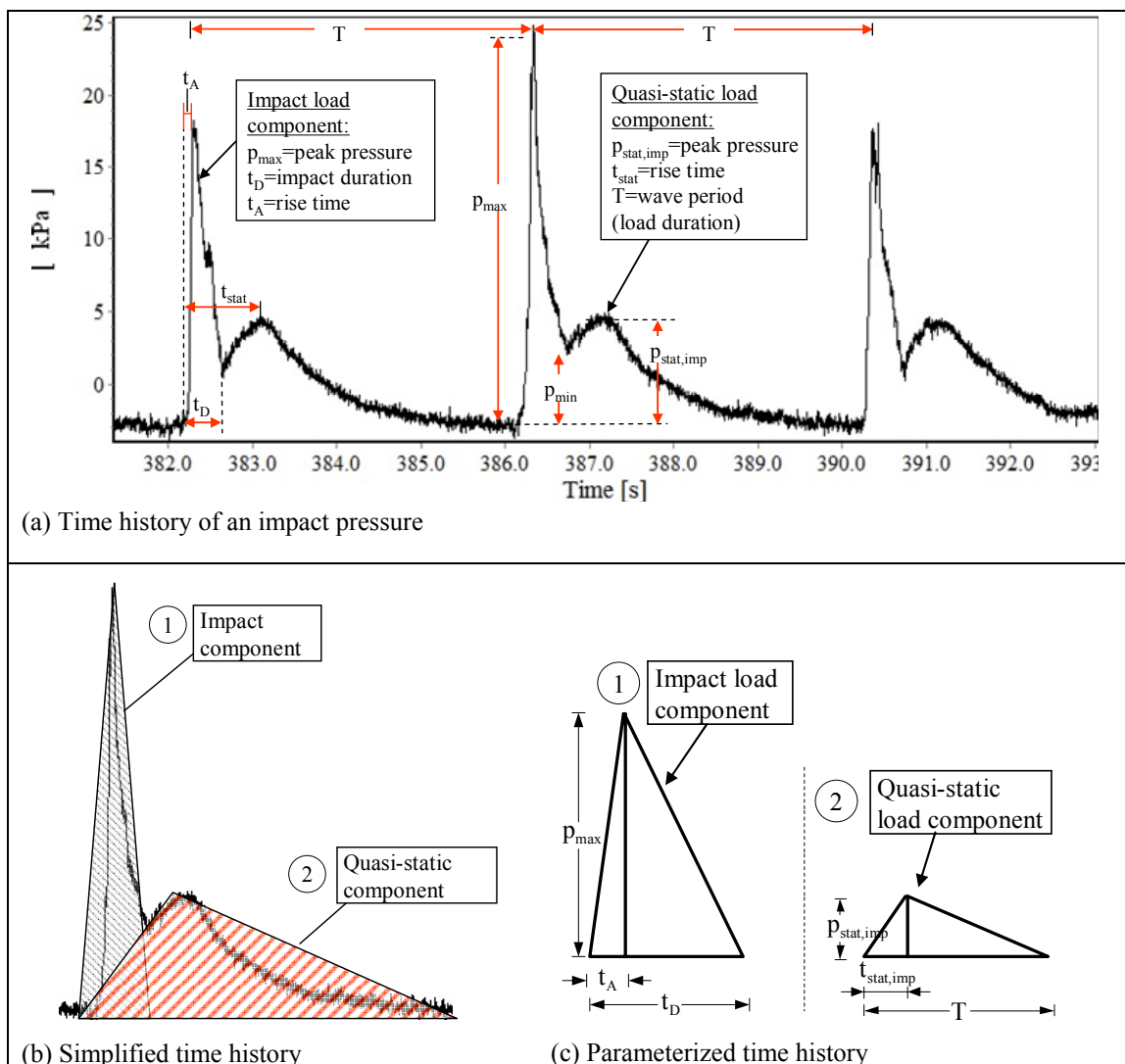
Fig. 5.4:   Parameterization of the pressure history for impact loads

The pressure distribution on the revetment surface is described by five pairs of parameters (p_i, z_i); each pair provides the magnitude of the local pressure p_i at elevation z_i beneath SWL. It is meaningful to relate the pressure p_i at different locations along the slope to the maximum peak pressure p_{max}, and the associated elevation z_i to the location of the maximum pressure z_{pmax}, thus providing five pairs of dimensionless parameters as shown in Fig. 5.5a. Similarly, the wave pressure distributions just beneath the revetment is described by parameter pairs (p_i', z_i'), each pair providing the magnitude of the local pressure p_i', at point i' and the associated elevation z_i' beneath SWL. Relating the local pressure p_i' to p_{max} (on the revetment surface) and the associated elevation z_i' to z_{pmax} will provide four pairs of dimensionless parameters as shown in Fig. 5.5b.

No.	0	1	2	3	4
p_i/p_{max}	1	p_1/p_{max}	p_2/p_{max}	p_3/p_{max}	$p_4/p_{max}=0$
z_i/z_{pmax}	1	z_1/z_{pmax}	z_2/z_{pmax}	z_3/z_{pmax}	z_4/z_{pmax}

with $z_4=R_{u2\%}$

(a) Wave pressure on the surface of the revetment

No.	0	2	3	4
p_{i2}'/p_{max}	p_0'/p_{max}	p_2'/p_{max}	p_3'/p_{max}	$p_4'/p_{max}=0$
z_{i2}'/z_{pmax}	z_0'/z_{imp}	z_2'/z_{pmax}	z_3'/z_{pmax}	z_4'/z_{pmax}

with $z_4'=R_{u2\%}$

(b) Wave pressure just beneath the revetment
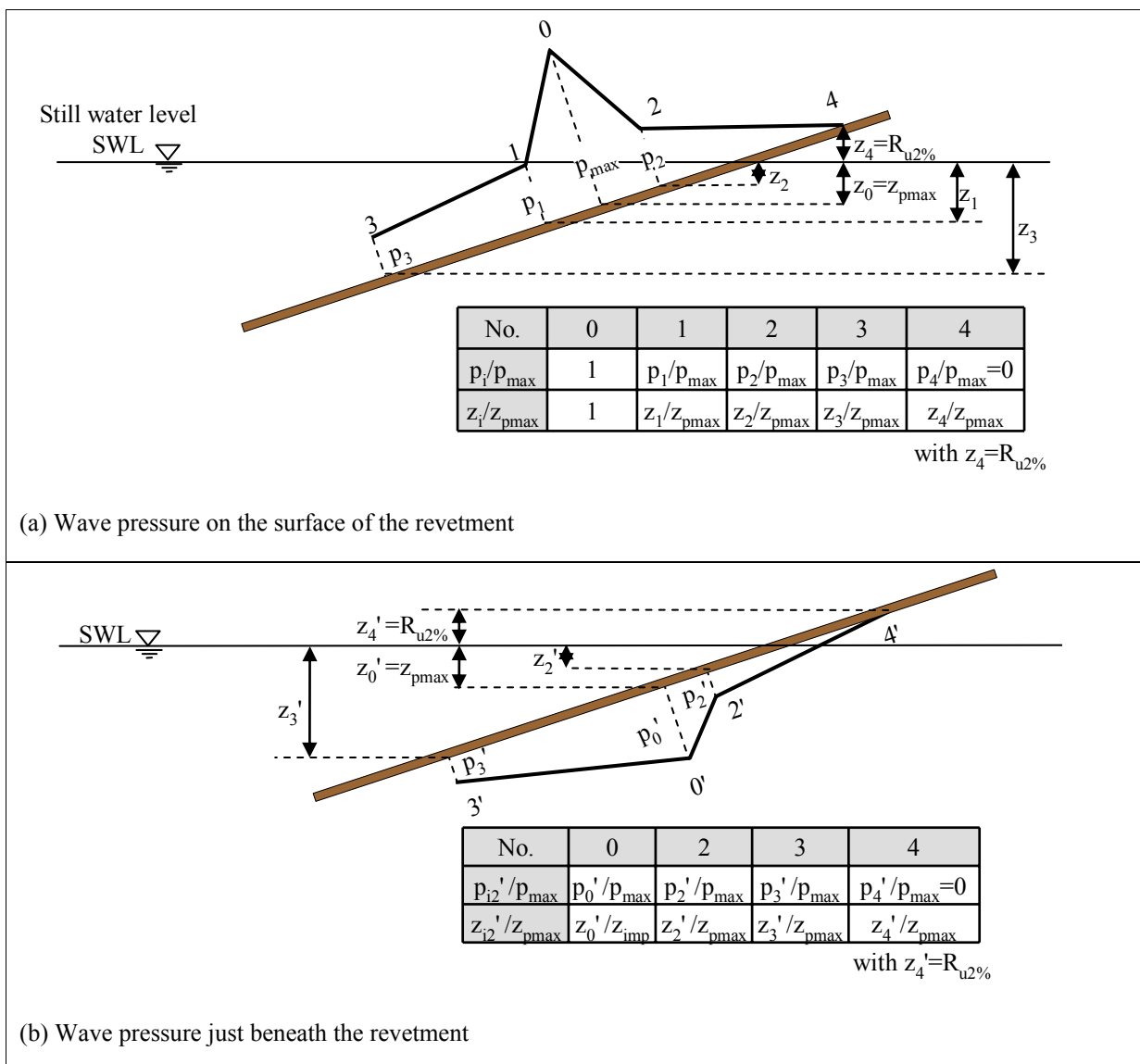
Fig. 5.5: Parameterization of wave pressure distributions on and beneath the revetment for impact load (see also Fig. 5.4)

(d)   Parameterisation of quasi-static load (non-impact)

The quasi-static load induced by waves surging on the slope is characterized by pressure cyclicly varying with the wave motion (wave period T), and is therefore similar to the quasi-static load component following the impact load component in Fig. 5.4a. This is shown in Fig. 5.6 which also depicts the pressure and the time related parameters. The static load is idealised by a trapezoid (Fig. 5.6b), so that the entire pressure history for non-impact load can be parameterized as illustrated by Fig. 5.6c:

The quasi-static load is described by four parameters: peak pressure $p_{max} \stackrel{\triangle}{=} p_{stat}$, rise time $t_{stat,1}$, time till pressure decrease $t_{stat,2}$ and load duration T which corresponds to the period of the incident waves.

(a) Time history of pressure for quasi-static load

(b) Simplified time history

(c) Parameterized time history
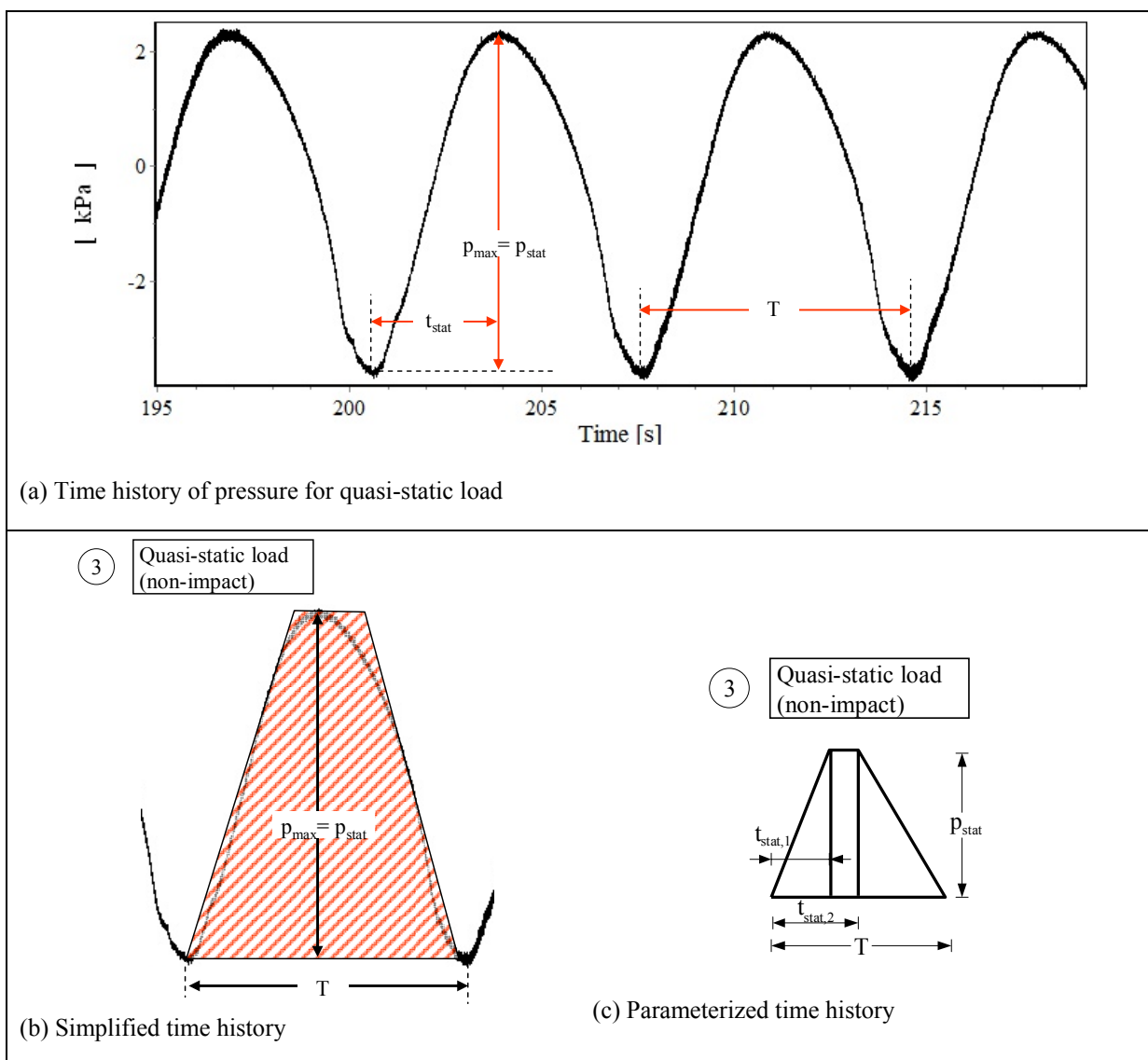
Fig. 5.6:   Parameterisation of the pressure history for quasi-static load

The same parameterization applies for the non-impact load beneath the revetment. The parameterization of the non-impact load in space is illustrated in Fig. 5.7 for the pressure on and beneath the revetment.

The pressure distribution on the revetment surface is described by three pairs of parameters (p_i, z_i), each pair providing the magnitude of the local pressure p_i at elevation z_i beneath the SWL. It is meaningful to relate the pressure p_i to the maximum peak pressure p_{max} and the elevation z_i to the location of the maximum pressure z_{pmax}, thus providing three pairs of dimensionless parameters as shown in Fig. 5.7a. Similarly the wave pressure distributions just beneath the revetment is described by pairs of parameters (p_i', z_i'), each pair providing the magnitude of the local pressure p_i', at point i' and the associated elevation z_i' beneath SWL. Relating the local pressure p_i' to p_{max} (on the revetment surface) and the associated elevation z_i' to z_{pmax} will also provide three pairs of dimensionless parameters as shown in Fig. 5.7b.

No.	0	3	4
p_i/p_{max}	1	p_3/p_{max}	$p_4/p_{max}=0$
z_i/z_{pmax}	1	z_3/z_{pmax}	z_4/z_{pmax}

with $z_4=R_{u2\%}$

a) Wave pressure on the surface of the revetment

No.	0	3	4
p_{i2}'/p_{max}	p_0'/p_{max}	p_3'/p_{max}	$p_4'/p_{max}=0$
z_{i2}'/z_{pmax}	z_0'/z_{imp}	z_3'/z_{pmax}	z_4'/z_{pmax}

with $z_4'=R_{u2\%}$

b) Wave pressure just beneath the revetment
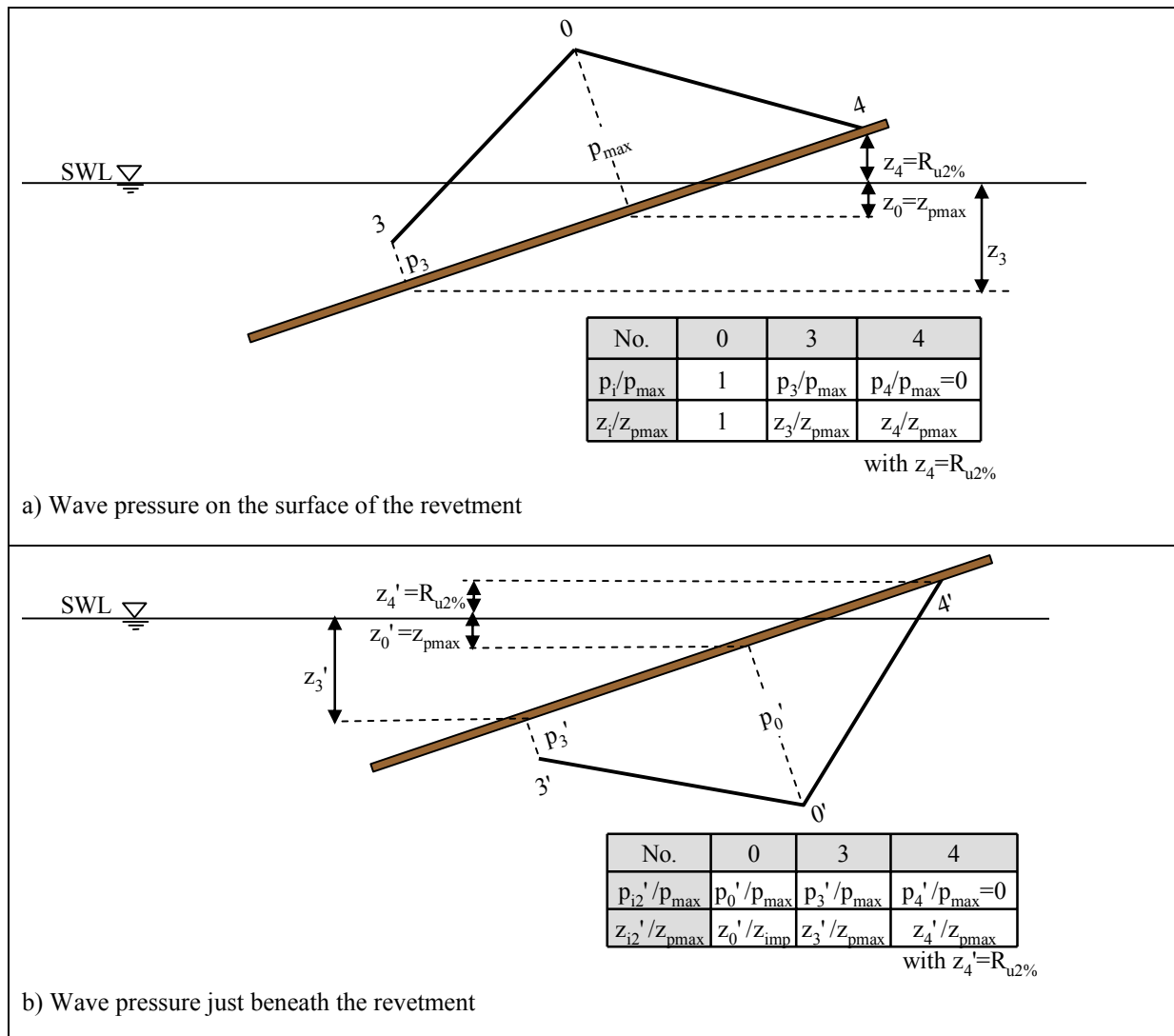
Fig. 5.7: Parameterization of wave pressure distribution on and beneath the revetment for non-impact load (see also Fig. 5.6)

5.2   Maximum pressure on and beneath the revetment

The maximum (peak) pressure, together with its location along the slope (see section 5.3) represents the key parameters since both are used as reference parameters for the calculation of other pressures and their locations along the slope, and thus for the prediction of the entire wave pressure distribution on and beneath the revetment (see Fig. 5.5). Therefore, this section is primarily aimed at developing prediction formulae for maximum pressure by considering both impact and non-impact load on and beneath the revetment.

5.2.1   Maximum wave pressure on the revetment

5.2.1.1   *Pre-processing and preliminary analysis of pressure data*

The maximum pressure for both impact and non-impact load is defined in Fig. 5.4 and Fig. 5.6, respectively. The pressure data considered for the irregular wave tests are those related to *Model Alternative B* (Fig. 2.17). This is due to the early failure of *Model Alternative A* (Fig. 2.16), which was only tested for regular waves and the substitution of *Model Alternative A* by *Model Alternative C* (Fig. 2.18), which could not include pressure transducers on the revetment. The irregular wave tests were generally performed with 1000 waves per test, including four tests with about 500 waves at a later stage. Therefore, the analysis is mainly based on the pressure recorded on the revetment by pressure transducers PT26-PT34 (Fig. 2.17).

Before starting with the analysis, all data were carefully checked (e.g. removing the signals of mal-functioning transducers and the first abnormal signals at the beginning of the tests) and pre-processed (e.g. filtering and classification). The maximum pressure $p_{max} = p_{max,N}$ considered in the analysis for each test with a duration of N-waves (N generally equal to 1000) is the highest pressure recorded on the revetment over the entire time series.

The most common approach used in the analysis of wave pressures on sloped structures is to consider a non-dimensional pressure

$$\bar{p}_{max} = \frac{p_{max}}{\rho \cdot g \cdot H_{m0}} \tag{5.2}$$

as a function of the surf similarity parameter $\xi_{m-1,0}$ (see Eq. (3.3)). Instead of the surf similarity parameter the deep water wave steepness (H_0/L_0) has also been used in few studies (e.g. Stive, 1984). Both approaches were compared for all data in a systematic preliminary analysis (Ludwigs, 2009) and as a result the approach using the surf similarity parameter as a governing factor is selected for the detailed analysis. Particularly for irregular waves, the surf similarity parameter $\xi_{m-1,0}$ provides a better correlation with the pressure data than the wave steepness H_0/L_0.

Therefore, all pressure data $\overline{p}_{max} = p_{max}/\rho g H_{m0}$ are plotted against $\xi_{m-1,0}$ like in Fig. 5.8, showing that the highest pressures generally occur for plunging waves with $\xi_{m-1,0} < 2$ with values up to $p_{max}/\rho g H_{m0} \approx 6$ for $\xi_{m-1,0} = 1.6$ and an outlier of $p_{max}/\rho g H_{m0} \approx 7.5$ for $\xi_{m-1,0} = 2.2$.
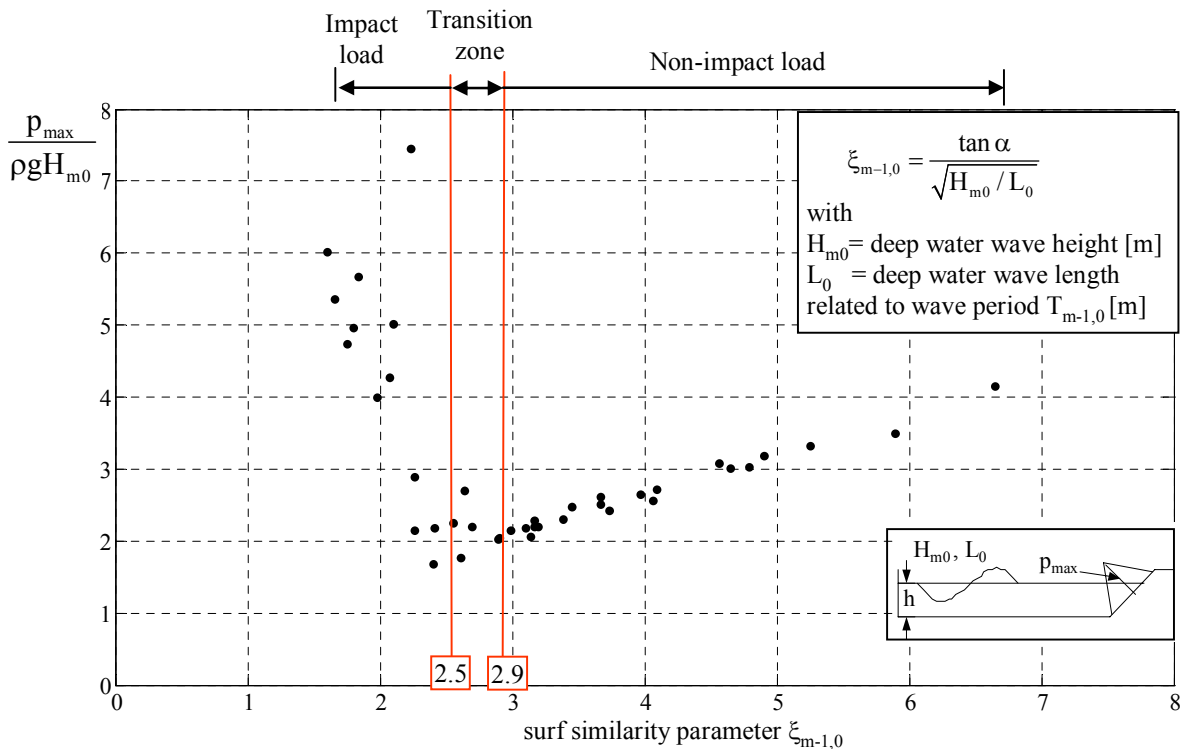
Fig. 5.8: Maximum pressure $p_{max}/\rho g H_{m0}$ on the revetment against surf similarity parameter $\xi_{m-1,0}$ for irregular wave tests

For the range of tested $\xi_{m-1,0}$-values ($\xi_{m-1,0} = 1.6 - 6.6$) and ignoring the outlier at $\xi_{m-1,0} = 2.2$, a linear relationship (decreasing) for $\xi_{m-1,0}$-values from $\xi_{m-1,0} = 1.6$ to 2.5 seems to exist while another linear relationship (increasing) prevails for $\xi_{m-1,0} > 2.9$. The intermediate $\xi_{m-1,0}$-values ($2.5 < \xi_{m-1,0} < 2.9$) correspond to the transition zone as defined in Fig. 5.2. Expectedly, the data in the impact load and transition zone ($\xi_{m-1,0} < 2.9$) are much more scattered than for the non-impact load ($\xi_{m-1,0} > 2.9$). It is also seen from Fig. 5.8 that high relative pressure may occur for very large $\xi_{m-1,0}$-values, i.e. for large wave periods.

For a better understanding of the large pressure values which result for non-impact load with large $\xi_{m-1,0}$ the test with the largest $\xi_{m-1,0}$-value ($\xi_{m-1,0} = 6.6$) is analysed in Fig. 5.9, showing the maximum wave run-up/run-down (Fig. 5.9a) and the pressure time series in which the maximum pressure p_{max} occurred at pressure transducer PT28 (Fig. 5.9b). The maximum pressure p_{max} occurs at pressure transducer PT28 with the highest wave run-up on the *ELASTO-COAST* revetment as shown in Fig. 5.9a.

a) Wave run-up and run-down situation for p_{max} under non-impact load

b) Pressure time series with p_{max} for test 090610_01 with $\xi_{m-1,0} = 6.6$ (non-impact load)
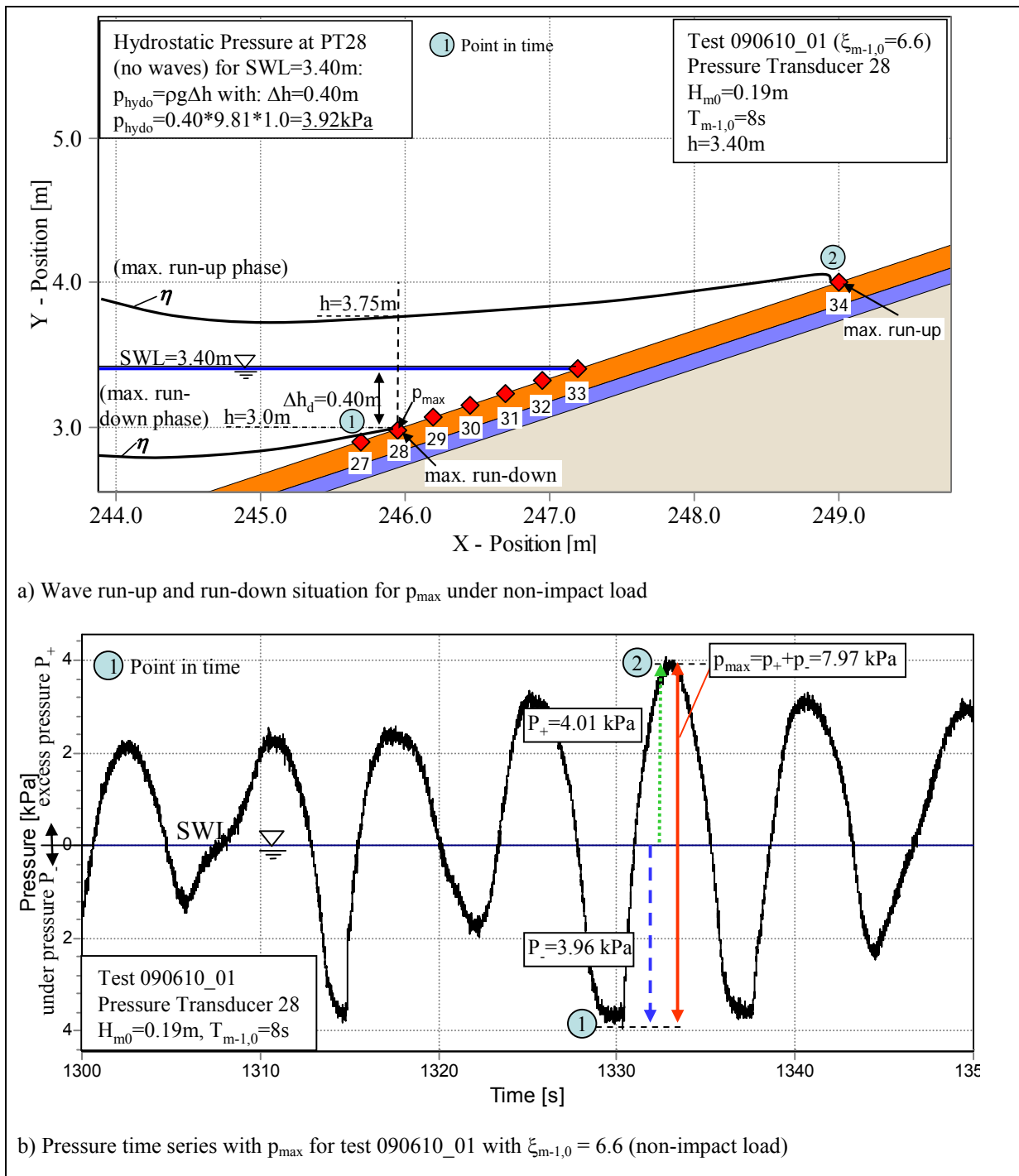
Fig. 5.9:   Example for pressure values with large $\xi_{m-1,0}$-values (non-impact load)

Like the other pressure transducers PT28 was set to p = 0 before starting the test (SWL without waves). Any variation of the surface elevation above PT28 is caused by wave motion: "under pressure" p- for η lower than SWL and "excess pressure" p+ for η higher than SWL.

At minimum wave run-down the pressure head is Δh_d=0.40 m leading to an "under pressure" p- = 3.92 kPa ((1) in Fig. 5.9a) which corresponds to the maximum pressure p-=3.96 kPa recorded at PT28 ((1) in Fig. 5.9b).

At maximum wave run-up the pressure head Δh_u = 0.41 m ((2) in Fig. 5.9a) corresponding to the excess pressure p_+ = 4.01 kPa recorded at PT28 ((2) in Fig. 5.9b). As p_{max} is defined as p_{max}=│p_+│+│p-│ a large pressure generally results for large ξ-values providing large run-up and run-down.

> *Remark:*
>
> *As compared to the results of regular wave test in Annex D the impact pressure values for irregular wave tests are much lower and the scatter of the data is much less pronounced.*

5.2.1.2 *Maximum pressure on the revetment for impact load and transition zone*

For the range of wave steepness (H_{m0}/L_0 = 0.0025-0.0434) and surf similarity ($\xi_{m-1,0}$ = 1.6-6.6) tested, both non-linear and linear functions were comparatively examined to fit the relative pressure data $p_{max}/\rho g H_{m0}$ within a systematic preliminary data analysis (Ludwigs, 2009). As a result, a linear function between relative maximum pressure and surf similarity parameter was favoured since (i) it provides the best fit and (ii) it is simpler than any non-linear function and more practical. Moreover, as will be seen in section 5.2.2, the maximum pressure transmitted just beneath the revetment also linearly decreases with increasing $\xi_{m-1,0}$ (for ξ-range tested!), so that the same linear function can be used by only introducing a reduction (damping) factor (Fig. 5.17).

The pressure data for both impact load ($\xi_{m-1,0}$ = 1.6-2.5) and transition zone ($\xi_{m-1,0}$ = 2.5-2.9) are plotted against the surf similarity parameter $\xi_{m-1,0}$ in Fig. 5.10, resulting in the following linear function for impact load ($\xi_{m-1,0}$<2.5) with a coefficient of variation of σ'=37.6%:

$$\frac{p_{max}}{\rho \cdot g \cdot H_{m0}} = -4 \cdot \xi_{m-1,0} + 12.5 \quad \text{for } 1.6 < \xi_{m-1,0} < 2.5 \qquad (5.3)$$

For the transition zone ($\xi_{m-1,0}$= 2.5 -2.9) a linear function is also adapted:

$$\frac{p_{max}}{\rho \cdot g \cdot H_{m0}} = -0.56 \cdot \xi_{m-1,0} + 3.7 \quad \text{for } 2.5 < \xi_{m-1,0} < 2.9 \qquad (5.4)$$

> *Remark:*
>
> *Comparatively, in the range of surf similarity parameters tested for regular waves (ξ=1.2 – 8.0), a constant function is obtained for impact load (ξ < 1.6) and a linearly decreasing function is obtained for the transition zone (ξ = 1.6-2.6) (Annex D.3.3) providing much lower $p_{max}/\rho g H_m$ values than for irregular waves.*
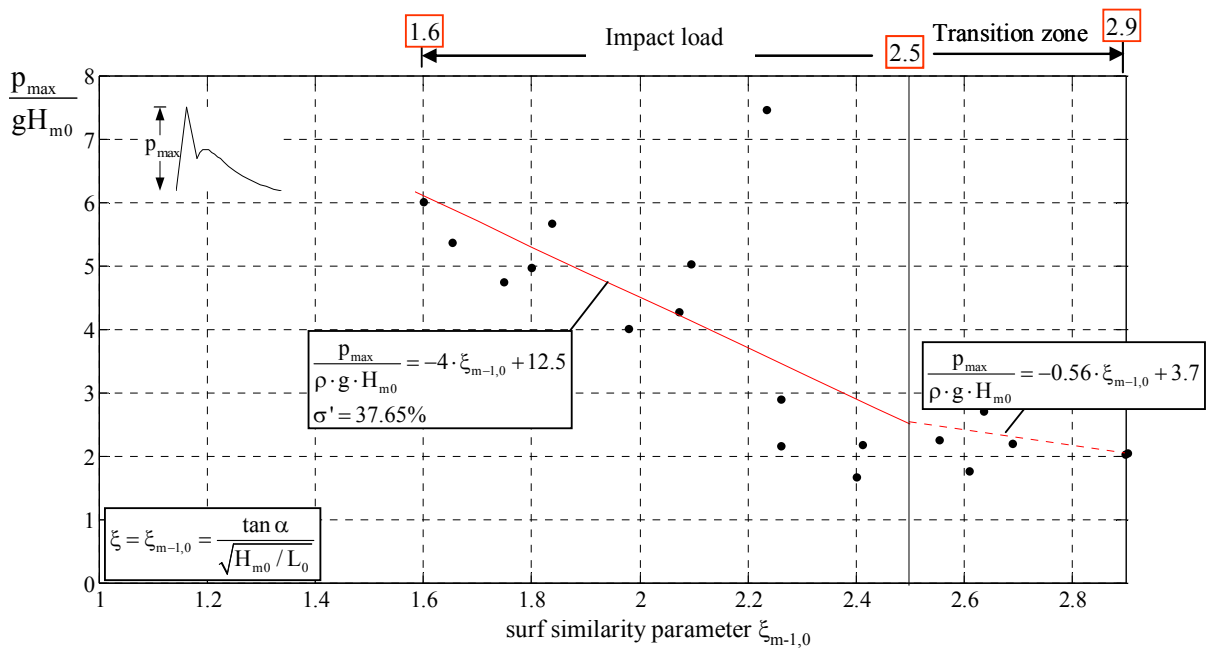
Fig. 5.10: Formulae for the impact pressure $p_{max}/\rho g H_{m0}$ on the revetment against surf similarity parameter $\xi_{m-1,0}$ for irregular wave tests

5.2.1.3 *Maximum pressure on the revetment for quasi-static loads*

Quasi-static pressures for the non-impact load (Fig. 5.6), like the quasi-static component of the impact load (Fig. 5.3 and Fig. 5.4), exhibit the same features and vary cyclicly with the wave period. Therefore, the same relationship between $p_{stat}/\rho g H_{m0}$ and $\xi_{m-1,0}$ is expected to apply for both types of loads for the entire range of $\xi_{m-1,0}$-values tested. This is indeed the case as shown by the results in Fig. 5.11, resulting in the following relationship:

$$\frac{p_{stat}}{\rho \cdot g \cdot H_{m0}} = 0.68 \cdot \xi_{m-1,0} \quad \text{for } 2.9 < \xi_{m-1,0} < 4.5 \tag{5.5}$$

and

$$\frac{p_{stat}}{\rho \cdot g \cdot H_{m0}} = 0.41 \cdot \xi_{m-1,0} + 1.2 \quad \text{for } \xi_{m-1,0} > 4.5 \tag{5.6}$$

It is suggested, however, to use Eq. (5.5) for $\xi_{m-1,0} > 2.9$ since it is simpler and more conservative than using also Eq. (5.6) for $\xi_{m-1,0} > 4.5$. The behaviour suggested by both equations (5.5) and (5.6) better reflects the underlying physics (similar to wave run-up behaviour as a function of $\xi_{m-1,0}$), but this is less important for engineering practice.
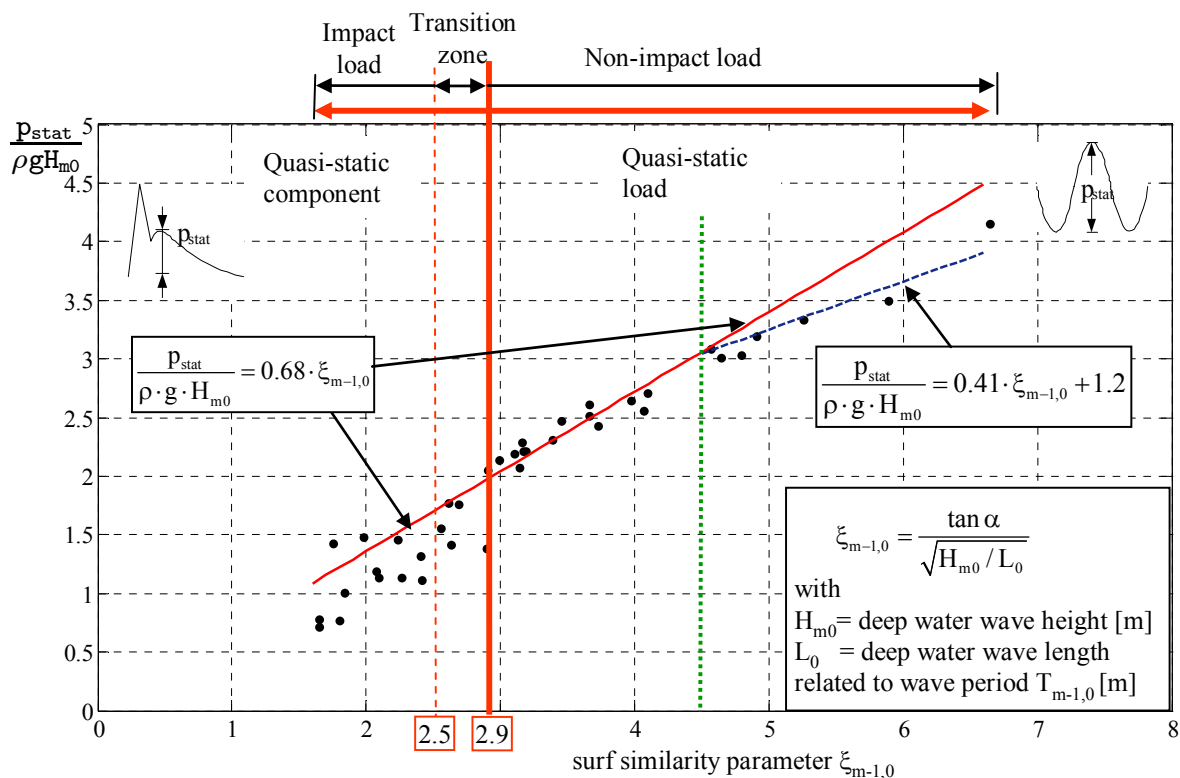
Fig. 5.11: Quasi-static load $p_{stat}/\rho g H_{m0}$ on the revetment plotted against surf similarity parameter $\xi_{m-1,0}$

Remark:

Comparatively, for regular wave tests, a similar function is obtained providing 10-20% lower peak pressure $p_{stat}/\rho g H_m$ (see Annex D3.4).

5.2.2 Maximum pressure just beneath the revetment

5.2.2.1 Pre-processing and preliminary analysis of pressure data

The same procedure as for the maximum pressure on the revetment is applied (see section 5.2.1). Because many of the transducers, installed just beneath the revetment of *Model Alternative B* were malfunctioning, the analysis is based on the pressure recorded by pressure transducers PT10-PT14 of *Model Alternative C* (Fig. 2.18). The same definition of the maximum pressure is also applied for both impact and non-impact load (Fig. 5.4 and Fig. 5.6). To discriminate between the pressure on and beneath the revetment an index 2 (second layer of pressure transducers) is added to the notations of the pressure (p_2) and other parameters related to this second layer of transducers (Fig. 5.12).
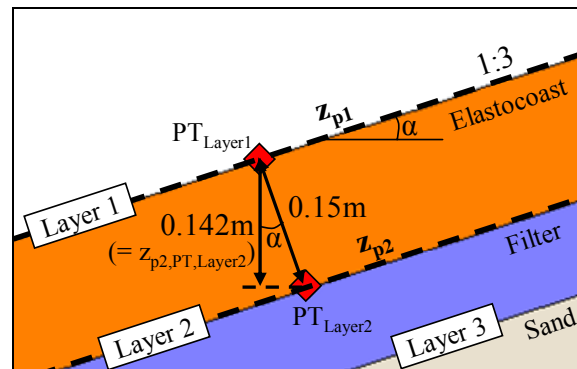
Fig. 5.12: Definition of index 2 for discrimination between pressures measured on the revetment and just beneath the revetment

In a similar way as in Fig. 5.8, all pressure data $\overline{p}_{2,max} = p_{2,max} / \rho g H_{m0}$ are plotted against $\xi_{m-1,0}$ in Fig. 5.13 for pressures beneath the revetment. Overall, more scatter than for the pressures on the revetment can be noted. This particularly applies for the non-impact loading case. Moreover, for impact loads ($\xi_{m-1,0} < 2.5$) the peak pressure is substantially reduced ($p_{2,max}/\rho g H_{m0} \approx 3.7$) as compared to the peak pressure in Fig. 5.8 ($p_{max}/\rho g H_{m0} \approx 7.5$) while this is not the case for the non-impact loads ($\xi_{m-1,0} > 2.9$).
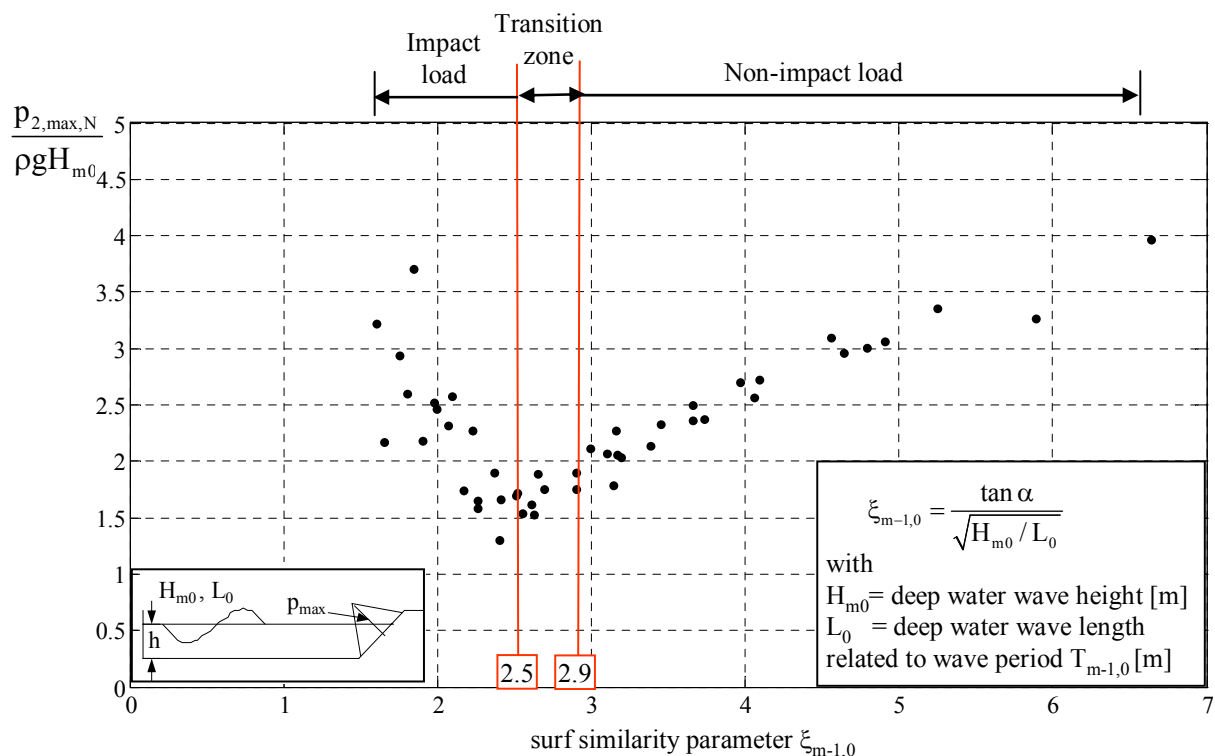
Fig. 5.13: Peak pressure $p_{2,max,N}/\rho g H_{mo}$ just beneath the revetment plotted against surf similarity parameter $\xi_{m-1,0}$ for irregular wave tests

Remark:
As compared to the results of regular wave test in Annex D.3.2.1 the impact pressure values for irregular wave tests are much lower and the scatter of the data is much less pronounced.

Moreover, it is also important to examine exemplary for single events how the impact pressure and the quasi-static pressure for non-impact load are damped by the revetment. For this purpose, pressure signals recorded simultaneously on and beneath the revetment at the locations of the maximum pressure p_{max} as well as the associated pressure distribution are selected which are typical for each loading case: impact load, transition zone and non-impact load. As shown in Fig. 5.14-Fig. 5.16 regular wave tests were preferred for this purpose because (i) the processes of interest are similar for regular and irregular waves and (ii) these processes are simpler to identify and understand than for irregular waves:

- Impact load: single events simultaneously recorded at the pressure transducers where the maximum pressure occurred on the revetment (PT7) and just beneath the revetment (PT13) are depicted in Fig. 5.14 for $\xi_0 = 1.22$, showing that:

  (i) The pressure of the impact load component is much more strongly damped (by about 40%) than those of the quasi-static component (Fig. 5.14a).

  (ii) The time shift between the occurrence of the peak pressure on and just beneath the revetment is negligible small ($\Delta t = 5 \cdot 10^{-3}$s) so that for the engineering practice it can be assumed the pressure on and just beneath the revetment occur simultaneously (Fig. 5.14a).

  (iii) The pressure distribution just beneath the revetment is similar to that on the revetment, but strongly damped in the impact zone and less outside the impact zone (Fig. 5.14b).

- Transition zone: single events simultaneously recorded at the pressure transducers where the maximum pressure occurred on the revetment (PT5) and just beneath the revetment (PT12) are depicted in Fig. 5.15 for $\xi_0 = 2.57$, showing that:

  (i) The pressures are much less damped (by ca. 20%) than those of the impact load. Surprisingly the damping occurs at the "troughs" of the pressure signals while at the "crest" almost no damping is observed.

  (ii) The time shift between the occurrence of the peak pressure on and just beneath the revetment is about one order of magnitude larger than for the impact load ($\Delta t = 0.03$s), but this shift is still extremely small and is therefore negligible for the engineering.

  (iii) The pressure distribution just beneath the revetment is very similar to that on the revetment and the damping which is relatively weak around the area of maximum pressure becomes even weaker outside this area.

- Non-impact load: singe events simultaneously recorded at the pressure transducers PT5 on the revetment and PT12 beneath the revetment are depicted in Fig. 5.16 for $\xi_0 = 4.49$, showing that:

(i) The pressures are less damped (by ca. 10%) than those in the transition zone. In contrast to the latter (see Fig. 5.15a) the damping occurs at the "crest" and not at the "troughs" of the pressure signals.

(ii) There is practically no time shift between pressure on and just beneath the revetment.

(iii) The pressure distributions on and just beneath the revetment are similar. Since the damping is very small (less than 10%), the same distribution can be adopted on and beneath the revetment.
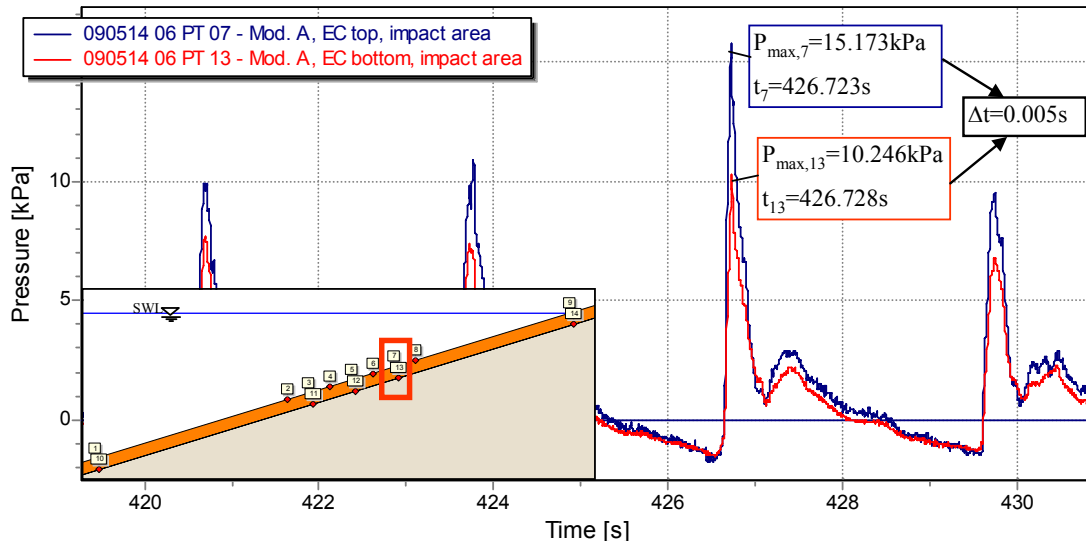
a) Time series for PT7 on the revetment and PT13 beneath the revetment
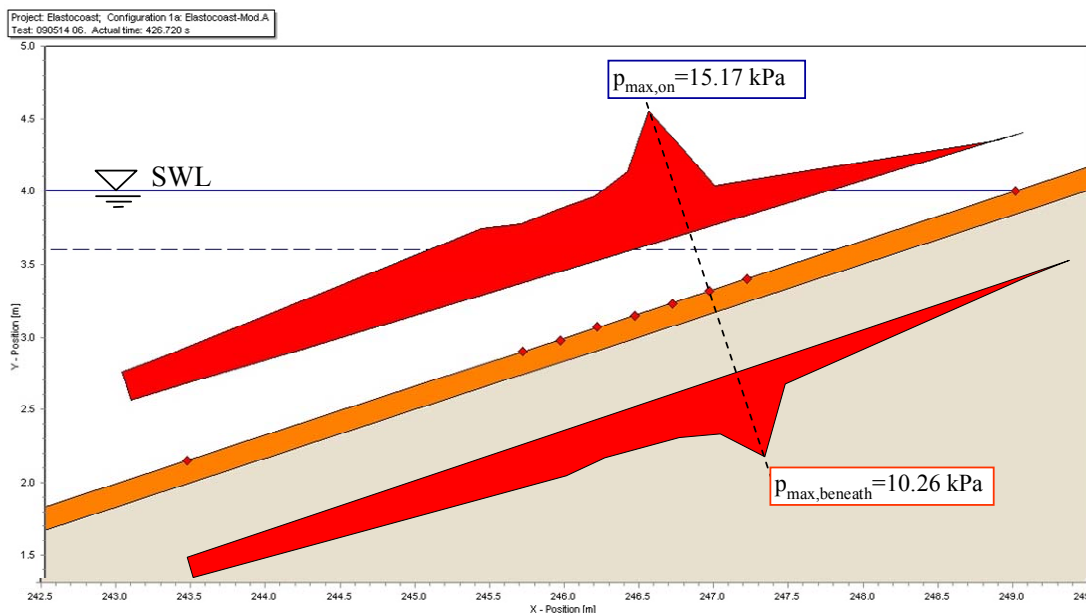
b) Pressure distribution on and beneath the revetment

Fig. 5.14: Time series and pressure distribution for impact load ($\xi_0 = 1.22$)
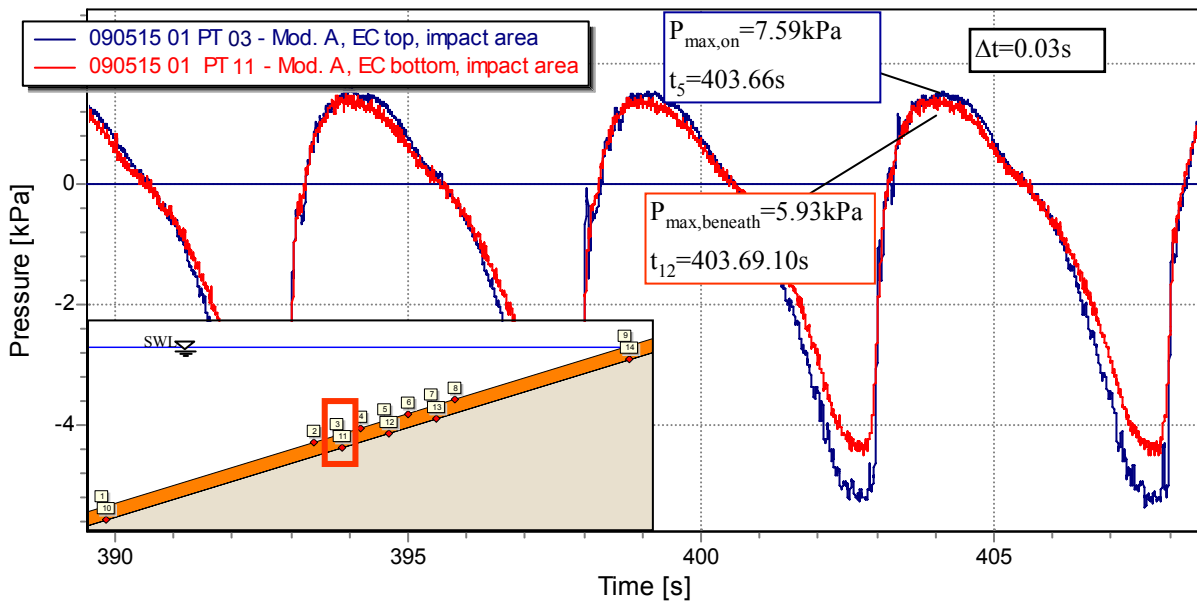
a) Time series for PT5 and PT12 p_{max}
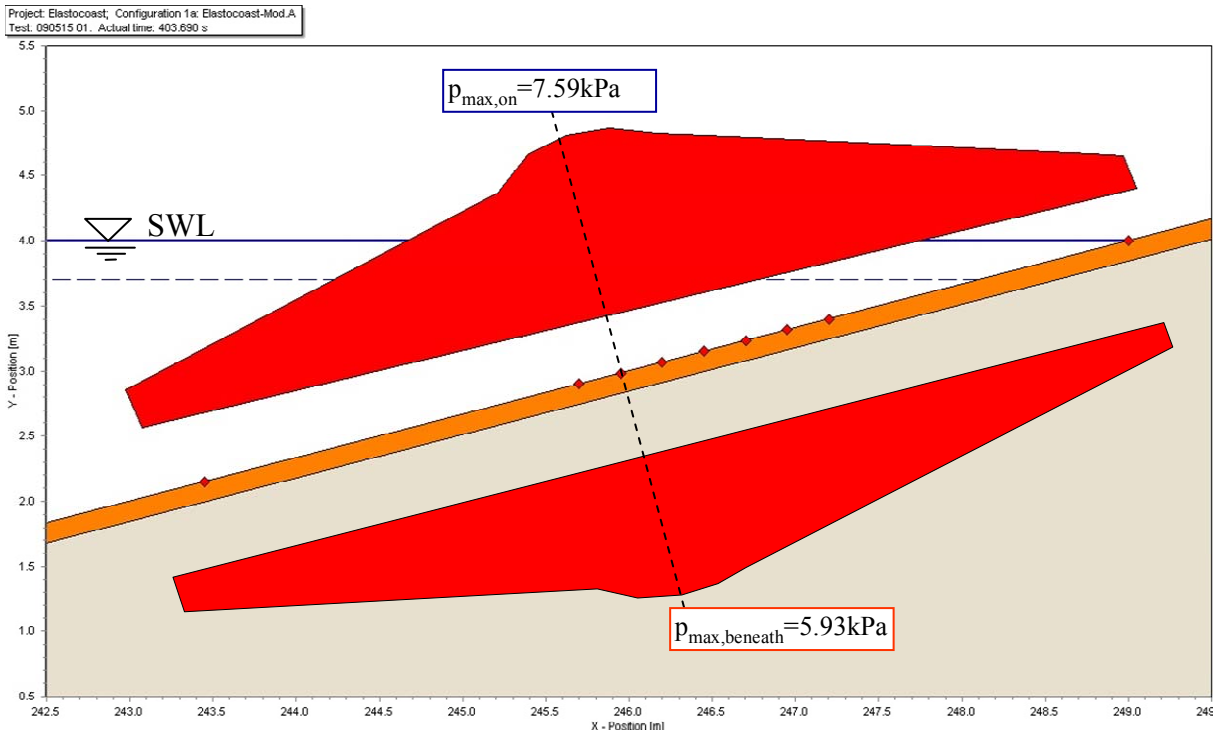
b) Pressure distribution on and beneath the revetment

Fig. 5.15: Time series and pressure distribution for transition zone ($\xi_0 = 2.57$)
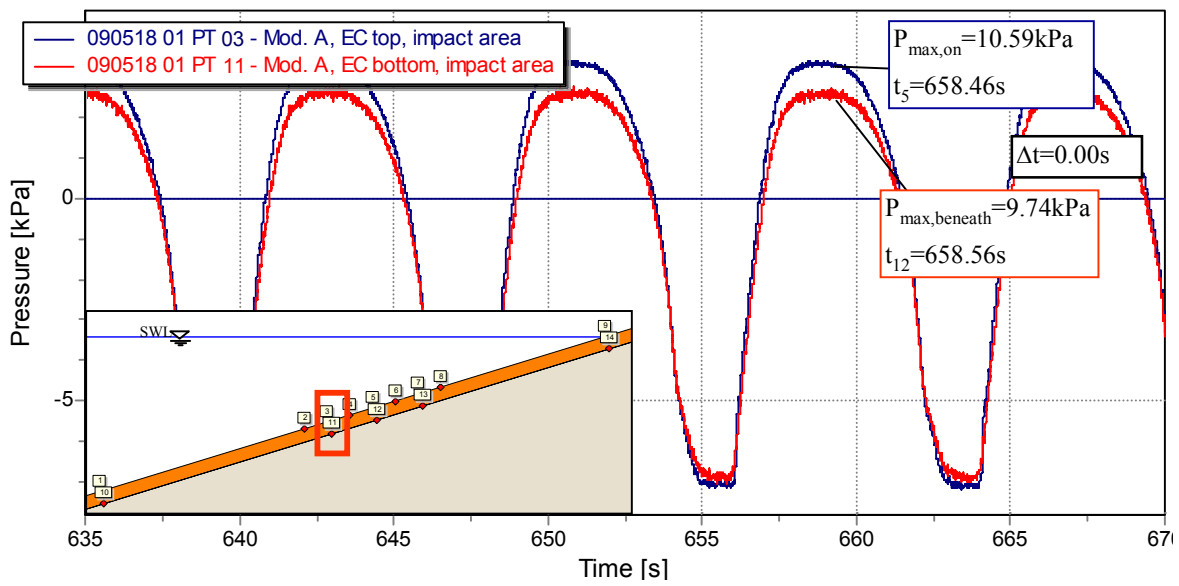
a) Time series for PT5 and PT12 p_{max}
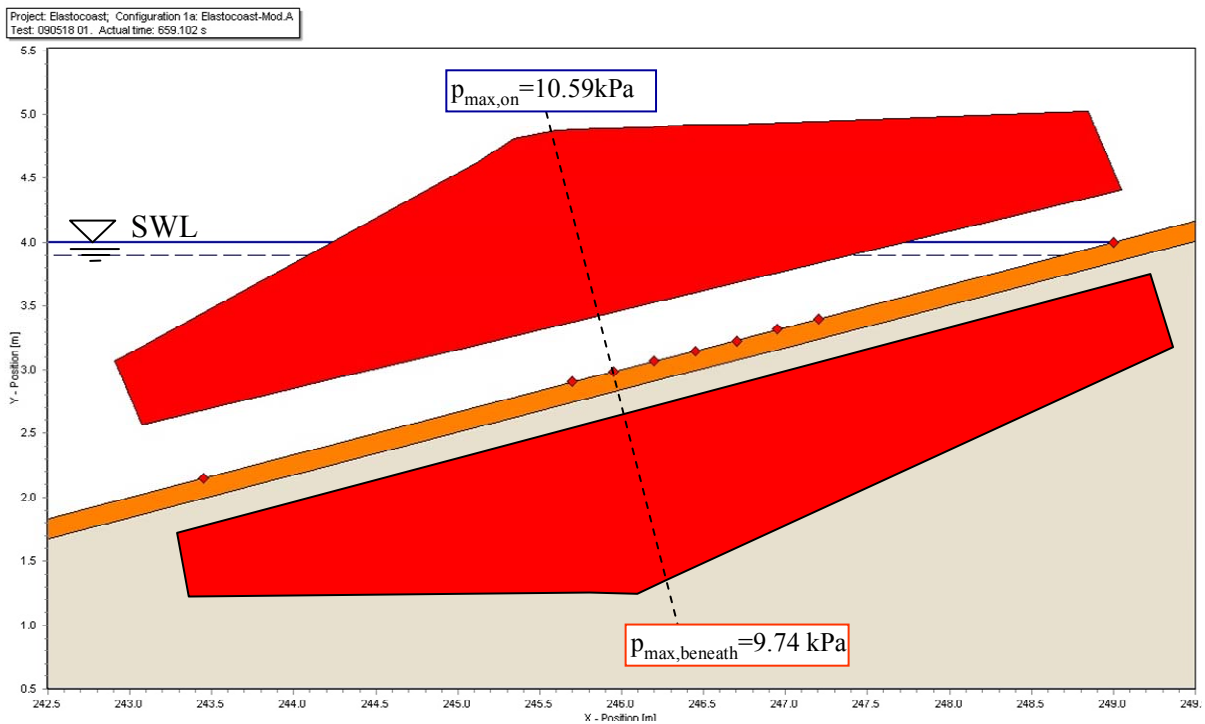
b) Pressure distribution on and beneath the revetment

Fig. 5.16: Time series and pressure distribution for non-impact load ($\xi_0 = 4.49$)

5.2.2.2 *Maximum pressure just beneath the revetment for impact load and transition zone*

Like in section 5.2.2, the pressure data $p_{2,max}/\rho g H_{m0}$ for both impact load and transition zone are plotted against surf similarity parameter $\xi_{m-1,0}$ in the same figure (see Fig. 5.10) in order to compare directly both pressures on and beneath the revetment. The result is shown in Fig. 5.17 which clearly illustrates that the peak pressure beneath the revetment $p_{2,max}$ for impact load can be described by the same linear function as for the pressures on the revetment (Eq. (5.3)) by introducing a reduction (damping) factor of 60% (with a coefficient of variation of $\sigma' \approx 19\%$):

$$\frac{p_{2,max}}{\rho \cdot g \cdot H_{m0}} = 0.6 \cdot \left[-4.0 \cdot \xi_{m-1,0} + 12.5 \right] \quad \text{for } 1.6 < \xi_{m-1,0} < 2.5 \qquad (5.7)$$
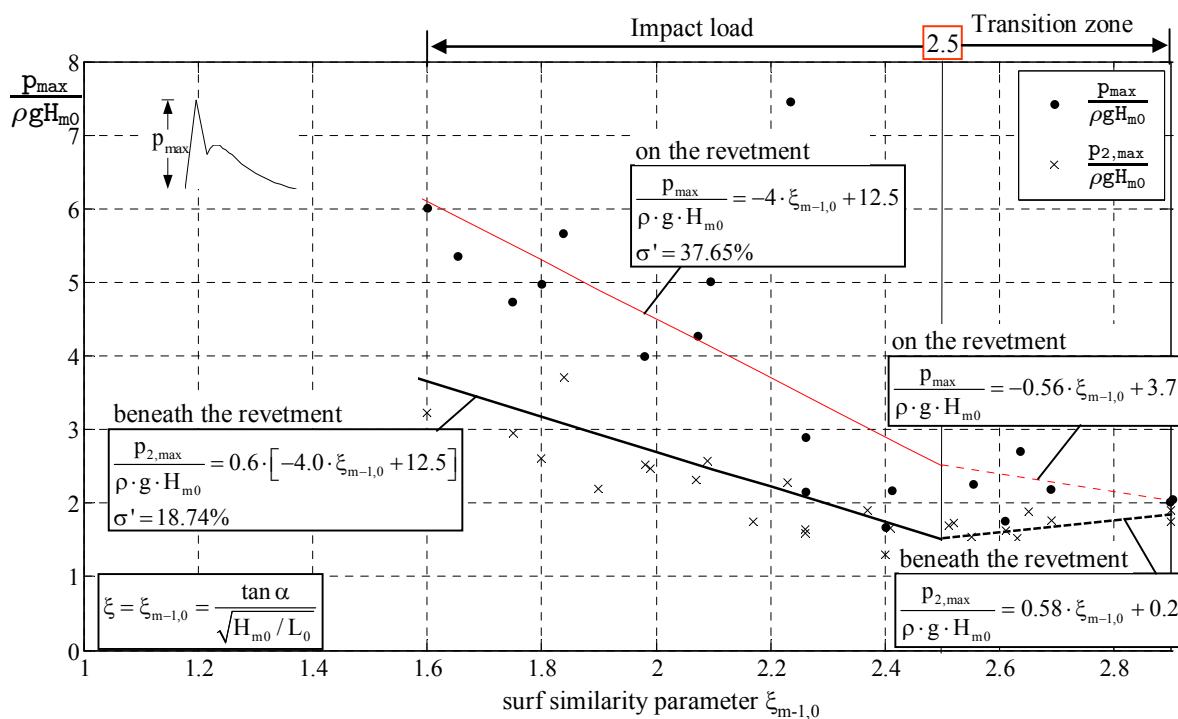
Fig. 5.17: Impact pressures $p_{max}/\rho g H_{m0}$ and $p_{2,max}/\rho g H_{m0}$ on and beneath the revetment against surf similarity parameter $\xi_{m-1,0}$ for irregular wave tests

For the transition zone ($2.5 < \xi_{m-1,0} < 2.9$) a linear function is adopted by considering that for $\xi_{m-1,0} \geq 2.9$ (non-impact load) the pressure are transmitted beneath the revetment without any noticeable damping (see also Fig. 5.18)

$$\frac{p_{2,max}}{\rho \cdot g \cdot H_{m0}} = 0.58 \cdot \xi_{m-1,0} + 0.2 \quad \text{for } 2.5 < \xi_{m-1,0} < 2.9 \qquad (5.8)$$

> *Remark:*
>
> *Comparatively, in the range of surf similarity parameters tested for regular waves (ξ=1.2 – 8.0), a constant function is obtained for impact load (ξ < 1.6) and a linearly increasing function is obtained for the transition zone (ξ = 1.6-2.6) (Annex D, Fig. D.3.5) providing much lower $p_{2,max}/\rho g H_m$ values than for irregular waves.*

5.2.2.3 Maximum pressure just beneath the revetment for quasi-static load

Since no noticeable damping of the quasi-static pressure by the revetment is expected, the pressure data beneath the revetment are directly plotted on the same figure as for the pressure on the revetment (see Fig. 5.11). The results are obtained in Fig. 5.18, showing that indeed no noticeable damping occurs for the entire range of $\xi_{m-1,0}$-values tested and that the maximum pressure $p_{2,max}$ can be predicted by the same relationship as for the pressures on the revetment (see Eqs. (5.5) and (5.6)). For design purpose, it is more simple to use only Eq. (5.5) for the entire range of tested surf similarity paramteres which is on the safe side.
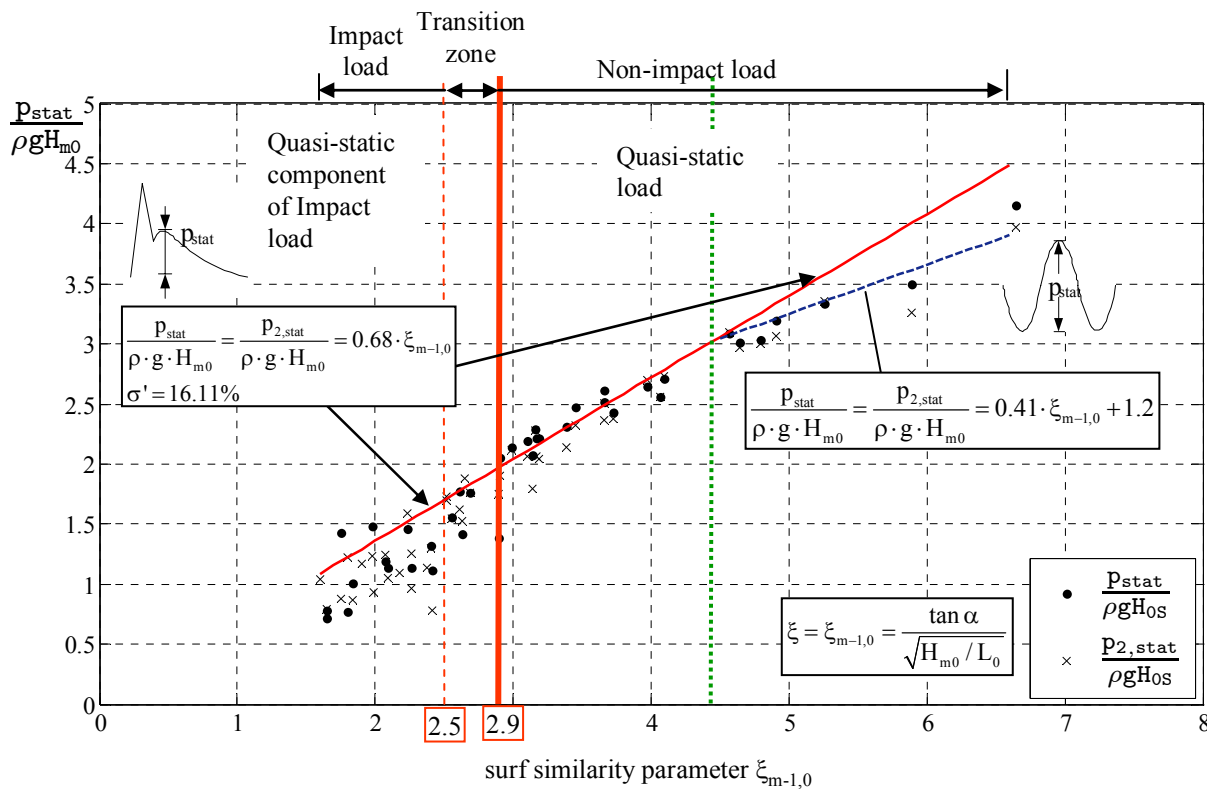
Fig. 5.18: Formulae for the quasi-static load $p_{stat}/\rho g H_{m0}$ on and beneath the revetment against surf similarity parameter $\xi_{m-1,0}$ for irregular wave tests
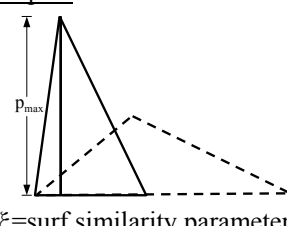
Remark:

Comparatively, for regular wave tests, a similar function is obtained providing 20-25% lower peak pressures (see Annex D, Fig. D.3.6).

5.2.3 Summary of results for maximum wave pressure

All the proposed formulae for the prediction of the maximum pressure for impact load and non-impact load are summarized in Tab. 5.1.

Tab. 5.1: Summary of results for maximum wave pressure

	Definition	Pressure on the revetment	Pressure beneath the revetment
Impact load (1.6<ξ<2.5)	**Impact** p_{max} ξ=surf similarity parameter	$\dfrac{p_{max}}{\rho \cdot g \cdot H_{m0}} = -4 \cdot \xi_{m-1,0} + 12.5$ (5.3)	$\dfrac{p_{2,max}}{\rho \cdot g \cdot H_{m0}} = 0.6 \cdot \left[-4.0 \cdot \xi_{m-1,0} + 12.5 \right]$ (5.7)
	Quasi-static component $p_{stat,imp}$		
Non-impact load (ξ>2.9)	**Non-impact pressure** $t_{stat,1}$ p_{stat}	$\dfrac{p_{stat,imp}}{\rho \cdot g \cdot H_{m0}} = 0.68 \cdot \xi_{m-1,0}$ (5.5)	$\dfrac{p_{2,stat,imp}}{\rho \cdot g \cdot H_{m0}} = 0.68 \cdot \xi_{m-1,0}$ (5.5)

5.3 Location of maximum wave pressure on and beneath the revetment

As mentioned in the introduction of section 5.2, the location of the maximum pressure represents a key parameter in the parameterization of the pressure distribution on and beneath the revetment (Fig. 5.5). It is therefore the primary aim of this section to develop formulae to predict the location of the maximum (peak) pressure beneath still water level (SWL). In contrast to section 5.2 and as shown by previous studies (e.g. Schüttrumpf, 2001 and Klein Breteler, 2007) there is no need to distinguish between the different loading cases for the analysis. Discrimination is required only between the pressures on and beneath the revetment.

5.3.1 Location of peak pressure on the revetment

5.3.1.1 Preliminary Analysis

Previous studies have generally used the wave steepness (H_0/L_0) or the surf similarity parameter (ξ) as a governing factor to analyse the non-dimensional elevation of the maximum (peak) pressure beneath still water level (SWL):

$$\bar{z}_{p\,max} = \frac{z_{p\,max}}{H_{m0}} \qquad (5.9)$$

A preliminary analysis using the two approaches has shown that there were no significant differences (Ludwigs, 2009). Since for the analysis of the maximum pressure, the surf similarity parameter ξ was adopted as the governing parameter (see section 5.2.1), the same approach is therefore also used for the analysis of z_{pmax}/H_{m0}.

The data of the location of peak pressure z_{pmax}/H_{m0} are plotted against surf similarity parameter $\xi_{m-1,0}$ in Fig. 5.19, suggesting that either a steady tanh-function as proposed by Schüttrumpf, 2001 for smooth impermeable slopes or two linear functions proposed by Klein Breteler, 2007 with a transition at $\xi_{m-1,0}=3.2$ are appropriate for data fitting. Therefore, both approaches will be used to derive the prediction formulae $\dfrac{z_{p\,max}}{H_{m0}} = f(\xi_{m-1,0})$.
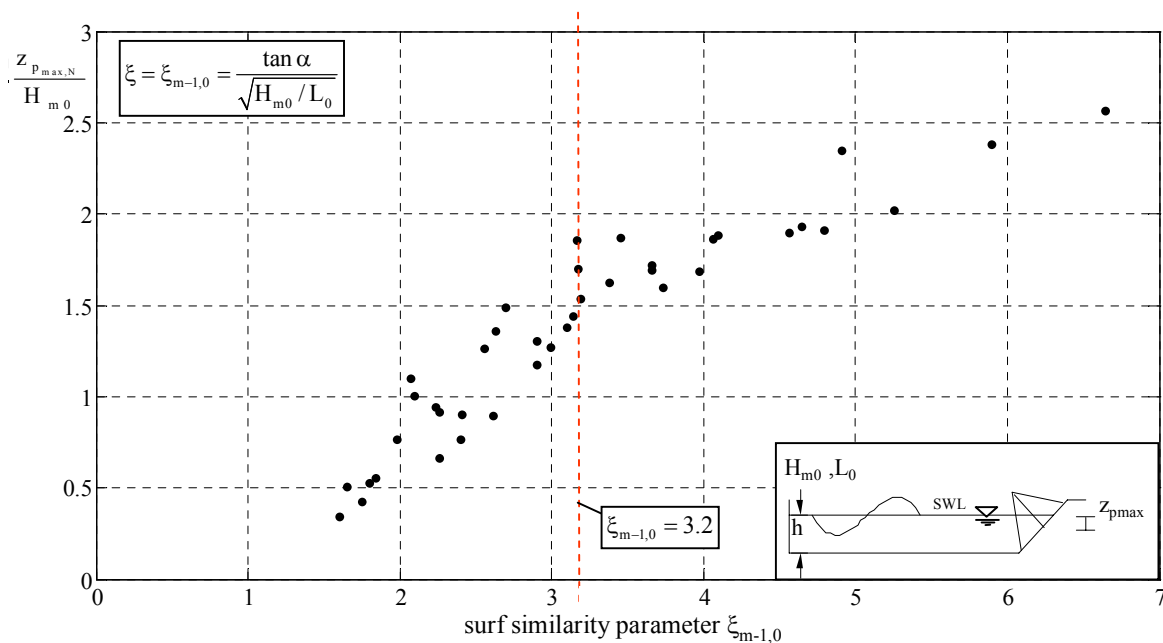
Fig. 5.19: Location of the maximum pressure on the revetment z_{pmax}/H_{m0} against surf similarity parameter $\xi_{m-1,0}$ for irregular wave tests

> *Remark:*
>
> *Comparatively, a similar behaviour is observed for regular waves but with larger scatter of the data than for irregular waves (see Annex D, Fig. D.3.7).*

5.3.1.2 *Prediction formula using Schüttrumpf's approach*

The z_{pmax}/H_{m0}-data are plotted against surf similarity parameter $\xi_{m-1,0}$ in Fig. 5.20, showing that the prediction formula for the *ELASTOCOAST* revetment can simply be obtained by multiplying Schüttrumpf's formula for smooth impermeable slopes:

$$\frac{z_{p\,max}}{H_{m0}} = 0.8 + 0.6 \cdot \tan(\xi - 2.1) \tag{5.10}$$

by a constant amplification factor (≈ 1.3). As a result the following formula is obtained ($\sigma' \approx 22.9\%$):

$$\frac{z_{p\,max}}{H_{m0}} = 1.3 \cdot \left[0.8 + 0.6 \cdot \tan(\xi - 2.1)\right] \tag{5.11}$$
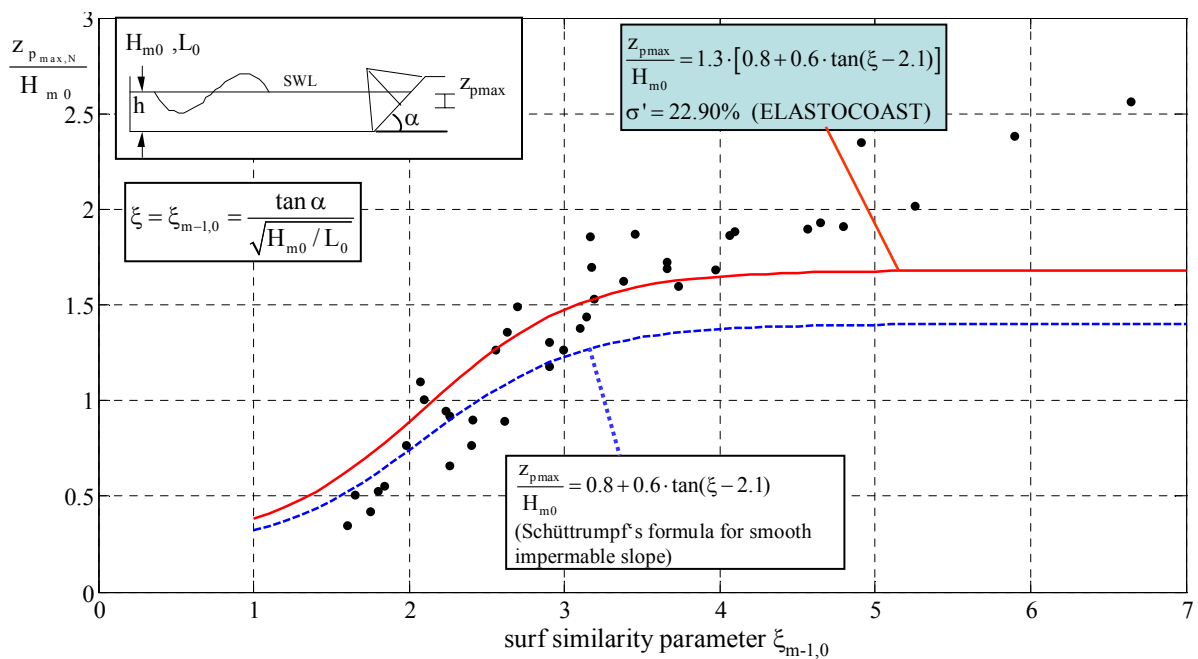
Fig. 5.20: Prediction formula for the location of peak pressure on the revetment z_{pmax}/H_{m0} against surf similarity parameter $\xi_{m-1,0}$ using Schüttrumpf's approach

> *Remark:*
>
> *As for the regular wave tests the difference between Schüttrumpf's formula and the prediction formula for the ELASTOCOAST revetment is much less (amplification factor of 1.15 instead of 1.3) see Annex D, Fig. D.3.8.*

5.3.1.3 *Prediction formula using Klein Breteler's approach*

Using Klein Breteler's approach (Eq. (5.12)) is less straightforward because the prediction formula for the *ELASTOCOAST* revetment cannot be simply obtained by introducing an amplification factor.

$$\frac{z_{p\,max}}{H_{m0}} = \min \begin{pmatrix} 0.45 \cdot \xi - 0.3 \\ 1.7 \end{pmatrix} \tag{5.12}$$

The results are plotted in Fig. 5.21, showing indeed that the transition between the two functions is $\xi_{m-1,0}=3.2$ for *ELASTOCOAST* (instead of $\xi_{m-1,0}=4.45$ in Klein Breteler's formula) and that the second function increase linearly with increasing $\xi_{m-1,0}$ (instead of being constant in Klein Breteler's formula). As a result the following prediction formulae are obtained ($\sigma' \approx 15.57\%$):

$$\frac{z_{p\,max}}{H_{m0}} = \min \begin{pmatrix} 0.7 \cdot \xi - 0.6 \\ 0.2 \cdot \xi + 1.0 \end{pmatrix} \quad \text{for } 1.6 < \xi_{m-1,0} < 6.6 \tag{5.13}$$
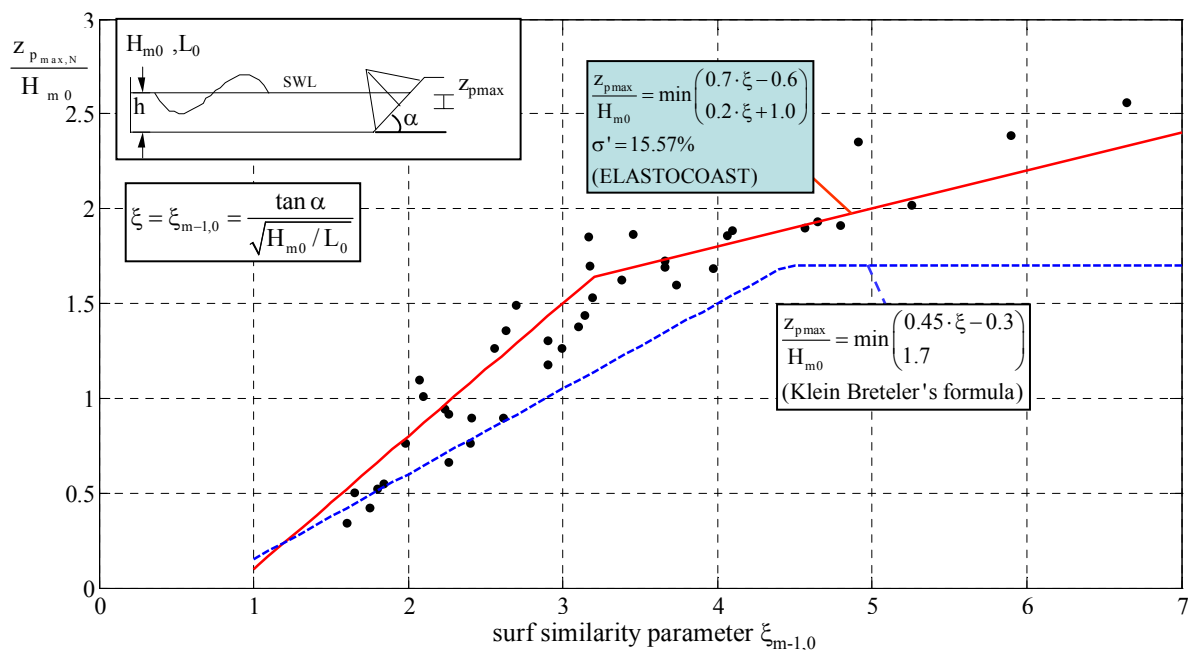
Fig. 5.21: Prediction formula for the location of peak pressures on the revetment z_{pmax}/H_{m0} against surf similarity parameter $\xi_{m-1,0}$ using Klein Breteler's approach

For engineering practice the formula based on the approach by Klein Breteler (Eq. (5.13) and Fig. 5.21) would be more favoured since it is simpler and more conservative than the formula based on Schüttrumpf's approach.

> *Remark:*
>
> *As for the regular wave tests the difference between Klein Breteler's formulae and the prediction formulae for the ELASTOCOAST revetment is not significant for smaller ξ-values, but strongly increases for larger ξ -values (see Annex D, Fig. D.3.10).*

5.3.2   Location of peak pressure beneath the revetment

5.3.2.1   Preliminary analysis

Like for the location (z_{pmax}/H_{m0}) of the peak pressure on the revetment in Fig. 5.19, the data z_{2pmax}/H_{m0} are plotted against surf similarity parameter $\xi_{m-1,0}$ for the peak pressure beneath the revetment, thus providing the results in Fig. 5.22. Like in Fig. 5.19, it shows that the transition is also around $\xi_{m-1,0}$=3.2, but the scatter of the data is larger with an outlier at $\xi_{m-1,0} = 2.4$. The z_{2pmax}/H_{m0} values are also larger, i.e. the location of the peak pressure beneath the revetment is at a lower elevation beneath still water level (SWL) than the location of the peak pressure on the revetment.
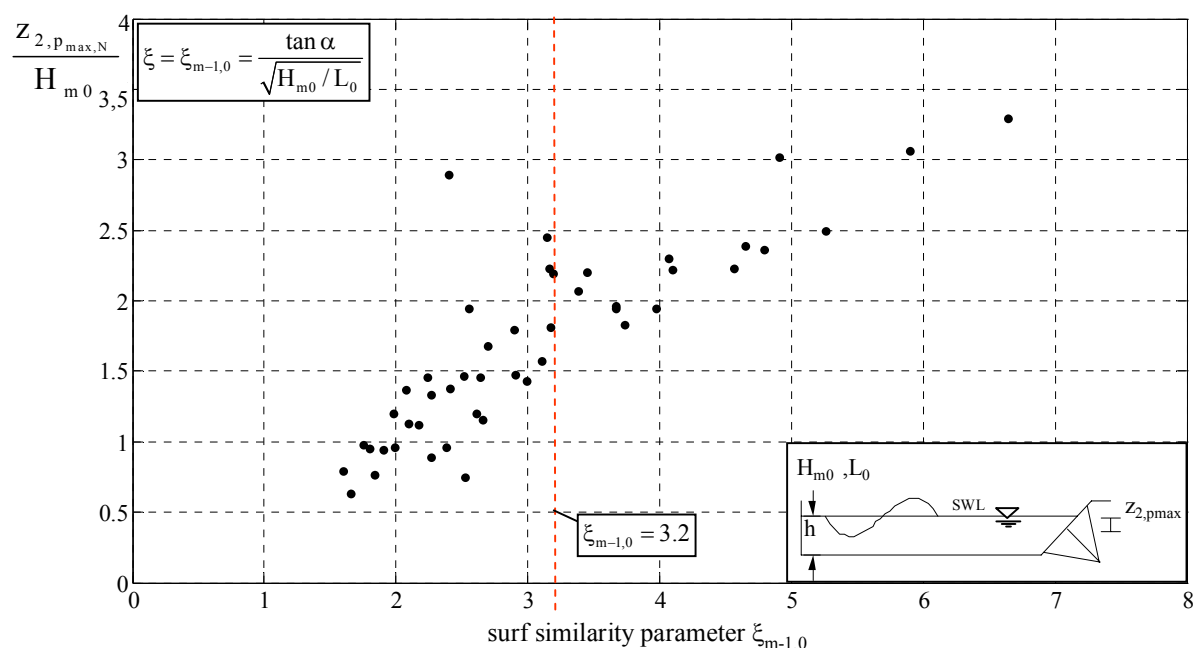

Fig. 5.22: Peak pressure location $z_{2,pmax}/H_{m0}$ beneath the revetment against surf similarity parameter $\xi_{m-1,0}$ for irregular wave tests

5.3.2.2   Prediction formula using Schüttrumpf's approach

The z_{2pmax}/H_{m0} data are plotted in Fig. 5.23 in a similar way as in Fig. 5.20, resulting in a prediction formula which is simply obtained by multiplying Schüttrumpf's approach (Eq. (5.10))

by the constant amplification factor 1.55 (instead of 1.3 for the peak pressure on the revetment). The proposed formula for the location of the peak pressure just beneath the revetment is ($\sigma' \approx 22.9\%$):

$$\frac{z_{2p\max}}{H_{m0}} = 1.55 \cdot \left[0.8 + 0.6 \cdot \tan(\xi - 2.1)\right] \tag{5.14}$$

or

$$\frac{z_{2p\max}}{H_{m0}} = 1.2 \cdot \frac{z_{p\max}}{H_{m0}} \tag{5.15}$$

Eq. (5.15) means that the peak pressures underneath the revetment are located about 20% lower than the peak pressures on the revetment.
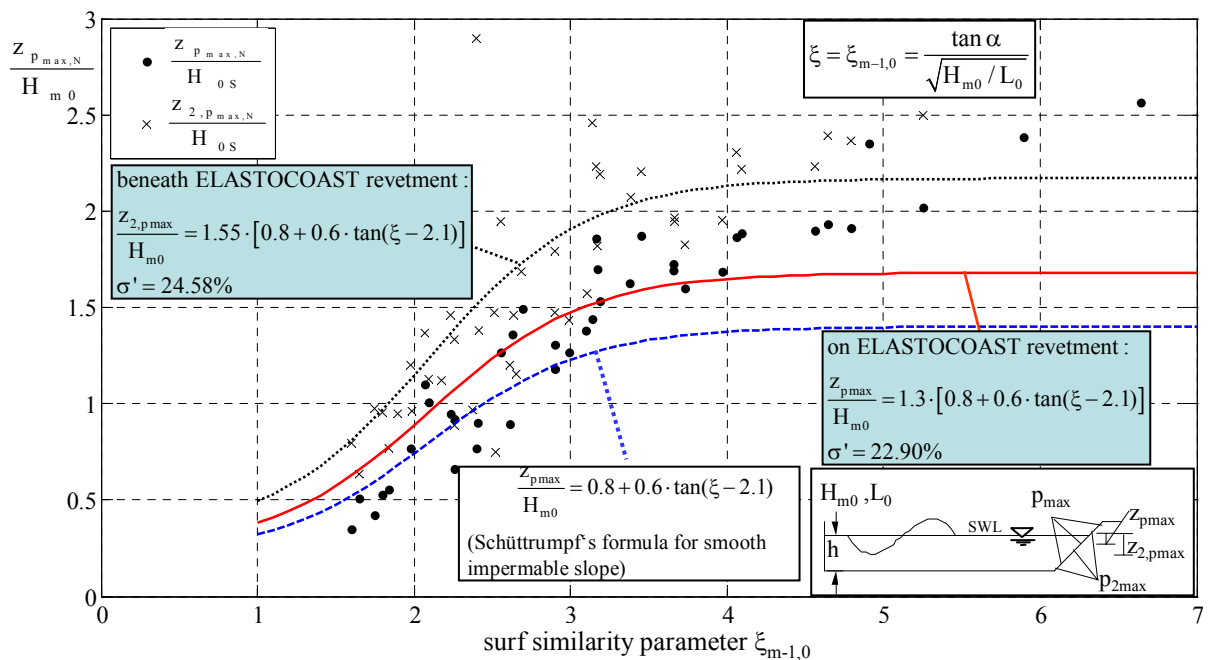
Fig. 5.23: Location the peak pressures on ($z_{,p\max}/H_{m0}$) and beneath the revetment ($z_{2,p\max}/H_{m0}$) plotted against surf similarity parameter $\xi_{m-1,0}$ and comparison to Schüttrumpf's approach

Remark:

As for the regular wave tests the difference between the location of the peak pressure on and beneath the revetment is about 40% instead of 20% for irregular waves (see Eq. (5.15)); i.e. for regular waves the location of the peak pressures beneath the revetment is generally lower than for irregular waves while the location of the peak pressures on the revetment is slightly higher (see Annex D, Fig. D.3.9).

5.3.2.3 *Prediction formula using Klein Breteler's approach*

Plotting the z_{2pmax}/H_{m0}-data for the peak pressures beneath the revetment in the same way than in Fig. 5.21 (peak pressure on the revetment), the result in Fig. 5.24 is obtained. showing that the following prediction formulae can be derived for the *ELASTOCOAST* revetment by multiplying the obtained prediction formulae for the location of the peak pressure on the revetment (Eq. (5.13)) by an amplification factor 1.2 in the same way as in Eq. (5.15). As a result the following prediction formula is obtained ($\sigma' \approx 23.02\%$):

$$\frac{z_{2p\max}}{H_{m0}} = 1.2 \cdot \min\begin{pmatrix} 0.7 \cdot \xi - 0.6 \\ 0.2 \cdot \xi + 1 \end{pmatrix} \tag{5.16}$$
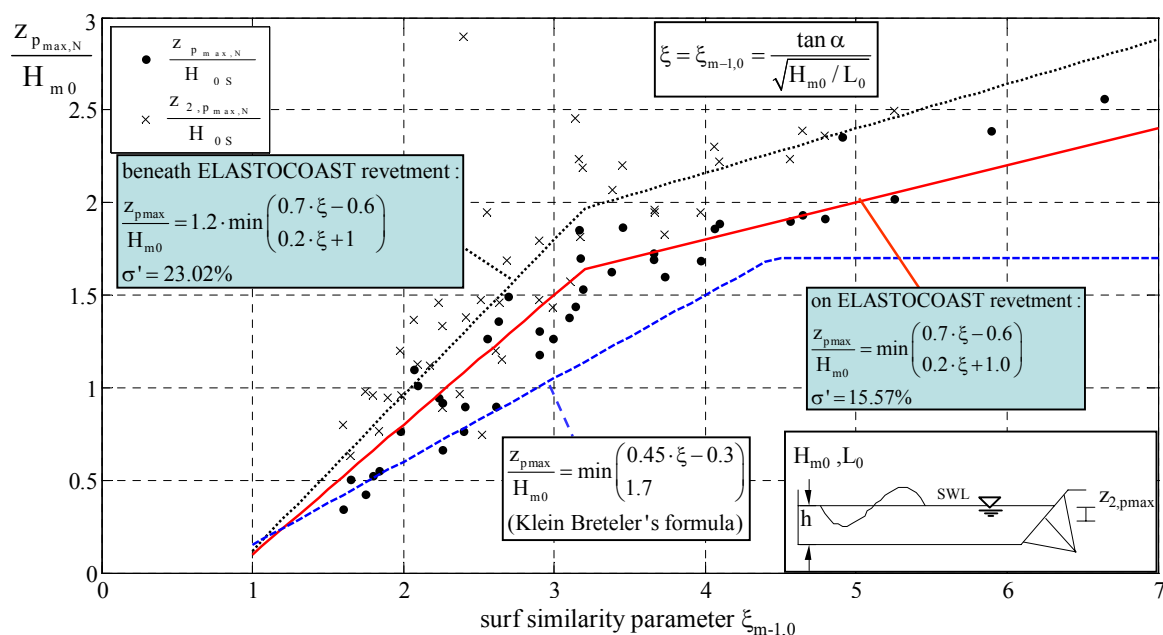
Fig. 5.24: Location of peak pressure beneath the revetment $z_{2,pmax}/H_{m0}$ plotted against surf similarity parameter $\xi_{m-1,0}$ and comparison to Klein Breteler's approach

The formula based on Klein Breteler's approach (Eqs. (5.16) and Fig. 5.24) is favoured for design purpose, since it is more practical and more conservative than the formula based on Schüttrumpf's approach (Eq. (5.14) and Fig. 5.23).
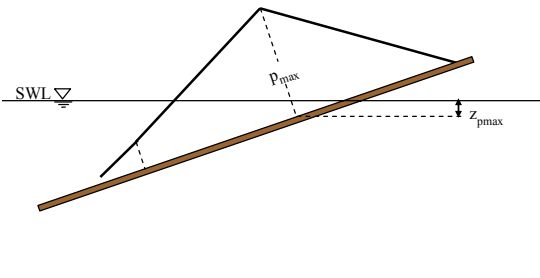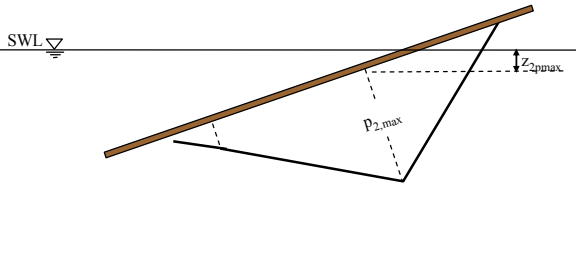
> *Remark:*
> *As for the regular wave tests the difference between the location of the peak pressure on and beneath the revetment is about 40% instead of 20% for irregular waves (see Eq. (5.16)); i.e. for regular waves the location of the peak pressure beneath the revetment is generally lower than for irregular waves while that of the peak pressure on the revetment is slightly higher (see Annex D, Fig. D.3.11).*

5.3.3 Summary of results regarding the location of maximum pressures

All the proposed formulae for the prediction of the location of the peak pressure beneath still water level are summarized in Tab. 5.2 for the pressures on and just beneath the revetment. No distribution needs to be made explicitly between impact and non-impact load.

Tab. 5.2: Summary of results regarding the location of maximum pressures

Pressure on the revetment	Pressure beneath the revetment
Schüttrumpf's approach: $$\frac{z_{p\,max}}{H_{m0}} = 1.3 \cdot \left[0.8 + 0.6 \cdot \tan(\xi - 2.1)\right] \qquad (5.11)$$ Klein Breteler's approach: $$\frac{z_{p\,max}}{H_{m0}} = \min \begin{pmatrix} 0.7 \cdot \xi - 0.6 \\ 0.2 \cdot \xi + 1.0 \end{pmatrix} \qquad (5.13)$$	Schüttrumpf's approach: $$\frac{z_{2p\,max}}{H_{m0}} = 1.55 \cdot \left[0.8 + 0.6 \cdot \tan(\xi - 2.1)\right] \qquad (5.14)$$ Klein Breteler's approach: $$\frac{z_{2p\,max}}{H_{m0}} = 1.2 \cdot \min \begin{pmatrix} 0.7 \cdot \xi - 0.6 \\ 0.2 \cdot \xi + 1 \end{pmatrix} \qquad (5.16)$$

As already mentioned above Eqs. (5.13) and (5.16) would be favoured for design purpose.

5.4 Pressure distribution on and just beneath the revetment

The distributions of the wave-induced pressure on and just beneath the revetment are important for the calculation of the resulting wave loads on the entire revetment. As shown in Fig. 5.5 the pressure distribution for impact loads on the revetment is described by five pairs of parameters (p_i, z_i) while the pressure distribution beneath the revetment is described by four pairs of parameters (p_i', z_i'), each parameter pair representing the magnitude of the local wave pressure p_i (p_i') at point i (i') with the elevation z_i (z_i') beneath still water level (SWL). For non-impact loads only three parameter pairs are needed to describe the pressure distribution on and beneath the revetment (Fig. 5.7). Prediction formulae for the maximum (peak) pressure (p_{max}) on and just beneath the revetment as well as for the associated location (z_{pmax}) beneath SWL have been determined for both impact and non-impact loads in sections 5.2 and 5.3, respectively. As mentioned in section 5.1, the two parameters (p_{max}, z_{pmax}) build the reference parameters to which the remaining parameters of the pressure figure in Fig. 5.5a and Fig. 5.5b are related. It is therefore the aim of this section to derive formulae for the prediction of the remaining parameters (p_i, z_i) for the pressure distribution on the revetment and (p_i',

z_i') for the pressure distribution beneath the revetment in order to fully describe the pressure figure on (Fig. 5.5a and Fig. 5.7a) and beneath the revetment (Fig. 5.5band Fig. 5.7b) for both impact and non-impact loads.

5.4.1 Pressure distribution on the revetment

5.4.1.1 Preliminary analysis

The pressure signals recorded at different locations on the revetment for impact loads are exemplary shown in Fig. 5.25 for $H_{m0} = 0.98$ m, $T_{m,-1,0} = 2.99$ s and $h = 3.60$ m. Fig. 5.25 illustrates that not only the magnitude of the peak pressure, but also the type of wave load and thus other features of the pressure signals also differ, depending on the location considered.
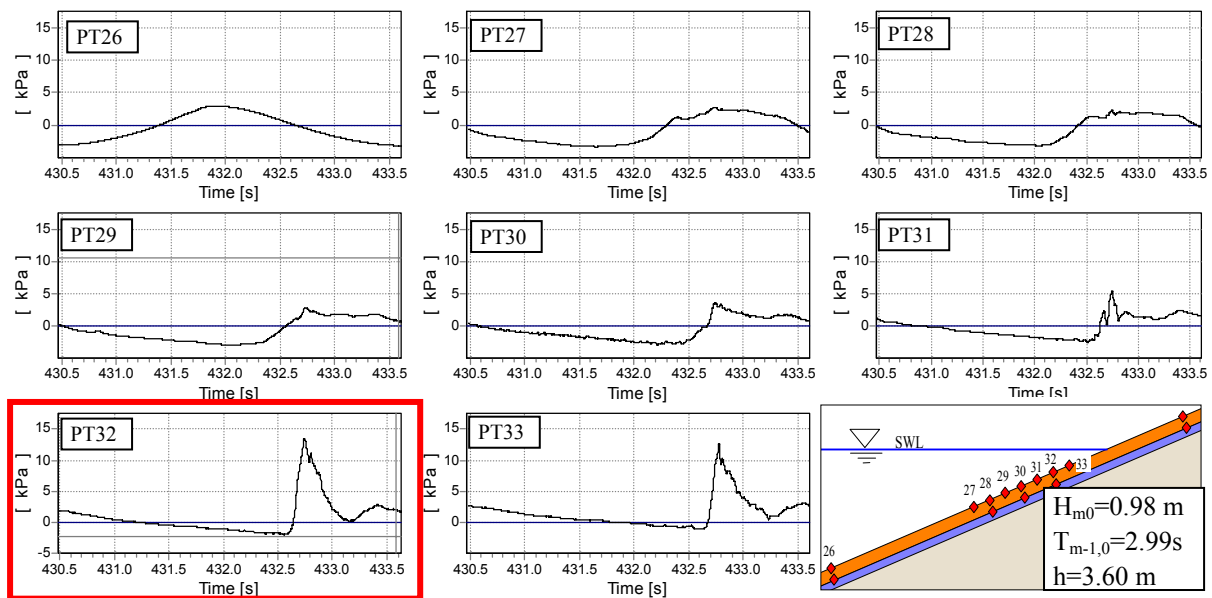
Fig. 5.25: Recorded pressure signals at transducers on the revetment for impact load ($\xi_{m-1,0} < 2.5$)

The pressure signals recorded at different locations on the revetment for non-impact loads are exemplary shown in Fig. 5.26 for $H_{m0} = 0.59$ m, $T_{m-1,0} = 7.98$ s and $h = 3.90$ m, to illustrate that in contrast to the impact load in Fig. 5.25, the features of the pressure signals do not noticeably vary from location to location.
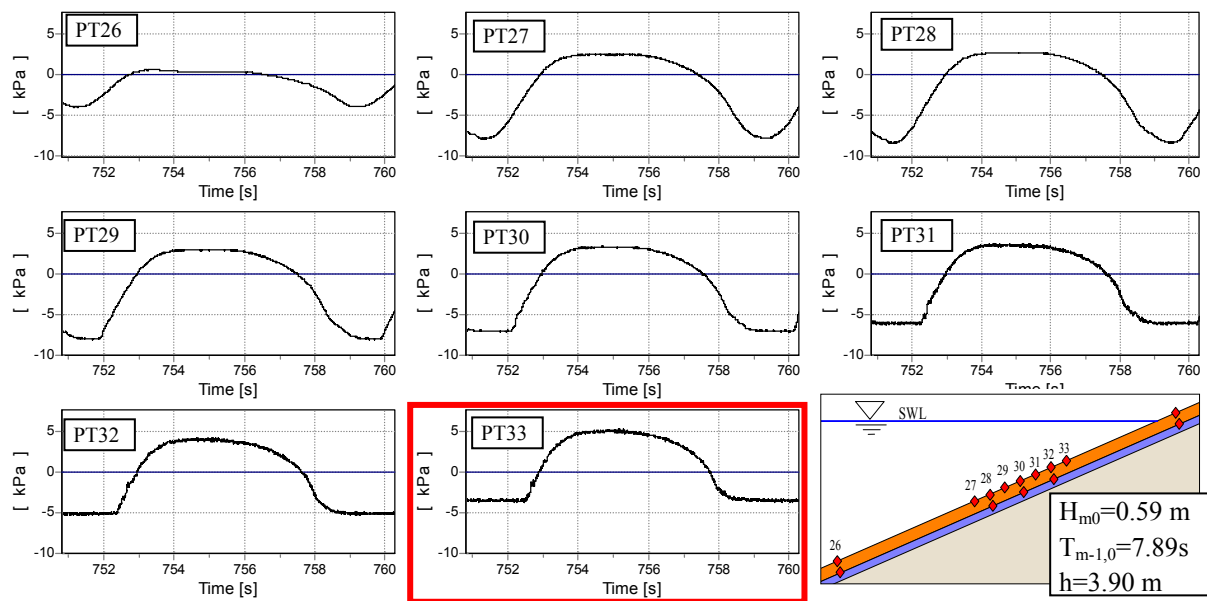
Fig. 5.26: Recorded pressure signals at transducers on the revetment for non-impact load ($\xi_{m-1,0}$>2.9)

In order to get a better insight in the range of variation of the pressure figure on and beneath the revetment from test to test, the pressure distributions recorded at the transducer on the revetment were first plotted for several irregular wave tests by discriminating between impact loads, including transition zone (1.6<$\xi_{m-1,0}$<2.9) and non impact loads ($\xi_{m-1,0}$>2.9).

(a) Impact load (and transition zone)

As illustrated by Fig. 5.27 for the pressure distribution on the revetment, the variation of the pressure figure for impact load ($\xi_{m-1,0}$<2.5) is surprisingly much smaller than initially expected. The "outliers" in Fig. 5.27 rather belong to the transition zone (2.5< $\xi_{m-1,0}$<2.9) which is indeed associated with the largest variations.
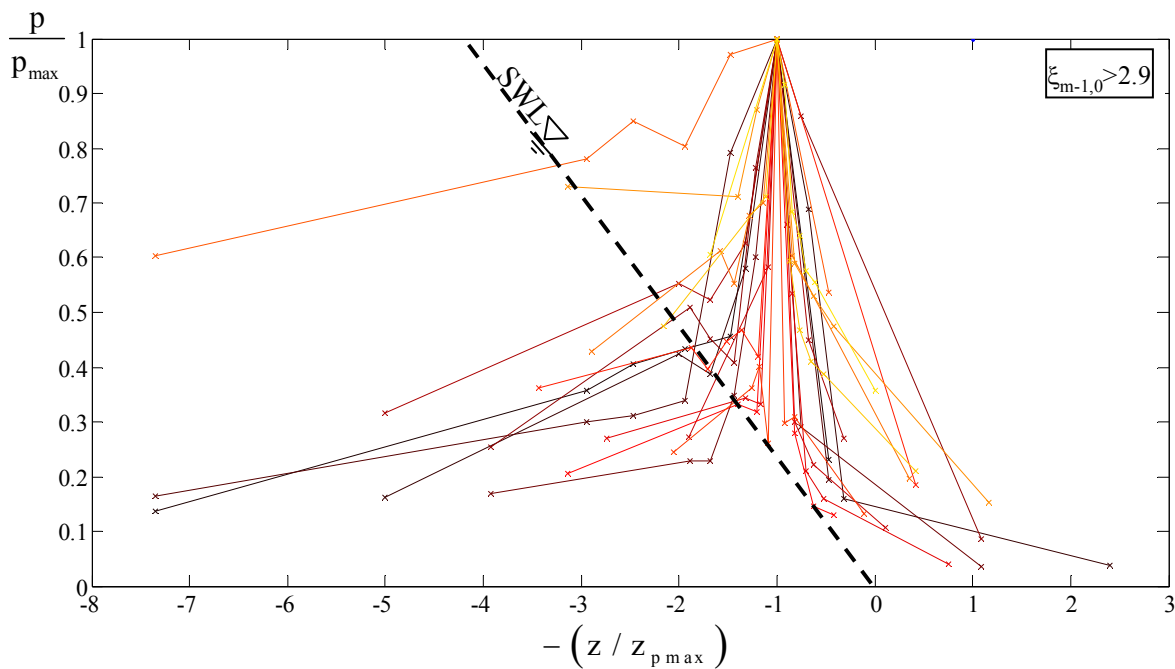
Fig. 5.27: Spatial pressure distribution on the revetment for impact load and transition zone (irregular waves)

The result in Fig. 5.27 therefore supports the parameterisation proposed in Fig. 5.5a for impact load. This will be shown more clearly in section 5.4.1.2.

> *Remark:*
>
> *A similar figure plotted for regular waves (see Annex D, Fig. D.3.12) shows less variation of the pressure figure from test to test and supports even more the proposed parameterization in Fig. 5.5a.*

Moreover, the threshold $\xi_{m-1,0}=2.9$ between the two basically different types of wave loads (impact and non-impact) is also supported by examining the pressure figures recorded for $\xi_{m-1,0} = 2.9$. As shown in Fig. 5.28 for two selected tests with $\xi_{m-1,0} \approx 2.9$ both types of loads may occur: the upper pressure figure is typical for non-impact load shape (triangle) while the lower pressure figure is rather typical for an impact load shape (triangle followed by different linear pressure distributions seaward and landward).

Wave pressure on and just beneath the revetment
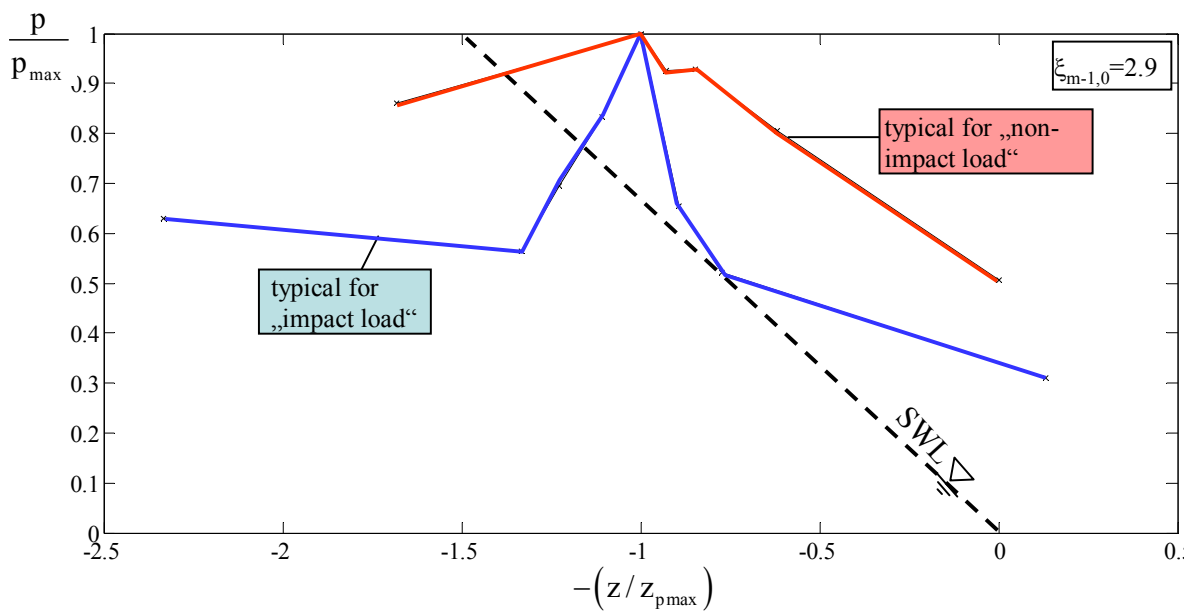
Fig. 5.28: Spatial pressure distribution on the revetment for $\xi_{m-1,0} \approx 2.9$ for irregular waves

(b) <u>Non-impact load</u>

Plotting in non-dimensional form the pressure distribution on the revetment for non-impact loads ($\xi_{m-1,0} > 2.9$) in a similar manner as for the impact load in Fig. 5.27, the result in Fig. 5.29 is obtained showing that the pressure figure for all tests can indeed be approximately described by a simple triangle. This supports the parameterization of the non-impact pressure distribution on the revetment as proposed in Fig. 5.7a. This will be seen more clearly in section 5.4.1.3.
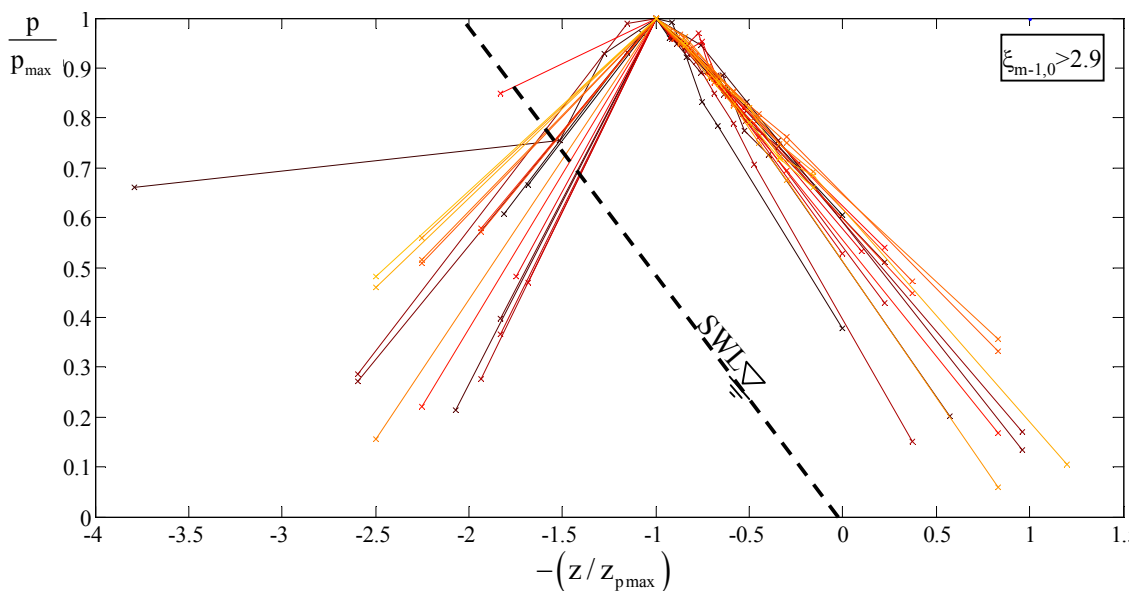
Fig. 5.29: Spatial pressure distribution on the revetment for $\xi_{m-1,0} > 2.9$ for non-impact load (irregular waves)

> *Remark:*
>
> *A similar figure plotted for regular waves (see Annex D, Fig. D.3.15) also shows that a simple triangular shape for non-impact load can be adopted, but the variation of the pressure figures is surprisingly much larger than for irregular waves.*

5.4.1.2   Parameterized pressure distribution on the revetment for impact loads ($\xi_{m-1,0}<2.5$)

For impact loads ($\xi_{m-1,0}<2.5$) the pressure distribution induced by irregular waves on the revetment has been analysed (see section 5.2 and Ludwigs, 2009). The results may be summarized in Fig. 5.30 and Fig. 5.31.

It is shown in Fig. 5.30 that the resulting pressure figure is described by five points (0, 1, 2, 3, 4) connected linearly ($\overline{01}$, $\overline{02}$, $\overline{24}$ and $\overline{13}$). Seawards of point 3 the wave pressure continues to decrease linearly at the same rate while shoreward of point 2 the wave induced pressure decreases linearly up to $p_4=0$ at maximum run up. The linear connections of points 0, 1, 2, 3 and 4 are resulting in the parameterized pressure distribution as shown in Fig. 5.31. It can be seen that all pressure p_i are normalized by the maximum (peak) pressure p_{max} for which a prediction formula has already been determined in section 5.2.1.2 (Eq. (5.3) and Fig. 5.10) which is again provided here:

$$\frac{p_{max}}{\rho \cdot g \cdot H_{m0}} = -4 \cdot \xi_{m-1,0} + 12.5 \quad \text{for } 1.6 < \xi_{m-1,0} < 2.5 \tag{5.3}$$

The associated locations z_i as related to still water level (SWL) are normalized by the location of z_{pmax} of the maximum (peak) pressure p_{max} for which prediction formulae have been proposed in sections 5.3.1.2 and 5.3.1.3 (Eq. (5.11) and Fig. 5.20 as well as Eq. (5.13) and Fig. 5.21). For instance, if prediction formula according to Schüttrumpf's approach is adopted (Eq. (5.11)):

$$\frac{z_{pmax}}{H_{m0}} = 1.3 \cdot \left[0.8 + 0.6 \cdot \tan(\xi - 2.1) \right] \quad \text{for } 1.6 < \xi_{m-1,0} < 2.5 \tag{5.11}$$
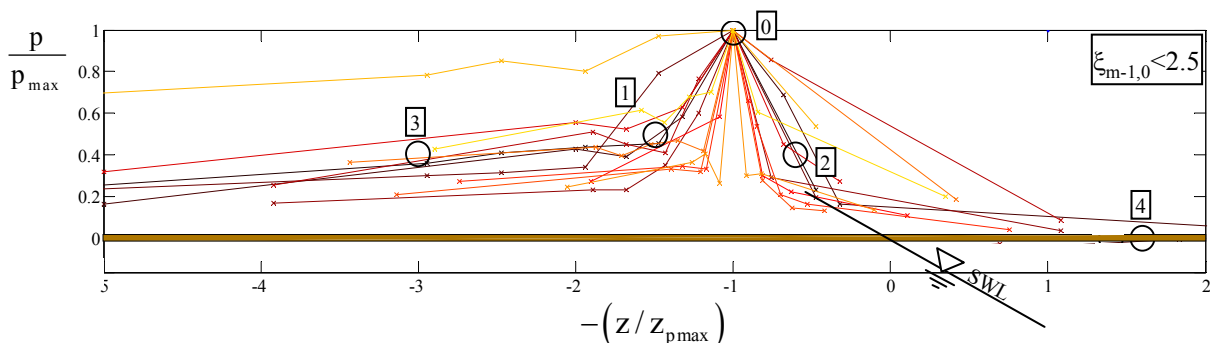
Fig. 5.30: Pressure distribution on the revetment for impact loads ($\xi_{m-1,0}<2.5$)
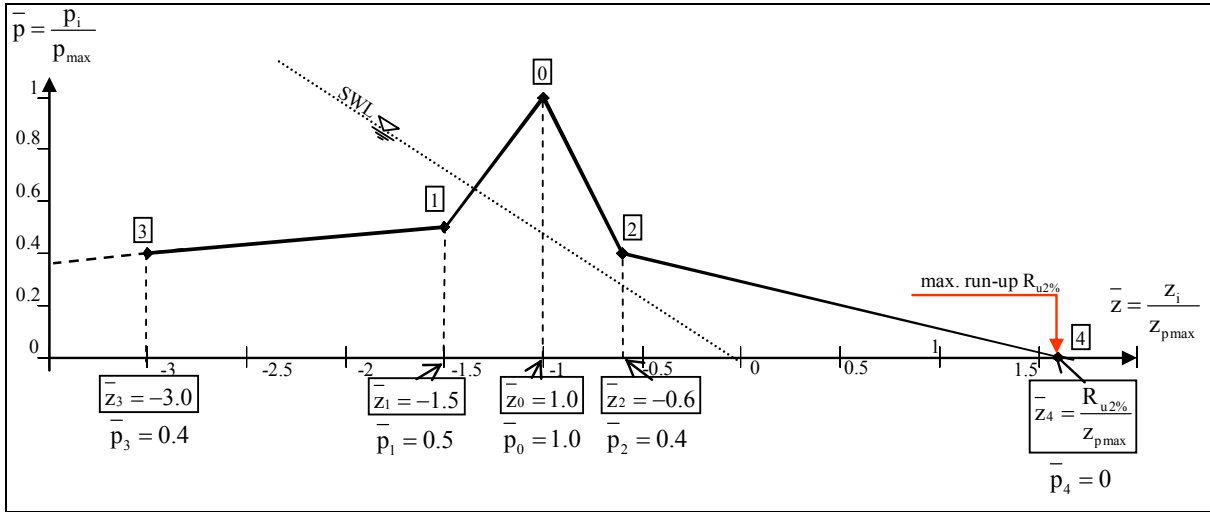
Fig. 5.31: Parameterized pressure distribution on the revetment for impact load ($\xi_{m-1,0}$<2.5)

Moreover, the wave run-up formulae for $\xi_{m-1,0}$<2.5 proposed in section 4.1 are also needed to determine the location of point 4 while the pressure becomes zero (p_4=0):

$$\frac{R_{u2\%}}{H_{m0}} = 0.54 \cdot \left[1.65 \cdot \xi_{m-1,0}\right] \quad \text{for Model B and C} \tag{4.7}$$

The non-dimensional coordinates (p_i/p_{max}, z_i/z_{pmax}) of points 0-4 in Fig. 5.31 can then be determined as follows:

$$\text{Point 0}: \quad \frac{p_0}{p_{max}} = 1.0 \text{ with } \frac{z_0}{z_{pmax}} = 1.0 \tag{5.17}$$

$$\text{Point 1}: \quad \frac{p_1}{p_{max}} = 0.5 \text{ with } \frac{z_1}{z_{pmax}} = -1.5 \tag{5.18}$$

$$\text{Point 2}: \quad \frac{p_2}{p_{max}} = 0.4 \text{ with } \frac{z_2}{z_{pmax}} = -0.6 \tag{5.19}$$

$$\text{Point 3}: \quad \frac{p_3}{p_{max}} = 0.4 \text{ with } \frac{z_3}{z_{pmax}} = -3.0 \tag{5.20}$$

$$\text{Point 4}: \quad \frac{p_4}{p_{max}} = 0.0 \text{ with } \frac{z_4}{z_{pmax}} = \frac{R_{u2\%}}{z_{pmax}} \tag{5.21}$$

All formulae required to determine the five parameter pairs (p_i/p_{max}, z_i/z_{pmax}) which fully describe the pressure distribution on the revetment for impact load ($\xi_{m-1,0}$ <2.5) according to Fig. 5.31 are summarized in Tab. 5.3 in section 5.4.3.

Remark:

Similar results with slight differences are also obtained for regular waves as shown in Fig. D.3.14 and section D.3.4.1 in Annex D.

5.4.1.3 Parameterized pressure distribution on the revetment for non-impact loads ($\xi_{m-1,0}$>2.9)

For non-impact loads ($\xi_{m-1,0}$>2.9) the pressure distribution induced by irregular waves on the revetment have been analyzed in a similar way as for the impact loads in section 5.4.1.2. The results are summarized in Fig. 5.32 and Fig. 5.33.

As shown in Fig. 5.32 the resulting pressure figure on the revetment for non-impact loads can be described by a triangle defined by three points 0, 3 and 4. The location of p_4=0 corresponds to the maximum wave run-up $R_{u2\%}$. Seawards of point 3 the pressure continues to linearly decrease at the same rate as between point 0 and point 3. Based on this result the parameterized pressure distribution shown in Fig. 5.33 is proposed.
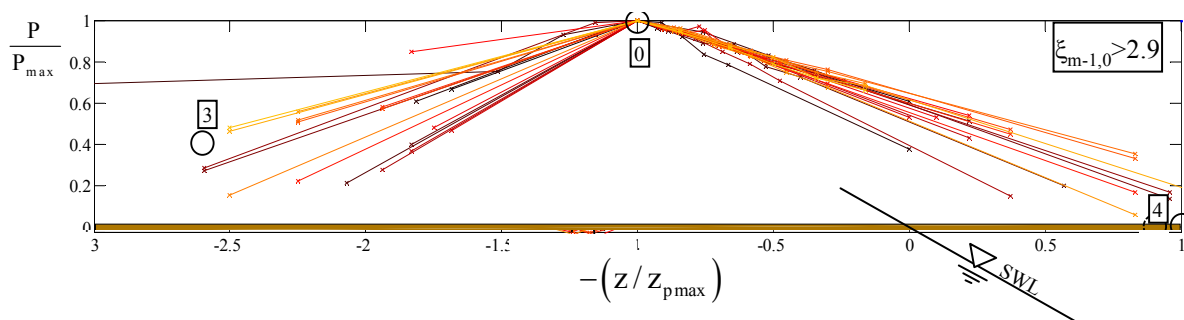
Fig. 5.32: Pressure distribution on the revetment for non-impact loads (ξ>2.9)
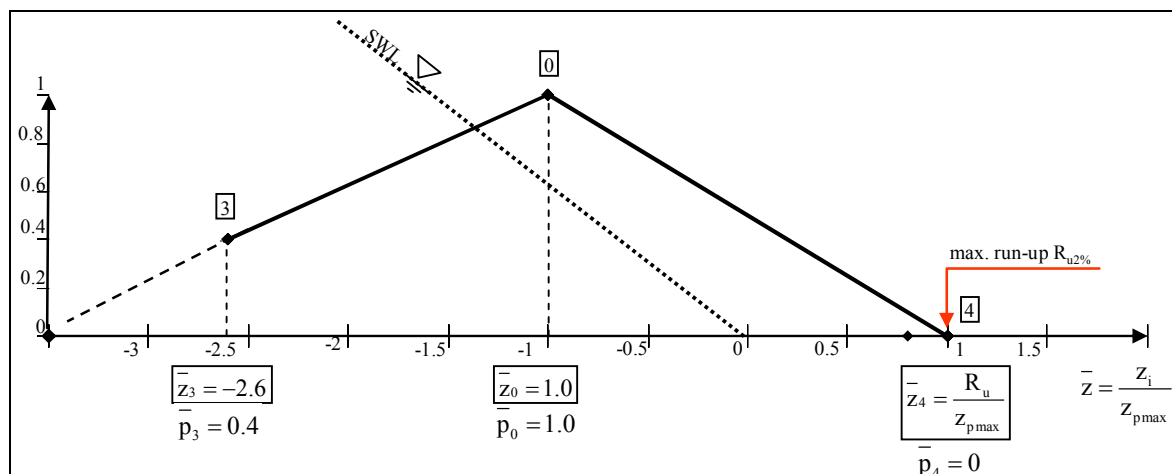
Fig. 5.33: Parameterized pressure distribution on the revetment for non-impact load ($\xi_{m-1,0}$>2.9)

As for the impact load in section 5.4.1.2 the pressure p_i are normalized by the maximum pressure p_{stat} for which prediction formulae have been determined in section 5.2.1.3 (Eqs. (5.5) and (5.6) as well as Fig. 5.11):

$$\frac{p_{stat}}{\rho \cdot g \cdot H_{m0}} = 0.68 \cdot \xi_{m-1,0} \quad \text{for } \xi_{m-1,0} < 4.5 \tag{5.5}$$

$$\frac{p_{stat}}{\rho \cdot g \cdot H_{m0}} = 0.41 \cdot \xi_{m-1,0} + 1.2 \quad \text{for } \xi_{m-1,0} > 4.5 \tag{5.6}$$

The associated locations z_i as related to still water level (SWL) are normalized by the location of the maximum pressure p_{stat} beneath SWL for which the same formulae as for impact load are applied (see section 5.4.1.2). To determine the location of point 4 the wave run-up formulae developed in section 4.1 (Fig. 4.4 and Eq. (4.8)) for Model B have been applied for $\xi_{m-1,0} > 2.9$:

$$\frac{R_{u2\%}}{H_{m0}} = 0.77 \cdot \left[4.0 - \frac{1.5}{\sqrt{\xi_{m-1,0}}} \right] \quad \text{for Model B and C} \tag{4.8}$$

The non-dimensional coordinates (p_i/p_{stat}, z_i/z_{pmax}) of the three points 0, 3 and 4 in Fig. 5.33 can then be determined as follows:

$$\text{Point 0}: \quad \frac{p_0}{p_{stat}} = 1.0 \quad \text{with } \frac{z_0}{z_{pmax}} = 1.0 \tag{5.22}$$

$$\text{Point 3}: \quad \frac{p_3}{p_{stat}} = 0.4 \quad \text{with } \frac{z_3}{z_{pmax}} = -2.6 \tag{5.23}$$

$$\text{Point 4}: \quad \frac{p_4}{p_{stat}} = 0.0 \quad \text{with } \frac{z_4}{z_{pmax}} = \frac{R_{u2\%}}{z_{pmax}} \tag{5.24}$$

Remark:

For comparison with the results of regular wave tests see section D.3.4.2 in Annex D.

5.4.2 Pressure distribution beneath the revetment

5.4.2.1 Preliminary analysis

The pressure signals recorded at different locations beneath the revetment for impact loads are shown in Fig. 5.34 for the same wave as in Fig. 5.25 in order to illustrate how the impact pressures are damped through the porous revetment and how the features of the pressure histories at different locations are modified just beneath the revetment. In addition, the signals of

the pressure transducer PT32 <u>on</u> the revetment is also shown in order to illustrate how the signal is damped and smoothed through the *ELASTOCOAST* revetment as recorded just beneath by PT38.
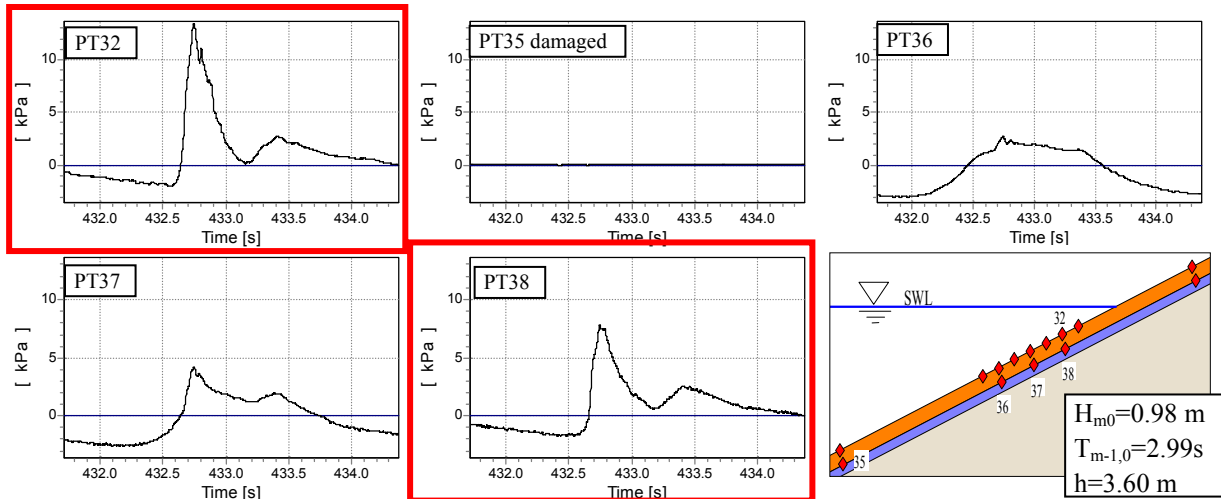
Fig. 5.34: Recorded pressure signals at transducers beneath the revetment for impact loads ($\xi_{m-1,0}$<2.5)

The pressure signals recorded at different locations beneath the revetment for non-impact loads are shown in Fig. 5.35 for the same wave as in Fig. 5.26. In addition the pressure signal of PT32 on the revetment is added for comparison with PT38 directly underneath, showing that in contrast to the impact load in Fig. 5.34 almost no damping occurs.

In the same manner as for the pressures on the revetment (section 5.4.1.1), the pressure distributions beneath the revetment are also plotted for several irregular wave tests by discriminating between impact load and non-impact load.
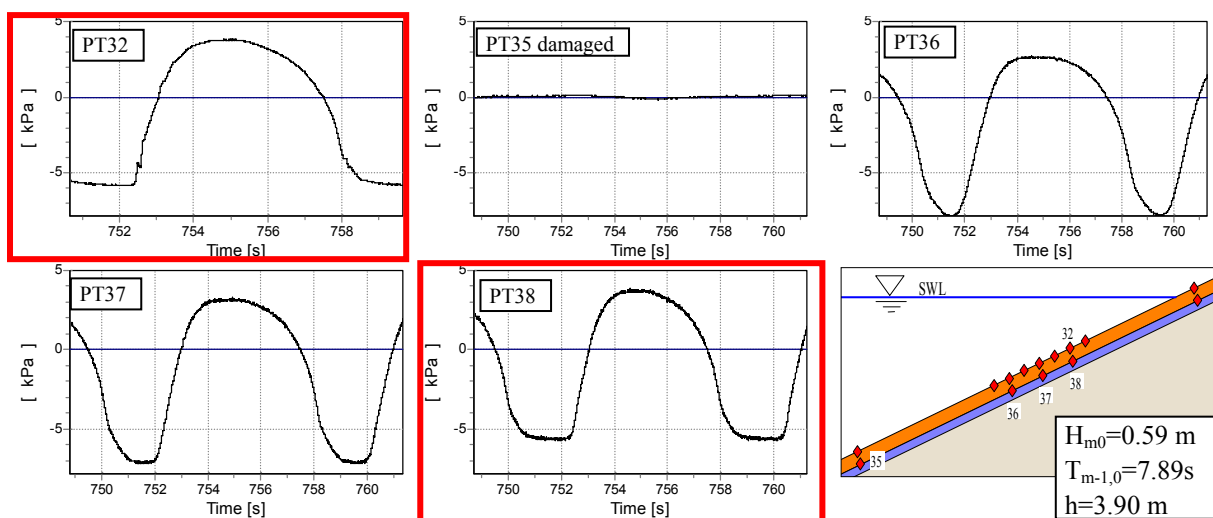
Fig. 5.35: Recorded pressure signals at transducers beneath the revetment for non-impact load ($\xi_{m-1,0}$>2.9)

(a) Impact load

Like in Fig. 5.27 for the pressure distribution on the revetment, the pressure distributions recorded at the transducers beneath the revetment are plotted in Fig. 5.36, showing less variability from test than the pressure distribution in Fig. 5.27. The results in Fig. 5.36 also strongly support the parameterization proposed in Fig. 5.5b for the pressure distribution just beneath the revetment (see also section 5.4.2.2)
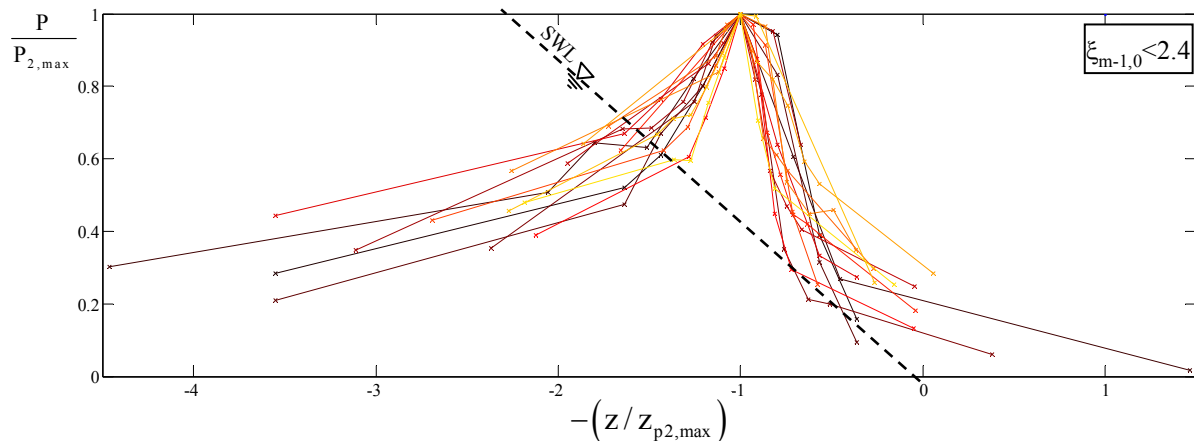
Fig. 5.36: Spatial pressure distribution beneath the revetment for impact loads and transition zone (irregular waves)

Remark:

For comparison with regular wave tests see Fig. D3.13 in Annex D which also supports the parameterization proposed in Fig. 5.5b.

(b) Non-impact load

Like for the non-impact load in Fig. 5.29, the pressure distribution beneath the revetment for non-impact load are plotted for several tests in Fig. 5.37, also showing that the pressure figure can be approximated by a single triangle for all tests. This result also supports the parameterization of the non-impact pressure distribution beneath the revetment as proposed in Fig. 5.7b. (see also section 5.4.2.3).
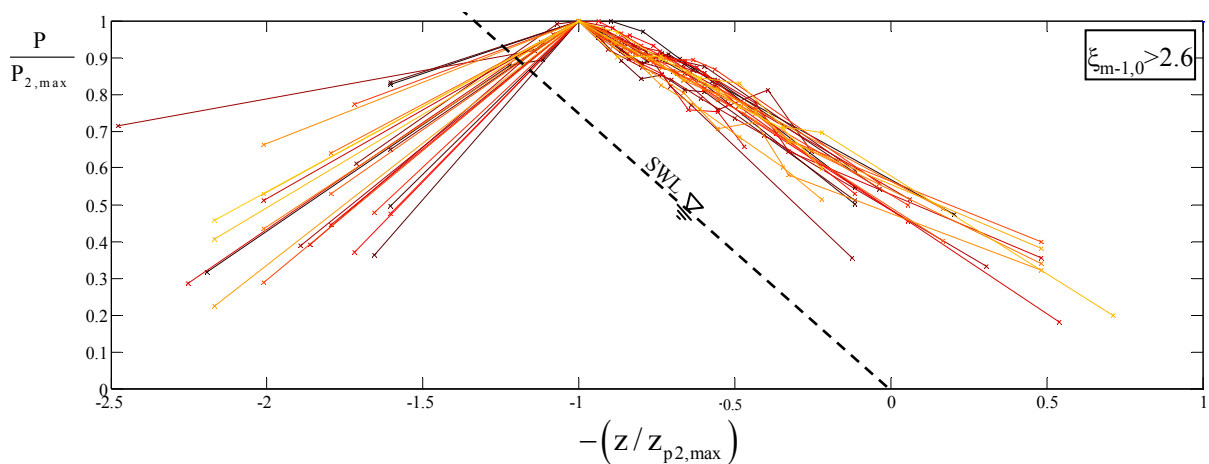
Fig. 5.37: Spatial pressure distribution beneath the revetment for $\xi_{m-1,0}>2.9$ for non-impact loads (irregular waves)

Remark:

For comparison with regular wave tests see Fig. D3.16 in Annex D showing more scatter than Fig. 5.37 but still supports the parameterization proposed in Fig. 5.7b.

5.4.2.2 Parameterized pressure distribution beneath the revetment for impact load ($\xi_{m-1,0}<2.5$)

Plotting the pressure distribution beneath the revetment for impact load on the same figure as for the distribution on the revetment (Fig. 5.30), the result is shown in Fig. 5.38.

It is seen that the pressures within the impact area are substantially damped when transferred just beneath the revetment and that the pressure figures beneath the revetment are slightly shifted downwards. Based on this and further similar results with regular wave tests the parameterized pressure distribution in Fig. 5.39 is proposed.
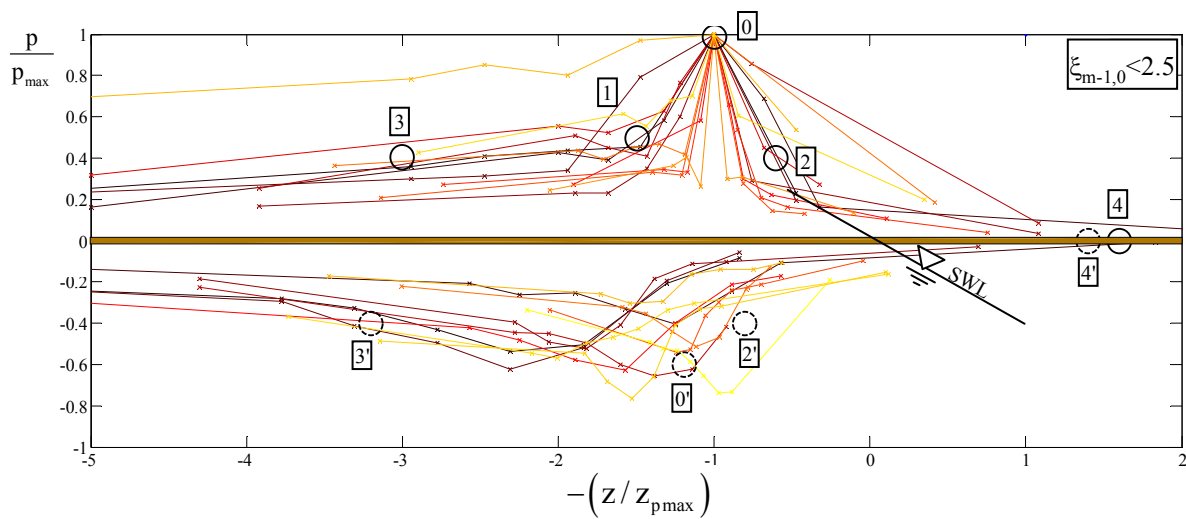
Fig. 5.38: Pressure distribution on and beneath the revetment for impact load ($\xi_{m-1,0}<2.5$)
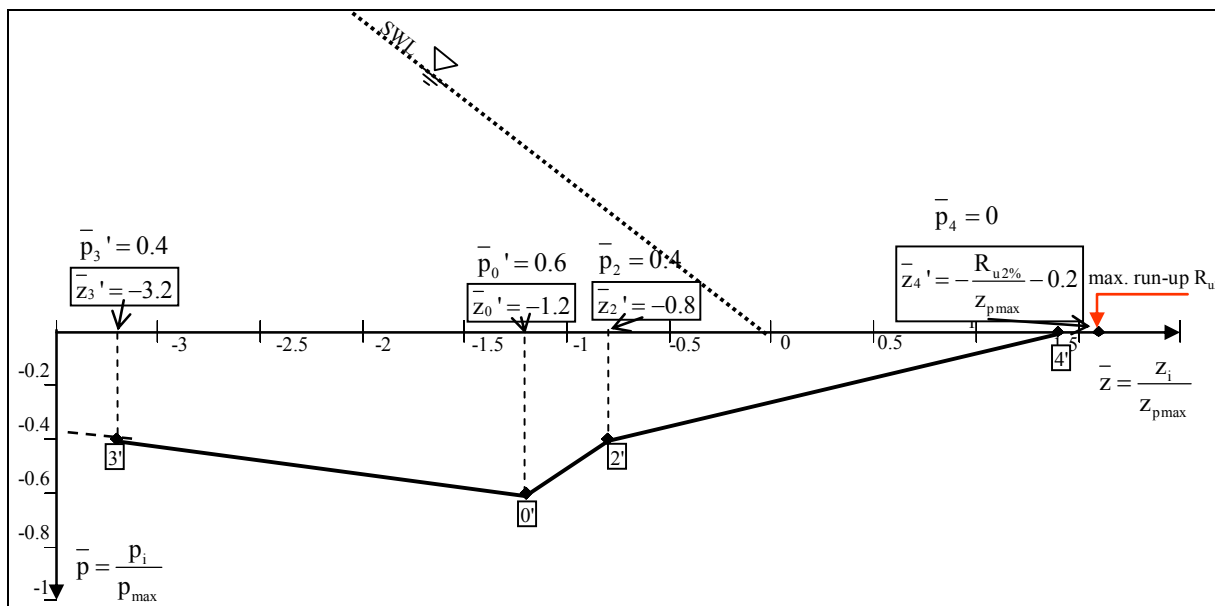
Fig. 5.39: Parameterized pressure distribution beneath the revetment for impact loads ($\xi_{m-1,0}<2.5$) (see Fig. 5.31 for comparison)

> *Remark:*
>
> *For comparison with regular wave tests see Fig. D3.14 in Annex D which also supports the parameterization proposed in Fig. 5.7a.*

The pressures p_0', p_2', p_3' and p_4' are normalized by the maximum (peak) pressure p_{max} on the revetment which is predicted by Eq. (5.3). The associated locations related to still water level (SWL) z_0', z_2', z_3' and z_4' are normalized by the location of the peak pressure on the revetment

z_{pmax} which is predicted by Eq. (5.11). As shown by the findings in section 5.2.2 the peak pressure p_{max} is damped by a factor of 0.6 beneath the revetment (see Eq. (5.7)) so that the peak pressure p_0' beneath the revetment is:

$$\frac{p_0{}'}{p_{max}} = 0.6 \tag{5.7}$$

Outside the impact zone, the damping of the pressure is smaller and decreases for increasing distance from the impact point. As shown by the findings in section 5.3.2 the location of the impact pressure beneath the revetment shifted downwards by a factor of 1.2 (see Eq. (5.15)), so that the location of the peak pressure z_0' beneath the revetment is:

$$\frac{z_0{}'}{z_{p\,max}} = -1.2 \tag{5.15}$$

Based on these findings and the results of the analysis of the pressure figures of all irregular wave tests for impact loads, the parameters describing the pressure distribution beneath the revetment in Fig. 5.39 may be summarized as follows:

$$\text{Point 0':} \quad \frac{p_0{}'}{p_{max}} = 0.6 \ \text{ with } \ \frac{z_0{}'}{z_{p\,max}} = -1.2 \tag{5.25}$$

$$\text{Point 2':} \quad \frac{p_2{}'}{p_{max}} = 0.4 \ \text{ with } \ \frac{z_2{}'}{z_{p\,max}} = -0.8 \tag{5.26}$$

$$\text{Point 3':} \quad \frac{p_3{}'}{p_{max}} = 0.4 \ \text{ with } \ \frac{z_3{}'}{z_{p\,max}} = -3.2 \tag{5.27}$$

$$\text{Point 4':} \quad \frac{p_4{}'}{p_{max}} = 0.0 \ \text{ with } \ \frac{z_4{}'}{z_{p\,max}} = -\frac{R_{u2\%}}{z_{p\,max}} - 0.2 \tag{5.28}$$

> *Remark:*
>
> *For comparison with regular wave tests see section D.3.4.1 in Annex D showing slight differences the results of irregular wave tests.*

5.4.2.3 *Parameterized pressure distribution beneath the revetment for non-impact loads ($\xi_{m-1,0} > 2.9$)*

Plotting the pressure distribution beneath the revetment for non-impact load on the same figure as for the distribution on the revetment (Fig. 5.32), the result is shown in Fig. 5.40.
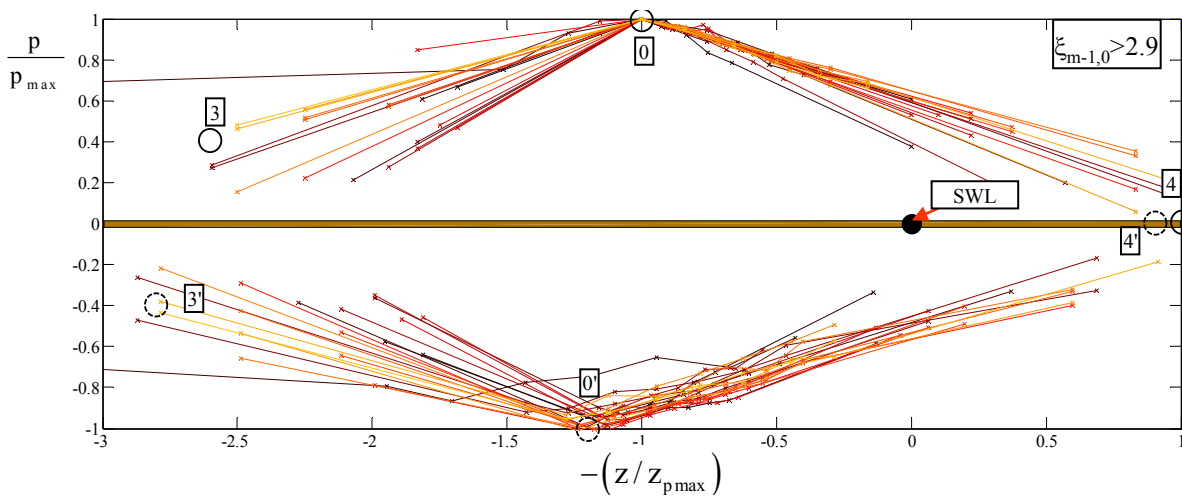
Fig. 5.40: Pressure distribution on and beneath the revetment for non-impact load ($\xi_{m-1,0}$>2.9)

It is seen that the maximum pressure p_{stat} is only slightly damped when transferred just beneath the revetment and that the pressure figures beneath the revetment are slightly shifted downwards. Based on this and similar results for regular wave tests the parameterized pressure distribution in Fig. 5.41 is proposed.
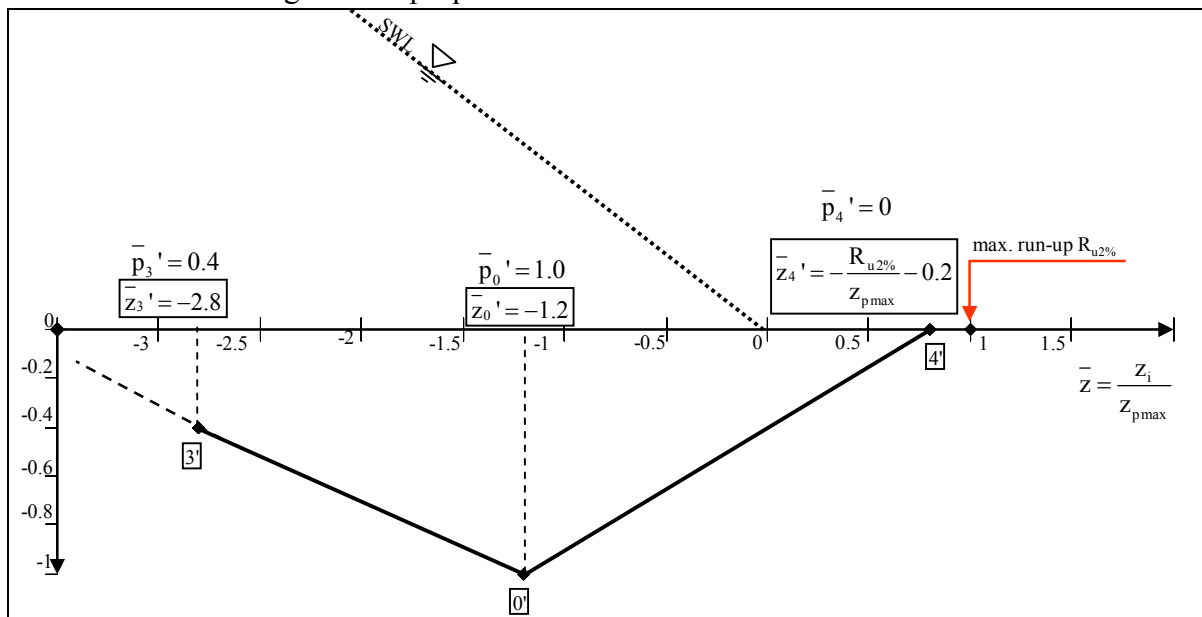
Fig. 5.41: Parameterized pressure distribution beneath the revetment for non-impact load ($\xi_{m-1,0}$>2.9) (see Fig. 5.33 for comparison)

The pressures p_0', p_3' and p_4' are normalized by the maximum (peak) pressure p_{stat} on the revetment which is predicted by Eq. (5.5) for $\xi_{m-1,0}$ < 4.5 and by (5.6) for $\xi_{m-1,0}$ > 4.5. The associated locations z_i as related to still water level (SWL) are normalized by the location z_{pmax} of the maximum pressure p_{stat} beneath SWL for which the same formulae as for impact load are

applied (see section 5.4.1.2). As shown by the findings in section 5.2.2 the peak pressure p_{stat} can be assumed as not damped beneath the revetment so that the peak pressure p_0' beneath the revetment is:

$$\frac{p_0'}{p_{stat}} = 1.0 \tag{5.29}$$

As shown by the findings in section 5.3.2, the location of the impact pressure beneath the revetment has shifted downwards by a factor 1.2 (see Eq. (5.15)), so that the location of the peak pressure z_0' beneath the revetment is:

$$\frac{z_0'}{z_{pmax}} = -1.2 \tag{5.15}$$

Based on these findings and the results of the analysis of the pressure figures of all irregular wave tests for non-impact load, the parameters describing the pressure distribution beneath the revetment in Fig. 5.39 may be summarized as follows:

$$\text{Point } 0': \quad \frac{p_0'}{p_{stat}} = 1.0 \quad \text{with} \quad \frac{z_0'}{z_{pmax}} = -1.2 \tag{5.30}$$

$$\text{Point } 3': \quad \frac{p_3'}{p_{stat}} = 0.4 \quad \text{with} \quad \frac{z_3'}{z_{pmax}} = -2.8 \tag{5.31}$$

$$\text{Point } 4': \quad \frac{p_4'}{p_{stat}} = 0.0 \quad \text{with} \quad \frac{z_4'}{z_{pmax}} = -\frac{R_{u2\%}}{z_{pmax}} - 0.2 \tag{5.32}$$

> *Remark:*
>
> *For comparison with regular wave tests see section D.3.1.7 and section D.3.4.2 showing that the differences are relatively small.*

5.4.3   Summary of results pressure distribution

All the proposed formulae for the prediction of the parameters which are required to describe the parameterized pressure distribution on and beneath the revetment for impact load in Fig. 5.5 and non-impact load in Fig. 5.7 are summarized in Tab. 5.3.

Tab. 5.3: Summary of results location of maximum pressure

Impact load $(1.6<\xi_{m-1,0}<2.9)$	Non-impact load $(\xi_{m-1,0}>2.9)$

Pressure on the revetment

Point 0 : $\dfrac{p_0}{p_{max}}=1.0$ with $\dfrac{z_0}{z_{pmax}}=1.0$ (5.17)

Point 1 : $\dfrac{p_1}{p_{max}}=0.5$ with $\dfrac{z_1}{z_{pmax}}=-1.5$ (5.18)

Point 2 : $\dfrac{p_2}{p_{max}}=0.4$ with $\dfrac{z_2}{z_{pmax}}=-0.6$ (5.19)

Point 3 : $\dfrac{p_3}{p_{max}}=0.4$ with $\dfrac{z_3}{z_{pmax}}=-3.0$ (5.20)

Point 4 : $\dfrac{p_4}{p_{max}}=0.0$ with $\dfrac{z_4}{z_{pmax}}=\dfrac{R_{u2\%}}{z_{pmax}}$ (5.21)

with:

$\dfrac{R_{u2\%}}{H_{m0}}=0.54\cdot\left[1.65\cdot\xi_{m-1,0}\right]$ for Model B   (4.7)

Point 0 : $\dfrac{p_0}{p_{stat}}=1.0$ with $\dfrac{z_0}{z_{pmax}}=1.0$ (5.22)

Point 3 : $\dfrac{p_3}{p_{stat}}=0.4$ with $\dfrac{z_3}{z_{pmax}}=-2.6$ (5.23)

Point 4 : $\dfrac{p_4}{p_{stat}}=0.0$ with $\dfrac{z_4}{z_{pmax}}=\dfrac{R_{u2\%}}{z_{pmax}}$ (5.24)

with:

$\dfrac{R_{u2\%}}{H_{m0}}=0.77\cdot\left[4.0-\dfrac{1.5}{\sqrt{\xi_{m-1,0}}}\right]$ for Model B and C   (4.8)

Pressure beneath the revetment

Point 0' : $\dfrac{p_0'}{p_{max}}=0.6$ with $\dfrac{z_0'}{z_{pmax}}=-1.2$ (5.25)

Point 2' : $\dfrac{p_2'}{p_{max}}=0.4$ with $\dfrac{z_2'}{z_{pmax}}=-0.8$ (5.26)

Point 3' : $\dfrac{p_3'}{p_{max}}=0.4$ with $\dfrac{z_3'}{z_{pmax}}=-3.2$ (5.27)

Point 4' : $\dfrac{p_4'}{p_{max}}=0.0$ (5.28)

with $\dfrac{z_4'}{p_{max}}=-\dfrac{R_{u2\%}}{z_{pmax}}-0.2$

Point 0' : $\dfrac{p_0'}{p_{stat}}=1.0$ with $\dfrac{z_0'}{z_{pmax}}=-1.2$ (5.30)

Point 3' : $\dfrac{p_3'}{p_{stat}}=0.4$ with $\dfrac{z_3'}{z_{pmax}}=-2.8$ (5.31)

Point 4' : $\dfrac{p_4'}{p_{stat}}=0.0$ (5.32)

with $\dfrac{z_4'}{z_{pmax}}=-\dfrac{R_{u2\%}}{z_{pmax}}-0.2$

5.5 Parameters for pressure time histories on and beneath the revetment

Based on the parameterization of the pressure time histories proposed in section 5.1, a preliminary analysis of irregular and regular wave tests was performed to determine all the parameters which are required to describe both fundamental load cases in the time domain (Ludwigs, 2009):

(i) **The impact load** (see Fig. 5.4): t_A; t_D; $t_{stat,imp}$; p_{max} and $p_{stat,imp}$ for the pressure on the revetment. Associated parameters used for the pressure beneath the revetment are t_{2A}; t_{2D}; $t_{2stat,imp}$; $p_{max,2}$ and $p_{2stat,imp}$.

(ii) **The non-impact load** (see Fig. 5.6): $t_{stat,1}$; $t_{stat,2}$ and p_{stat} for the pressure on the revetment. Associated parameters used for the pressure beneath the revetment are $t_{2stat,1}$; $t_{2stat,2}$ and $p_{stat,2}$.

The results of the preliminary analysis (Ludwigs, 2009) have shown that for the determination of the pressure parameters in the time domain, a discrimination between the pressure on and beneath the revetment is required only for p_{max} (see impact load parameterization in Fig. 5.4), since p_{max} is substantially damped through the revetment. In fact, no discrimination is needed for all other parameters associated with the pressure beneath the revetment. The differences were found in the range of the scatter of the data.

Moreover, the results of the preliminary analysis have also confirmed the experience made in former similar analysis conducted to determine the time related parameters of the wave loads on structures (e.g. Oumeraci et al., 2001); i.e. a very large inherent scatter of the data is generally observed, due to the highly stochastic nature of the wave pressure development in time. This makes the determination of any clear relationship between the time related parameters of the parameterized wave pressure and the incident wave parameters (e.g. wave steepness, surf similarity parameter) extremely difficult. Despite these inherent difficulties, a first attempt is made below to propose very rough and thus very tentative formulae to predict all the parameters required describing the parameterized pressure histories for impact load in Fig. 5.4 and for non-impact load in Fig. 5.6. As already mentioned above and in contrast to previous sections no discrimination is made between the cases "pressure on the revetment" and "pressure beneath the revetment", except for the peak pressure parameter p_{max} for impact load. Like in the previous sections, only the results of irregular wave tests are considered below, while those related to regular wave tests are provided where appropriate in Annex D.

5.5.1 Impact loads

As already mentioned above all parameters required to describe the parameterized components of impact loads are defined in Fig. 5.4, including the parameters of the impact component and those of the quasi-static component.

5.5.1.1   *Parameters of the impact component*

(i) <u>Rise time t_A</u>

The rise time t_A is expected to decrease with increasing peak pressure p_{max} for the wave conditions tested. The rise time t_A normalized by the wave period T is plotted against the relative pressure $p_{max}/\rho g H_{m0}$ in Fig. 5.42 for both cases "pressure on the revetment" and "pressure beneath the revetment". As expected a considerable scatter is observed, showing that it is not meaningful to distinguish between the two aforementioned cases and that it is difficult to derive a clear relationship between t_A/T and $p_{max}/\rho g H_{m0}$. Nevertheless, the following conservative relationship is tentatively proposed as an upper envelope (see Fig. 5.42):

$$\frac{t_A}{T} = 0.047 \cdot \left(\frac{p_{max}}{\rho \cdot g \cdot H_{m0}} \right)^{-0.71} \quad \text{for } 1.6 < \frac{p_{max}}{\rho \cdot g \cdot H_{m0}} < 7.5 \qquad (5.33)$$
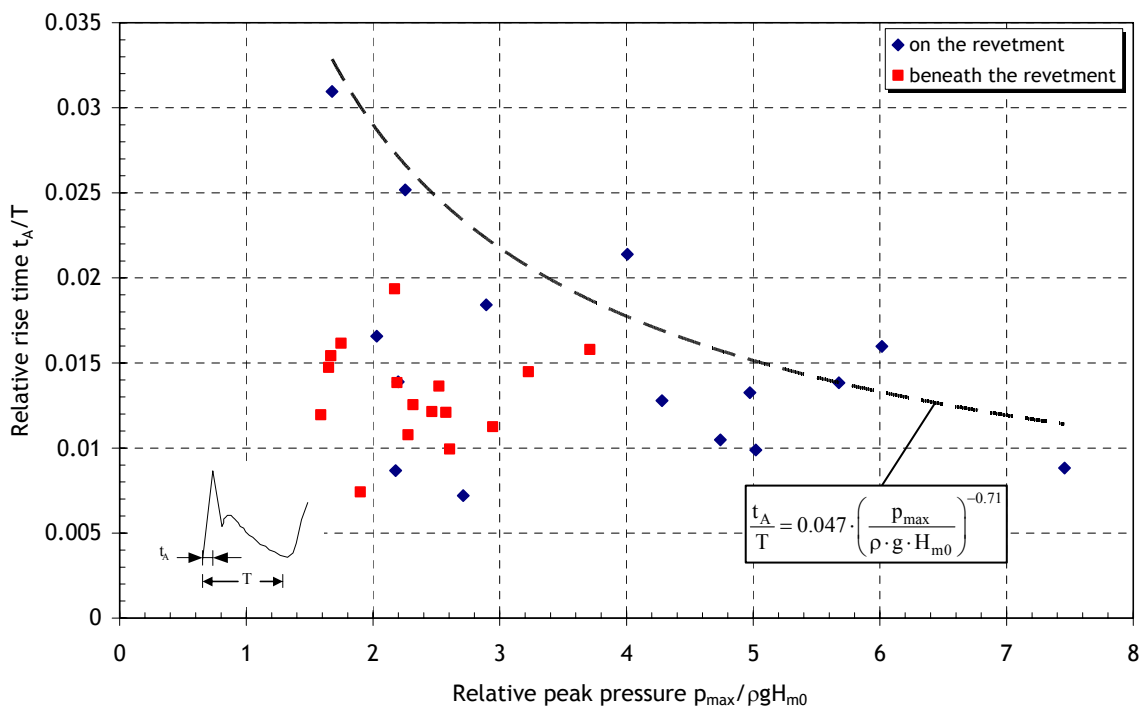
Fig. 5.42: Relative rise time t_A/T for impact loads on and beneath the revetment

A further analysis using a validated numerical model to perform a detailed parameter study is required to come up with an improved prediction formula.

(ii) <u>Impact duration t_D</u>

The relative impact duration t_D/t_A is plotted against the relative pressure $p_{max}/\rho g H_{m0}$ in Fig. 5.43. As expected a considerable scatter is observed, suggesting that t_D/t_A has a tendency to increase with increasing relative pressure $p_{max}/\rho g H_{m0}$. The scatter however makes it very

difficult to derive a physically meaningful and practically simple prediction formula for the impact duration. It is suggested here that the t_D/t_A ratio must exceed 2.0 (t_D/t_A means that rise time and fall time are identical) and not much larger than 12.0 where the latter number is difficult to assess since there are very few data points available for higher impact loads only. Hence, the following simple relationship is tentatively proposed:

$$\frac{t_D}{t_A} = 6.2 + 2.7 \cdot \tanh\left(\frac{p_{max}}{\rho \cdot g \cdot H_{m0}} - 4.5\right) \quad \text{for } 1.6 < \frac{p_{max}}{\rho \cdot g \cdot H_{m0}} < 7.5 \qquad (5.34)$$

with an upper bound of

$$\max \frac{t_D}{t_A} = 9.7 + 2.7 \cdot \tanh\left(\frac{p_{max}}{\rho \cdot g \cdot H_{m0}} - 4.5\right) \qquad (5.35)$$

and a lower bound of

$$\min \frac{t_D}{t_A} = 4.7 + 2.7 \cdot \tanh\left(\frac{p_{max}}{\rho \cdot g \cdot H_{m0}} - 4.5\right) \qquad (5.36)$$
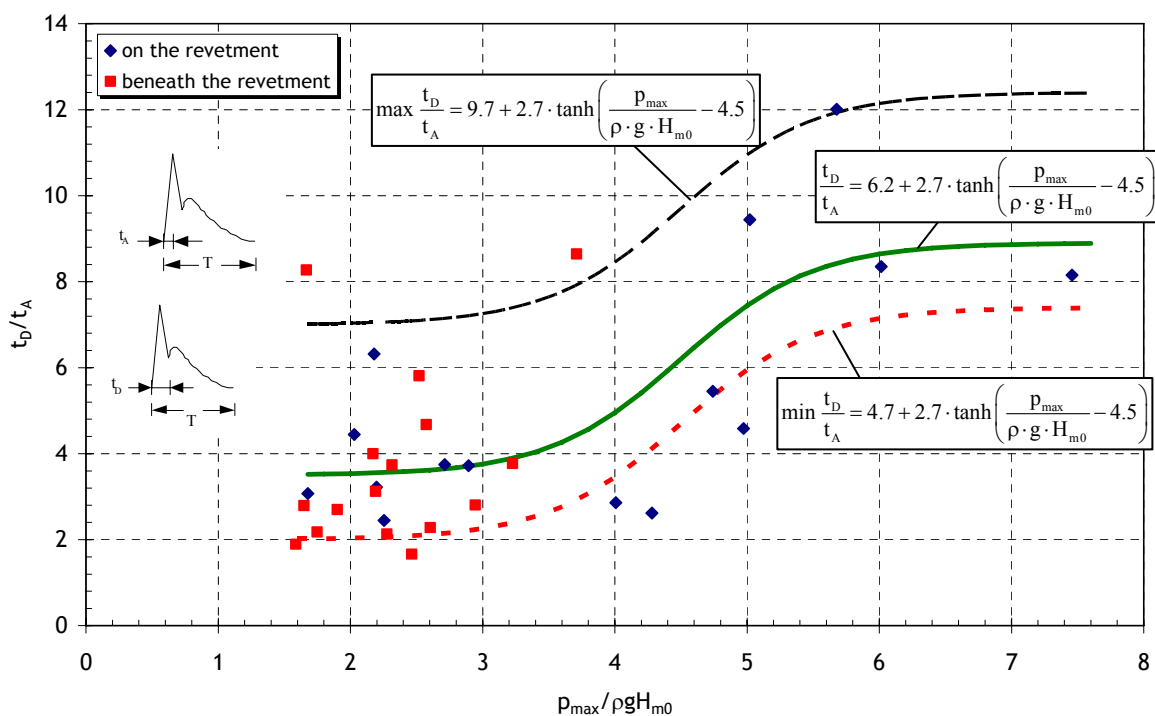
Fig. 5.43: Relative impact load duration t_D/t_A on and beneath the revetment

A more detailed parameter study, using a validated numerical model would be required to develop improved formulae.

(iii) <u>Peak pressure p_{max}</u>

The prediction formulae for the peak pressure on and beneath the revetment are already derived in section 5.2 and are given by Eq. (5.3) and Eq. (5.7), respectively:

$$\frac{p_{max}}{\rho \cdot g \cdot H_{m0}} = -4 \cdot \xi_{m-1,0} + 12.5 \quad \text{for } 1.6 < \xi_{m-1,0} < 2.5 \tag{5.3}$$

$$\frac{p_{2,max}}{\rho \cdot g \cdot H_{m0}} = 0.6 \cdot \left[-4.0 \cdot \xi_{m-1,0} + 12.5 \right] \quad \text{for } 1.6 < \xi_{m-1,0} < 2.5 \tag{5.7}$$

5.5.1.2 *Parameters of the quasi-static pressure component*

(i) <u>Rise time $t_{stat,imp}$</u>

The analysis of $t_{stat,imp}$ for the quasi-static component of the impact load is performed together with the data related to the non-impact load as shown in Fig. 5.44 of section 5.5.2. The data related to $t_{stat,imp}/T$ are those in the surf similarity parameter range $\xi_{m-1,0}$=1.6-2.5. It is again observed that a considerable scatter of the data occurs, particularly for $\xi_{m-1,0}$<2.0. Nevertheless, the following simple formula is proposed for the prediction of $t_{stat,imp}/T$ which is based on the results of the preliminary analysis (Ludwigs, 2009):

$$\frac{t_{stat,imp}}{T} \approx \frac{t_{2stat,imp}}{T} = 0.12 \quad \text{for } 1.6 < \xi_{m-1,0} < 2.5 \tag{5.37}$$

in which the wave period T represents also the total duration of the quasi-static pressure component, and thus the duration of the entire impact load including both impact and quasi-static component (see Fig. 5.4).

Considering the significant scatter of the data it may not be meaningful to favour a more complicated relationship. Ideally, a systematic parameter study using a validated numerical model has to be used to come up with an improved formula.

(ii) <u>Peak pressure of quasi-static component $p_{stat,imp}$</u>

The prediction formula for $p_{stat,imp}$ has already been derived in section 5.2 which is similar for both pressures on and beneath the revetment (see Fig. 5.11 and Eq. (5.5)):

$$\frac{p_{stat}}{\rho \cdot g \cdot H_{m0}} = 0.68 \cdot \xi_{m-1,0} \quad \text{for } 1.5 < \xi_{m-1,0} < 2.5 \tag{5.5}$$

5.5.2 Non-impact load

All parameters required to describe the parameterized non-impact load (pulsating wave load) are described in Fig. 5.6.

(i) Time parameters $t_{stat,1}$ and $t_{stat,2}$

In Fig. 5.44 the parameters $t_{stat,1}/T$ and $t_{stat,2}/T$ (for layer 1) and $t_{2stat,1}/T$ and $t_{2stat,2}/T$ (for layer 2) are plotted against the surf similarity parameter $\xi_{m-1,0}$. For $\xi_{m-1,0}>2.9$, the data exhibit a very large scatter as expected, so that differences between the data for both cases ("pressure on the revetment" and "pressure beneath the revetment") are in the range of the observed scatter.
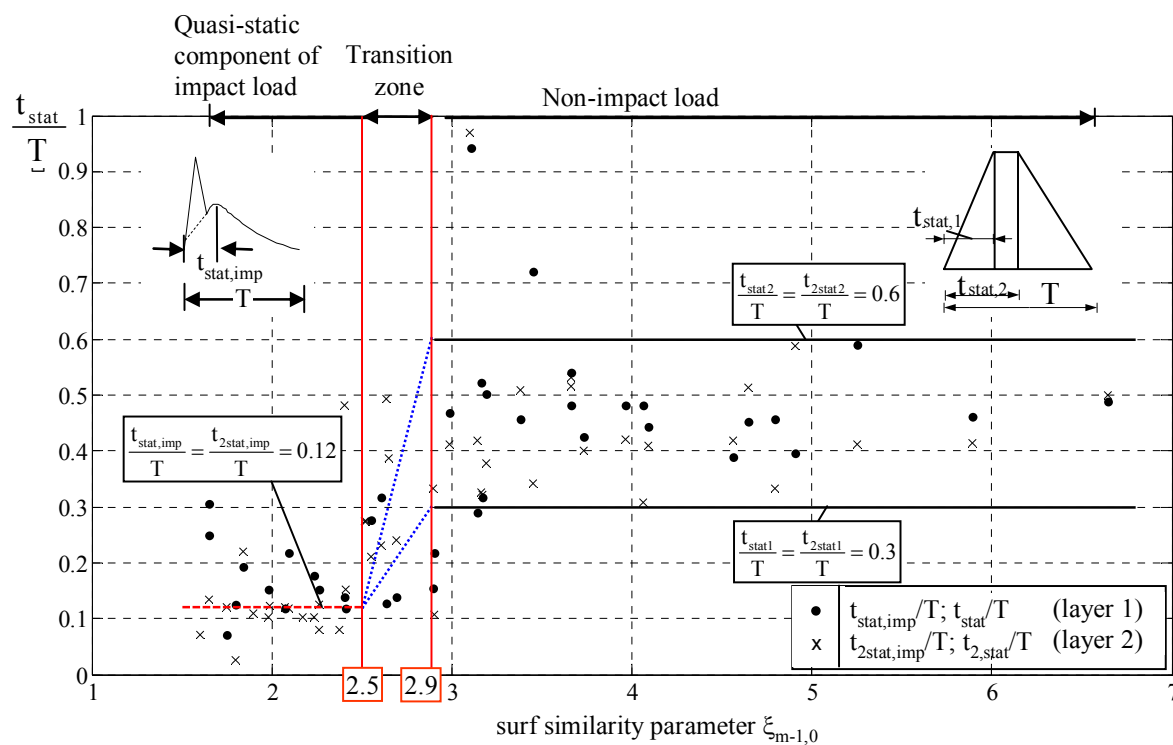
Fig. 5.44: Time parameters for non-impact load and quasi-static component for irregular waves

The large scatter of data also makes it difficult to develop a clear relationship between the time parameters ($t_{stat,1}/T$ and $t_{stat,2}/T$) and surf similarity parameter $\xi_{m-1,0}$. Therefore, at this stage only very tentative formulae can be proposed as on upper ($t_{stat,2}/T$) and a lower envelope ($t_{stat,1}/T$) as a result of the preliminary analysis (Ludwigs, 2009):

$$\frac{t_{stat,1}}{T} = \frac{t_{2stat,1}}{T} = 0.3 \tag{5.38}$$

$$\frac{t_{stat,2}}{T} = \frac{t_{2stat,2}}{T} = 0.6 \tag{5.39}$$

Using only the data obtained from the scale model tests performed, including both regular and irregular wave tests, it is hardly possible to come up with improved formulae. Therefore, the best alternative is to use a validated numerical model for a systematic parameter study.

(ii) <u>Peak pressure of the non-impact load p_{stat}</u>

The prediction formulae for p_{stat} have already been derived in section 5.2 (see Fig. 5.11):

$$\frac{p_{stat}}{\rho \cdot g \cdot H_{m0}} = 0.68 \cdot \xi_{m-1,0} \quad \text{for } 2.9 < \xi_{m-1,0} < 4.5 \tag{5.5}$$
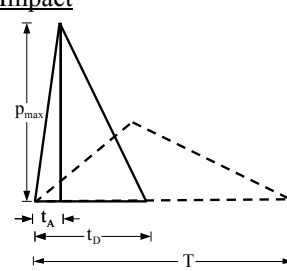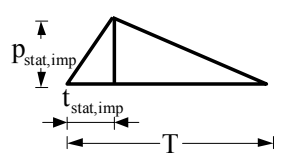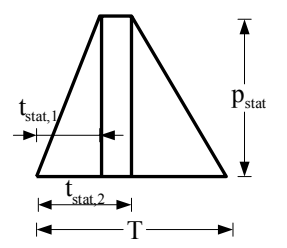
$$\frac{p_{stat}}{\rho \cdot g \cdot H_{m0}} = 0.41 \cdot \xi_{m-1,0} + 1.2 \quad \text{for } \xi_{m-1,0} > 4.5 \tag{5.6}$$

5.5.3   Summary of results for time related pressure parameters

All the proposed formulae for the prediction of the parameters which are required to describe the parameterized pressure histories for impact load in Fig. 5.4 and non-impact load in Fig. 5.6 are summarized in Tab. 5.4.

For the transition zone, a linear interpolation between the two loading cases "impact load" and "non-impact load" is suggested. Moreover, it is important to stress that the proposed formulae for the time related parameters are very tentative due to inherent large scatter of the data. Even considering the data for regular wave tests could not bring any improvement as shown by the preliminary analysis (Ludwigs, 2009). As mentioned above, the only alternative is to select the best CF-D model yet available, to validate it using the result of the experimental data obtained in this project, and then to use it for a more systematic parameter study, including a sensitivity analysis. The results would lead to more consistent prediction formulae, including the quantification of the uncertainties involved.

Tab. 5.4: Summary of results of time related pressure parameters

	Definition	Pressure on the revetment	Pressure beneath the revetment
Impact load (1.5<ξ<2.5)	**Impact** t_A=rise time t_D=impact duration T=wave period ξ=surf similarity parameter	$\dfrac{t_A}{T} = 0.047\left(\dfrac{p_{max}}{\rho \cdot g \cdot H_{m0}}\right)^{-0.71}$ (5.33) $\dfrac{t_D}{t_A} = 6.2 + 2.7 \cdot \tanh\left(\dfrac{p_{max}}{\rho \cdot g \cdot H_{m0}} - 4.5\right)$ (5.34) $\dfrac{p_{max}}{\rho \cdot g \cdot H_{m0}} = -4 \cdot \xi_{m-1,0} + 12.5$ (5.3)	$\dfrac{t_{2A}}{T} = 0.047\left(\dfrac{p_{max}}{\rho \cdot g \cdot H_{m0}}\right)^{-0.71}$ (5.33) $\dfrac{t_{2D}}{t_{2A}} = 6.2 + 2.7 \cdot \tanh\left(\dfrac{p_{max}}{\rho \cdot g \cdot H_{m0}} - 4.5\right)$ (5.34) $\dfrac{p_{2,max}}{\rho \cdot g \cdot H_{m0}} = 0.6 \cdot \left[-4.0 \cdot \xi_{m-1,0} + 12.5\right]$ (5.7)
	Quasi-static component 	$\dfrac{t_{stat,imp}}{T} = 0.12$ (5.37) $\dfrac{p_{stat,imp}}{\rho \cdot g \cdot H_{m0}} = 0.68 \cdot \xi_{m-1,0}$ (5.5)	$\dfrac{t_{2stat,imp}}{T} = 0.12$ (5.37) $\dfrac{p_{2,stat,imp}}{\rho \cdot g \cdot H_{m0}} = 0.68 \cdot \xi_{m-1,0}$ (5.5)
Non-impact load (ξ>2.9)	**Non-impact pressure** 	$\dfrac{t_{stat,1}}{T} = 0.3$ (5.38) $\dfrac{t_{stat,2}}{T} = \dfrac{t_{2stat,2}}{T} = 0.6$ (5.39) $\dfrac{p_{stat}}{\rho \cdot g \cdot H_{m0}} = 0.68 \cdot \xi_{m-1,0}$ (5.5) for $2.9 < \xi_{m-1,0} < 4.5$ $\dfrac{p_{stat}}{\rho \cdot g \cdot H_{m0}} = 0.41 \cdot \xi_{m-1,0} + 1.2$ (5.6) for $\xi_{m-1,0} > 4.5$	$\dfrac{t_{2stat,1}}{T} = 0.3$ (5.38) $\dfrac{t_{2stat,2}}{T} = 0.6$ (5.39) $\dfrac{p_{2,stat}}{\rho \cdot g \cdot H_{m0}} = 0.68 \cdot \xi_{m-1,0}$ (5.5) for $2.9 < \xi_{m-1,0} < 4.5$ $\dfrac{p_{2,stat}}{\rho \cdot g \cdot H_{m0}} = 0.41 \cdot \xi_{m-1,0} + 1.2$ (5.6) for $\xi_{m-1,0} > 4.5$

6 Wave-induced pore-pressure beneath the revetment

In addition to the wave pressure on and just beneath the revetment measured at PT layers 1 and 2, respectively (see Fig. 6.1) pore pressure induced in the sand core beneath the revetment were also measured at PT layers 3,4 and 5 (Fig. 6.1).

The recorded signals were checked (plausibility, interferences, etc.) and used in the further analysis without removing the signal noise. Where residual pore pressure occurred, a pre-processing of the data was performed which allows to separate the recorded signal in its oscillating component and mean (residual) component. The applied procedure has been successfully used by Oumeraci & Kudella, 2004 for the pore pressure beneath a caisson breakwater and is outlined in Fig. 6.2.

First, a Fast Fourier Transformation was applied on the recorded signals to obtain the magnitude and the phase spectra of the signal. Only the pressure amplitude spectra are shown in Fig. 6.2. On these spectra a low passfilter set to 0.03 Hz was applied. The effect of the filter on the resulting time series was examined, showing that slight changes of the filter frequency do not affect the main characteristics of the resulting time series. Therefore, the same cut-off frequency (0.03 Hz) was used for all processed signals.

Second, an Inverse Fast Fourier Transformation was applied on the low frequency part of the spectra yielding the mean (residual) component of the initially recorded signal. Accordingly the Inverse Fast Fourier Transformation was applied on the high frequency part of the spectra, which yielded the oscillating component of the recorded signal. Both components were stored in binary files for further analysis of transient and residual pore pressure.

In this chapter the transient pore pressure of PT layers 3-5 (Fig. 6.1) will be analysed and prediction formulae will be proposed. Moreover, the residual pressure will also be analysed.

a) *Model Alternative* A (without gravel filter)

b) *Model Alternative* B (with 0.10 m thick gravel filter)

c) *Model Alternative* C (with 0.20 m thick gravel filter)
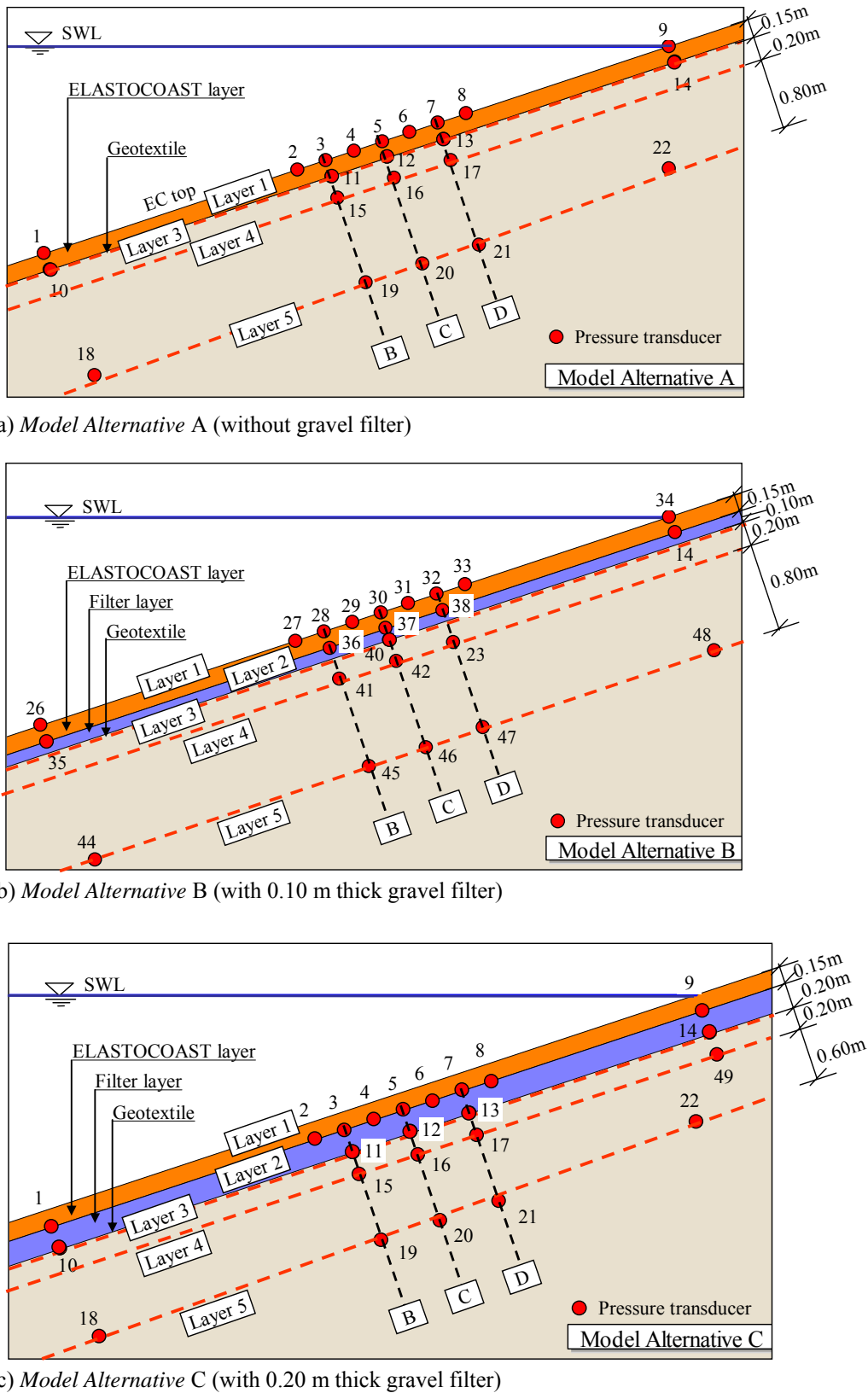
Fig. 6.1:   Definition of PT layers and locations of transducers for wave induced pore pressure
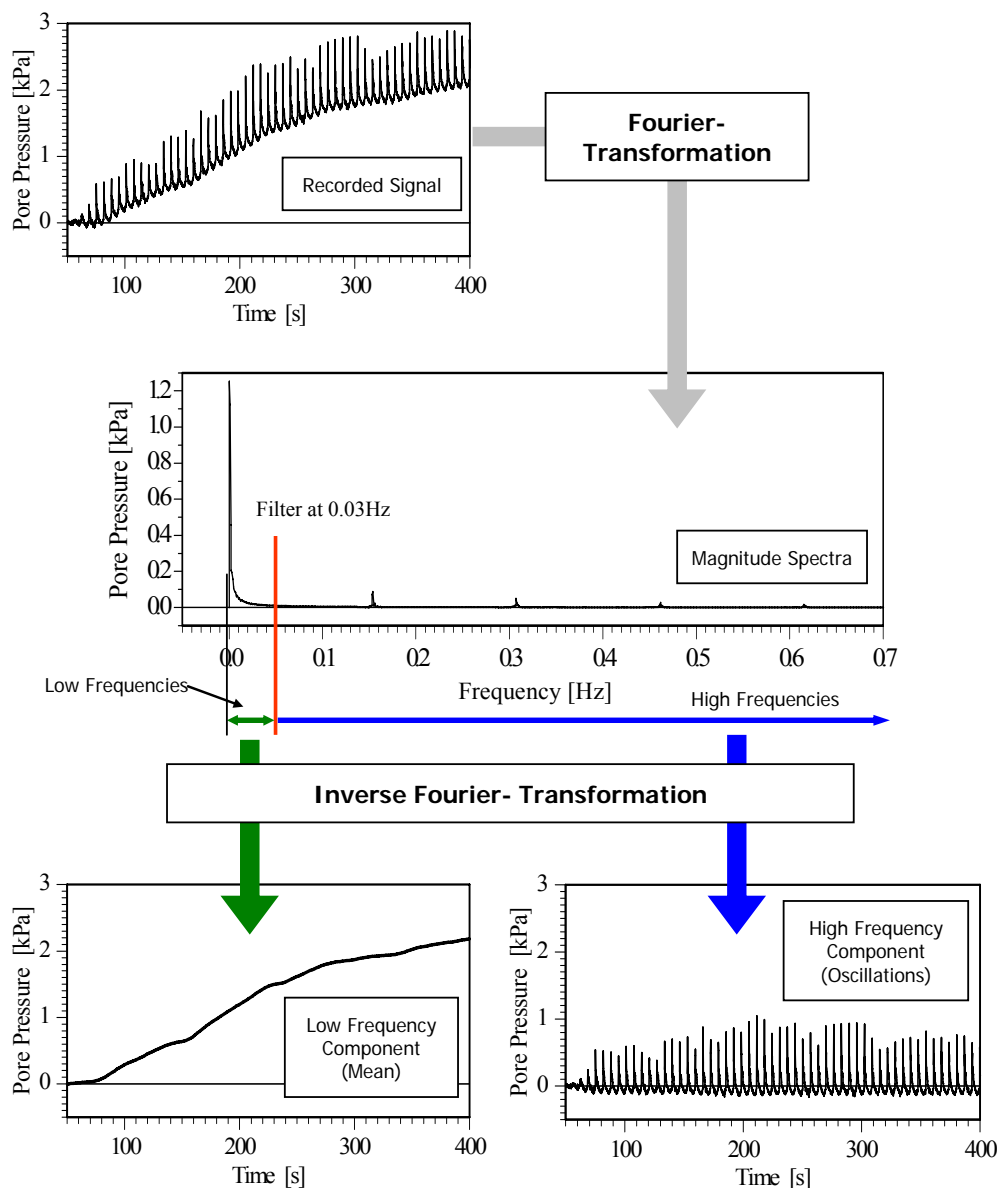
Fig. 6.2:   Separation of the recorded signal in a mean and oscillating component (modified from Oumeraci & Kudella, 2004)

6.1 Transient pore pressure

6.1.1 Maximum wave-induced pore-pressure beneath the revetment

6.1.1.1 Pre-processing and preliminary analysis of pore-pressure data

The same procedure as for the maximum wave induced pressure on the revetment is applied (see section 5.2.1). To discriminate between the pressures on and just beneath the revetment, and the wave induced pore pressure in the sand core, indices corresponding to the respective PT layers are introduced in the notation; e.g. maximum pore pressure at layer 3 is "$p_{3,max}$", at layer 4 "$p_{4,max}$" and at layer 5 "$p_{5,max}$".

Since no irregular wave tests could be performed for *Model Alternative A* (due to the total failure of Model A during regular wave tests), a comparison between *Model Alternatives A, B and C* is first shown for regular wave tests in terms of the transmission of the wave pressure in the sand core beneath the revetment for the two basic loading cases: impact load in Fig. 6.3 and non-impact load in Fig. 6.4. It should be noted that for Model C no pressure transducers were installed on the revetment as indicated in Fig. 6.1. Therefore, only the pressure at layers 2-5 will be analysed.

Impact load (Fig. 6.3)

The **impact component** recorded at PT layer 1 is substantially damped by layer 2 just beneath the revetment, apart from a slight time shift between the recorded pressure on and just beneath the revetment (layer 1 and layer 2) for *Model Alternative C*, no significant differences are observed for the different model alternatives.

Moreover, the **impact component** is entirely damped when transmitted to the sand core, so that **no impact pressure** is recorded at PT16 and PT42 located at a 0.20 m depth in the sand core. This is valid for all *Model Alternatives A, B* and *C*.

The **quasi-static component** recorded at PT layer 1 is not or only slightly damped at layer 2 just beneath the 0.15 m thick revetment. Differences between the different model alternatives become noticeable only when the wave-induced pressure is transmitted as transient pore pressure in the sand core beneath the revetment for *Model Alternative A* (Fig. 6.3a), it is hardly visible for *Model Alternative B* (Fig. 6.3b) and *Model Alternative C* (Fig. 6.3c).

Non-impact load (Fig. 6.4)

Basically, a similar behaviour as for the quasi-static component of the impact load in Fig. 6.3 is observed. However, many differences may be identified regarded the transmission of the wave-induced pressure into the sand core. In contrast to Fig. 6.3b and Fig. 6.3c, noticeable pore pressure at PT42 (Fig. 6.4b) and at PT16 (Fig. 6.4c) still occurs at a 0.20 m depth in the sand core beneath the revetment. Even at a deeper location (PT20 in Fig. 6.4c) in the sand core, noticeable pore pressure is recorded.

a) *Model Alternative* A

b) *Model Alternative* B

c) *Model Alternative* C
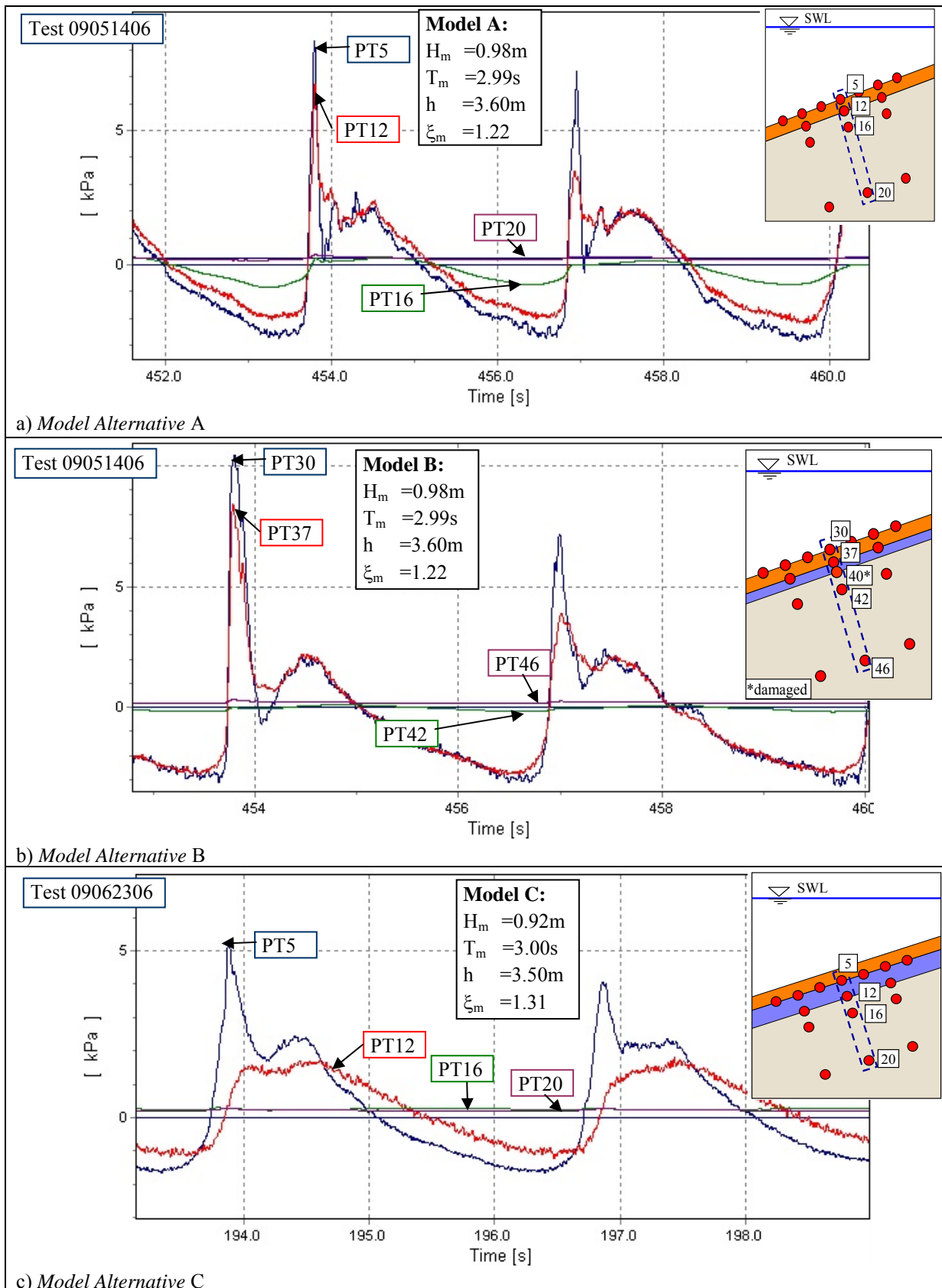
Fig. 6.3:   Pore pressure induced by regular waves for impact load

Wave-induced pore-pressure beneath the revetment

a) *Model Alternative* A

b) *Model Alternative* B

c) *Model Alternative* C
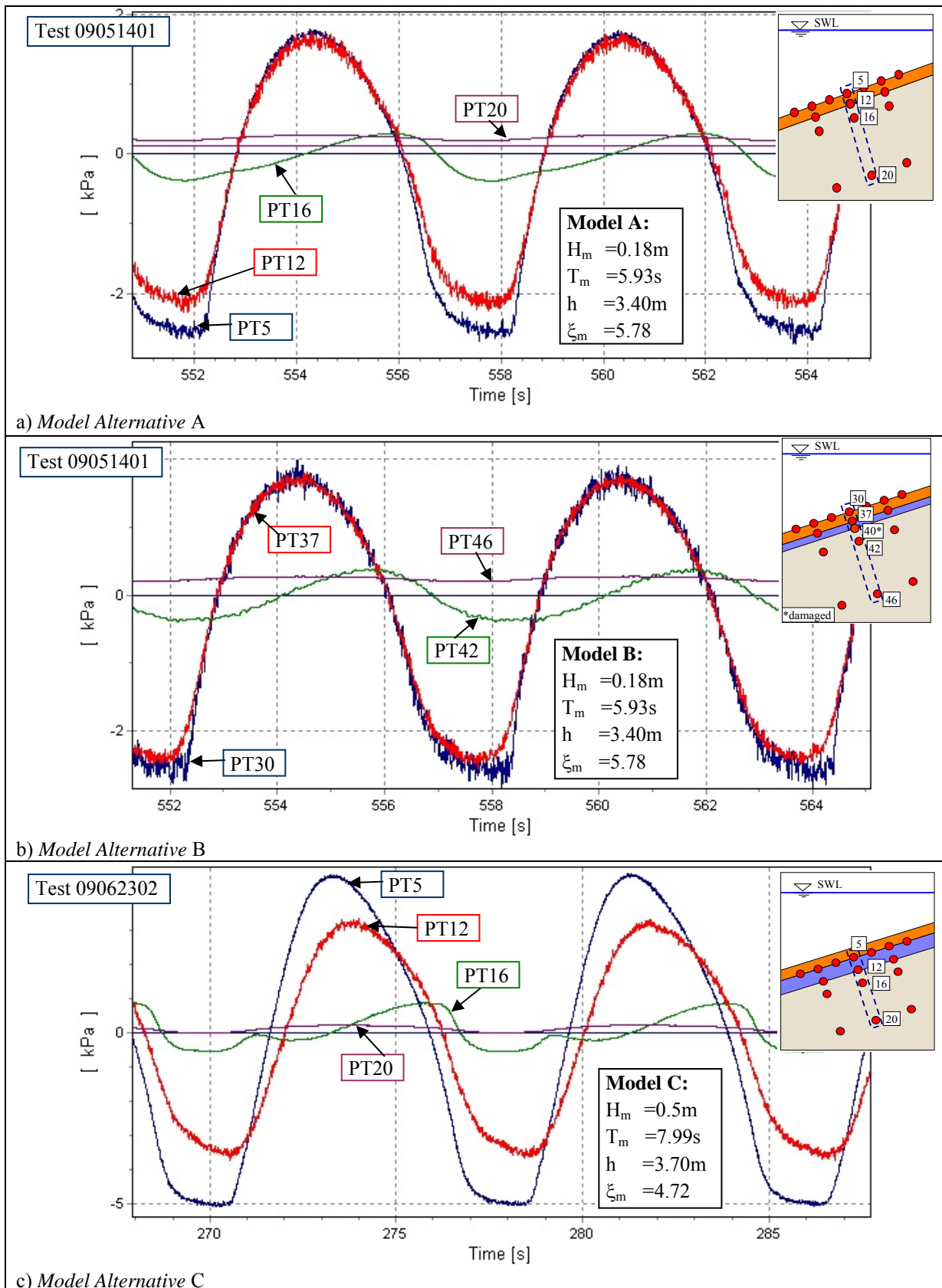
Fig. 6.4:   Pore pressure induced by regular waves for non-impact load (

Before starting with the preliminary analysis, all data were carefully checked (e.g. removing the signals of mal-functioning transducers and the first abnormal signals at the beginning of the tests) and pre-processed (e.g. classification). The maximum pressure $p_{i,max}$ considered in the analysis for each test is the highest pressure recorded at layer i.

Since many pressure transducers (PT10-PT13) were installed and have been well-functioning at the upper boundary of the sand core (layer 3) for *Model Alternative C* (Fig. 6.1) and since the pressure recorded at this upper layer represents the **initial pore pressure to be transmitted in the sand core** beneath the revetment, the preliminary analysis is first considered only for *Model Alternative C*.

Like in Fig. 5.8 and applying the same procedure as in section 5.2.1.1 for maximum wave-induced pressure on the revetment, all peak values of the pore pressure data recorded at layer 3 are plotted against $\xi_{m-1,0}$ in Fig. 6.5. In contrast to the results in Fig. 5.8, the highest pore pressure do not occur for impact load, but for non-impact loads induced by waves of larger periods ($\xi_{m-1,0} > 2.9$). Comparison with Fig. 5.8 shows that the wave-induced pressures on the revetment are considerably damped for impact load and much less for non-impact load. This is in line with the example time series shown in Fig. 6.3 and Fig. 6.4. For the non-impact loads, pore pressure up to $p_{3,max}/\rho g H_{m0} = 2.6$ (for $\xi_{m-1,0} = 6.6$) occurred while for impact loads only values up to $p_{3,max}/\rho g H_{m0} = 1.4$ (for $\xi_{m-1,0} = 2.2$) were recorded.
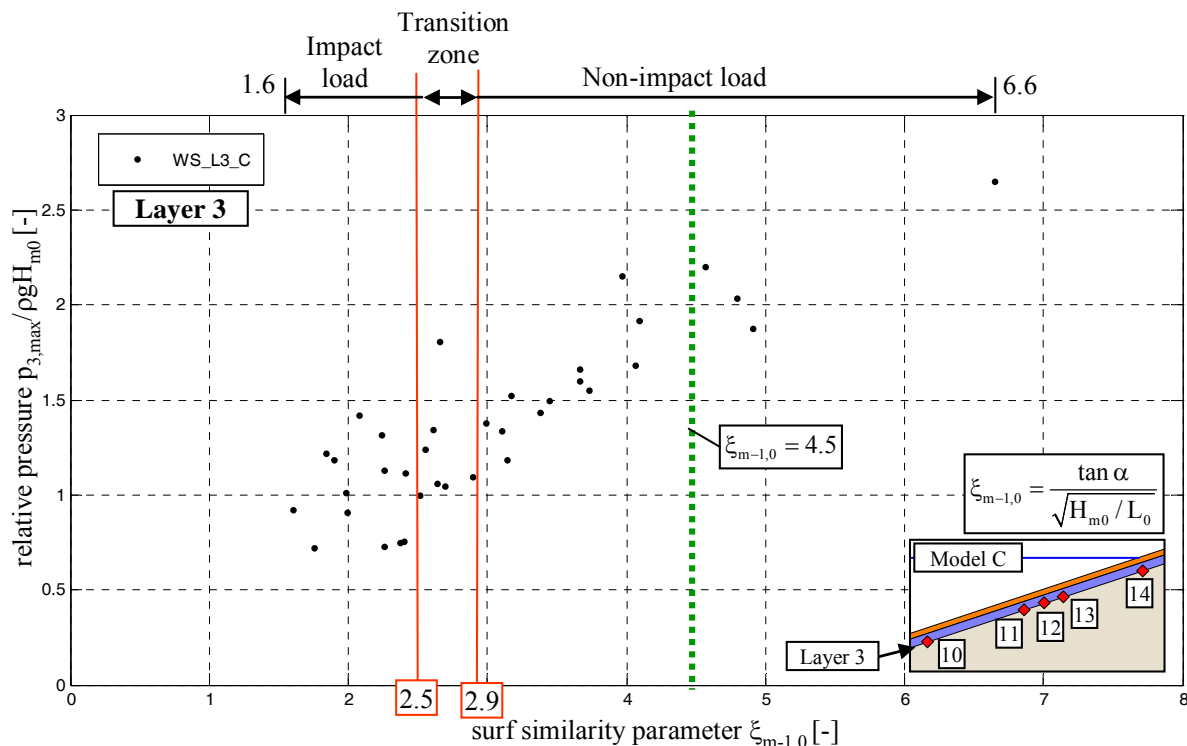
Fig. 6.5: Maximum pressure $p_{3,max}/\rho g H_{m0}$ at layer 3 against surf similarity parameter $\xi_{m-1,0}$ for irregular wave tests

Moreover, it is also seen from Fig. 6.5 that unlike the results of Fig. 5.8 it is not longer necessary to discriminate between the different load cases (impact, transition, non-impact) for the derivation of prediction formulae, since the maximum pore pressure $p_{3,max}$ continuously increase with increasing surf similarity parameter for the entire range of tested $\xi_{m-1,0}$-values ($\xi_{m-1,0} = 1.6$-6.6).

A comparison of Fig. 6.5 and Fig. 5.11 for maximum quasi-static pressure on the revetment (PT layer 1) clearly suggests that the pore pressure may be considered as quasi-static over the entire range of tested $\xi_{m-1,0}$-values, i.e. irrespective of the type of wave load on the revetment. Like in Fig. 5.11, the increase rate of pressure after $\xi_{m-1,0} \geq 4.5$ (see section 5.2.1.3) becomes lower but this tendency is less pronounced for pore pressure and therefore not be considered in the prediction formula for pore pressure. The result of this comparison again confirms the decision to not explicitly discriminate between the different load cases for the derivation of the prediction formulae for wave-induced pore pressure in the sand core beneath the revetment.

6.1.1.2   *Initial peak pore pressure in the sand core beneath the revetment*

As mentioned above the peak pore pressure ($p_{3,max}$) measured at the upper boundary of the sand core beneath the revetment (PT layer 3) is important as it represents the **initial wave-induced pore pressure in the sand core** to which the damped pore pressure recorded at the deeper PT layers in the sand core beneath the revetment have to be related.

Before starting with the detailed analysis all data were again carefully checked. This check has shown that pressure transducer 40 at layer 3 of *Model Alternative B* (see Fig. 6.1a) was damaged. Therefore, only the pressure transducers of *Model Alternative C* were used for the analysis of PT layer 3.

The maximum pore pressure data for PT layer 3 are plotted against surf similarity parameter $\xi_{m-1,0}$ in Fig. 6.6, resulting in the following linear function:

$$\frac{p_{3,max}}{\rho g H_{m0}} = 0.442 \cdot \xi_{m-1,0} \quad \text{for } 1.6 < \xi_{m-1,0} < 6.6 \tag{6.1}$$

The result in Fig. 6.6 illustrates that the maximum pore pressure $p_{3,max}$ at PT layer 3 can be described by the same linear function as the quasi-static load in section 5.2.1.3 (Eq. (5.5)) by introducing a reduction (damping) factor of 0.65:

$$\frac{p_{3,max}}{\rho g H_{m0}} = 0.65 \cdot \left[0.68 \cdot \xi_{m-1,0} \right] \triangleq 0.65 \cdot \frac{p_{stat}}{\rho g H_{m0}} \quad \text{for } 1.6 < \xi_{m-1,0} < 6.6 \tag{6.2}$$
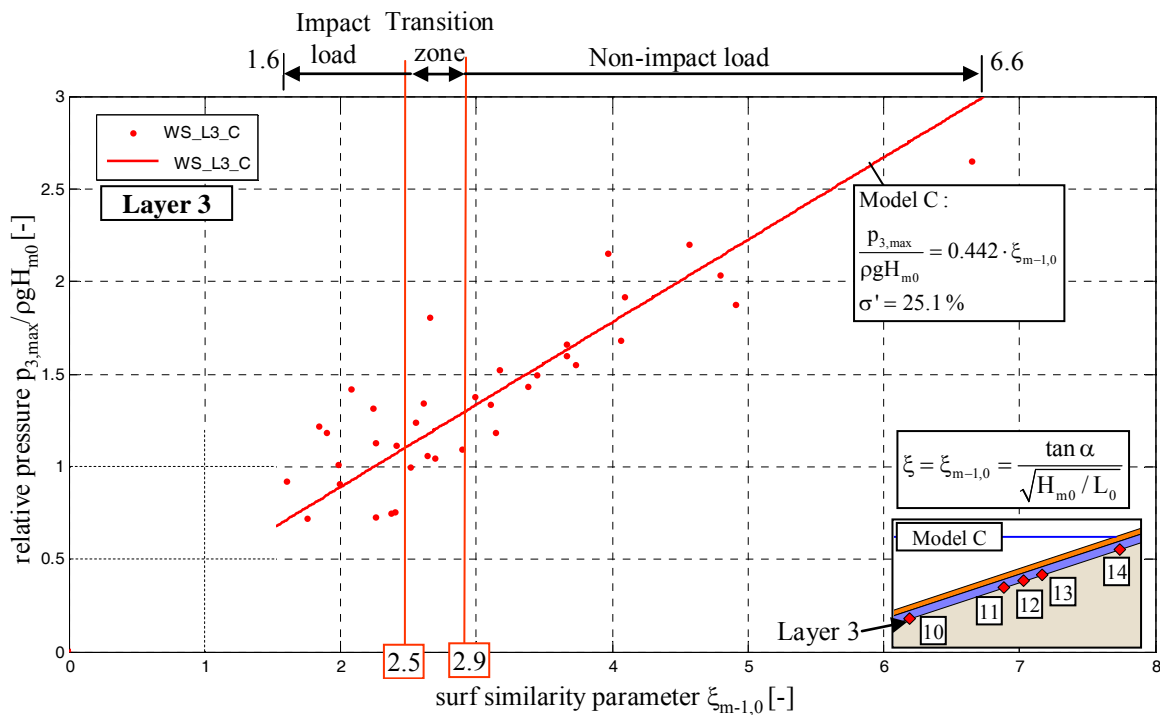
Fig. 6.6: Maximum pore pressure $p_{3,max}/\rho g H_{m0}$ at layer 3 plotted against surf similarity parameter $\xi_{m-1,0}$ for irregular wave tests

6.1.1.3 *Maximum wave-induced pore-pressure at layer 4 beneath the revetment*

A detailed check of the pore pressure transducers for layer 4 has shown that the pressure data of *Model Alternative B* as well as the data of *Model Alternative C* can be used for the analysis. The maximum pore pressure data for layer 4 are plotted against surf similarity parameter $\xi_{m-1,0}$ in Fig. 6.7, resulting in the following linear function for *Model Alternative B:*

$$\frac{p_{4,max}}{\rho g H_{m0}} = 0.116 \cdot \xi_{m-1,0} \triangleq 0.17 \cdot \frac{p_{stat}}{\rho g H_{m0}} \quad \text{for } 1.6 < \xi_{m-1,0} < 6.6 \tag{6.3}$$

and for *Model Alternative C:*

$$\frac{p_{4,max}}{\rho g H_{m0}} = 0.108 \cdot \xi_{m-1,0} \triangleq 0.16 \cdot \frac{p_{stat}}{\rho g H_{m0}} \quad \text{for } 1.6 < \xi_{m-1,0} < 6.6 \tag{6.4}$$

where $p_{stat}/\rho g H_{m0}$ is determined by Eq. (5.5) in section 5.2.1.3.

The result in Fig. 6.7 shows that the peak pressure at layer 4 $p_{4,max}$ can be described by the same linear function as the quasi-static load in Eq. (5.5) by introducing a reduction factor of 0.17 for *Model Alternative B* and 0.16 for *Model Alternative C.*

Wave-induced pore-pressure beneath the revetment
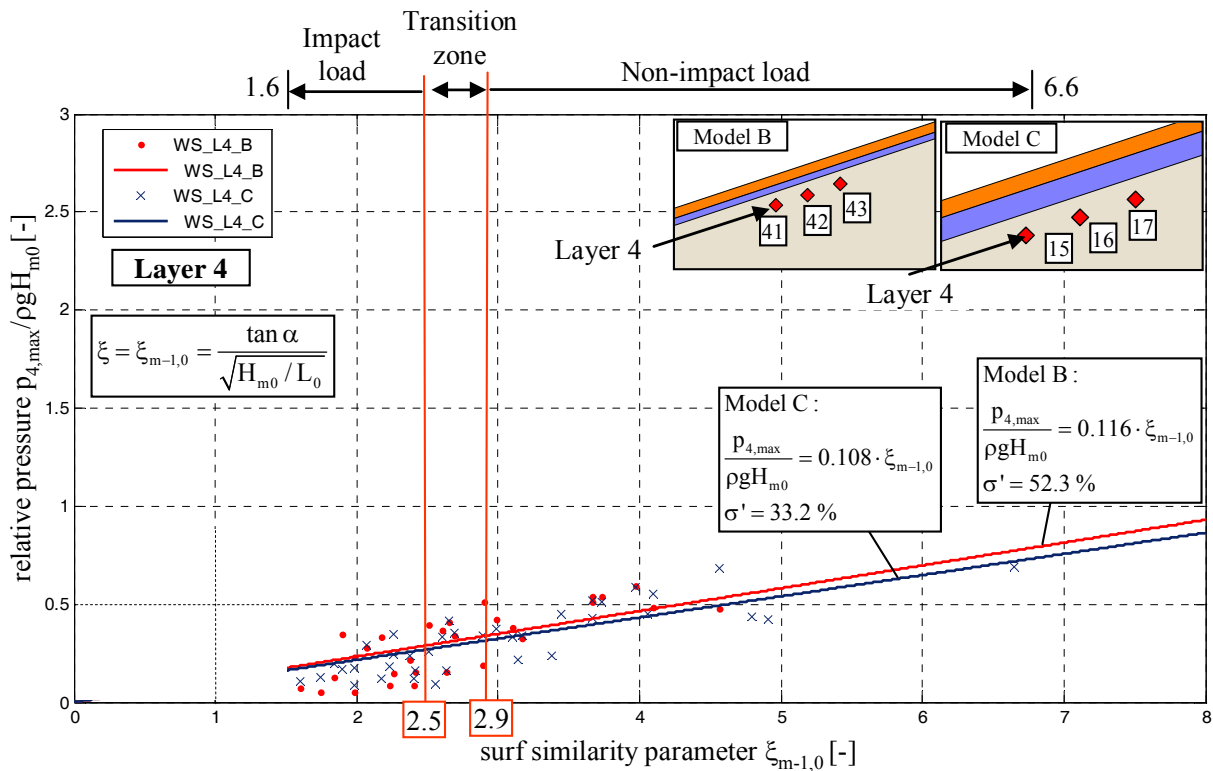
Fig. 6.7: Maximum pore pressure $p_{4,max}/\rho g H_{m0}$ at layer 4 plotted against surf similarity parameter $\xi_{m-1,0}$ for irregular wave tests, separated after *Model Alternatives* B and C

As expected, the comparison between Models B and C in Fig. 6.7 shows that the maximum pore pressure at layer 4 of *Model Alternative B* is slightly higher than the maximum pore pressure measured on *Model Alternative C*, due to the larger filter layer thickness of *Model Alternative C* (0.20 m instead of 0.10 m). The difference between *Model Alternative B* and *Model Alternative C* is negligibly small. Therefore, only one prediction formula is proposed for design purpose (see Fig. 6.8):

$$\frac{p_{4,max}}{\rho g H_{m0}} = 0.111 \cdot \xi_{m-1,0} \triangleq 0.16 \cdot \frac{p_{stat}}{\rho g H_{m0}} \quad \text{for } 1.6 < \xi_{m-1,0} < 6.6 \quad (6.5)$$

where $p_{stat}/\rho g H_{m0}$ is determined by Eq. (5.5) in section 5.2.1.3.
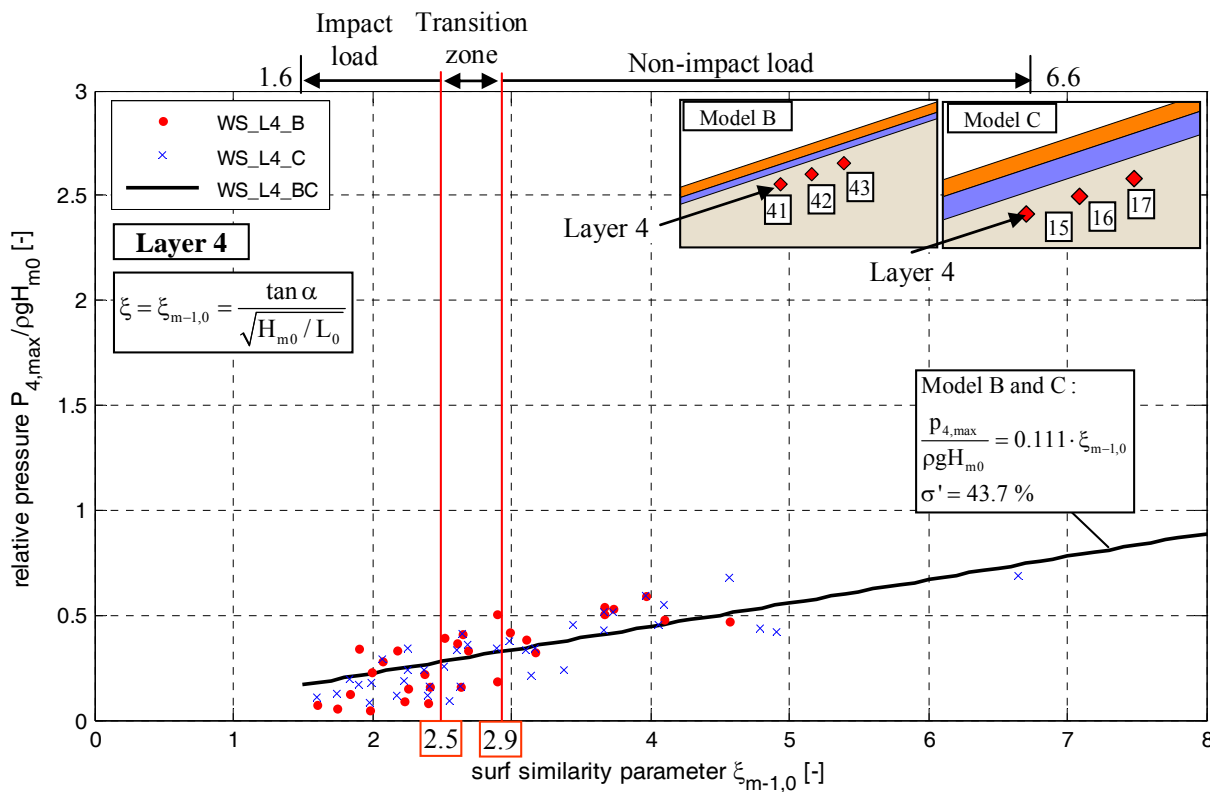
Fig. 6.8:   Maximum pore pressure $p_{4,max}/\rho g H_{m0}$ at layer 4 plotted against surf similarity parameter $\xi_{m-1,0}$ for irregular wave tests

The comparison with Fig. 6.6 also shows that the maximum pore pressure is much smaller than the pore pressure at layer 3, due to the considerable damping effect of the 0.20 m thick sand layer. So the main part of the damping process of the quasi static component of the wave load occurs in the sand core. The damping effect of the filter layer on quasi static wave loads is negligible.

6.1.1.4   Maximum wave-induced pore-pressure beneath the revetment at layer 5

As for PT layer 4, all pressure transducers of layer 5 can be used for the analysis of the maximum pressure. The maximum pore pressure data for layer 5 are plotted against surf similarity parameter $\xi_{m-1,0}$ in Fig. 6.9a at the same scale as for PT layers 3 and 4 for comparison (see Fig. 6.6 and Fig. 6.7). Due to the very low maximum pressure values of this layer, the same figure was replotted with a larger scale in Fig. 6.9b, resulting in the following linear function for *Model Alternative B:*

$$\frac{p_{max}}{\rho g H_{m0}} = 0.014 \cdot \xi_{m-1,0} \triangleq 0.02 \cdot \frac{p_{stat}}{\rho g H_{m0}} \quad \text{for } 1.6 < \xi_{m-1,0} < 6.6 \tag{6.6}$$

and for *Model Alternative C:*

$$\frac{p_{max}}{\rho g H_{m0}} = 0.013 \cdot \xi_{m-1,0} \triangleq 0.02 \cdot \frac{p_{stat}}{\rho g H_{m0}} \quad \text{for } 1.6 < \xi_{m-1,0} < 6.6 \tag{6.7}$$

Wave-induced pore-pressure beneath the revetment
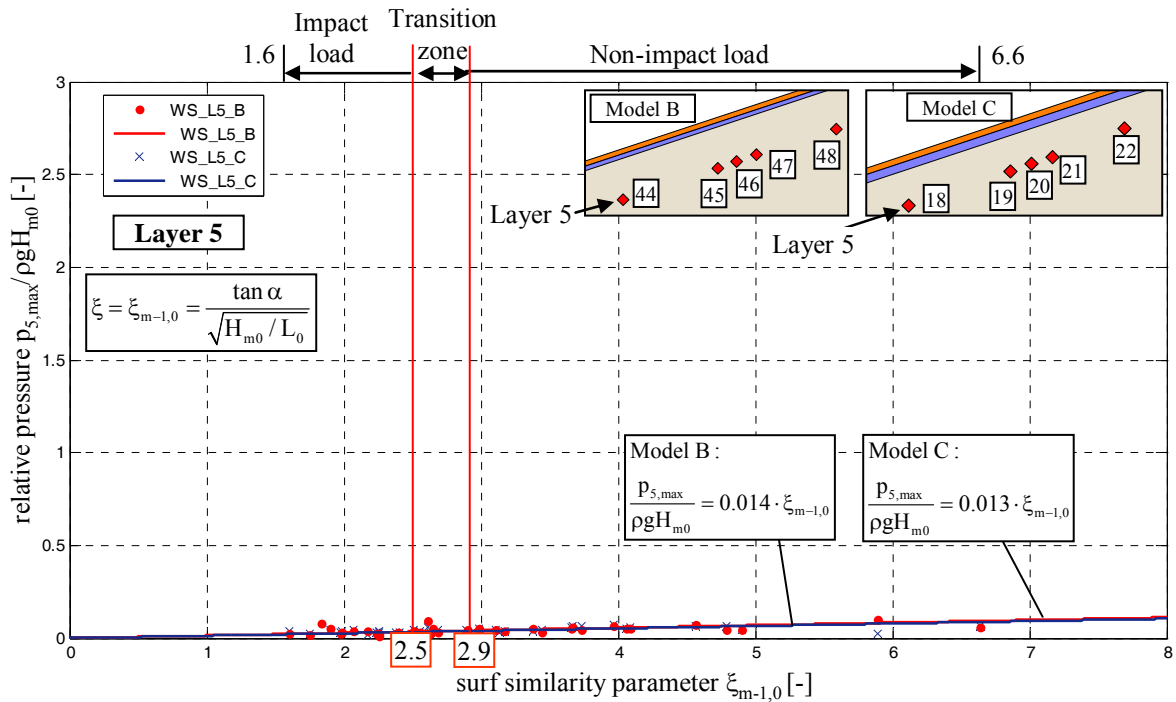
a) Maximum pore pressure $p_{5,max}/\rho g H_{m0}$ in layer 5 plotted against surf similarity parameter $\xi_{m-1,0}$ at the same scale as in Fig. 6.6 and Fig. 6.7
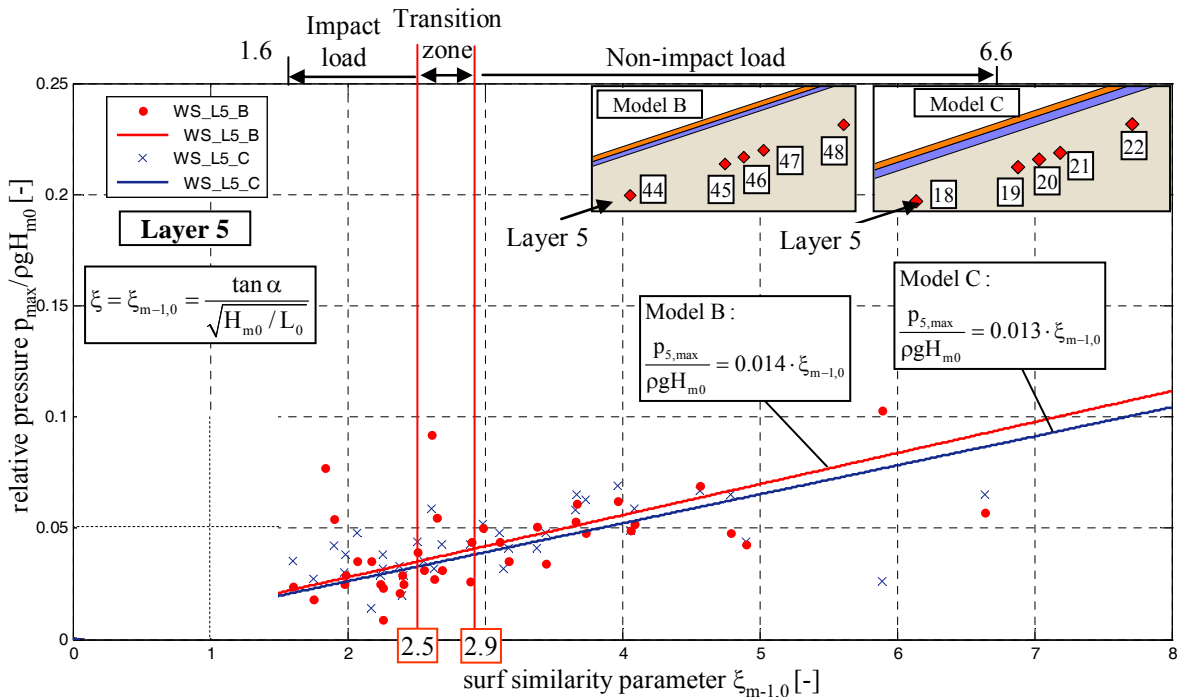
b) Fig. 6.9a replotted at larger scale

Fig. 6.9:   Maximum pore pressure $p_{max}/\rho g H_{m0}$ in layer 5 plotted against surf similarity parameter $\xi_{m-1,0}$ for irregular wave tests, separated after *Model Alternatives* B and C

As expected Fig. 6.9b shows that the maximum pressure at layer 5 of *Model Alternative B* is slightly higher than the maximum pressure measured on *Model Alternative C*, due to the larger filter layer thickness of *Model Alternative C* (0.20 m instead of 0.10 m). Again, the difference is is not significant. Therefore, also for layer 5 only one prediction formula is proposed for design purpose (see Fig. 6.10):

$$\frac{p_{4,max}}{\rho g H_{m0}} = 0.013 \cdot \xi_{m-1,0} \triangleq 0.02 \cdot \frac{p_{stat}}{\rho g H_{m0}} \quad \text{for } 1.6 < \xi_{m-1,0} < 6.6 \tag{6.8}$$

where $p_{stat}/\rho g H_{m0}$ is determined by Eq. (5.5) in section 5.2.1.3.
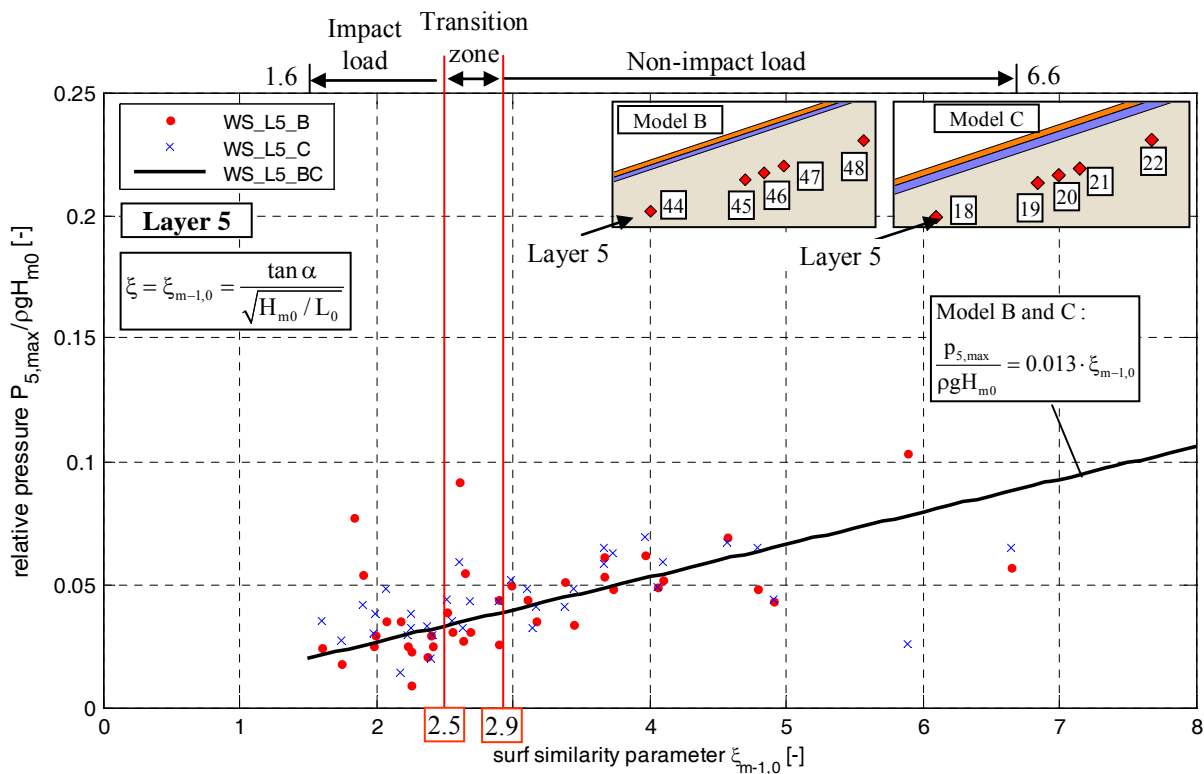
Fig. 6.10: Maximum pore pressure $p_{5,max}/\rho g H_{m0}$ at layer 5 plotted against surf similarity parameter $\xi_{m-1,0}$ for irregular wave tests

Compared to Fig. 6.6 and Fig. 6.8 the maximum pore pressure at Layer 5 is much smaller, which shows again the high damping capacity of the sand core.

6.1.1.5 Damping of the maximum (peak) pressure in the sand core beneath the revetment

The results of section 6.1.1 (see Fig. 6.6-Fig. 6.10) are summarized in Fig. 6.11 and Fig. 6.12 showing how the maximum pressures on the revetment are damped through the revetment (and filter layer) and the different layers in the sand core beneath the revetment. This damping has led to the reduction factors in Tab. 6.1 for the pore pressures at layers 3, 4 and 5 in the

sand core beneath the revetment as related to the maximum pressure $p_{1,max}$ on the revetment for *Model Alternatives B* and *C*.
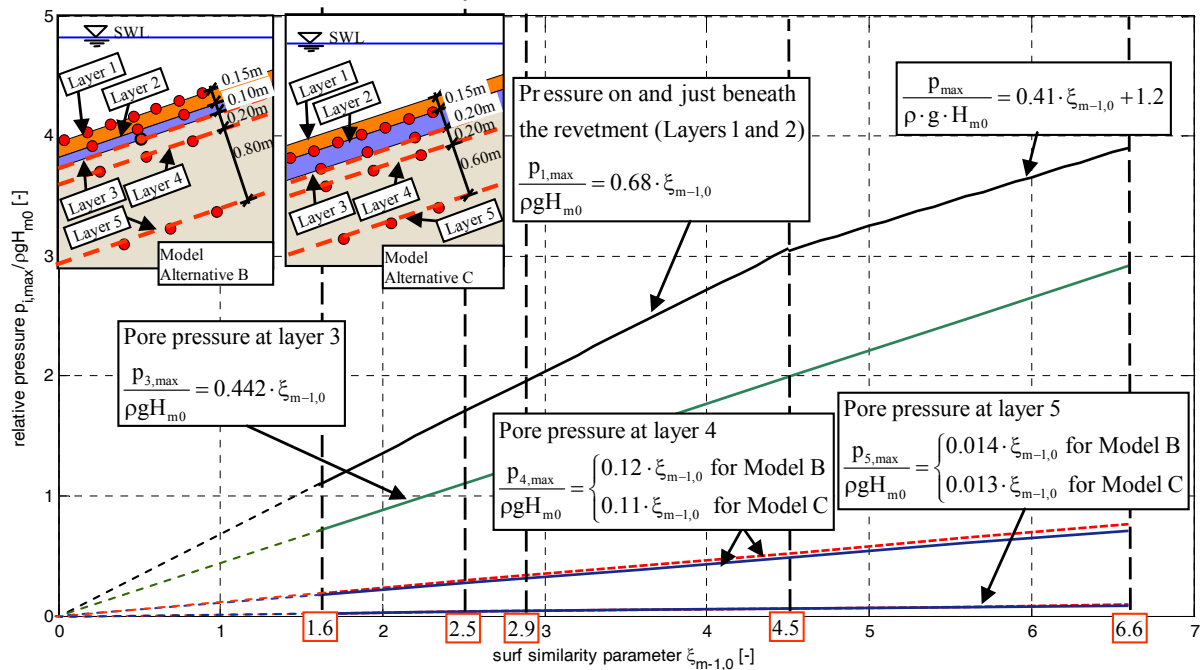
Fig. 6.11: Maximum wave induced pore pressure in the sand core beneath the revetment for irregular waves (all developed formulae)
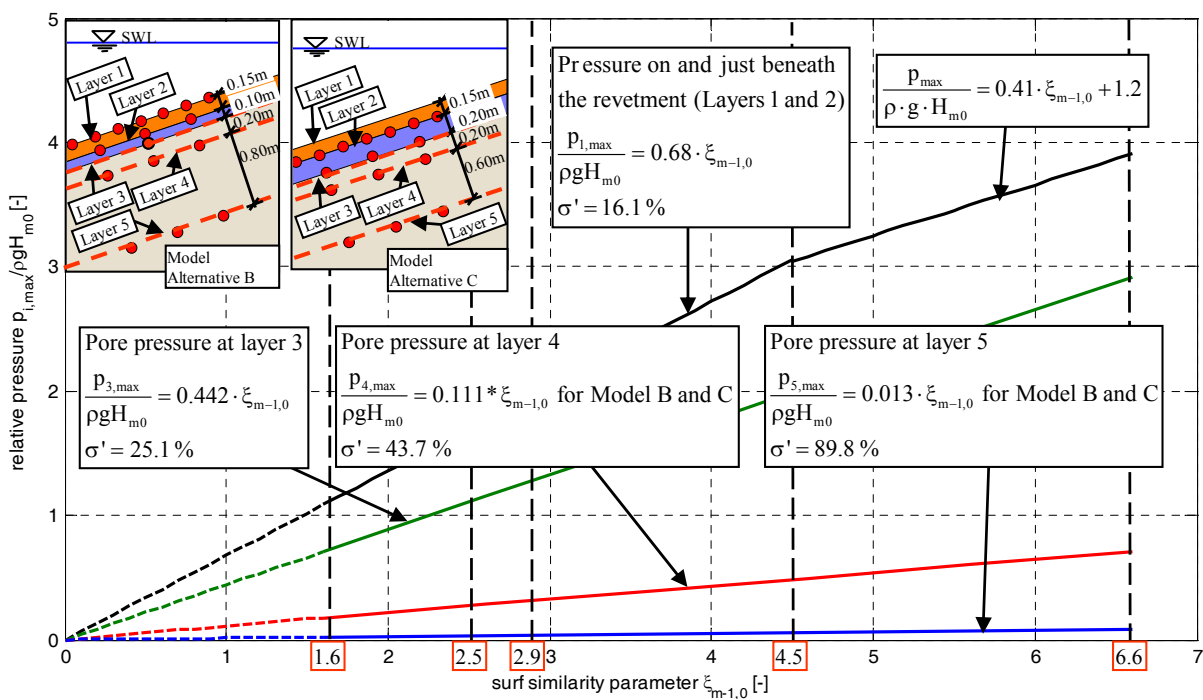
Fig. 6.12: Maximum wave induced pore pressure in the sand core beneath the revetment for irregular waves (only proposed prediction formulas)

The results in Tab. 6.1 show that the maximum pressure induced on the revetment is damped by about 35%, 85% and 98% at PT layers 3, 4 and 5 in the sand core, respectively; i.e. at a depth more than 0.80 m in the sand core beneath the revetment almost no wave-induced transient pore pressure occured.

Relating the reduced pore pressures at layers 4 and 5 to the initial maximum pore pressure $p_{3,max}$ at layer 3 provides the damping effect due to the sand material only (Tab. 6.2). The results in Tab. 6.2 show that the **initial pore pressure $p_{3,max}$** at the topmost layer of the sand core beneath the revetment (layer 3) is damped by about 75% and 97% at the deeper layers 4 and 5, respectively which are located at depth 0.20 m and 1.0 m (Model B) and 0.20 m and 0.80 m (Model C) beneath the revetment.

Tab. 6.1: Reduction factor for pore pressure as related to the maximum pressure on the revetment (layer 1)

PT layer	Model Alternative	
	B	C
3	-	0.65
4	0.17	0.16
5	0.02	0.02

Tab. 6.2: Reduction factor for pore pressure as related to $p_{3,max}$ at layer 3

PT layer	Model Alternative	
	B	C
4	0.26	0.24
5	0.03	0.03

Remark:

Between layer 1 and layer 2 there is almost no damping for quasi-static load (see Fig. 5.18) *while for the impact load a damping occurs according to* Fig. 5.17.

6.1.2 Distribution of wave-induced pore pressure in the sand core beneath the revetment

6.1.2.1 Definitions and preliminary analysis

It is expected that the damping of the wave-induced pore pressures when transmitted in the sand core beneath the revetment at different locations along the slope (e.g. plans B, C and D in Fig. 6.13) will be less than at the location where the maximum pressure $p_{3,max}$ occurs. Therefore, it is also useful to know how the pore pressure are distributed along different plans B, C and D normal to the slope (Fig. 6.13a). Based on this distribution, the distributions of pore pressure along PT layers 3, 4 and 5, i.e. at different depth and parallel to the slope, can also be determined (Fig. 6.13b).

The pore pressure of the distribution normal and parallel to the slope will be related in the following to the maximum pore pressure $p_{3,max}$ at PT layer 3, since the prediction formulae were developed in section 6.1.1 for $p_{3,max}/\rho g H_{m0}$ as a function of $\xi_{m-1,0}$ (see summary in

Fig. 6.11). Therefore, in the following analysis for the derivation of prediction formulae describing the wave-induced pore pressure distribution, $p_{3,max}$ will be set to the reference pore pressure p_0 at $z' = 0$ (layer 3):

$$p_{3,max} = p_0 \qquad (6.9)$$

In order to illustrate how the pore pressure are damped from layer 3 to layer 5 at different locations B, C and D along the slope, the pore pressure signals recorded at these locations are plotted in Fig. 6.14 for an impact load and in Fig. 6.15 for non-impact load. This shows that the damping effect is basically similar at the different locations B, C and D along the slope, when the pore pressure measured at deeper layers are related to the initial pore pressure recorded at the topmost layer in the sand core (PT11, PT12 and PT13 for Plans B, C and D, respectively).

a) Principal pore pressure distribution normal to the slope

b) Principal pore pressure distribution parallel to the slope
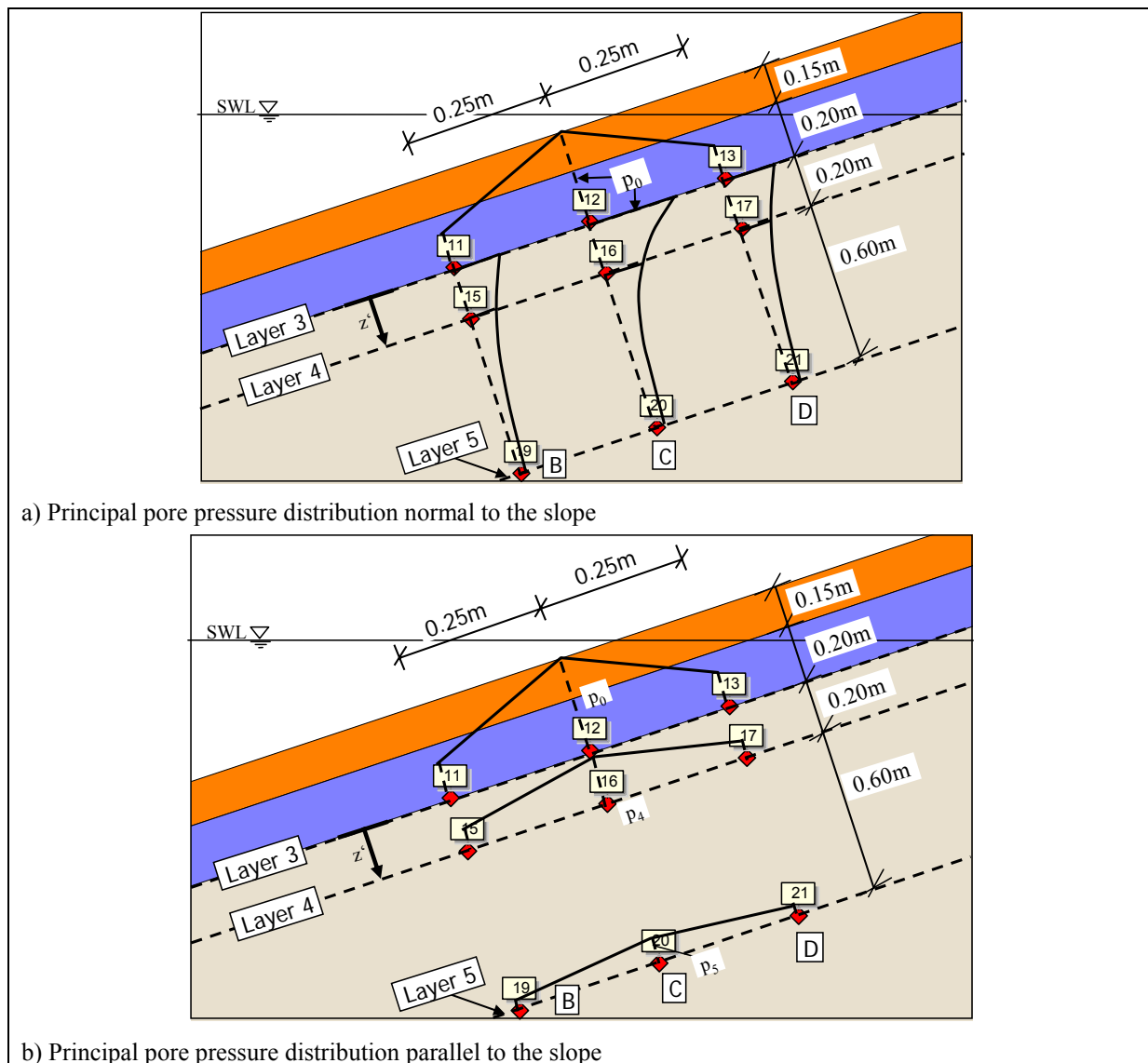
Fig. 6.13: Wave-induced pore pressure distribution in the sand core beneath the revetment (principle-sketches)

Wave-induced pore-pressure beneath the revetment
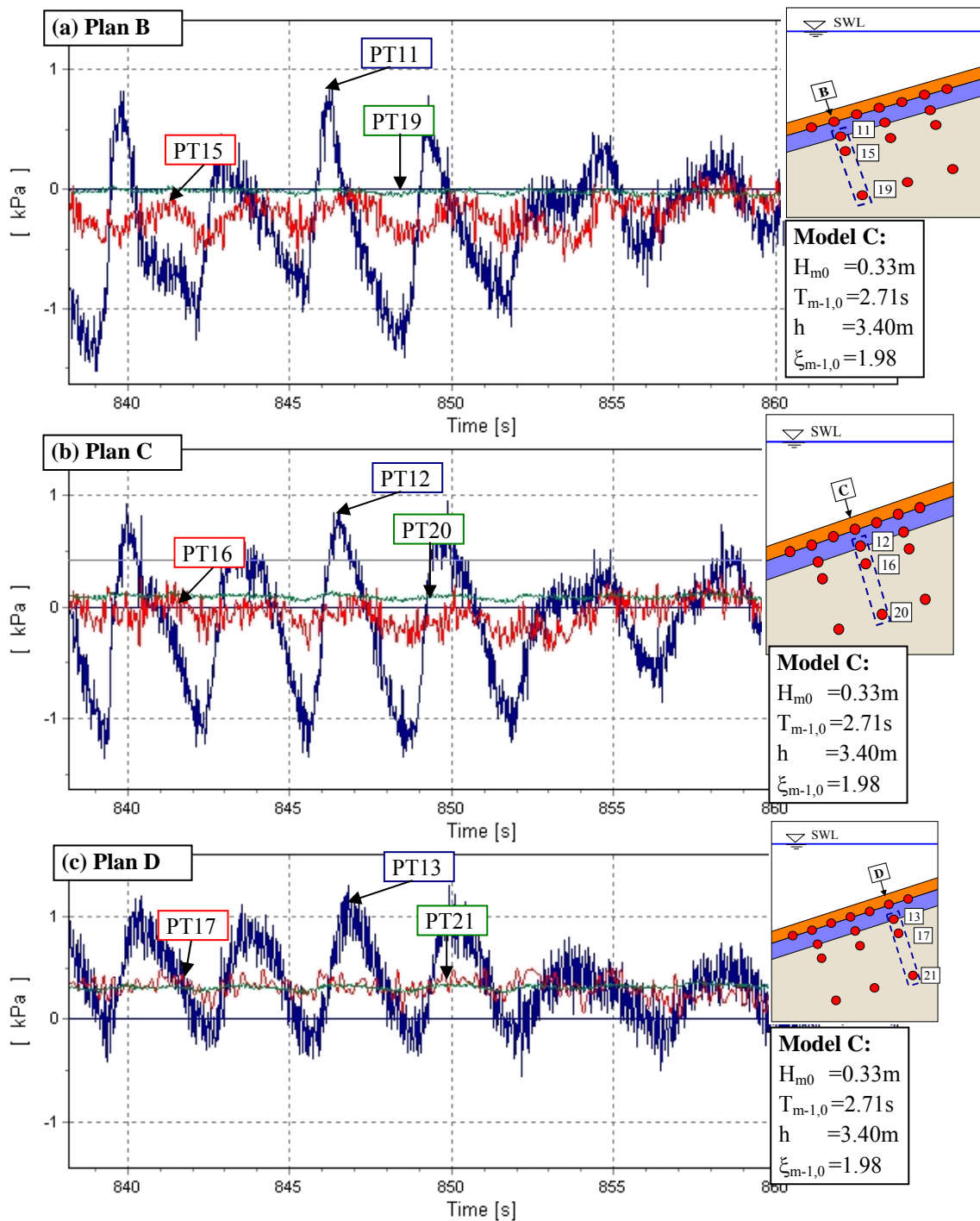
Fig. 6.14: Damping of pore pressures at different depths and locations in the sand core beneath the revetment for <u>impact loads</u> (*Model Alternative* C, test no. 09060804)
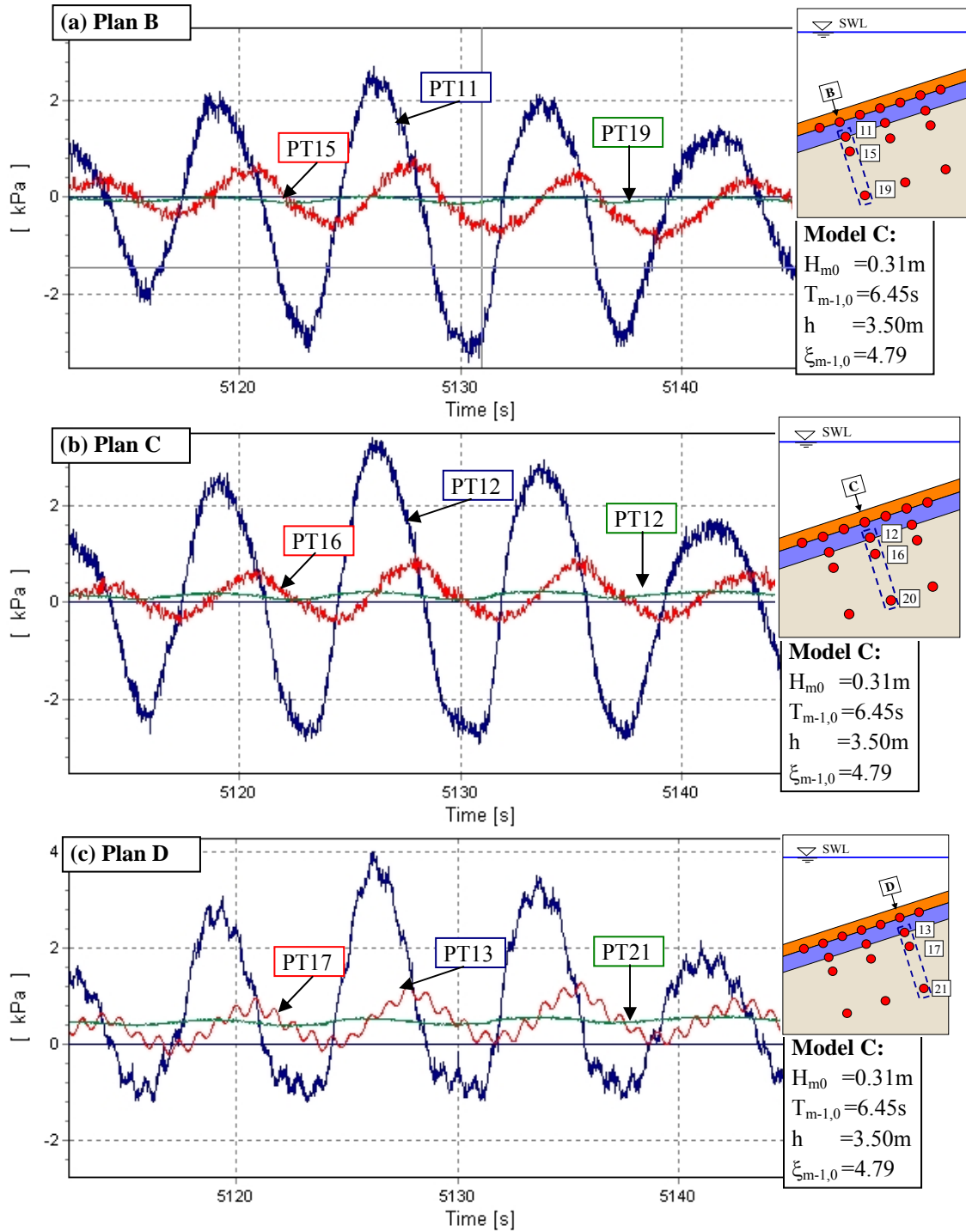
Fig. 6.15: Damping of pore pressure at different depth and locations in the sand core beneath the revetment for <u>non-impact load</u> (*Model Alternative* C, test no. 0906163)

6.1.2.2 *Pore pressure distribution*

In section 6.1.2.1 some differences were identified in terms of the magnitude of the damping at the different locations B, C and D. It is therefore important to examine these differences more closely. For this purpose, the pore pressures at different depths z' in the sand core beneath the revetment related to the corresponding maximum pore pressure $p_{3,max} = p_0$ at layer 3 (z' = 0) for the same location are plotted in Fig. 6.16 including both impact and non-impact load. The results in Fig. 6.16 show that:

(a) The damping of the initial pore pressure p_0 at different depths in the sand core is expectedly higher for larger p_0-values. This implies that the effect of the initial pore pressure p_0 should be accounted for by the prediction formula for pore pressures in the sand core.

(b) Taking the influence of the initial p_0 values on the magnitude of the damping effect, the apparent differences of the latter between locations B, C and D becomes less important, implying that a single prediction formula for the transient pore pressures in the sand core can be developed for different locations along the slope when directly related to the corresponding initial pore pressure p_0.

Since the magnitude of the initial (reference) pressure p_0 at z' = 0 considerably affects the damping of the pore pressure from layer 3 to layer 4 and layer 5 (see Fig. 6.16), $p_{(z')}/p_0$-data are plotted as a function of p_0 in Fig. 6.17 exemplary for location B. The results indeed confirm that the damping strongly increases with increasing p_0-values.

Based on the results in Fig. 6.16 the relative pore pressure data $p_{(z')}/p_0$ are plotted against the relative depth z'/L_0 in the sand core (L_0 = deep water wave length related to $T_{m-1,0}$) in Fig. 6.18, showing that for $z'/L_0 < 0.072$:

- Pore pressure $p_{(z')}$ decreases exponentially with relative depth z'/L_0 in the sand core.

The rate of decrease of $p_{(z')}$ with depth z'/L_0 strongly depends on the magnitude of the initial value p_0 which again depends on the surf similarity parameter $\xi_{m-1,0}$.

Wave-induced pore-pressure beneath the revetment
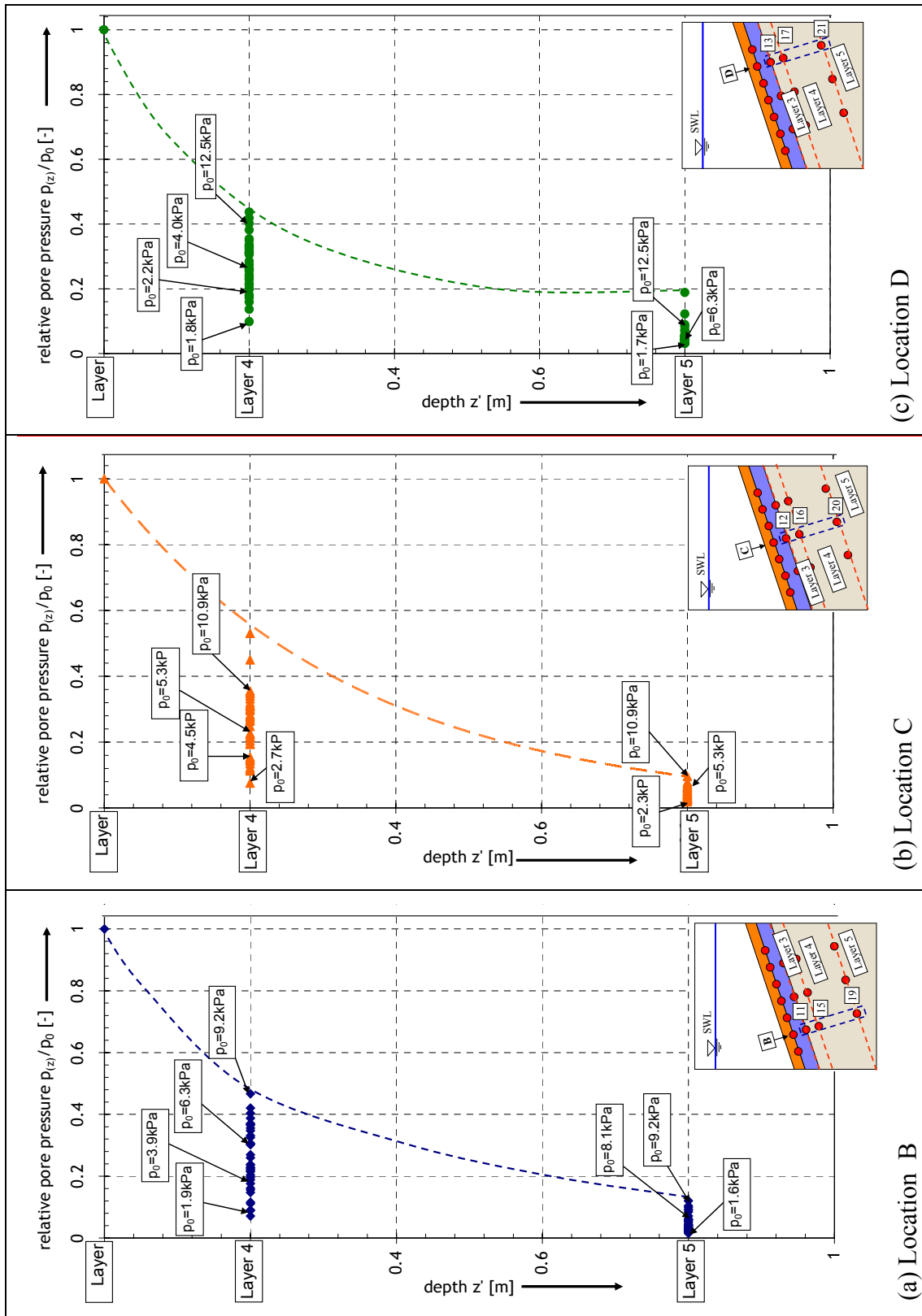
Fig. 6.16: Pore pressure distribution normal to the slope at locations B, C and D (see also Fig. 6.1)
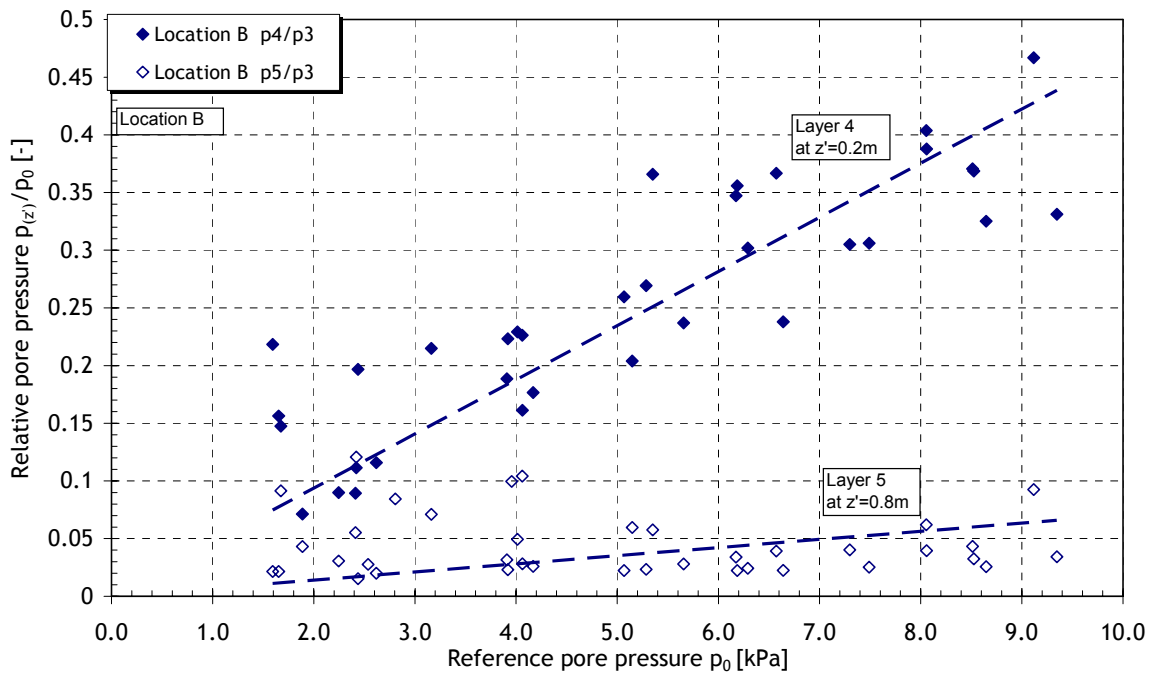
Fig. 6.17: Damping of pore pressure from layer 3 to layers 4 and 5 at location B as a function of the initial pressure p_0 (see also Fig. 6.1)

Finally, the following formulae for the pore pressure distribution normal to the slope may be suggested for $z'/L_0 \le 0.072$, depending on the range of the surf similarity parameter considered:

$$\frac{p_{(z')}}{p_0} = 0.93 \cdot \exp(-125 \cdot z/L_0) + 0.07 \quad \text{for } \xi_{m-1,0} = 1.8 \tag{6.10}$$

$$\frac{p_{(z')}}{p_0} = 0.96 \cdot \exp(-127 \cdot z/L_0) + 0.04 \quad \text{for } \xi_{m-1,0} = 2.0 \tag{6.11}$$

$$\frac{p_{(z')}}{p_0} = 0.975 \cdot \exp(-190 \cdot z/L_0) + 0.025 \quad \text{for } \xi_{m-1,0} = 2.5 \tag{6.12}$$

$$\frac{p_{(z')}}{p_0} = 0.99 \cdot \exp(-350 \cdot z/L_0) + 0.01 \quad \text{for } \xi_{m-1,0} = 4.0 \tag{6.13}$$

Since p_0 represents the initial pore pressure at $z' = 0$ at the considered location along the slope and since Eqs. (6.10)-(6.13) apply for all locations B, C and D (see Fig. 6.13a), the horizontal distribution of the pore pressure in Fig. 6.13b can also be determined using Eqs. (6.10)-(6.13).
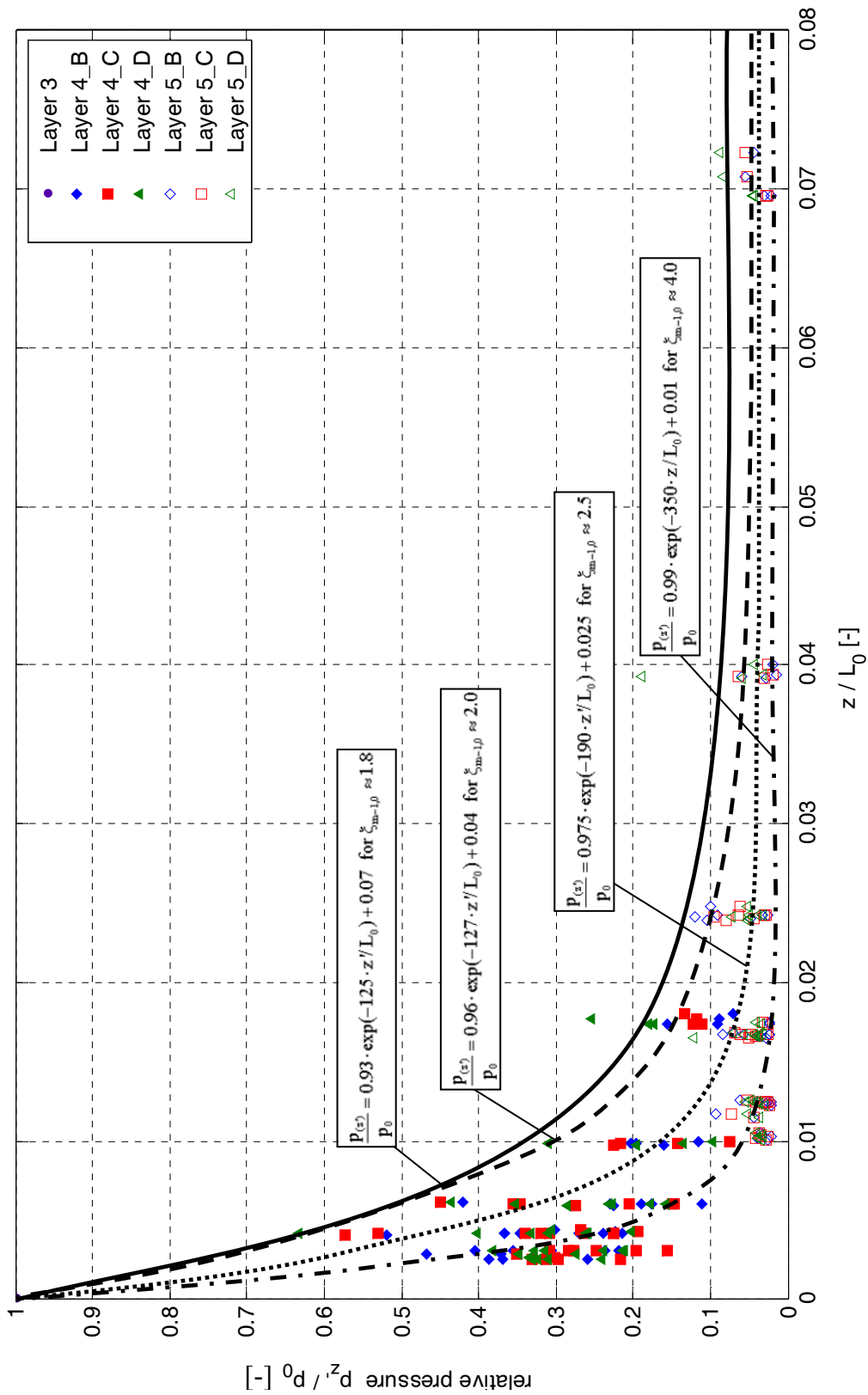
Fig. 6.18: Pressure damping factor $p_{(z)}/p_0$ against z'/L_0 for all layers and all locations

6.2   Residual pore pressure

6.2.1   Pre-processing and preliminary analysis of residual pore pressure

In addition to the pressure transducers which were used in section 6.1.1 (PT11-PT21) for the analysis of the transient pore pressure, four further pressure transducers (PT22-25) were used to record the development of the water table in the sand core underneath the *ELASTOCOAST* revetment for *Model Alternative A* and after the failure of Model A in *Model Alternative C* (see Fig. 6.19). The pressure transducers are located about 1.1 m underneath SWL for a water depth in the flume of h = 4.0m. The most shoreward transducer P26 is located beneath the crest of the revetment.
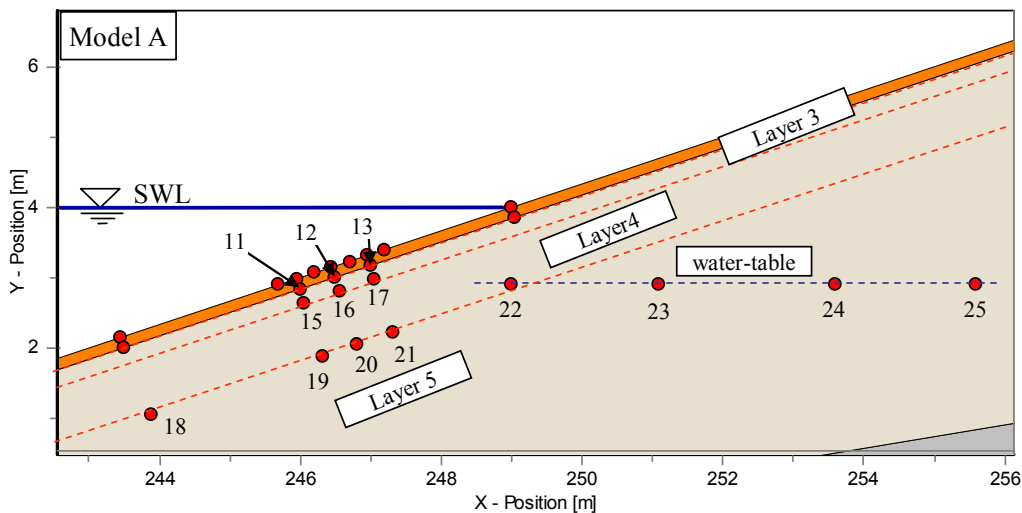
a) *Model Alternative* A (without gravel filter)
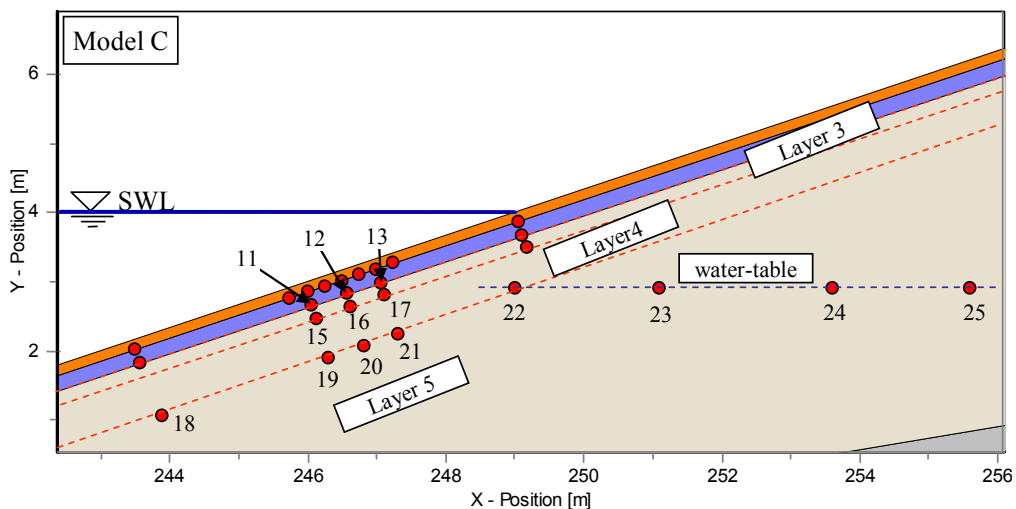
b) *Model Alternative* C (with 0.20 m thick gravel filter)

Fig. 6.19: Definition of layers and locations of pressure transducers used for the analysisi of residual pore pressure

The first step for pre-processing the data was to separate the recorded pressure signal in its oscillating component and mean (residual) component as already mentioned in the introduction of Chapter 6 (see Fig. 6.2). A time series of pressure transducer PT21 for a regular wave test is exemplarily shown in Fig. 6.20a. After the filtering process (f = 0.03 Hz), the two time series in Fig. 6.20b are obtained.
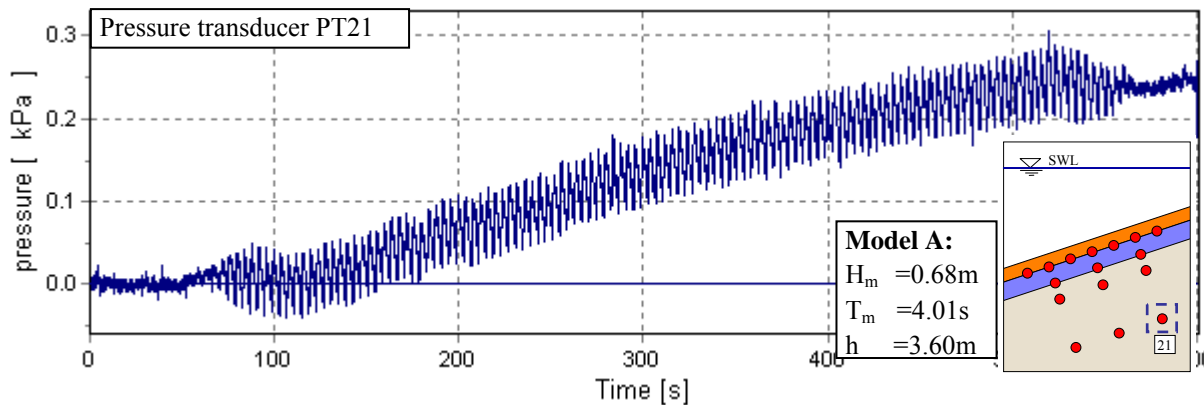
a) Time series of non filtered pore pressure (pressure transducer PT21)
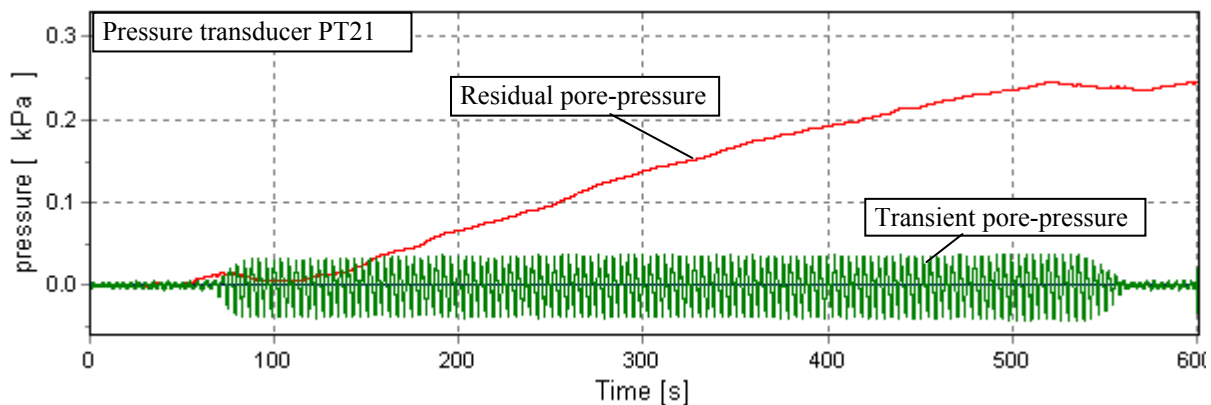
b) Time series of filtered pore pressure with transient and residual component (pressure transducer PT21)

Fig. 6.20: Transient and residual component of pore pressure with regular waves

Fig. 6.21 and Fig. 6.22 show example time series of the pore pressure recorded at PT18-PT25 for regular wave tests (Model A) and irregular wave tests (Model B), respectively. The unfiltered data of pressure transducers PT18-PT25 for a regular wave test, including transient pore pressure are shown in Fig. 6.21a while in Fig. 6.21b only the residual pore pressure for the same test is depicted. The same procedure was adopted for irregular wave tests as shown in Fig. 6.22a and Fig. 6.22b.
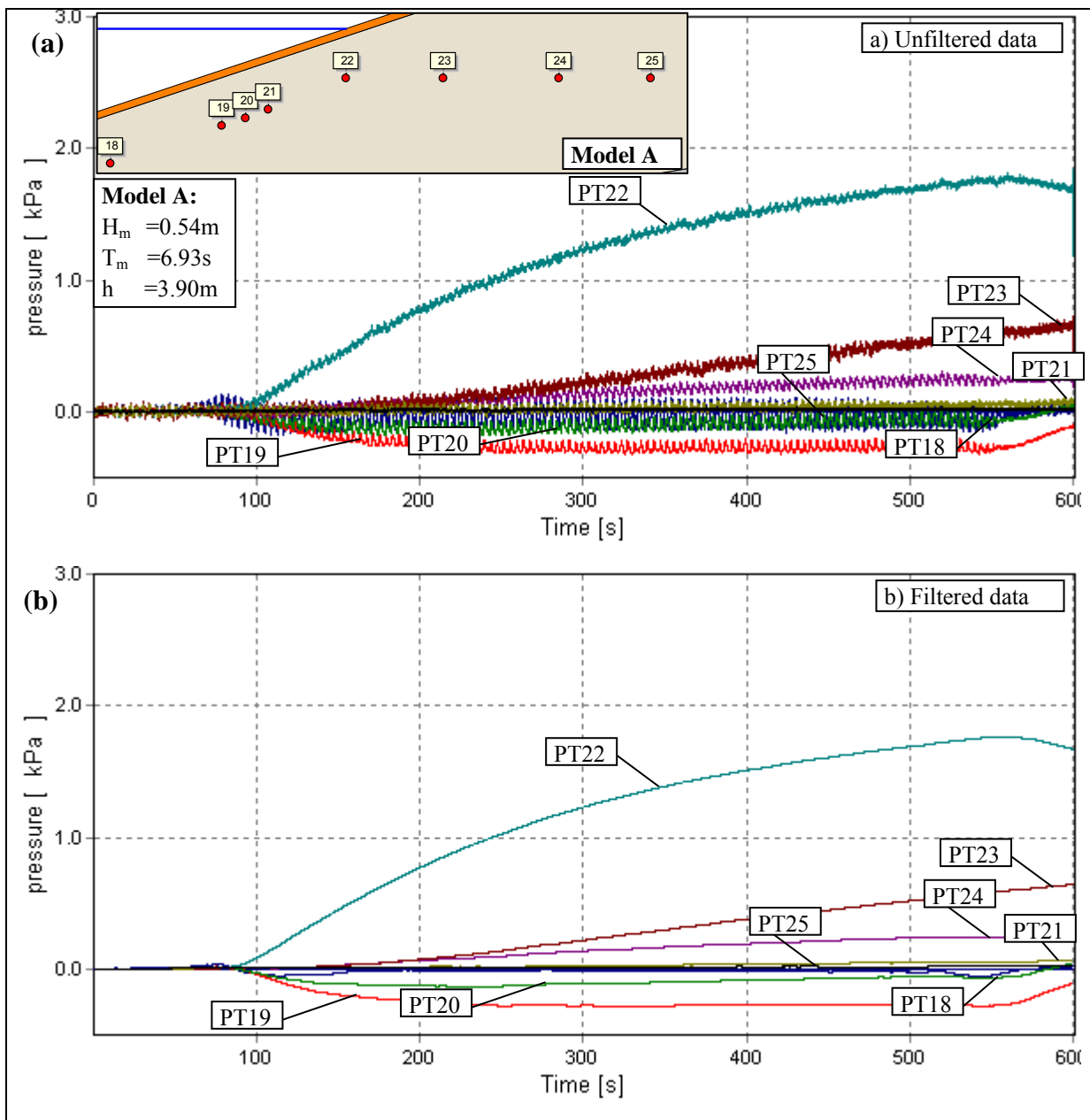
Fig. 6.21: Time series of residual pore pressure recorded at PT18-25 for regular waves (Model A)
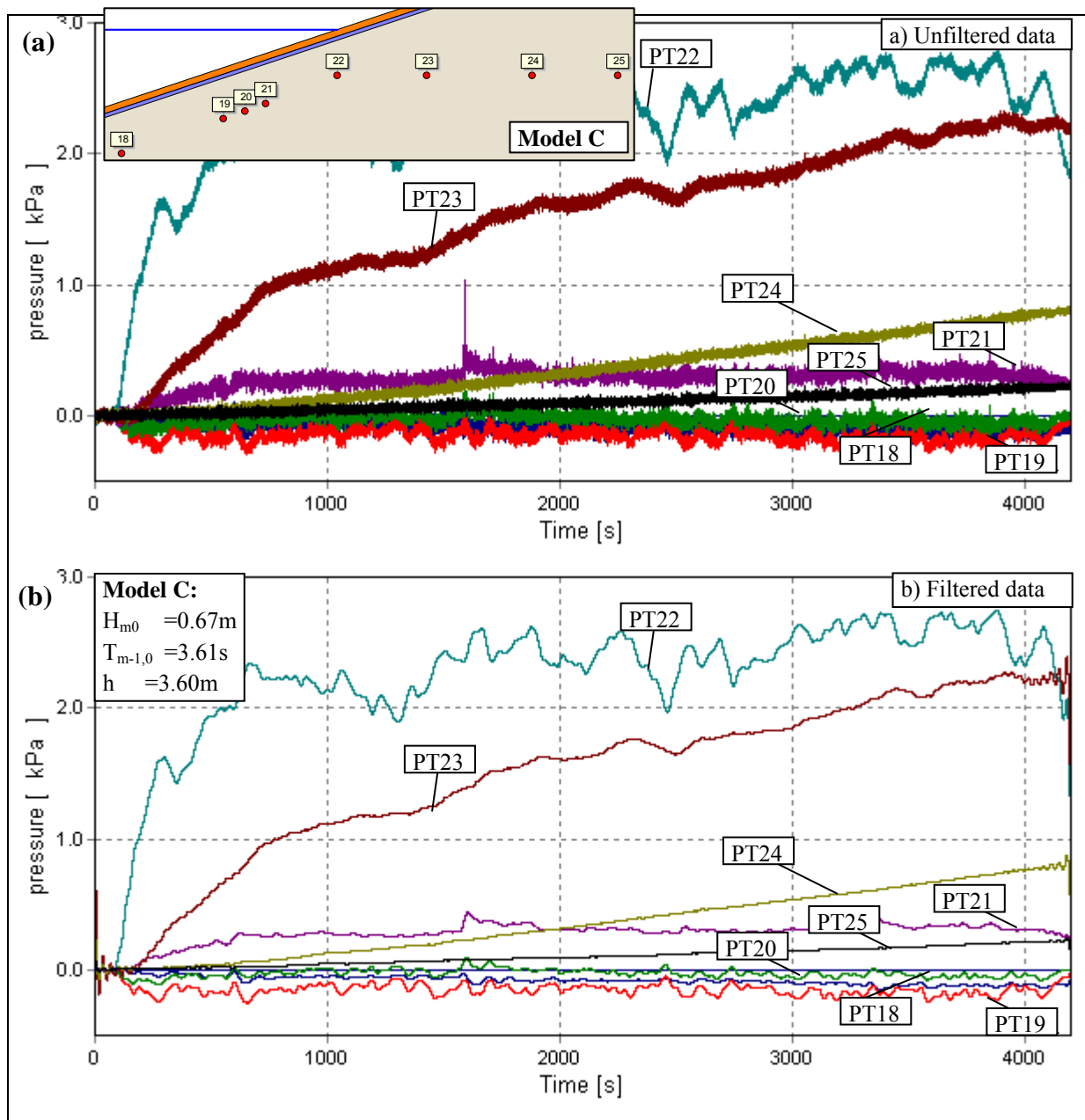
Fig. 6.22: Time series of residual pore pressure recorded at PT18-25 for irregular waves (Model C)

Fig. 6.21 and Fig. 6.22 show that the maximum residual pressure u_r occurs at pressure transducer PT22 for both regular and irregular wave tests. At pressure transducers PT18-PT21 the residual pore pressure is negligibly small. The water tables recorded by Pressure transducers PT18-25 for regular and irregular wave tests with similar wave parameters and similar water depth conditions are plotted in Fig. 6.23a-Fig. 6.23c. Since no similar wave parameters for regular and irregular wave tests were used for one Model, the two different *Model Alternatives A* and *C* were taken for the analysis.
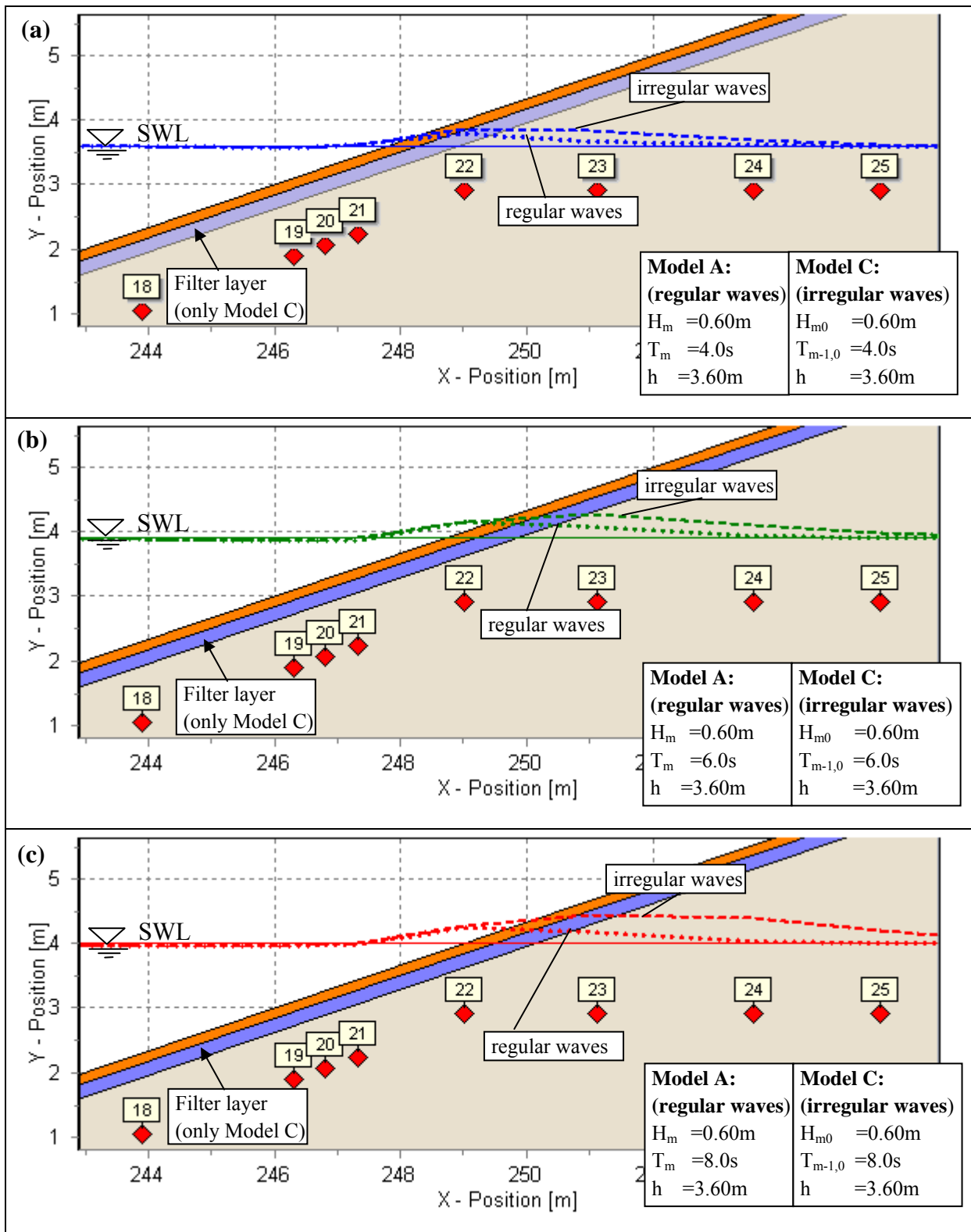
Fig. 6.23: Water table compared for regular and irregular wave tests

Fig. 6.23 shows that the water tables for irregular wave tests are always higher than for regular wave tests. The pressure measured at and shoreward of pressure transducer PT24 is for regular wave tests negligibly small while this is not the case for irregular wave tests with larger water depth (Fig. 6.23b and Fig. 6.23c).

6.2.2   Residual pore pressure distribution

Since it is difficult at this stage of the analysis to develop prediction formulae for the residual pore pressure distribution in a similar way as for the transient pore pressure in section 6.1.1 the following will focus on:

-       providing the distribution of residual pore pressure normal to the slope at locations B, C and D for both *Model Alternatives* B and C (see Fig. 6.1 for definition) based on the analysis of irregular wave tests (Fig. 6.21 and Fig. 6.22). Since PT47 at layer 5 for *Model Alternative* C is damaged the distribution for Location D is missing

-       providing the distribution of residual pore pressure together with the distribution of transient pore pressure normal to the slope at locations B, C and D (see Fig. 6.1 for definition) for both *Model Alternatives* B and C based on the analysis of test 09051602 with regular waves for which the failure of Model A occurred as well as on the analysis of test 09051503 with a similar wave height and a shorter period for which no failure occurred at Models A and B (Fig. 6.26 and Fig. 6.27) The results are used to perform the stability analysis which is required to explain the cause of failure of Model A in Chapter 8.

As seen in Fig. 6.24 for Model B and in Fig. 6.25 for Model C, the residual pore pressure expectedly increases from $u_r = 0$ at the upper boundary of the sand core ($z' = 0$) up to a certain depth z'. Moreover, it is also seen that "positive" residual pore pressure which actually affect soil stability are rather small.

A possible explanation of the occurrence of the negative pore pressure (not considered in the stability analysis) could be the drainage of the sand core in the sand layer beneath the revetment during wave run-down.

However, a more detailed analysis of the associated processes is required in order to physically interpret these results and to develop prediction formulae. This will be performed at a later stage after a more detailed verification of the data.

Wave-induced pore-pressure beneath the revetment
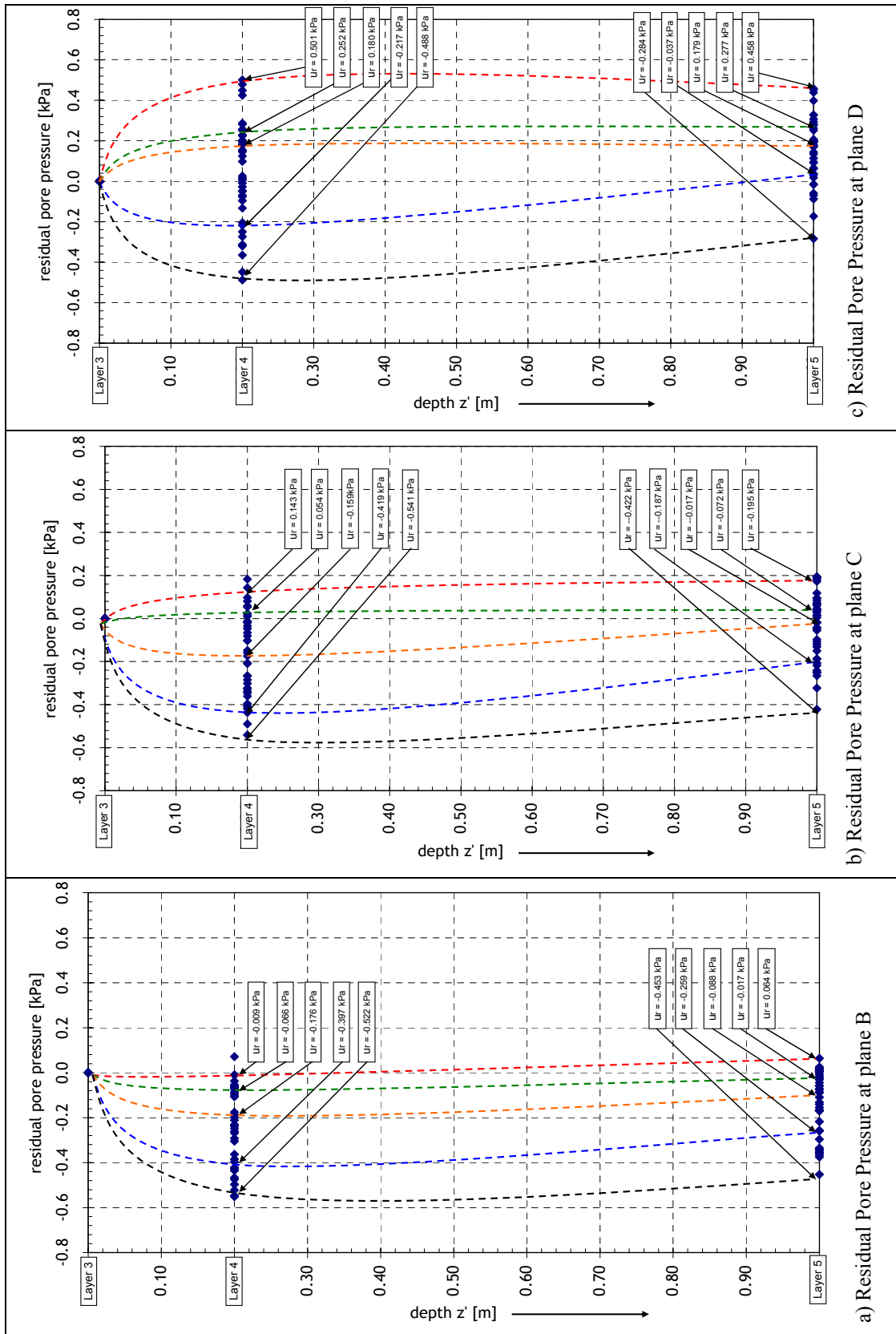
Fig. 6.24: Residual Pore pressure distribution normal to the slope at locations B, C and D for Model Alternative B (see also definition sketch Fig. 6.1)

c) Residual Pore Pressure at plane D

b) Residual Pore Pressure at plane C

a) Residual Pore Pressure at plane B

Wave-induced pore-pressure beneath the revetment
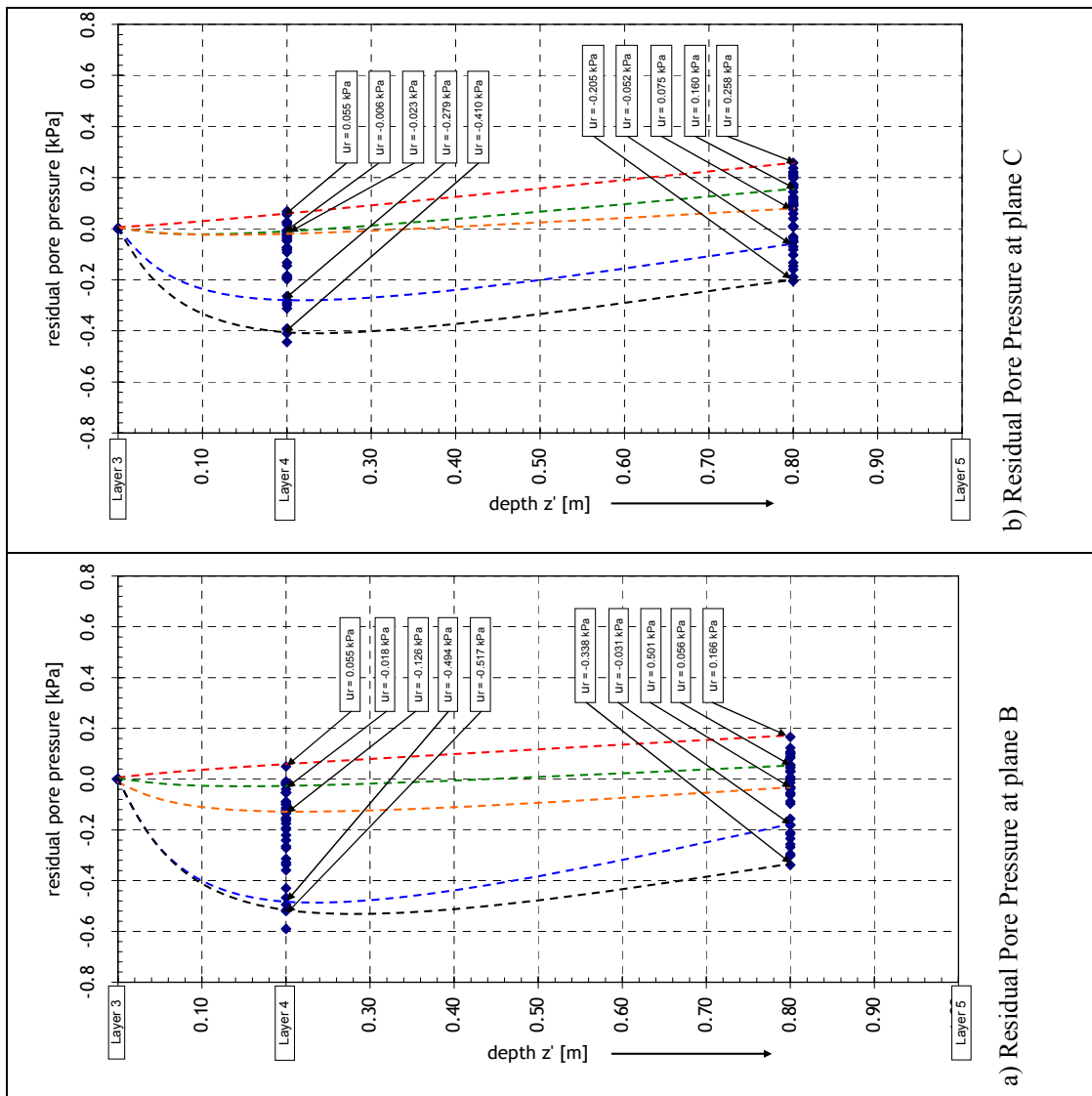
Fig. 6.25: Residual Pore pressure distribution normal to the slope at locations B and C for Model Alternative C

The "positive" pore pressure distributions which affect the stability of the sand core, together with the associated distribution of the transient pore pressure at locations B, C and D for the regular wave test at which the failure of Model A occurred are comparatively drawn in Fig. 6.26 for Models A and B, showing that the residual pore pressures are very small as compared to the uplift pressure gradient (u_0-u_t) resulting from the transient pore pressure (see Fig. 8.11) and are therefore much less relevant for the damage caused to Model A. It is seen that the highest uplift pressure gradient occurs at location B ($u_0-u_t = -6.37$ kPa for Model A and $u_0-u_t = -5.26$ kPa for Model B).

Similar distributions are drawn in Fig. 6.27 for test 09051503 (no failure), showing similar results as in Fig. 6.26 but with smaller uplift pressure gradient (u_0-u_t).
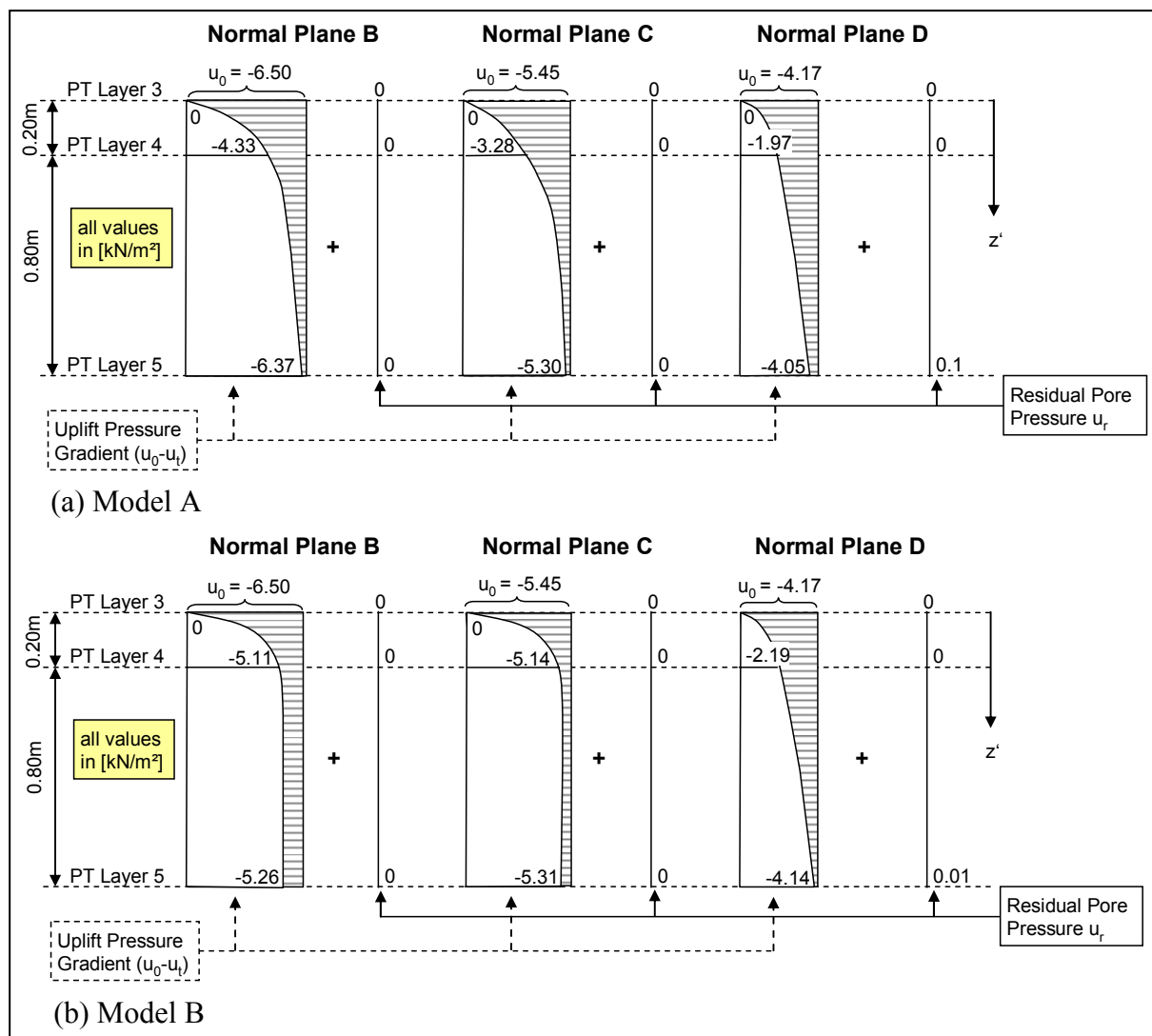
Fig. 6.26: Residual and Transient pore pressure distribution at Position B, C and D for test 09051802 (failure)
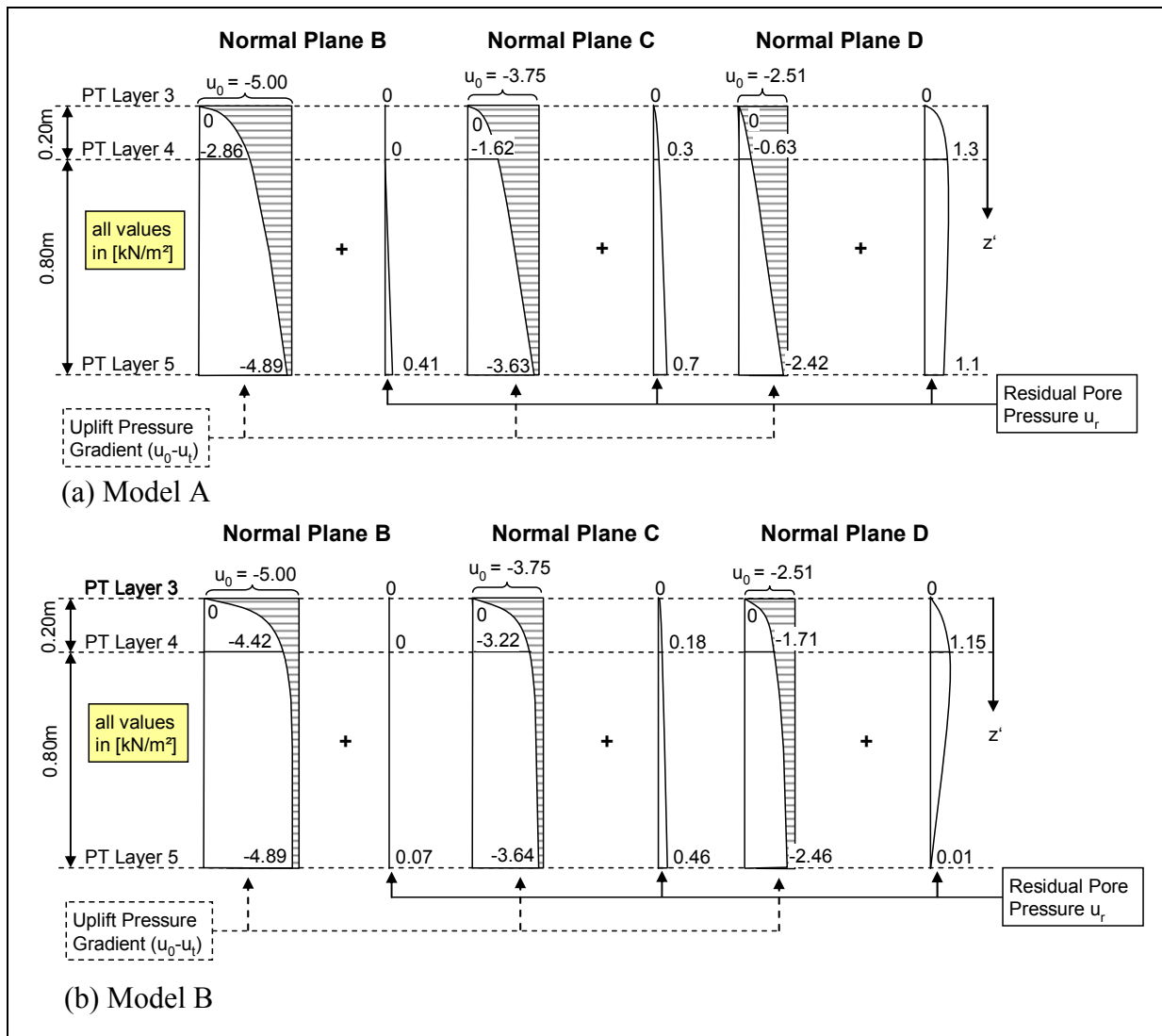
Fig. 6.27: Residual and Transient pore pressure distribution at locations B, C and D for test 09051503 (no failure)

7 Flexural displacement of the *ELASTOCOAST* revetment

The purpose of this chapter is to analyse the flexural displacement recorded by the displacement meters and to derive formulae for the prediction of the magnitude of these displacements as a function of the wave induced pressures p_{max} on the revetment.

7.1 Pre-processing and preliminary analysis

The displacement meters DT01/02 were installed on the revetment at only one location for each of the three *Model Alternatives A, B,* and *C* (see Fig. 7.1). It can be seen that this location is selected where most of the pressure transducers are concentrated, i.e. where the most severe loading conditions were expected. Therefore, it will be possible to directly correlate the displacement measurements with readings from the pressure transducers on the *ELASTOCOAST* revetment.

> *Remark:*
>
> *It should be noted that for Model C no pressure transducers were installed on the revetment as indicated in Fig. 7.1. Hence, for further analysis, the pressure transducers from Model B were considered to analyse the displacements observed in Model C.*

As already stated in Section 2.2.5, the displacement meters are very sensitive to high water pressures and sediments, so that the devices are located in a certain distance to the surface of the revetment. The motions were transferred by a stiff aluminium tube from the surface to the transducer which is fixed at a crossbeam spanning the flume (see Fig. 2.28a and Fig. 2.28b). Care was taken so that only displacements normal to the revetment are recorded.

Remark: Alternative C did not have pressure transducers installed on the top of the *ELASTOCOAST* revetment. Therefore, for later comparison to wave-induced pressures the displacements measured at Alternative C were correlated to pressures measured at Alternative B.
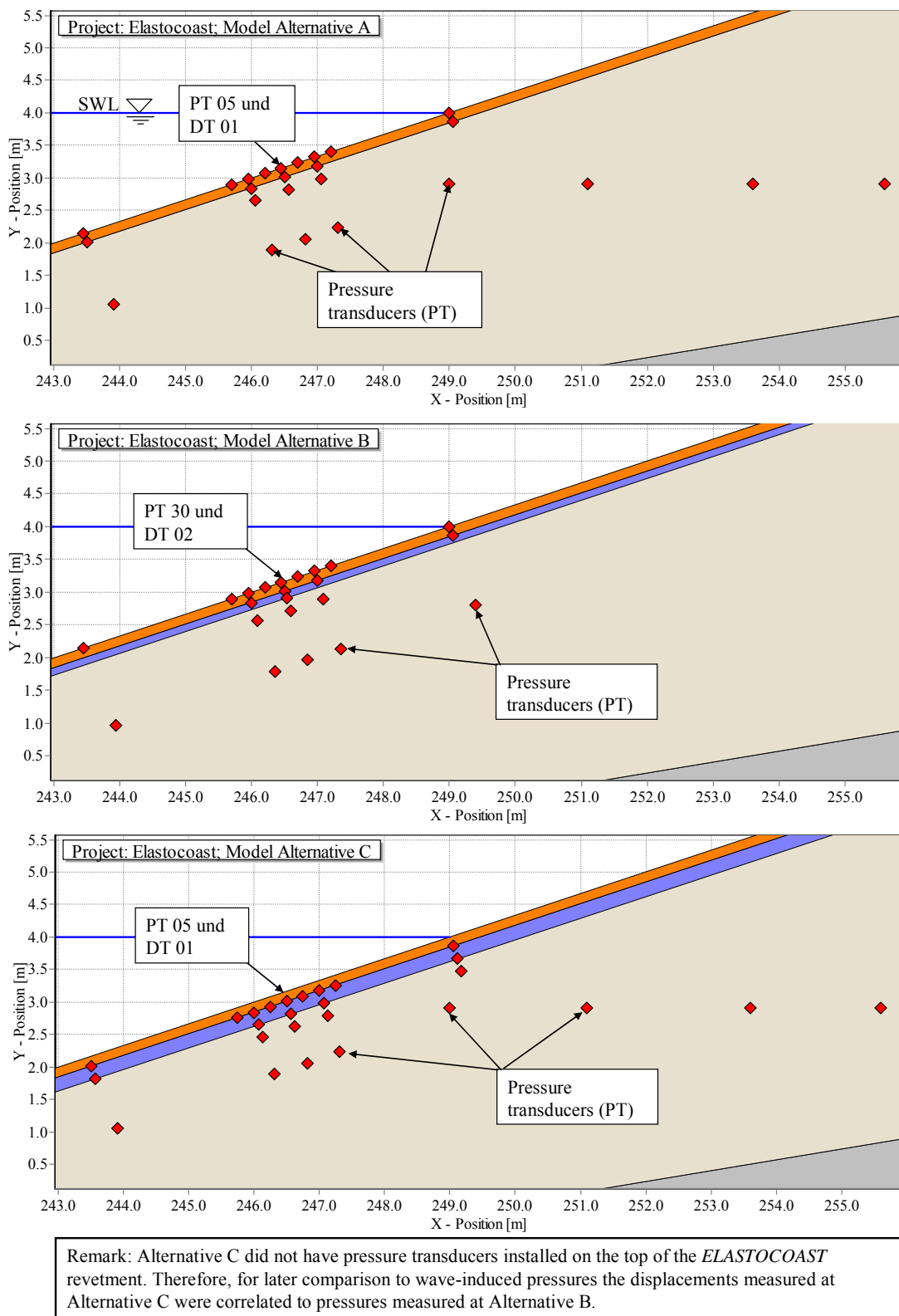
Fig. 7.1: Location of the displacement meter (DT) and pressure transducers (PT) for each of the configurations Alternative A, B, and C

In a first step, typical time series of the displacement transducers were plotted together with the time series of the nearest pressure transducers. The unfiltered signals were checked to identify possible high frequency noises or problems during measurements for regular and irregular wave tests as well as for impact and non-impact loading cases. Fig. 7.2- Fig. 7.5 show displacement signals with different filters (20 Hz and 5 Hz). The time series of the displacement signals filtered with 20 Hz clearly show high oscillations at the time when the wave hits the aluminium tube. These oscillations are of the same frequency for each of the waves (also in different tests) which suggests that they result from the fixation devices (fixation tube, cross beam, etc.) and/or amplifiers. A more detailed analysis of this phenomenon showed that the only suitable explanation is that the fixation tube is oscillating and hence results in an additional unwanted signal. However, this type of signal can be overcome by filtering the high frequency components. Therefore, the frequency of this oscillation (10 Hz) which is outside the range of wave relevant frequencies is filtered out.

The wave trough (see Fig. 7.2-Fig. 7.5) clearly shows the relation between pressures on the revetment and flexural displacements. When the wave trough is reached the revetment moves upwards (in positive direction) until the next wave crest rapidly approaches. This wave crest hits the aluminium tube which induces a small spike on top of the 'displacement crest' which is reached at the time of the wave trough. This spike suggests that the revetment is moving upwards when the wave hits the revetment. Since this cannot be the case here, the only explanation is that the aluminium beam is slightly moving sideward and thus decreasing its length which has then led to a larger signal.

Consequently, the preliminary analysis of the displacement signals has shown that (i) the high oscillations from the aluminium tube have to be filtered out, (ii) the spikes on top of the displacement crests when the wave hits the tube have to be ignored; and (iii) a displacement δ which corresponds to the same window in which p_{max} has to be considered. Displacement δ is hence defined as the entire height of the signal, i.e. from the displacement trough to the displacement crest (Fig. 7.6b).

To illustrate this and further definitions which will be used in further analysis definition sketches are given in Fig. 7.6 by considering exemplary three wave events from one test for *Model Alternative A*. The pressure events I ($p_{max,i}$ for impact component and $p_{stat,i}$ for quasi-static component) and the associated magnitude of the displacement δ_i are defined in Fig. 7.6a and Fig. 7.6b, respectively.
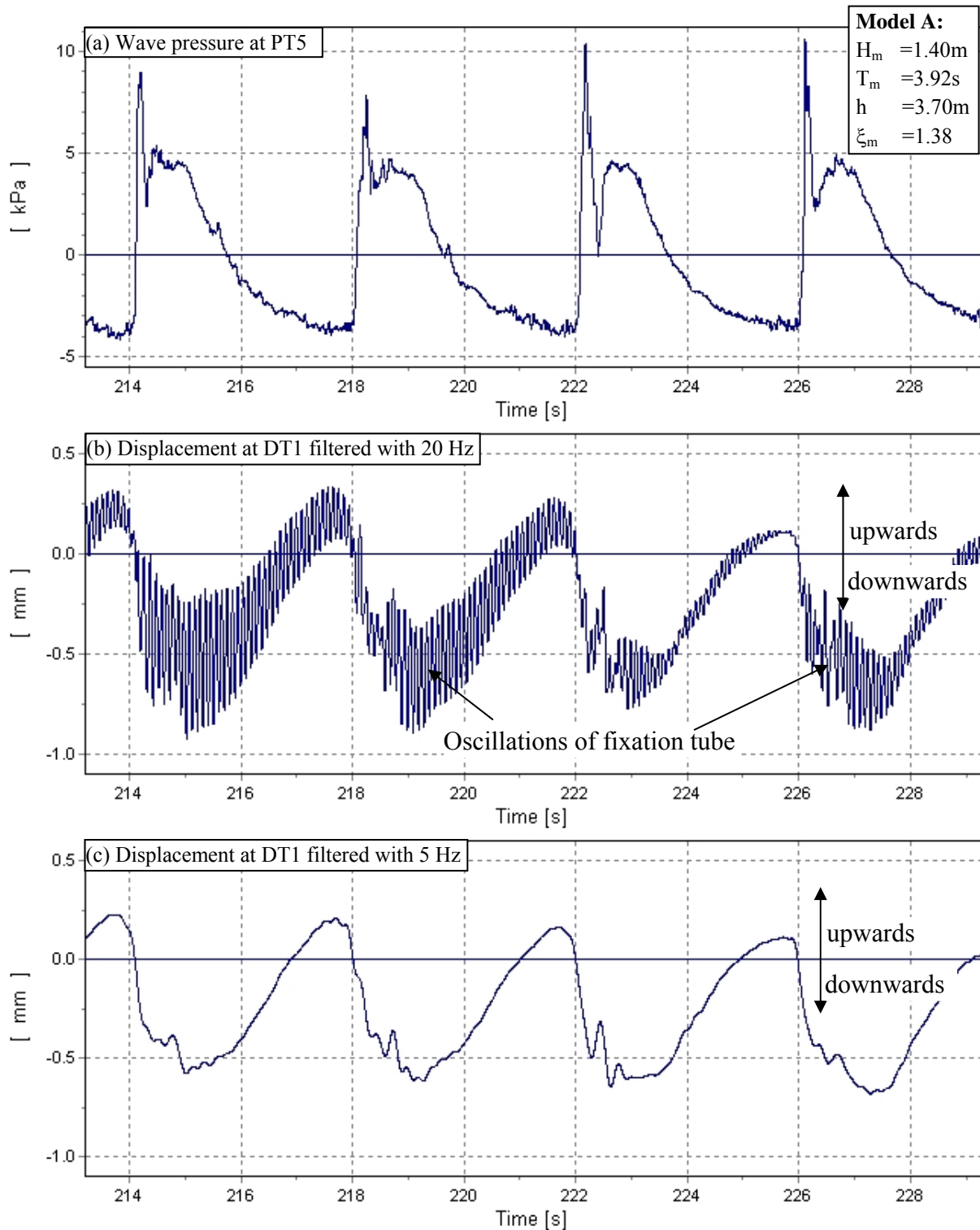
Fig. 7.2: Pressure and displacement time series on the revetment with different filters for impact loads, regular waves (Model A) (see also Fig. 7.1a)
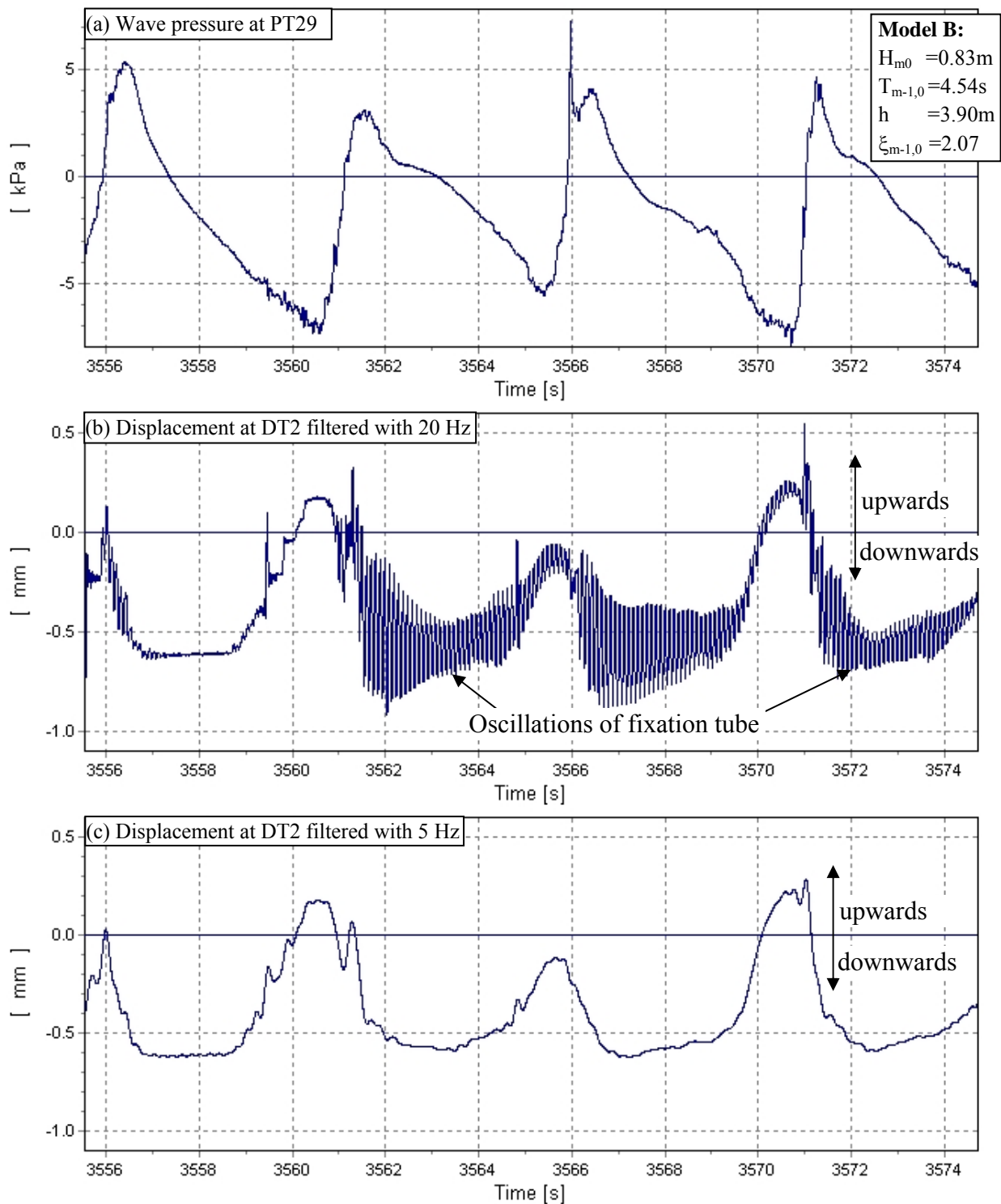
Fig. 7.3: Pressure and displacement time series on the revetment with different filters for <u>impact loads, irregular waves (Model B)</u> (see also Fig. 7.1b)
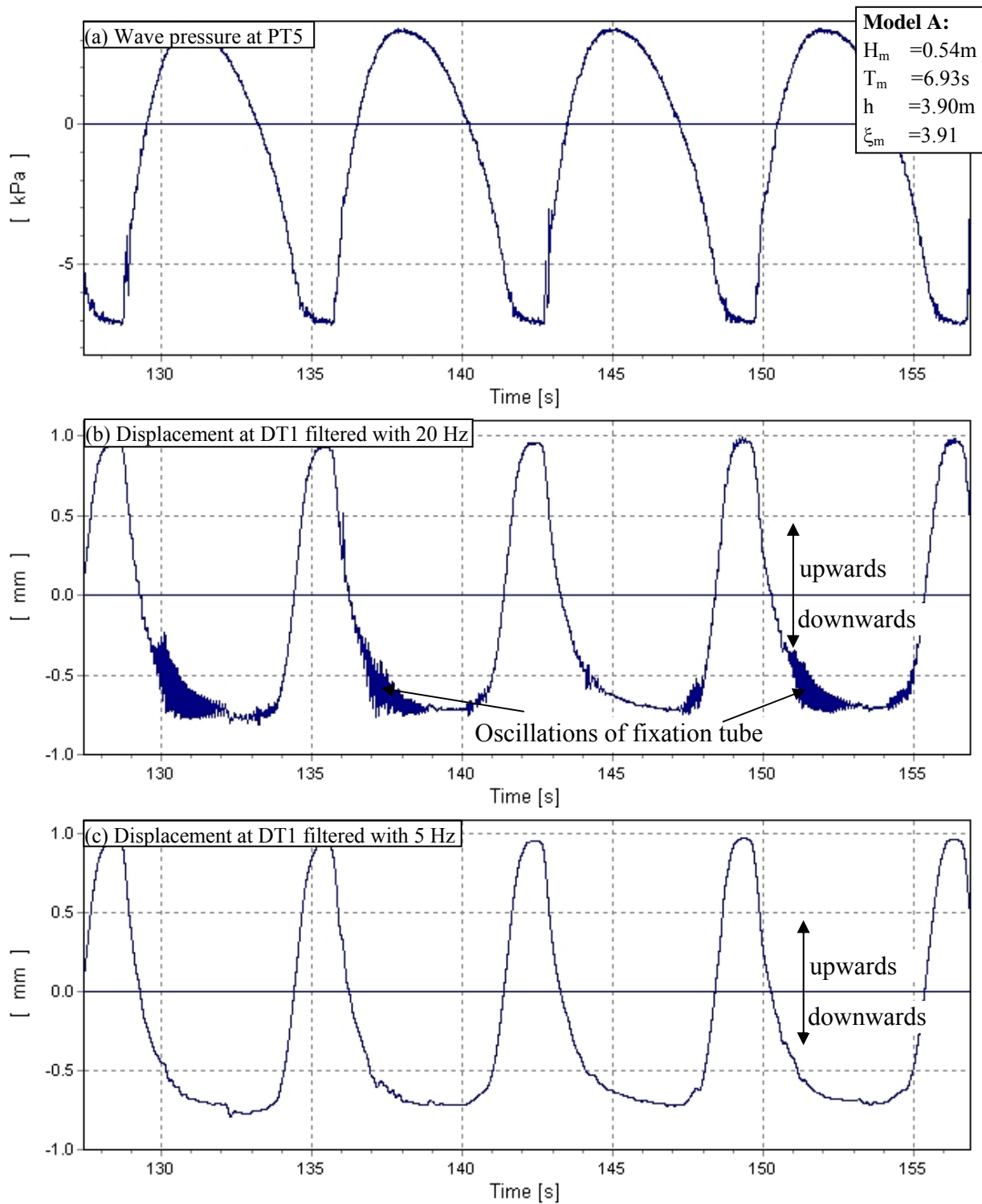
Fig. 7.4: Pressure and displacement time series on the revetment with different filters for <u>non-impact loads, regular waves (Model A)</u> (see also Fig. 7.1a)
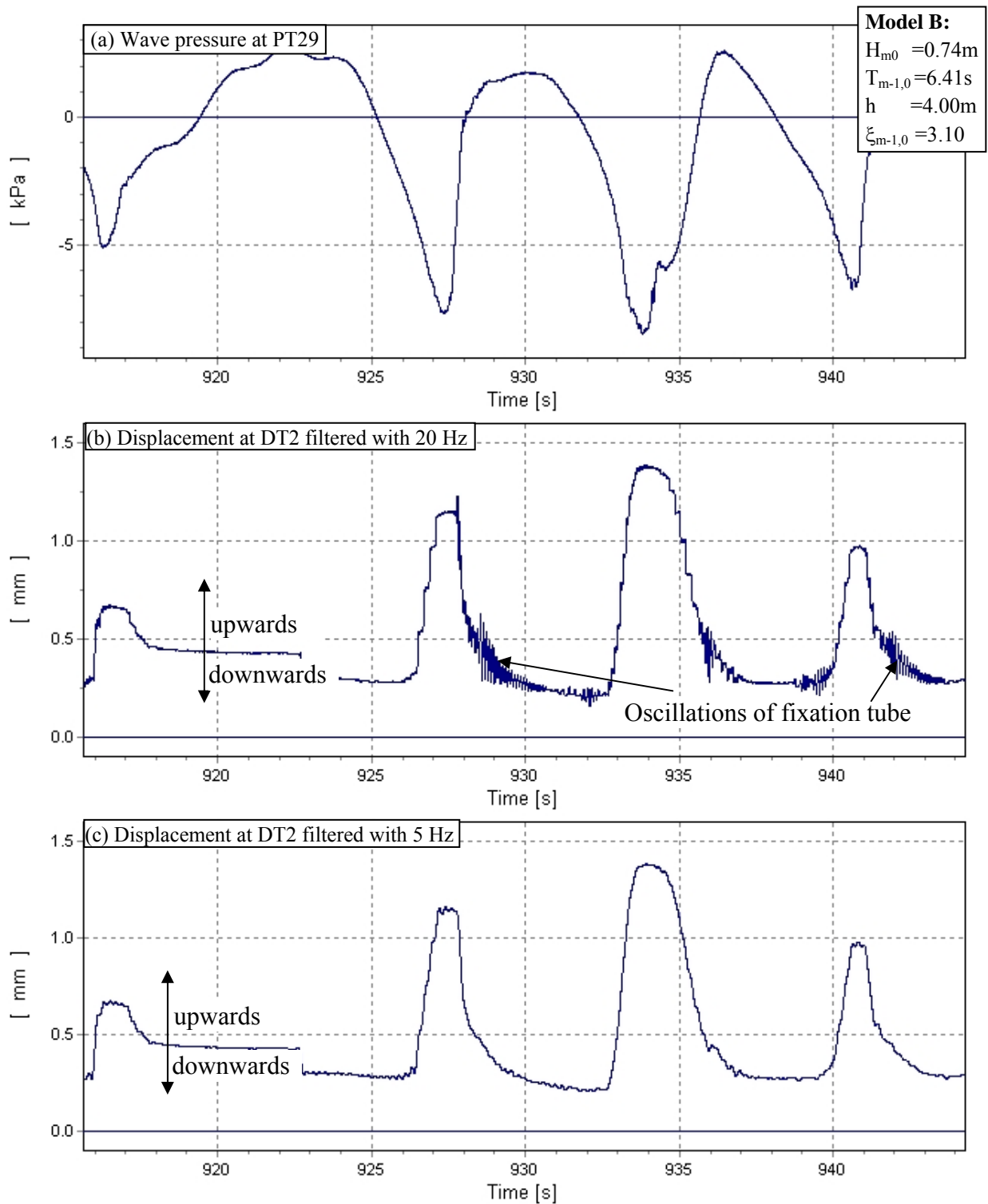
Fig. 7.5: Pressure and displacement time series on the revetment with different filters for <u>non-impact loads, irregular waves (Model B)</u> (see also Fig. 7.1b)
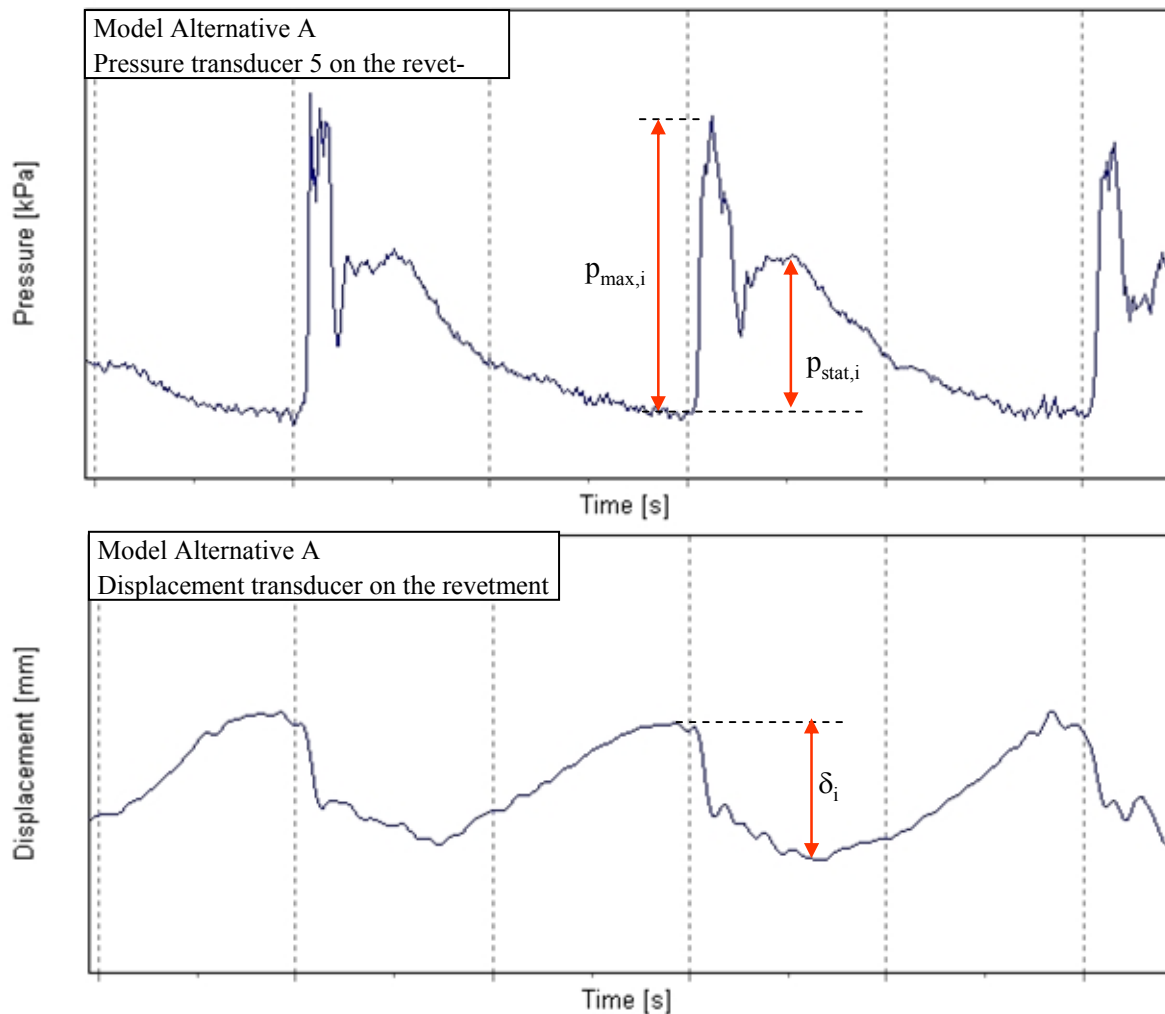
Fig. 7.6:   Definition of pressure event I ($p_{max,i}$ and $p_{stat,i}$) and associated δ_i

7.2   Maximum wave-induced displacements

Most of the tests were used for the analysis of the flexural displacement of *Model Alternatives A, B* and *C*.

For Model A the maximum displacement δ [mm] are plotted in Fig. 7.7 against maximum pressures on the revetment p_{max} for regular waves (p_{max} values taken from results in Chapter 5 for Model A). The range of surf similarity parameters ($\xi = 1.22 - 1.58$) is also given in the legend of the data points, indicating that the impact load is considerable (Fig. 7.7).

For Models B and C, similar plots for impact loads are given in Fig. 7.8 and Fig. 7.9. Since these models were tested with regular waves (RW) and irregular waves (WS), both types of wave tests are considered.
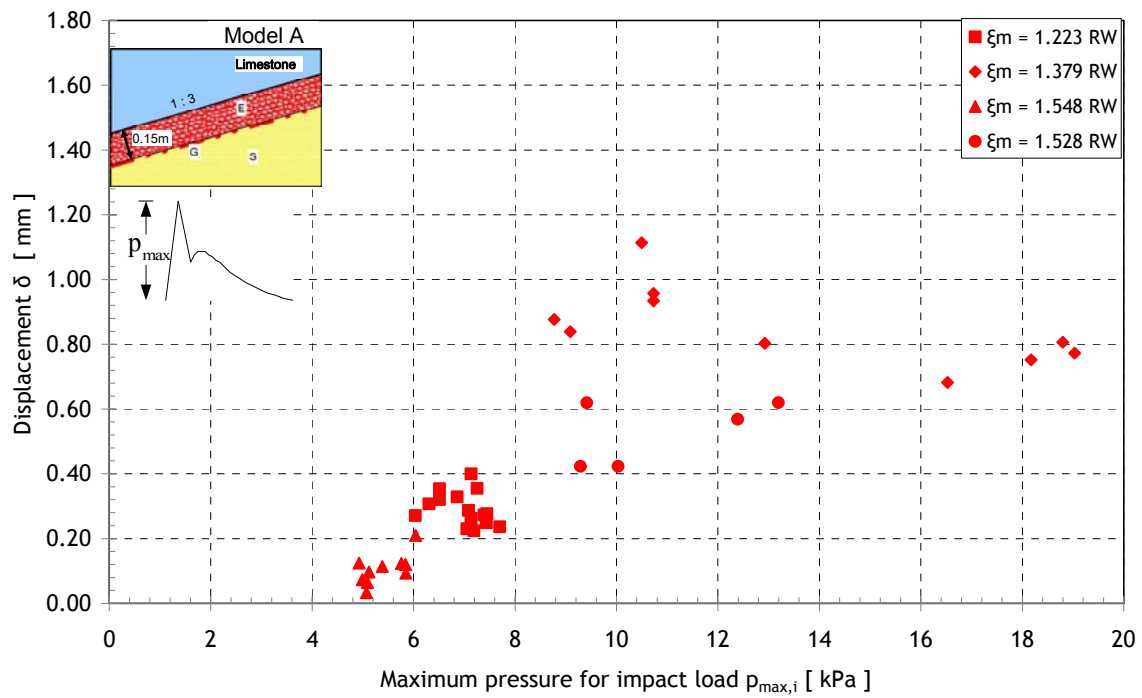
Fig. 7.7: Maximum displacements in all tests of Model A against maximum recorded pressures $p_{max,i}$ for impact loads on top of the revetment (regular waves)
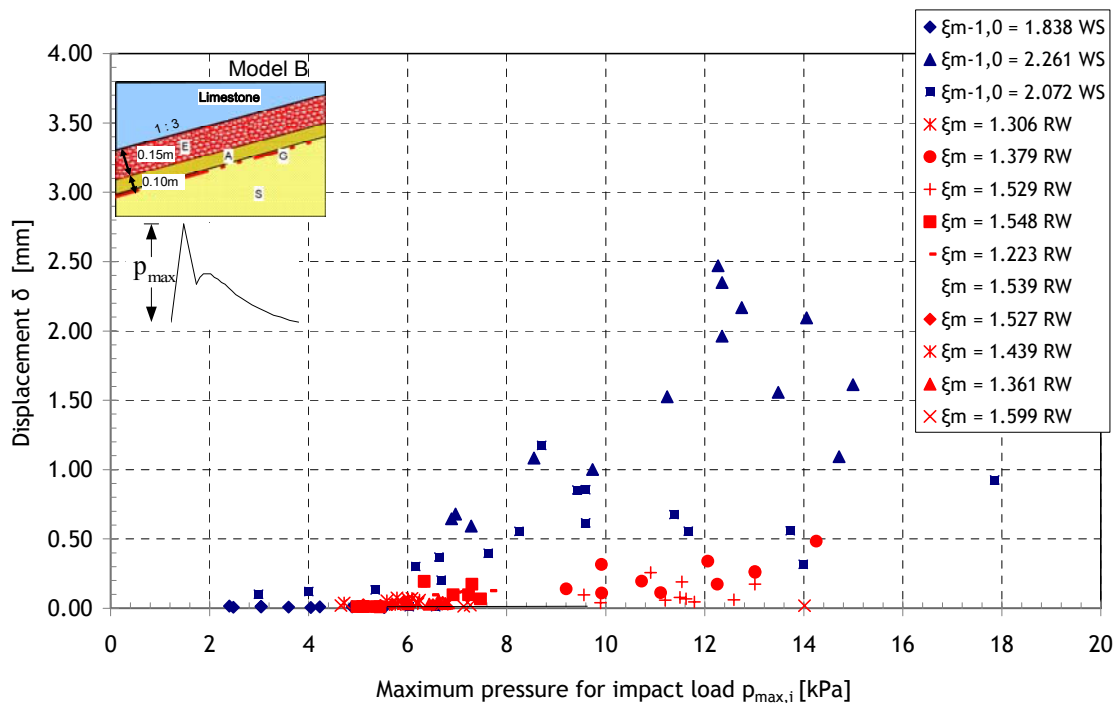
Fig. 7.8: Maximum displacements in all tests of Model B against maximum recorded pressures $p_{max,i}$ for impact loads on top of the revetment
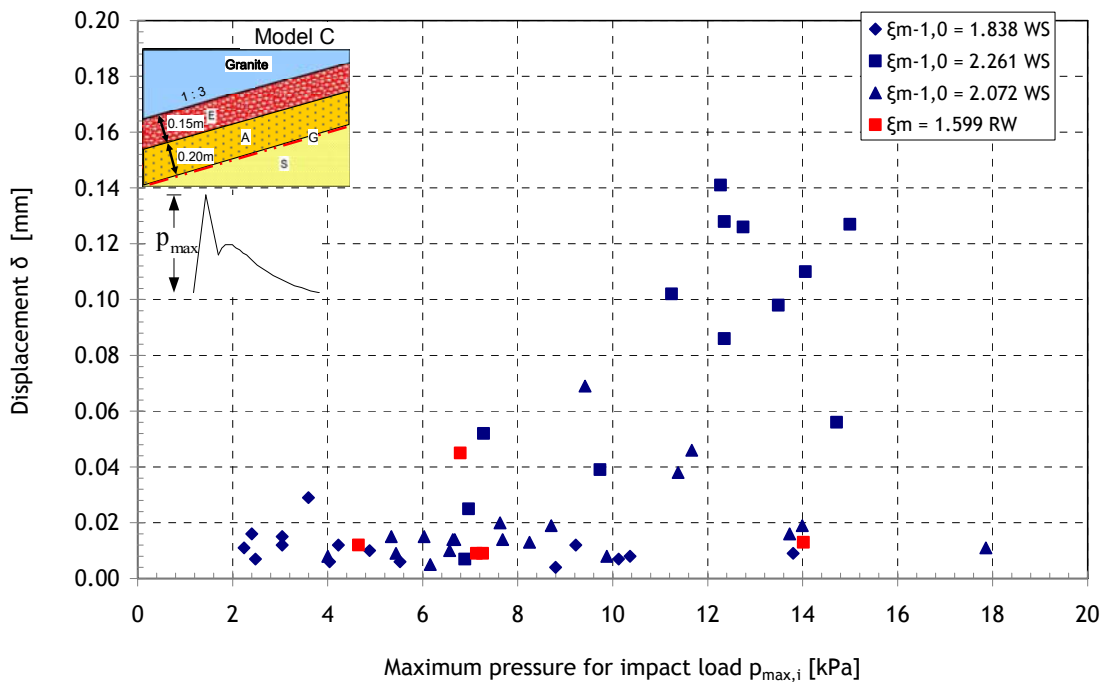
Fig. 7.9:   Maximum displacements in all tests of Model C against maximum recorded pressures $p_{max,i}$ for impact loads on top of the revetment

As expected, higher wave loads generally induce higher displacements (Fig. 7.7 - Fig. 7.9). However, a closer examination shows that the extreme pressure peaks of the impact load component are not necessarily associated with larger displacements of the revetment. This has been observed for both regular wave and random wave tests. The result suggests that these impact pressures might be too short to cause any significant displacement of the revetment. Hence, two alternatives for further analysis might be considered: (i) the duration of the wave pressures needs to be taken into account thus leading to a pressure impulse or (ii) only the quasi-static pressure p_{stat} is considered to cause significant displacements of the revetment.

Further analysis has shown that the duration of impacts for the tests performed is generally too short to cause any significant displacement of the revetment. Therefore, the first option is considered not relevant for this investigation and the second option is adopted.

In Fig. 7.10 - Fig. 7.12 maximum displacement δ [mm] is plotted versus quasi-static pressure p_{stat} [kPa] for all analysed regular and irregular wave tests for *Model Alternatives A, B and C*. It should be noted again that the pressures $p_{stat,i}$ used for the analysis of Model C are taken from Model B since no pressure measurements were performed in Model C in this case. For easier identification of data points, different tests are marked by different symbols.
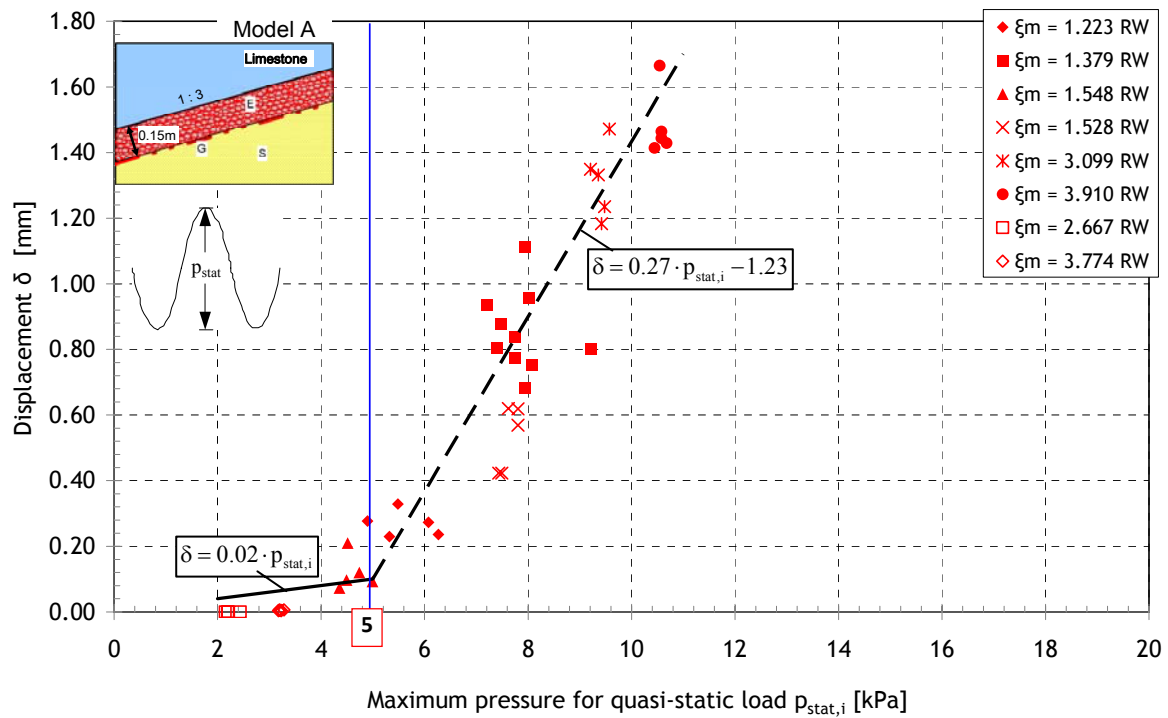
Fig. 7.10: Maximum displacements in all tests of Model A as a function of the maximum recorded quasi-static pressures $p_{stat,i}$ on top of the revetment (regular waves)
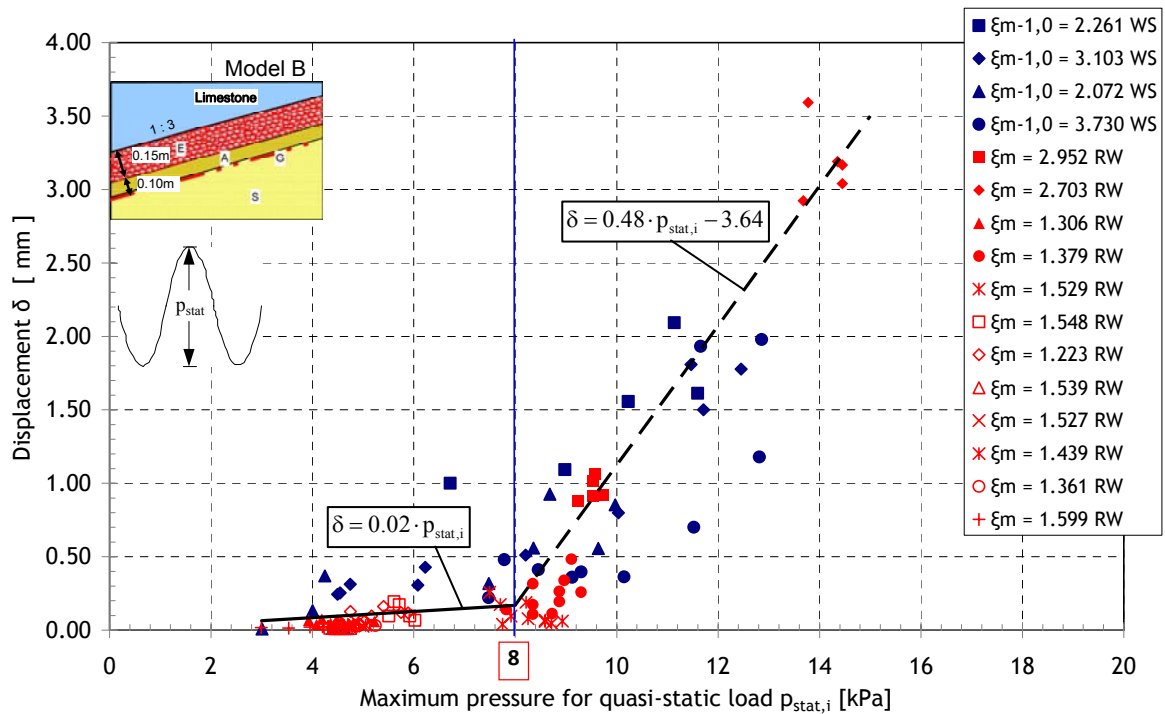
Fig. 7.11: Maximum displacements in all tests of Model B as a function of the maximum recorded quasi-static pressures $p_{stat,i}$ on top of the revetment (regular and irregular waves)
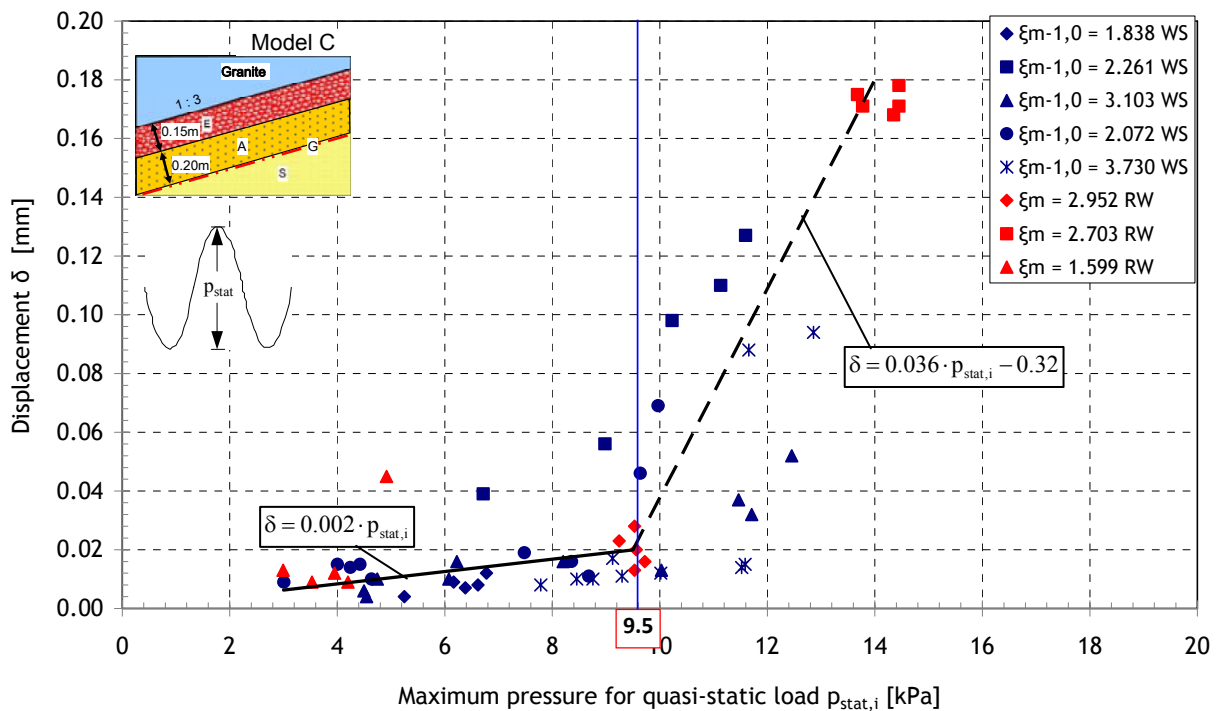
Fig. 7.12: Maximum displacements in all tests of Model C as a function of the maximum recorded quasi-static pressures $p_{stat,i}$ on top of the revetment (regular and irregular waves)

The results for quasi-static load in Fig. 7.10 - Fig. 7.12 show a much better correlation than for impact load in Fig. 7.7 - Fig. 7.9. The maximum displacements increase with increasing maximum quasi-static pressures, the relation seems to follow a linear behaviour. The displacements caused by quasi-static load are comparatively larger than those caused by impact loads.

In relation to Model A (regular waves), the following observations can be made:

- The increase of displacements of Model B and Model C starts later (i.e. with larger pressures) as compared to Model A results (about 8 kPa for Model B and 9.5 kPa for Model C)
- The absolute displacements of Model C are much smaller than for Model B and for Model A. For Model C, the maximum displacements observed are only up to about 0.2 mm whereas values close to 4.0 mm in case of Model B and close to 1.8 mm for Model A are reached. The displacements of Model C are hence about an order of magnitude smaller than for Model B and A.
- The maximum displacements seem to linearly increase with increasing maximum quasi-static pressure $p_{stat,i}$ up to certain threshold p_{stat} values which are 5 kPa (Model A), 8 kPa (Model B) and 9.5 kPa (Model C) as shown in Fig. 7.10 to Fig. 7.12. Beyond this threshold value, the rate of linear increase of displacement δ with increasing p_{stat} becomes much larger.

The different displacement behaviours of *Model Alternatives A, B* and *C* are certainly due to the presence and thickness of the filter layer beneath the *ELASTOCOAST* revetment since the thickness of the latter is the same (0.15 m) for the three model alternatives.

Based on the results in Fig. 7.10 to Fig. 7.12 the following relationship between the maximum displacements δ [mm] of the revetment and the maximum quasi-static pressures $p_{stat,i}$ [kPa] on the revetment are proposed for the three model alternatives:

- *For Model Alternative A:*

$$\delta = 0.27 \cdot p_{stat,i} - 1.23 \quad \text{for } p_{stat,i} > 5 \text{ kPa} \tag{7.1}$$

$$\delta = 0.02 \cdot p_{stat,i} \qquad \text{for } p_{stat,i} < 5 \text{ kPa} \tag{7.2}$$

- *For Model Alternative B*:

$$\delta = 0.48 \cdot p_{stat,i} - 3.64 \quad \text{for } p_{stat,i} > 8 \text{ kPa} \tag{7.3}$$

$$\delta = 0.02 \cdot p_{stat,i} \qquad \text{for } p_{stat,i} < 8 \text{ kPa} \tag{7.4}$$

- *For Model Alternative C:*

$$\delta = 0.036 \cdot p_{stat,i} - 0.32 \quad \text{for } p_{stat,i} > 9.5 \text{ kPa} \tag{7.5}$$

$$\delta = 0.002 \cdot p_{stat,i} \qquad \text{for } p_{stat,i} < 9.5 \text{ kPa} \tag{7.6}$$

For all equations (Eqs. (7.1) to (7.6)) which are inhomogeneous in terms of dimension, the displacement δ is in [mm] and the pressure $p_{stat,i}$ in [kPa].

All results of the displacement analysis of the *ELASTOCOAST* revetment are summarized in Fig. 7.13 comparing the displacement behaviour of the three Models A, B and C.

> *Remark:*
> *These formulae must not be extrapolated!*
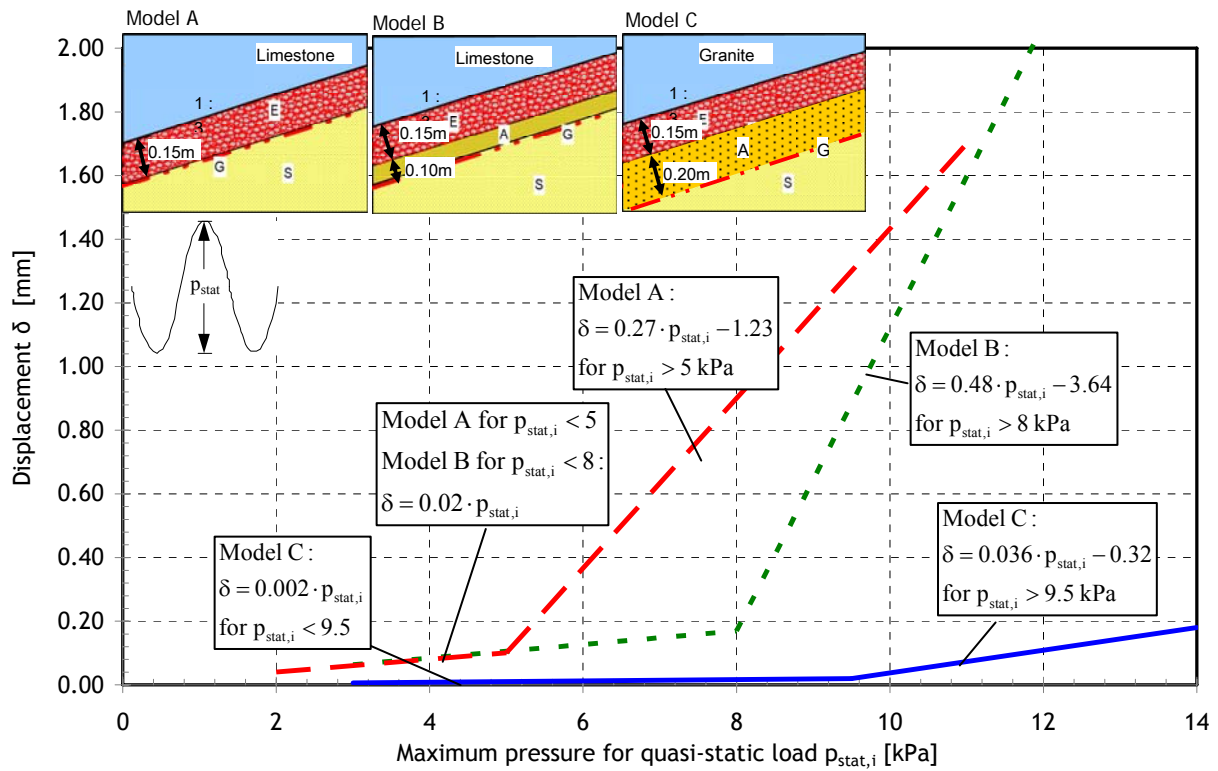
Fig. 7.13: Maximum displacements in all tests of *Model Alternatives* A, B and C as a function of the maximum recorded quasi-static pressures $p_{stat,i}$ on top of the revetment

8   Failure of the *ELASTOCOAST* revetment

On Monday 18th May 2009, the part of the *ELASTOCOAST* revetment without filter layer (*Model Alternative A*), unexpectedly failed under severe regular wave attack while *Model Alternative B* which was simultaneously subject to the same wave conditions experienced no damage. As shown in Fig. 8.1 the *ELASTOCOAST* layer lies directly on the geotextile-covered sand, while in *Model Alternative B* a filter layer made of the same crushed rock material as for the *ELASTOCOAST* revetment is additionally inserted between the *ELASTOCOAST* layer and the geotextile. The two *Model Alternatives A* and *B* are built side by side, each covering half of the wave flume width (2x2.5 m) and tested simultaneously using the same incident wave conditions. The thickness of the *ELASTOCOAST* layer for both *Model Alternatives A* and *B* is 15 cm. While no gravel filter is built for *Model Alternative A*, the thickness of the filter layer in *Model Alternative B* is 10cm, resulting in an overall revetment thickness of 25 cm in *Model Alternative B*. For the revetment and the filter layer, crushed limestone material with a grading of 20/40 [mm] is used.
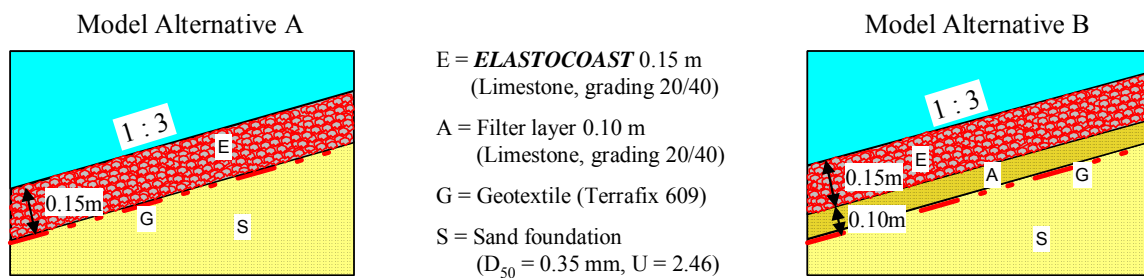
Fig. 8.1:   Cross sections of *Model Alternatives* A and B built side by side in GWK (FZK, 2008b)

The failure occurred under regular wave attack with H = 1.3 m and T = 5 s for a water depth of h = 3.90 m in the flume. In a previous test with the same water depth (h =3.90m), the same wave height (H = 1.3 m) but a shorter wave period (T = 4s), no apparent damage occurred for *Model Alternatives A* and *B*.

This section therefore aims at

(i)   Briefly describing the observed damage of *Model Alternatives A* for the regular wave test with H = 1.3 m and T = 5s , including the comparison of the associated wave induced load processes and displacements of the revetment simultaneously recorded at both *Model Alternatives A* and *B* for the same test. A comparison with the processes recorded in the previous test with the same wave height and a shorter period (H = 1.3 m and T = 4 s) for which no damaged occurred is also performed in order to better understand the causes of failure in the test with a longer wave period.

(ii)   Providing a possible physical interpretation of the experienced failure which is based on both video observations and the analysis of the recorded data related to the wave induced pressure and the associated displacement of the revetment.

8.1   Description of observed failure of *Model Alternative* A

The exact time at which the collapse of *Model Alternative A* occurred is identified by means of the records of the displacement meter as illustrated by Fig. 8.2 showing comparatively the recorded displacement for *Model Alternatives A* and *B*. It is seen that the collapse of *Model Alternative A* started after t = 450 s (t = 7:30 min), i.e. between the 74th and the 75th wave of the test (see also Fig. 8.3 and Fig. 8.4). In fact, the failure initiation started just after t = 430 s (t = 7:10min), i.e. just after the 70th wave, where a residual upward displacement started to build up for each cycle until the collapse occurred. The uplift of the revetment by each wave cycle causes a gap beneath the revetment thus allowing the sediment to move more freely. As a result, the residual upward displacement increases progressively until the collapse occurs. The maximum residual upward displacement (15 mm) was recorded by the displacement meter during the run down of the 75th wave which caused the collapse of the revetment. As observed visually during the tests the collapse occurred within a very short time interval (few seconds) without any visually perceptible precursors. Following the significant upward motion of the revetment and the resulting gaps beneath the revetment, considerable amount of sand were washed out by the receding waves on the slope (down rush flow) thus resulting in a significant settlement of the revetment and a subsequent breakage of the revetment .As shown in Fig. 8.5a the washed sand was deposited at the toe of the revetment. This figure together with Fig. 8.5b shows that the occurrence of the collapse was spatially concentrated just below still water level.

Comparatively, no build up of the residual displacement (Fig. 8.2) and no damage (Fig. 8.5) occurred for *Model Alternative B* which was subject to the same incident waves as *Model Alternative A*

> *Important remark:*
>
> *The fluctuations of transducer DT2 at Model B directly after the collapse are induced by motions of the upper support point of the transducers, which are caused by the large deformations of the measuring system at Model A. They don't represent the displacements of the revetment in Model B and must therefore be ignored.*
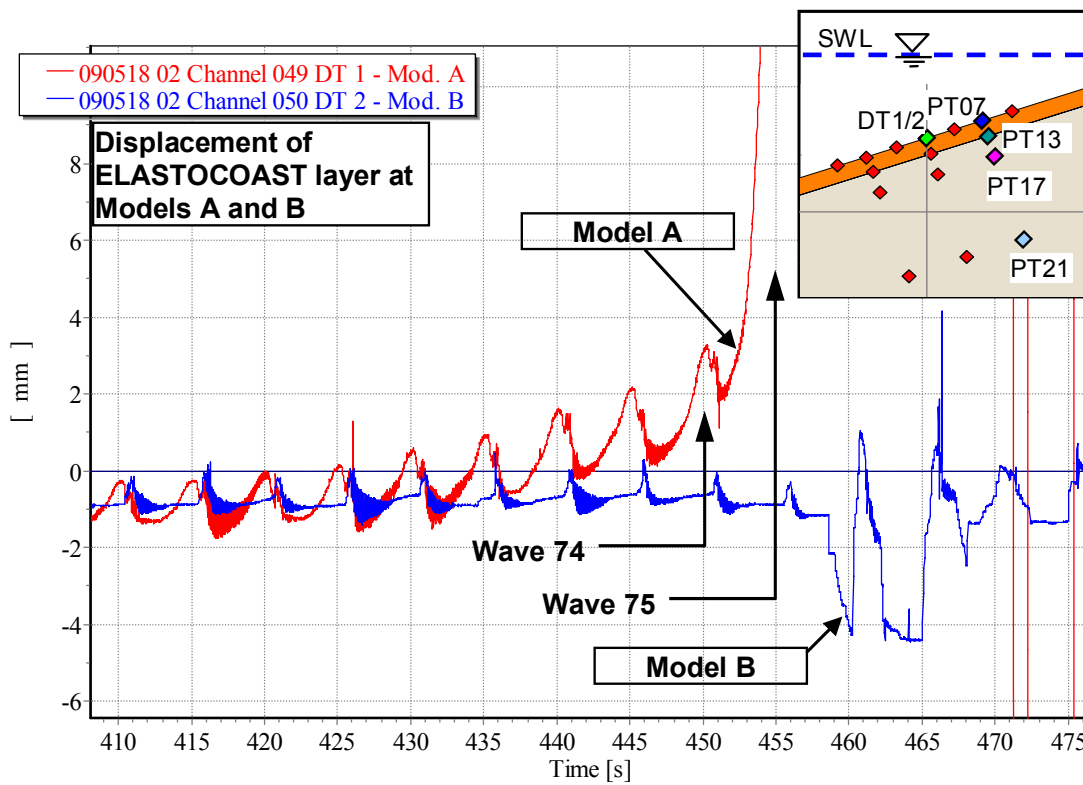
Fig. 8.2: Displacement signals for *Model Alternatives* A and B at the time of failure of Model A (Oumeraci et al, 2009)

(a) Wave records of entire test at WG13

(b) Wave record during failure of Model A
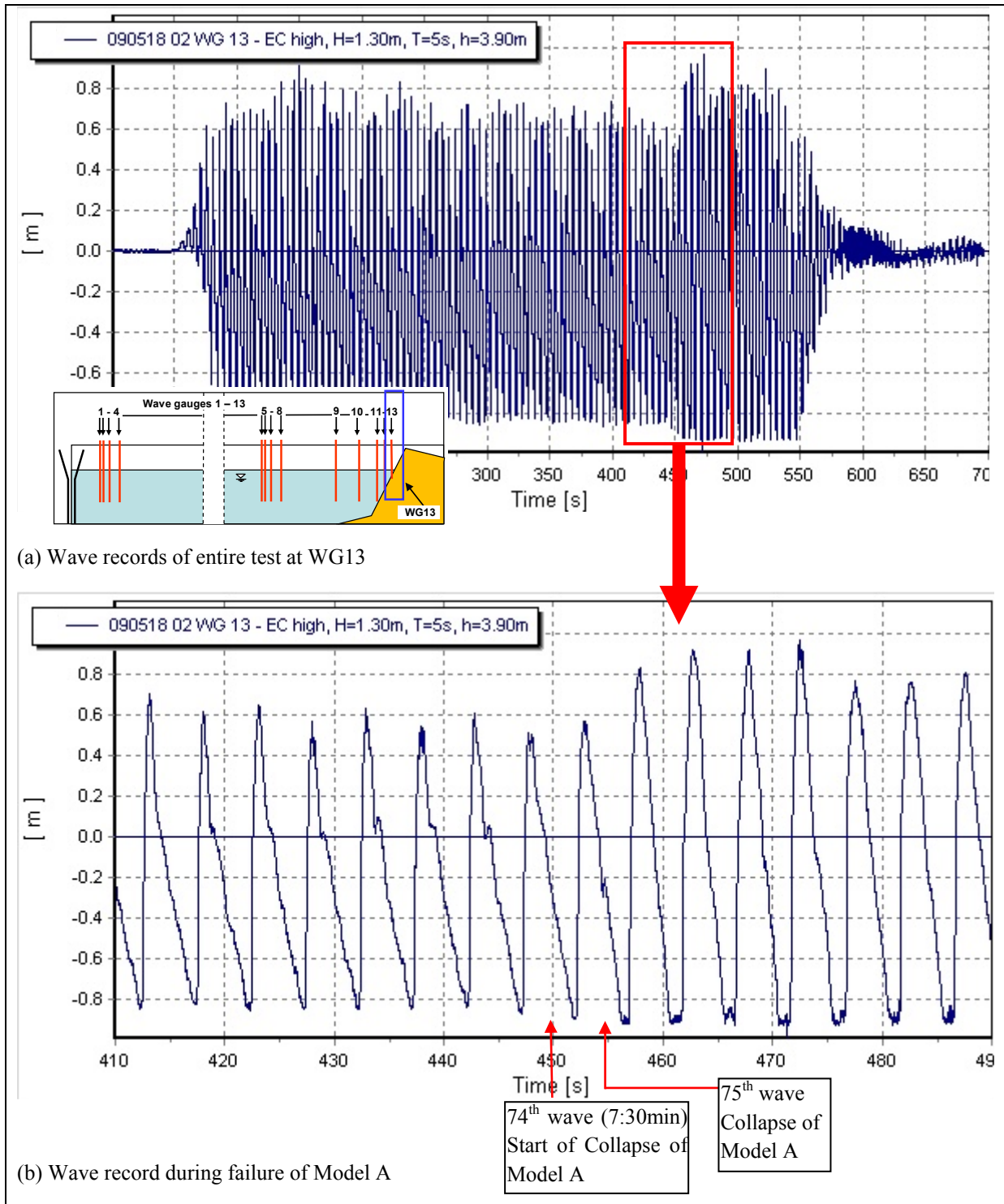
Fig. 8.3:   Wave records at wave gauge WG13

(a) 74th wave at t=450s (7:30min)

(b) 75th wave at t=457s

Fig. 8.4:   74th and 75th waves just before impact on the revetment in GWK
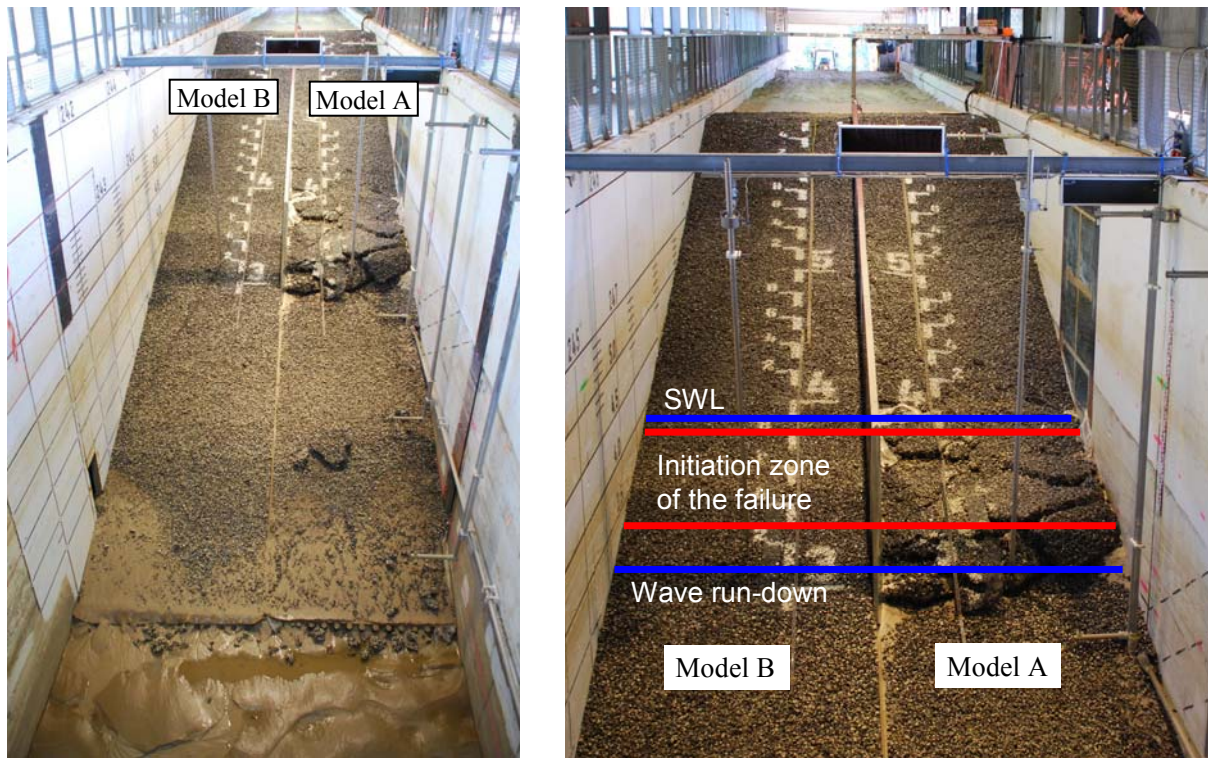
(a) Overall view

(b) Detailed view

Fig. 8.5: Extent of damage for Model A

Following the wash out of sand and the subsequent settlement, the revetment experienced an unexpected breakage behaviour in several smaller and larger block units occurred (Fig. 8.6a), leading to very large gaps in through the revetment (Fig. 8.6b). This unexpected breakage behaviour is certainly due to the use of limestones, since the failure planes are observed to generally go through the limestones and not through the polyurethane binding material (Fig. 8.7).

(a) Unexpected breakage in several blocks

(b) Large gaps in the revetment (breakage)

Fig. 8.6:   Breakage of revetment

Fig. 8.7:   Failure through limestones (Oumeraci et al, 2009a)

8.2   Physical interpretation of failure of *Model Alternative* A

8.2.1   Wave-induced pore pressure in the sand core

As described in the previous section 8.1 the primary difference between *Model Alternative A* which failed and *Model Alternative B* which did not fail under the same wave conditions is the 10 cm thick gravel filter layer which provides an additional weight and stiffness for *Model Alternative B* to resist against the instability (e.g. reduction of shear resistance and soil lique-fication) of the sand core beneath the revetment which is subject to different pore pressures in Model A and Model B.

As already shown by Oumeraci et al (2009a), the wave pressure on and beneath the revetment are almost similar for Maodel A and Model B with the uplift pressure being slightly higher for Model A than for Model B (see Fig. 3.1 p.3 in Oumeraci et al, 2009a). However, the response of the sand core beneath the revetment is different for Model A and Model B as shown by the development of the pore pressure in Fig. 8.8 before the failure occurs. It is seen that the "negative" pore pressure amplitudes measured in 20cm beneath the upper boundary of the sand core by PT17 on Model A and by PT43 in Model B significantly differ while the "positive" pore pressure amplitudes are in the same range for both models. In fact, the "negative" pore pressure amplitudes are almost twice for Model A (-2.3 kPa) than for Model B (-1.2 kPa). This extremely higher pressure gradient beneath Model A will result in a significantly stronger upward water flow in the sand core beneath the revetment as compared to Model B. It should be stressed that the pore pressure signals shown in Fig. 8.8 are measured long before the occurrence of the failure and that about 10 waves before the failure at t = 455s (Fig. 8.2) the pore pressure amplitudes remained almost constant over time.
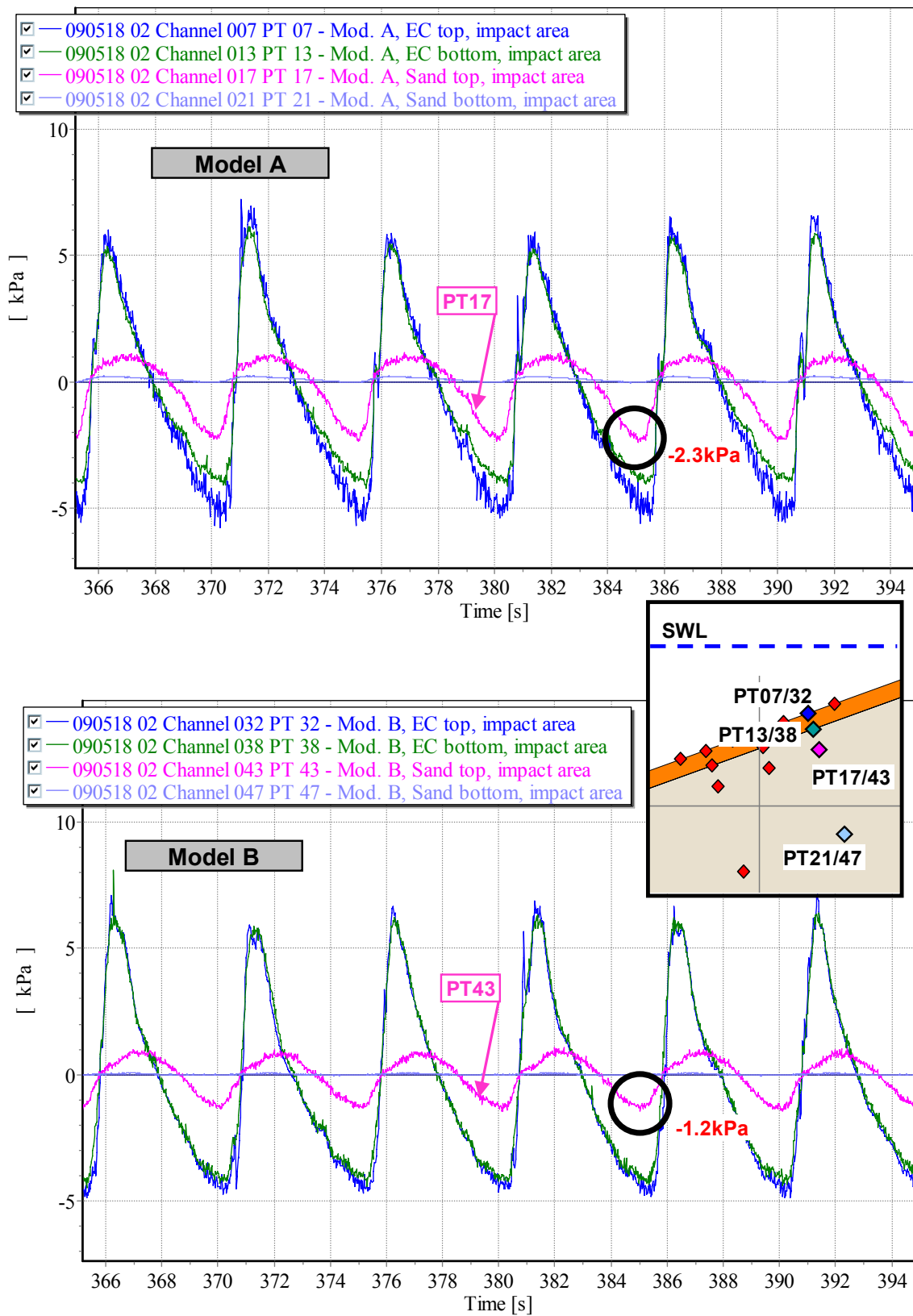
Fig. 8.8:   Pore pressure development in the sand underneath the revetment (Oumeraci et al, 2009a)

This is surprisingly not the case for the last 10 waves before the failure occurred. As shown in Fig. 8.10 together with Fig. 8.2, the "negative" pore pressure amplizudes at PT17 for Model A progressively increases from -2.4 kPa at t = 410s to -3.2 kPa before the incipience of the failure while the "positive" pore pressure amplitudes remained almost constant over time. As the failure started (74th wave at t = 455s), the pore pressure decreases to -5.6 kPa and droped to -11.4 kPa as the revetment collapsed (75th wave at t = 455s).

As shown in the simultaneously measured displacement in Fig. 8.2 the progressive increase in "negative" pore pressure amplitude is accompanied by a simultaneously progressive increase of the upward displacement of the revetment up to the time where the displacement meter collapsed.
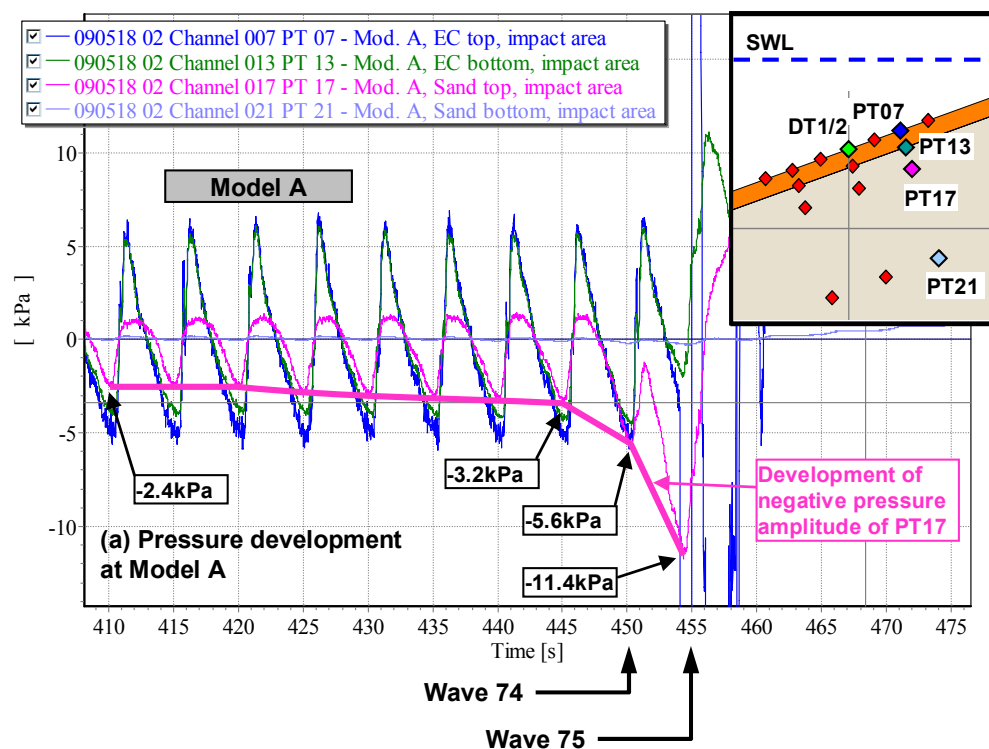
Fig. 8.9: Pore pressure development in the sand core beneath the revetment of Model A (Oumeraci et al, 2009a)

These results indicate that the primary cause of failure of Model A is most probably the liquefication of the sand core beneath the revetment. This has also been shown in the preliminary report by Oumeraci et al (2009a) in which the differences with Model B are explained in more detail, so that there is no needto duplicate them in the present report. Instead a comparative stability analysis of Models A and B for the same tests at which the failure of Model A occurred is provided below in order to confirm that the development of pore pressure and soil liquefication in the sand core beneath the revetment of Model A indeed represents the primary cause of the observed failure.

8.2.2 Stability analysis

(a) Physical background of soil liquefication and stability beneath the revetment

Generally, wave-induced cyclic loads generate both pore water pressure u and effective stresses σ' inside the subsoil. In the presence of sea waves the total pore pressure $u_{tot}(z,t)$ in the seabed is composed of the hydrostatic component $u_0(z)$ and the wave induced component $u(z,t)$:

$$u_{tot}(z,t) = u_0(z) + u(z,t) \tag{8.1}$$

The wave-induced component $u(z,t)$ is also called "excess pore pressure" (in excess of the hydrostatic pressure). Because of the resetting of the pressure transducers before each individual test, the initial hydrostatic component $u_0(z)$ is not considered in the following analysis.

Liquefaction occurs, if the excess pore pressure $u(z,t)$ inside the soil reaches the value of the initial effective stress σ'_0 which means, that the effective stress and therefore the shear resistance τ_s of the soil tends to zero ($\tau_s = (\sigma'-u)\tan\varphi$ with φ = internal friction angle). In general, soil liquefaction may be induced by two mechanisms:

- Upward pressure gradient in the soil during the passage of the wave trough (*transient or instantaneous liquefaction*)

- Increase of mean excess pore water pressure (*residual liquefaction*)

Transient liquefaction:

During the passage of a wave trough the induced excess pore pressure in the soil becomes negative. As the amplitude of the excess pore pressure diminishes with increasing depth, the spatial difference in pore pressure generates an upward pressure gradient (Fig. 8.10). If the pressure gradient at a certain location z in the sand core reaches the effective stress σ'_{vo} due to the submerged weight of the soil and the revetment at this location, the soil gets into suspension and behaves like a fluid.

$$\sigma'_{v0} = \underbrace{\rho'_s \cdot g \cdot z}_{(\sigma'_{v0})_s} + \underbrace{\rho_r \cdot g \cdot d_r}_{(\sigma_{v0})_r} \tag{8.2}$$

with:

σ'_{v0}	[N/m²]	Initial effective vertical stress
ρ'_s	[kg/m³]	Bulk density of submerged soil (sand)
ρ_s	[kg/m³]	Bulk density of soil (sand)
ρ_w	[kg/m³]	Mass density of water
g	[m/s²]	Gravitational acceleration
z	[m]	Depth of sand core
ρ_r	[kg/m³]	Density of revetment including filter layer
d_r	[m]	Thickness of filter layer and *ELASTOCOAST* revetment
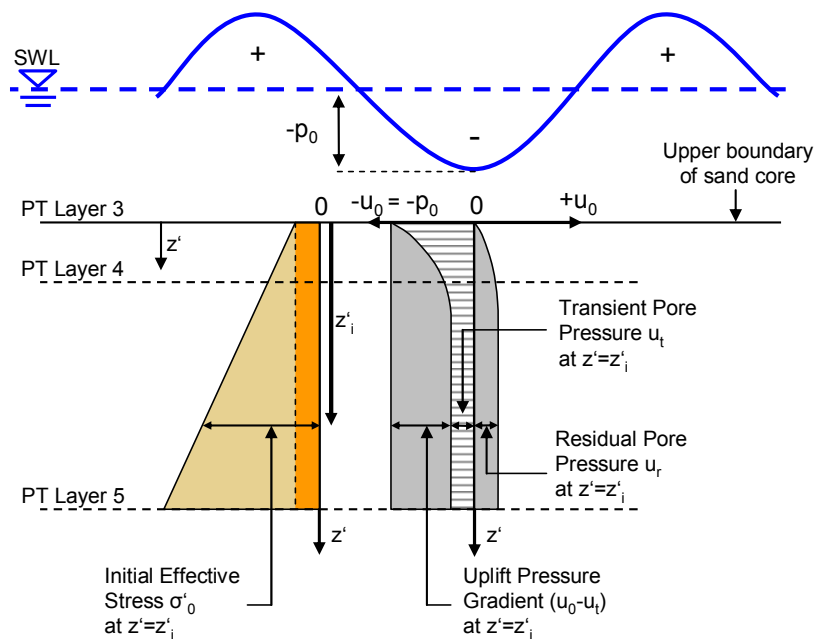
Fig. 8.10: Distribution of initial effective stress, excess pore pressure amplitude and uplift pressure gradient in the sand core under the passage of a wave trough (see Fig. 6.1 for definition of PT Layers)

This is called transient liquefaction, as this phenomenon is limited to the short period during the passage of the wave trough. Transient liquefaction occurs if the pressure difference $(u_0 - u_t)$ gets negative and corresponds to the initial effective stress σ'_{v0}:

$$\sigma'_{v0} - (u_0 - u_t) = 0 \qquad (8.3)$$

with:

σ'_{v0}	N/m²	Initial mean effective stress
u_0	[kg/m³]	Initial (hydrostatic) pore water pressure
u_t	Pa	Instantaneous (transient) excess pore water pressure

Residual liquefaction:

If the gradual increase of the mean pore pressure u_r inside the sand core reaches the value of the initial effective normal stress σ'_{v0}, the contact between the soil grains vanishes and the soil behaves like a fluid:

$$\sigma'_{v0} - u_r = 0 \qquad (8.4)$$

with:

u_r	[Pa]	Residual excess pore water pressure

Under wave action and increased mean excess pore pressure u_r, the excess pore pressure u is a superposition of both residual pore pressure u_r and transient pore pressure u_t:

$$\sigma'_{v0} - \left[(u_0 - u_t) + u_r \right] = 0 \tag{8.5}$$

Based on eq. (8.5) the stability analysis of the sand core beneath the revetment can be performed as schematically illustrated in Fig. 8.11, showing:

- the distribution of the initial effective stress σ'_{v0} in the sand core beneath the revetment starting at the upper boundary (PT Layer 3). The effective stress σ'_{v0} is composed of the linearly increasing component $(\sigma'_{v0})_s$ due to the submerged weight of the sandmaterial and the component $(\sigma_{v0})_r$ due to the weight of the revetment and filter layer which remains constant over the entire depth in the sand core (see also definition sketches Fig. 6.1, a,b). While the first component $(\sigma'_{v0})_s$ is the same for both Models A and B, the second component $(\sigma'_{v0})_r$ is higher for Model B $((\sigma'_{v0})_r = 3.826 \text{ kN/m}^2)$ than for Model A $((\sigma'_{v0})_r = 2.296 \text{ kN/m}^2)$.

- The initial "negative" pore pressure amplitude $-u_0$ caused by the wave pressure at the upper boundary of the sand core beneath the revetment is a transient pore pressure and therefore decrease with the depth like the total transient pore pressure described in section 6.1. As a result, an upward directed pressure gradient $(u_0 - u_t)$ is generated.

- The residual pore pressure u_r which is zero at the upper boundary of the sand layer $(u_r = 0$ for $z' = 0)$ and increase with the depth in the first layers (see Section 6.2.).
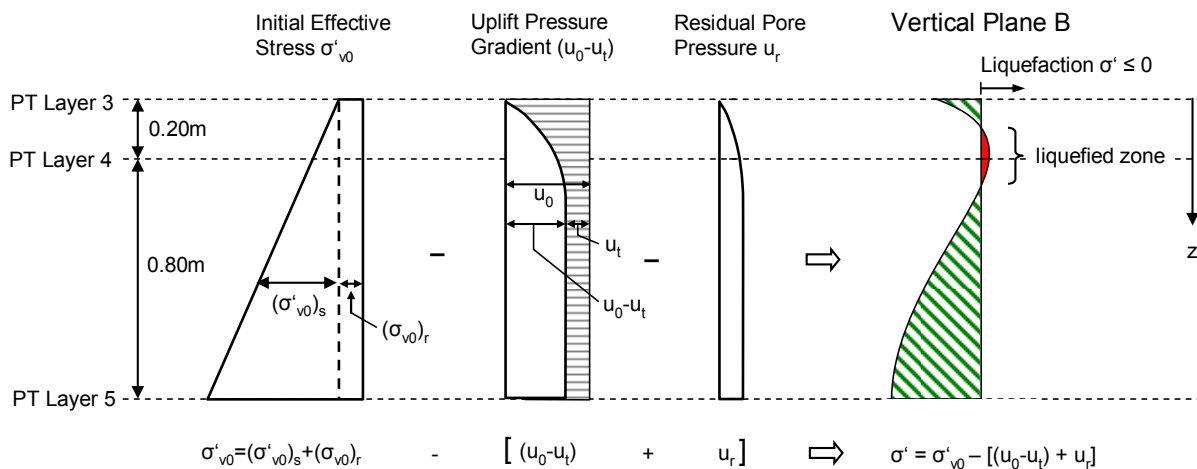
Fig. 8.11: Superposition of initial effective Stress σ'_0, uplift pressure gradient (u_0-u_t) and residual pore pressure u_r for stability analysis

In the stability analysis the first term (σ'_{v0}) in Eq. (8.5) and Fig. 8.11 represent the resistance (R) while the second term (u_0-u_t) and the third term (u_r) represent the wave-induced load, so that the stability is described by the following limit state equation:

$$\sigma' = \sigma'_{v0} - \left[(u_0 - u_t) + u_r \right] = 0 \tag{8.6}$$

Which means that liquefication occurs when

$$\sigma' \geq 0 \tag{8.7}$$

(b) Physical background of soil liquefication and stability beneath the revetment

Based on the approach illustrated by Fig. 8.11, the stability analysis is conducted below comparatively for both *Model Alternatives* A and B by considering:

-   Test 09051802 (with $H_m = 1.37$ m, $T_m = 4.9$ s and $h = 3.90$ m) at which the failure of Model A occurred and called hereafter "failure test".
-   Test 09051503 with a similar wave height and a shorter period (with $H_m = 1.40$ m, $T_m = 3.92$ s and $h = 3.70$ m) at which no failure occurred and called hereafter "no failure test".

Moreover, the stability analysis is conducted for the three planes B, C and D normal to the slope as defined in Fig. 6.1 in order to better localize the initiation of the failure along the slope.

(i) Stability analysis for "failure test"
     The results of the stability analysis for Model A and Model B are comparatively depicted in Fig. 8.12 and Fig. 8.13, showing that a soil liquefaction indeed occurred beneath the revetment of Model A while the soil remained stable under the revetment of Model B. Moreover, it is shown that the soil liquefaction is initiated at the deepest of the three considered locations beneath SWL (Planes B, C and D) which might correspond to the maximum run-down.

(ii) Stability analysis for "no failure test"
     The results are comparatively depicted in Fig. 8.14 and Fig. 8.15 showing that the soil beneath the revetment remained stable in both Models A and B, thus confirming the observations during the test.

(a) location B

(b) location C

(c) location D
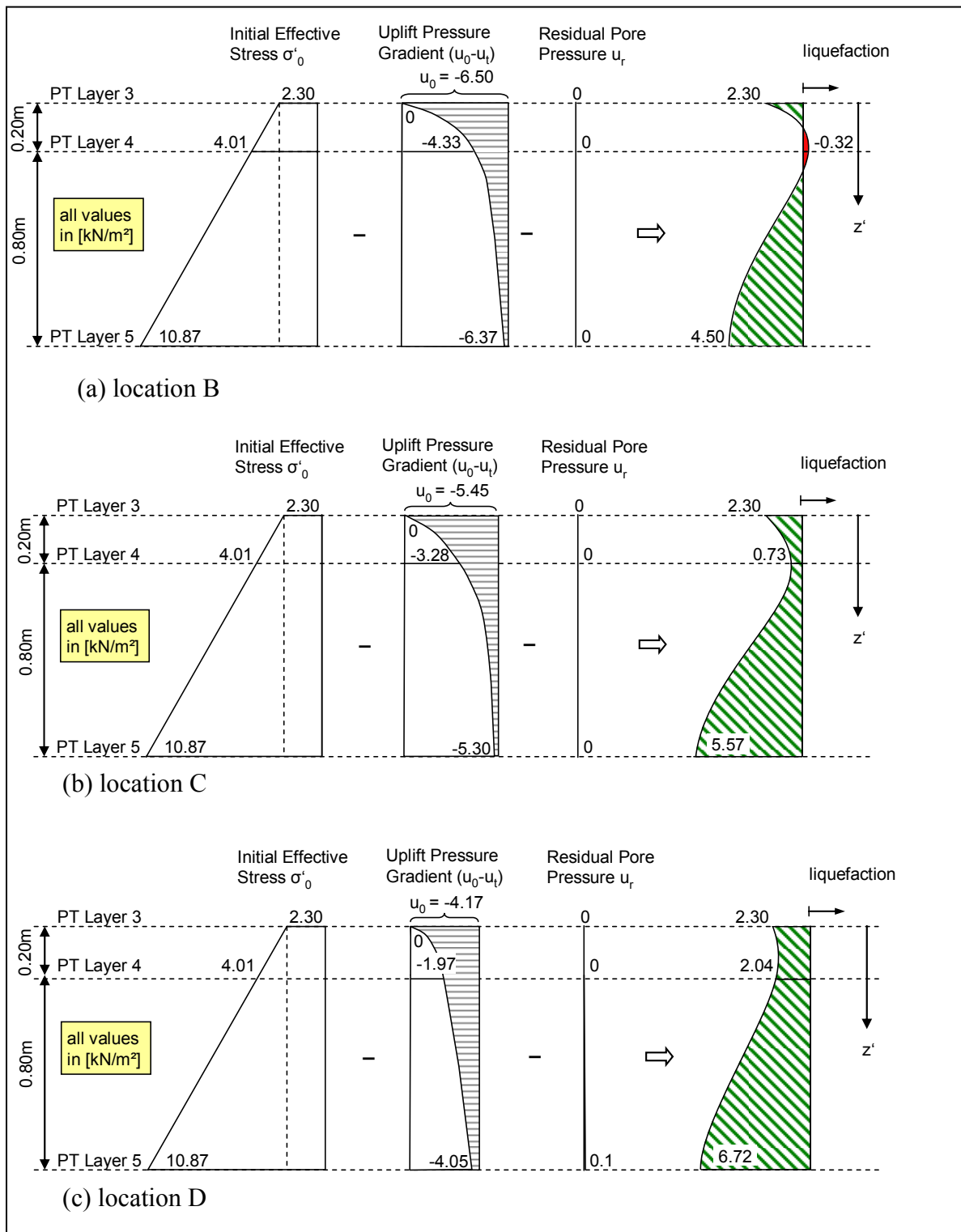
Fig. 8.12: Stability analysis for failure test **(Model A)**
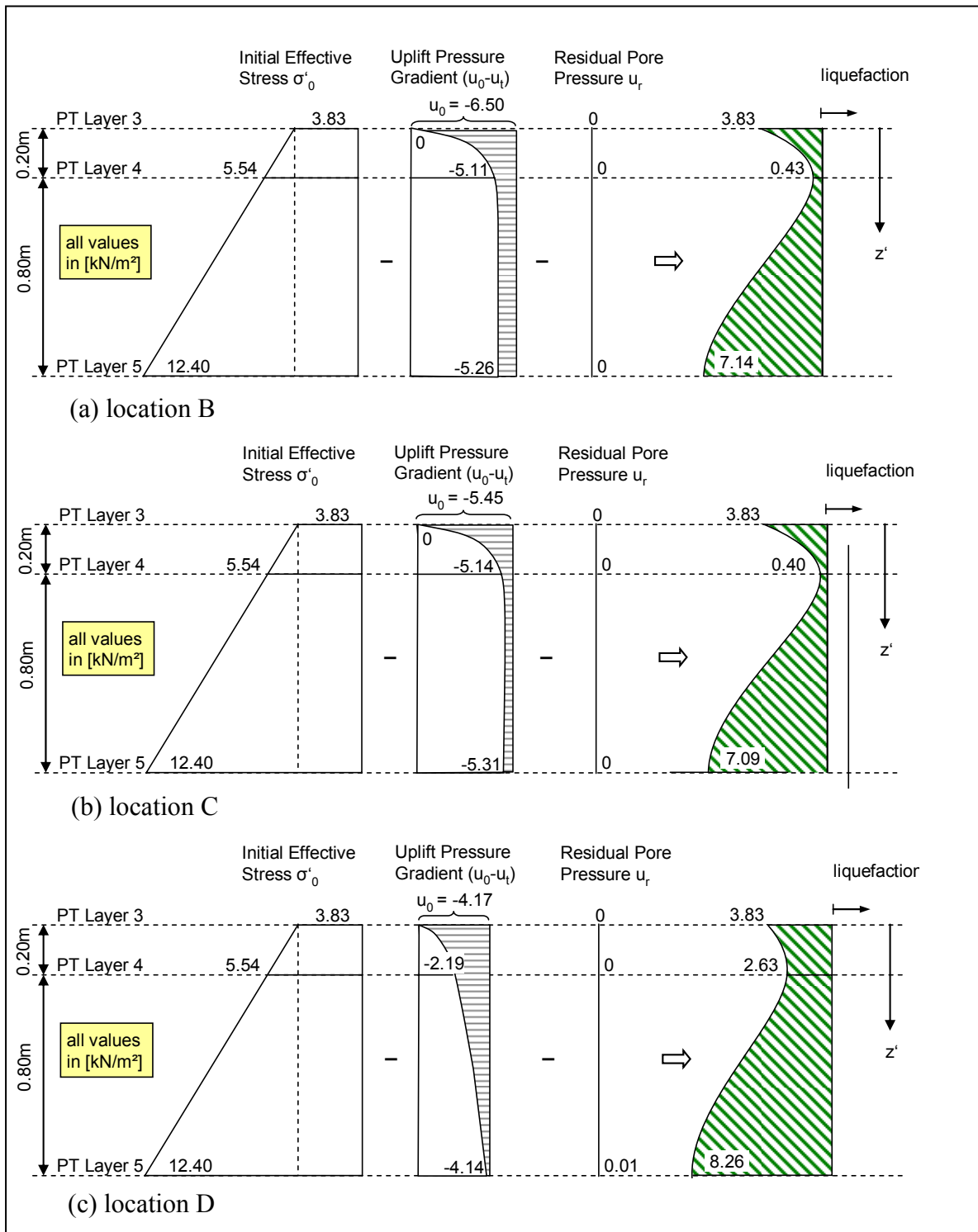
Fig. 8.13: Stability analysis for failure test **(Model B)**
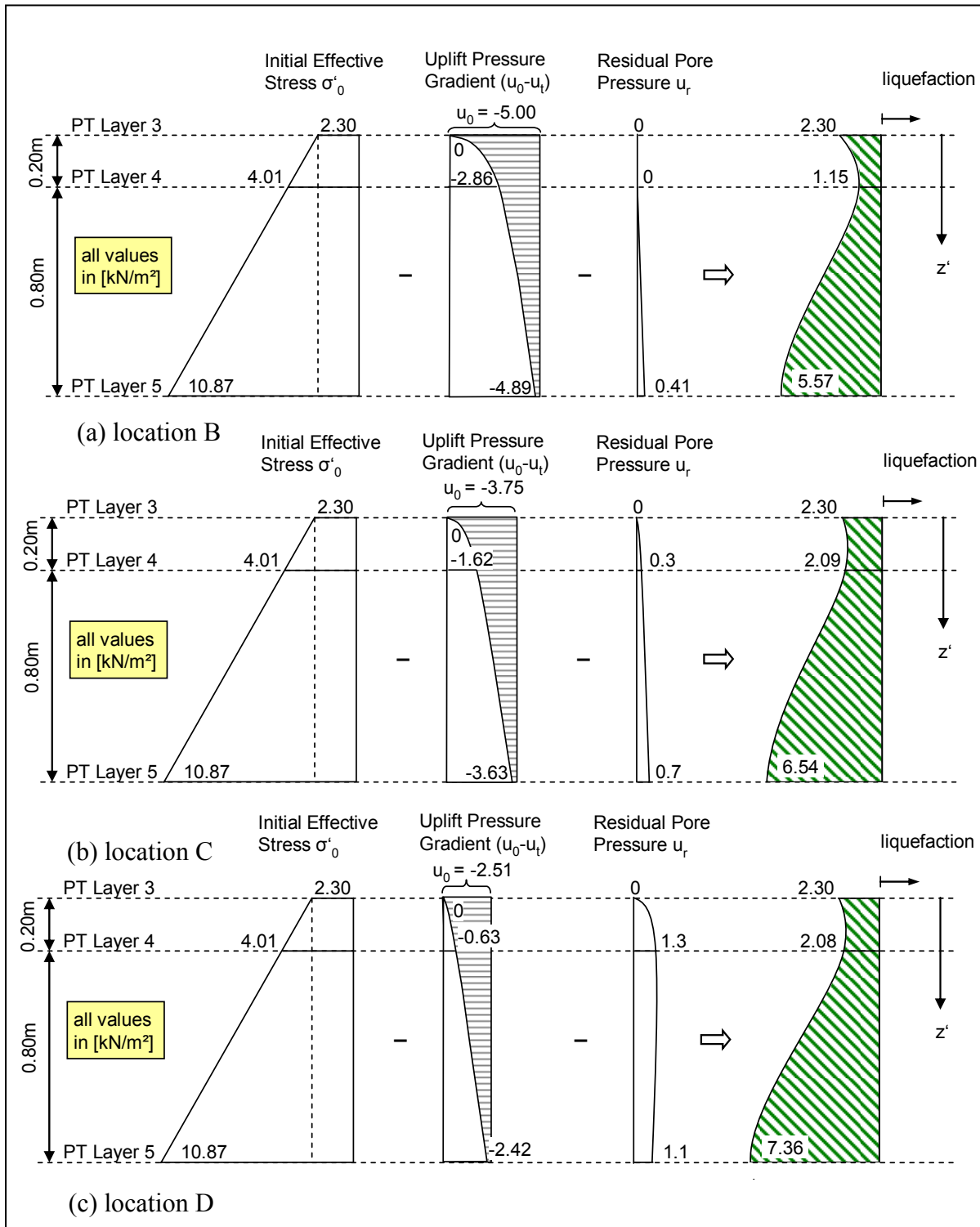
Fig. 8.14: Stability analysis for no failure test **(Model A)**
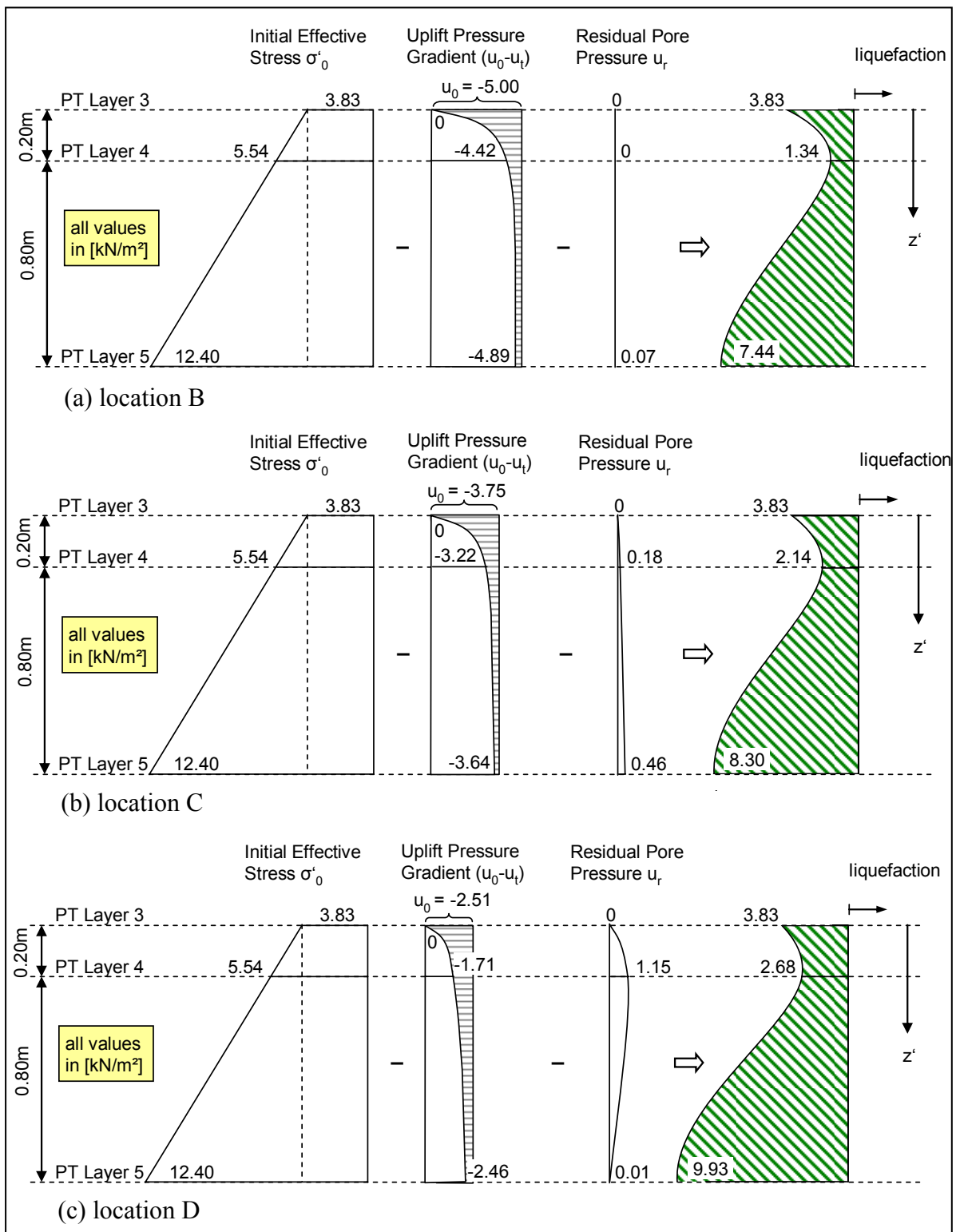
Fig. 8.15: Stability analysis for no failure test (**Model B**)

9   Summary and Concluding Remarks

More than 35 tests with regular waves and about 40 tests with irregular waves were performed in the Large Wave Flume (GWK) of the Forschungszentrum Küste (FZK) in Hannover, Germany. Initially two *Model Alternatives A* and *B* (see Fig. 1.1) were built side by side in the wave flume and tested simultaneously using the same incident wave conditions (regular waves only). After the failure of *Model Alternative A* which occurred at an unexpected early stage under regular waves (h = 3.90 m, H ≈ 1.3 m and T ≈ 5 s), *Model Alternative A* was replaced by *Model Alternative C* (Fig. 1.2), so that the full testing programme could be performed for both regular and irregular waves with *Model Alternatives B* and *C* built in the wave flume side by side.

Both regular and irregular wave tests were analysed with the objective of deriving empirical formulae/diagrams for (i) the reflection performance of the *ELASTOCOAST* revetment, (ii) the wave run-up and run-down, (iii) the pressure induced by the waves on and just beneath the revetment, (iv) the pore pressure in the sand core beneath the revetment. This objective is in line with the terms of reference as specified in the proposal (FZK, 2008b). In addition, this report also includes the description and analysis of the collapse experienced by *Model Alternative A*, which was already reported by Oumeraci et al (2009a). Moreover, much more work than initially planned for the verification, pre-processing and analysis of the data was necessary, due to the damaged transducers after the failure of *Model Alternative A* and to further related unexpected difficulties. Nevertheless, much more has been achieved than initially specified in the proposal (FZK, 2008b).

Although the analysis of the data has been systematically performed for both regular and irregular waves, the focus in the report is put on the irregular wave tests, because they are more relevant for design purposes. In order to make the report easier to read, the results related to the regular wave tests are briefly summarized in Annex D for comparison

Hydraulic Performance

For the prediction of the wave reflection performance a formula providing the reflection coefficient C_r as a function of the surf similarity parameter $\xi_{m-1,0}$ is proposed (see Fig. 9.1):

$$C_r = \frac{0.84 \cdot \xi_{m-1,0}^{2}}{4.8 + \xi_{m-1,0}^{2}} \qquad \text{with } \sigma' = 12.5 \text{ \%}$$

The *ELASTOCOAST* revetments have expectedly smaller reflection coefficients than smooth impermeable slopes, but larger reflection coefficients than conventional rubble mound structures. Moreover, the results also show that the surf similarity parameter does not account suf-

ficiently for the effect of the incident wave period and that a more appropriate governing parameter should be developed in future research.
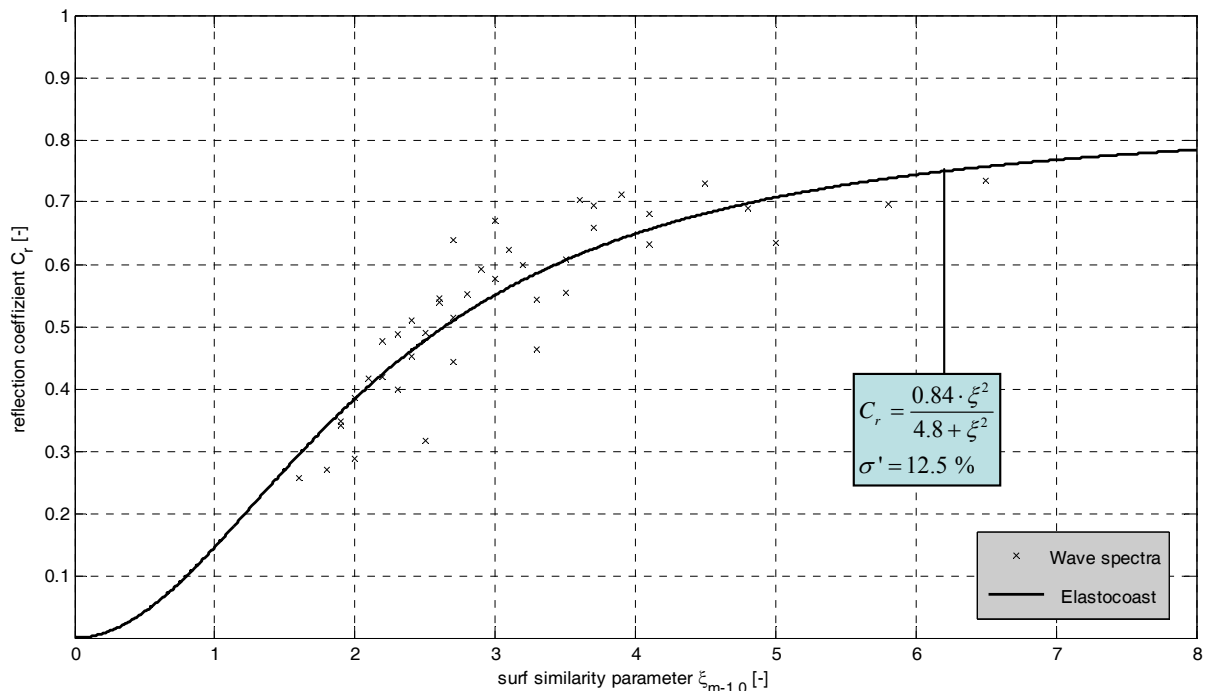
Fig. 9.1:   Proposed reflection coefficient for *ELASTOCOAST* revetment

For the prediction of wave run-up $R_{u2\%}$ the formulae proposed by EurOtop Manual for smooth impermeable slopes have been adopted by introducing reduction factors for the *ELASTOCOAST* revetment (s. Fig. 9.2). The following formulae are obtained with $\sigma' = 15.9\ \%$:

$$\frac{R_{u2\%}}{H_{m0}} = 0.54 \cdot \left[1.65 \cdot \xi_{m-1,0}\right] \quad \text{for } \xi_{m-1,0} < 2.7$$

$$\frac{R_{u2\%}}{H_{m0}} = 0.77 \cdot \left[4.0 - \frac{1.5}{\sqrt{\xi_{m-1,0}}}\right] \quad \text{for } \xi_{m-1,0} > 2.7$$

The difference between *Model Alternative B* and *Model Alternative C* is negligibly small. However, wave run-up of *ELASTOCOAST* revetments is 25% to 50% less than for smooth impermeable slopes, depending on the range of surf similarity parameter considered (Fig. 4.4).
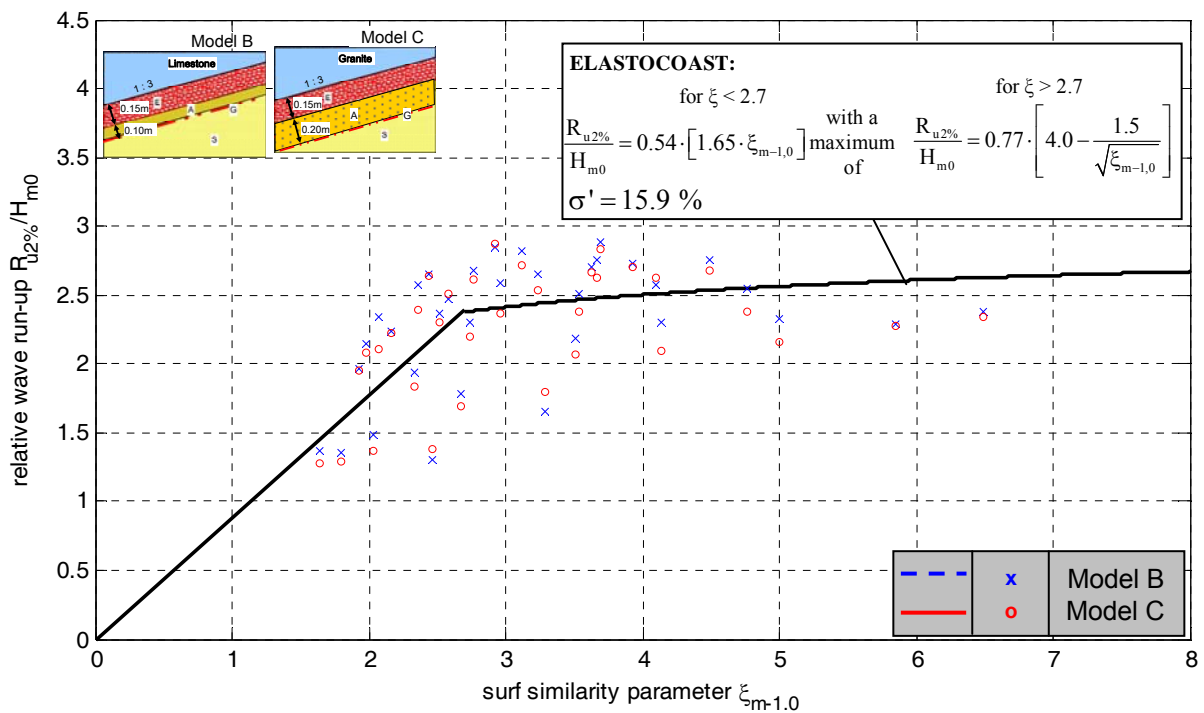
Fig. 9.2:   Proposed wave run-up for *ELASTOCOAST* revetment

For the prediction of wave run-down $R_{d2\%}$ formulae are developed providing $R_{d2\%}$ as a function of the surf similarity parameter $\xi_{m-1,0}$ with $\sigma' = 6.1\ \%$ (s. Fig. 9.3):

$$\frac{R_{d2\%}}{H_{mo}} = -0.42 \cdot \xi_{m-1.0} + 0.17 \text{ for } \xi_{m-1.0} < 5.7$$

$$\frac{R_{d2\%}}{H_{mo}} = -2.25 \text{ for } \xi_{m-1.0} \geq 5.7$$

Compared to the formulae for other types of revetment (Fig. 4.8), showing that the wave run-down of *ELASTOCOAST* revetment is between that of a smooth impermeable slope and that of a revetment of placed concrete blocks.
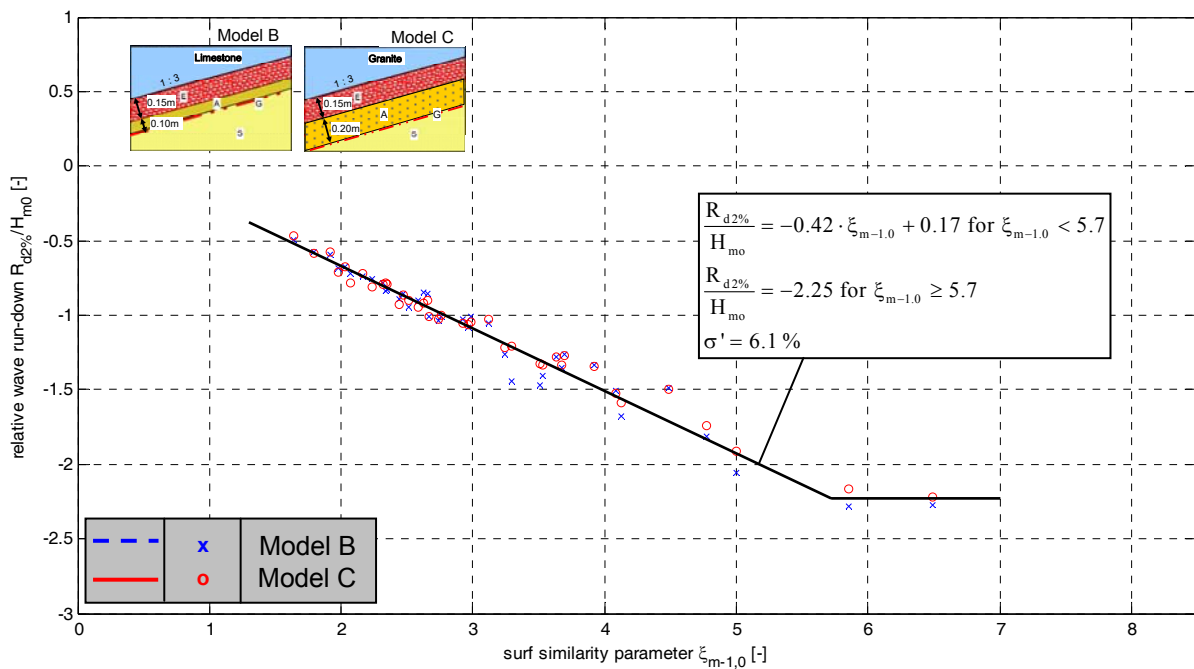
Fig. 9.3: Proposed wave run-down for *ELASTOCOAST* revetment

Wave Load on and just beneath Revetment

The most extensive part of the analysis is dedicated to the analysis of the pressure induced by the waves on and just beneath the revetment (Chapter 5), including a wave load classification and parameterization in both space and time as well as the development of empirical formulae for the prediction of the parameters which are needed to describe the wave load.

Depending on the surf similarity parameter $\xi_{m-1,0}$ tested ($\xi_{m-1,0}$ = 1.6 - 6.6) a **wave load classification** is proposed, including impact load ($\xi_{m-1,0}$ = 1.6 - 2.5), non-impact load ($\xi_{m-1,0}$ > 2.9) and a transition zone ($\xi_{m-1,0}$ 1.6 – 2.5).

A parameterization for both impact load (Fig. 5.4 and Fig. 5.5) and non-impact load (Fig. 5.6 and Fig. 5.7) is proposed in time (Fig. 5.4 and Fig. 5.6) and space (Fig. 5.5 and Fig. 5.7). The maximum (peak) pressure and its location along the slope, represent the key parameters since both parameters are used as reference parameters for the calculation of other related parameters which are required to calculate the wave pressure distribution on and beneath the revetment.

For the prediction of maximum pressure p_{max} for impact load on the revetment as a function of the surf similarity a formulae is proposed with $\sigma' = 37.6\%$:

$$\frac{p_{max}}{\rho \cdot g \cdot H_{m0}} = -4 \cdot \xi_{m-1,0} + 12.5$$

Fig. 9.4 shows that $p_{max}/\rho g H_{m0}$-values up to 6 can be obtained. For the transition zone $p_{max}/\rho g H_{m0}$-values in the order of 2 are obtained according to Eq. (5.4) and Fig. 9.4. Just beneath the revetment the $p_{max}/\rho g H_{m0}$-values are reduced by a factor of about 0.6 (see Eqs. (5.7) -(5.8) and Fig. 9.4).
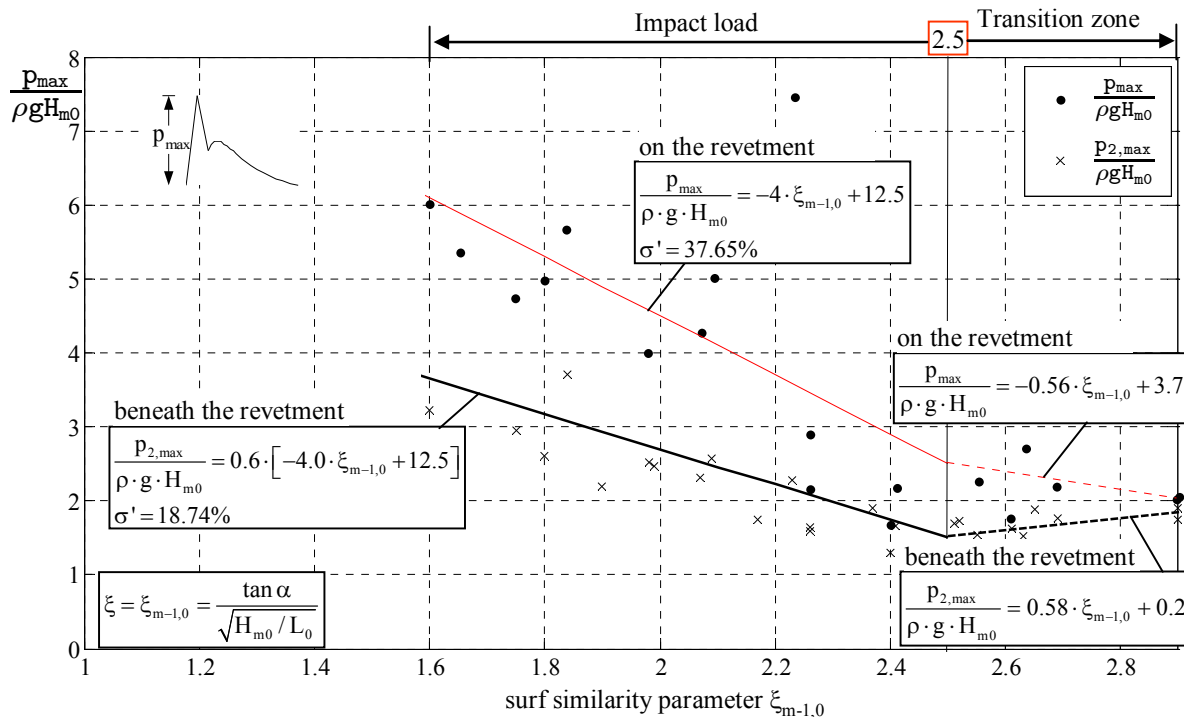
Fig. 9.4: Proposed maximum pressures on and beneath the revetment for impact load

For the prediction of the maximum pressure p_{stat} for the non-impact load, two formulae are proposed depending on the range of the surf similarity parameter $\xi_{m-1,0}$ which also covers the quasi-static component of the impact load (Eqs. (5.5) and (5.6)). For design purpose it might be simpler to use only (with $\sigma' = 16.11$ %):

$$\frac{p_{stat}}{\rho \cdot g \cdot H_{m0}} = 0.68 \cdot \xi_{m-1,0}$$

over the whole range of $\xi_{m-1,0}$ – values, which is on the safe side (see Fig. 9.5). All formulae proposed for the prediction of the maximum pressure on and just beneath the revetment, including both impact load and non-impact load, are summarized in Tab. 5.1. It is important to stress that the **pressure on and just beneath the revetment occur almost simultaneously** and that this should be accounted for in the stability analysis of the revetment accordingly.
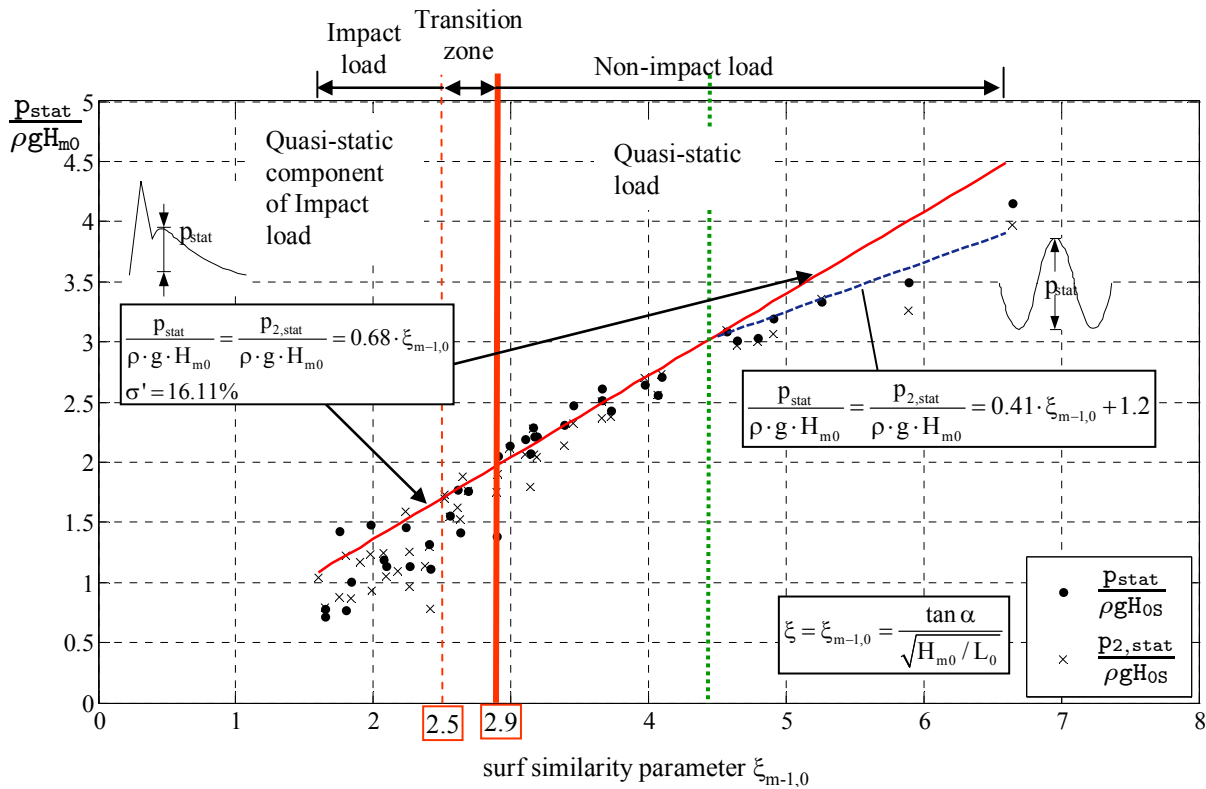
Fig. 9.5: Proposed maximum pressures on and beneath the revetment for non-impact load

For the prediction of the location of the maximum pressure along the slope two approaches leading to different formulae are proposed. For design purpose the formula based on Klein Breteler's approach with σ' = 15.57 % (s. Fig. 9.6)

$$\frac{z_{p\,max}}{H_{m0}} = min\begin{pmatrix} 0.7 \cdot \xi - 0.6 \\ 0.2 \cdot \xi + 1.0 \end{pmatrix}$$

should be favoured since it is more practical and more conservative than the formula based on Schüttrumpf's approach (Eq. (5.11) and Fig. 5.20). For the location of the maximum pressure induced beneath the revetment the same formulae as for the maximum pressure on the revetment are used by applying an amplification factor of 1.2 (see Eq. (5.16) and Fig. 5.24). All the proposed formulae are summarized in Tab. 5.2.
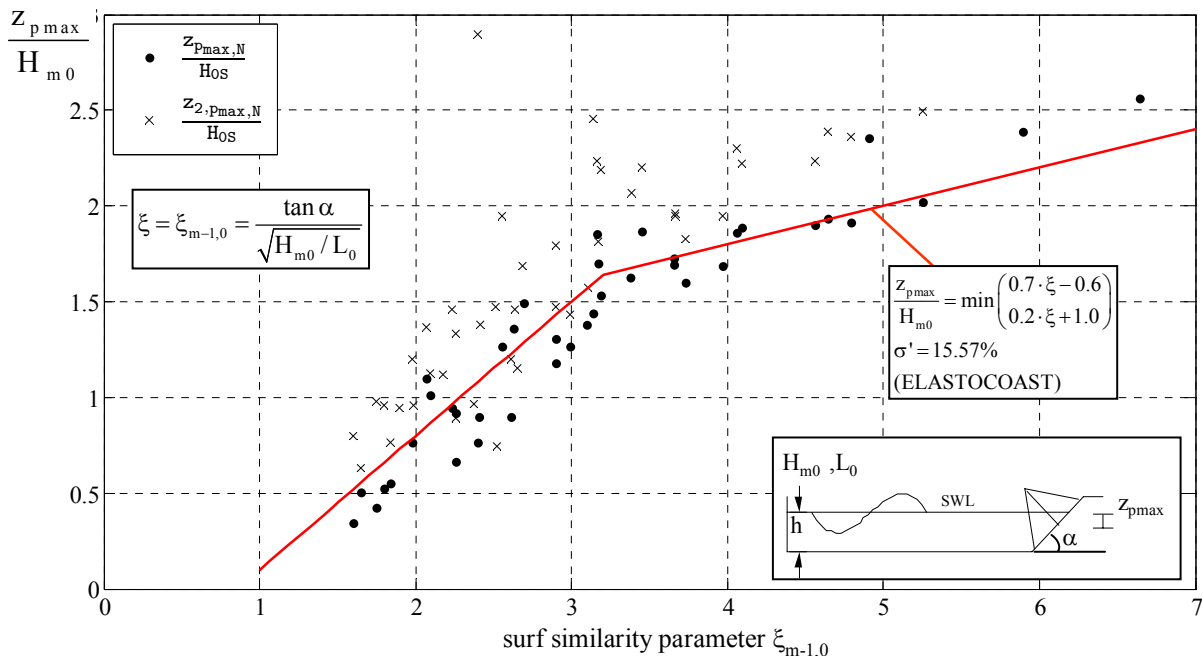
Fig. 9.6:   Proposed location of the maximum pressure on and just beneath the revetment

For the prediction of the spatial pressure distribution on and just beneath the revetment, which is based on the proposed parameterization in space for impact load (Fig. 5.5) and non-impact load (Fig. 5.7), formulae are proposed to calculate all the required parameters. All these formulae for both impact and non-impact load are summarized in Tab. 5.3, thus allowing to calculate the pressure distribution on and just beneath the revetment. It is important to stress that the latter occur almost simultaneously and should be accounted for in the design accordingly. While the pressure distribution for impact load is considerably damped when transmitted just beneath the revetment, this is not the case for non-impact load for which the damping is negligibly small for practical purpose.

For the prediction of the time related parameters which are based on the parameterization proposed for impact load (Fig. 5.4) and non-impact load (Fig. 5.6), very approximate formulae are tentatively proposed which are summarized in Tab. 5.4. Due to the highly stochastic nature of the wave-induced pressure variations in time, the uncertainties associated with these formulae are very high, making the latter very tentative. An improvement can be achieved only through numerical modelling in future research.

Wave Induced Pore Pressure in the Sand Core beneath the Revetment

The analysis of the wave-induced pore pressure in the sand core beneath the revetment represents one of the most important parts of the project, including both transient and residual pore pressure, the focus being however on the transient component which is more critical for the stability of the sand core beneath the revetment.

For the prediction of the transient pore pressure it was first focused on the development of formulae to calculate the initial pressure p_{3max} at the upper boundary of the sand core beneath the revetment (PT Layer 3), since p_{3max} represents the reference pore pressure to which the damped pore pressure occurring at deeper layers are related. Surprisingly, no impact pressure component is transmitted as such into the sand core, so that all pore pressure recorded in the sand core have a rather quasi-static character, irrespective of the type of wave load considered on the revetment. This made the derivation of formulae for the maximum pore pressure at Layer 3 (p_{3max}) and deeper Layers 4-5 (p_{4max} and p_{5max}) easier. In fact, these could be directly derived by introducing a corresponding damping factor for each layer in Eq. (5.5) for the maximum pressure p_{stat} on the revetment.

The obtained prediction formulae for the maximum pore pressure at layers 3, 4 and 5 in the sand core are summarized in Fig. 9.7, also including Eq. (5.5) for p_{stat} on the revetment. These formulae show that the pore pressure is almost completely damped at a depth of about 80 cm in the sand core beneath the revetment.
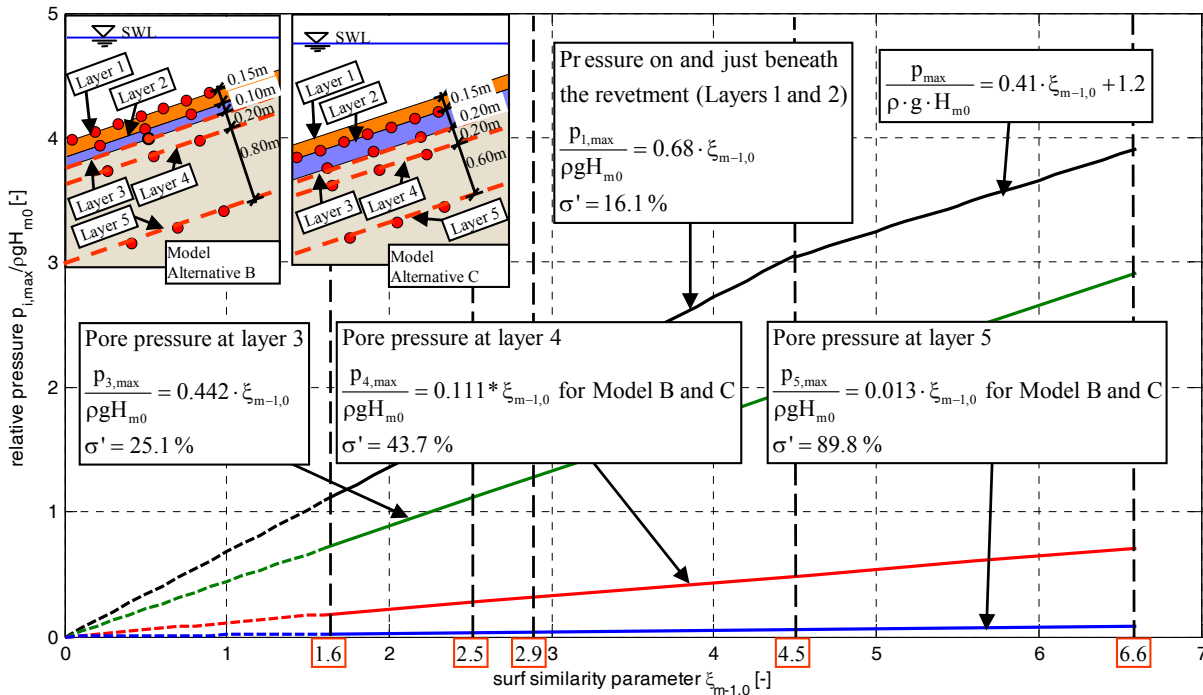
Fig. 9.7: Proposed damping of pressure beneth the revetment

Based on the initial pressure p_{3max} at the upper boundary of the sand core beneath the revetment (Layer 3) which is used as a reference value p_0 (= p_{3max}) the distribution of the pore pressure in deeper layers is analysed at three planes B, C and D normal to the slope, showing that the damping effect is similar for all planes B, C, and D and that the damping rate significantly depends on the initial pressure p_0 (see Fig. 6.16 and Fig. 6.17). Based on the results of this analysis, preliminary formulae are proposed for different ranges of the surf similarity parameter $\xi_{m-1,0}$ (Eqs. (6.13) and Fig. 6.18).

In addition to the formulae in Fig. 9.7 which rather describe the total transient pore pressure, including both "positive" and "negative" components, the "negative" component only is also needed. For the analysis of the stability of the sand core beneath the revetment against soil liquefaction the upwards directed pressure gradient which results from $\Delta u = u_0(z = 0)\text{-}u_t(z)$ (u_0 and u_t are the reference "negative" transient pore pressure at the upper boundary of the sand core ($z = 0$) and the deeper layer at depth z, respectively). Therefore, formulae providing the relative pressure $\Delta \bar{u}(z)$ (Eq. 9.1) as a function of the surf similarity parameter $\xi_{m\text{-}1,0}$ are developed in Annex E (Eqs. E.2.1 and E.2.2, Fig. E.2.3), showing that the upper sand layer just beneath the revetment is rather susceptible to transient soil liquefaction.

$$\Delta \bar{u}(z) = \frac{u_0 - u_t(z)}{\rho g H_{m0}} \tag{9.1}$$

Flexural Displacements

For the prediction of the flexural displacements of the *ELASTOCOAST* revetment, formulae for non-impact load are developed relating linearly the displacement δ [mm] and the maximum pressure p_{stat} on the revetment (kPa):
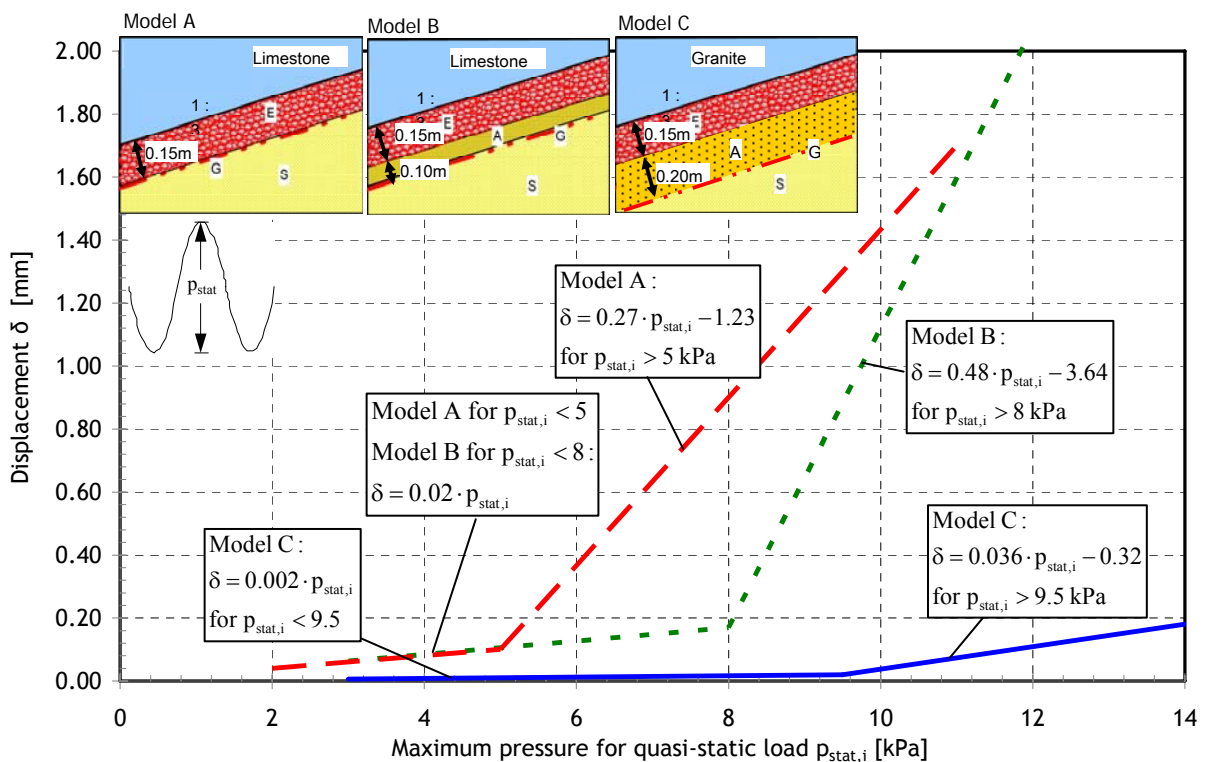
Fig. 9.8: Proposed prediction of the flexural displacement of the *ELASTOCOAST* revetment

In fact, the impact load induces comparatively smaller displacements and the relationship between δ and p_{max} exhibits a considerable scatter, so that a derivation of formulae for impact load is not necessary (see Fig. 7.7 - Fig. 7.9).

Expectedly, the smallest displacement occurs for *Model Alternative C*.

Failure of *Model Alternative A*

Based on the results of the preliminary analysis of the failure reported by Oumeraci et al (2009a), a more detailed analysis has shown that the primary cause of the failure is due to the development of excessive pore pressure in the sand core beneath the revetment which resulted in transient soil liquefaction.
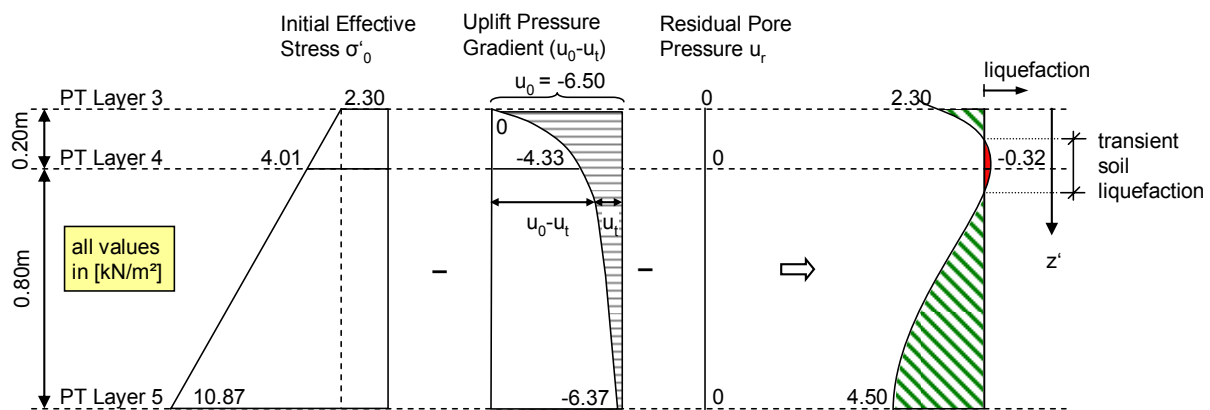
Fig. 9.9:   Failure of *Model Alternative* A due to transient soil liquefaction between layer 3 and 4, Location B

A comparison with stability analysis of *Model Alternative B* for the same regular wave test which caused the failure of *Model Alternative A* illustrates why *Model Alternative B* did not fail. A comparison of the stability of both *Model Alternatives A* and *B* from a previous test with similar wave height and a shorter wave period also illustrates why none of the models failed.

A more detailed analysis of the failure should be performed later (outside this project) by using a numerical model validated by the experimental data.

References

BAW (2005): Prüfbericht zum Geotextil Terrafix 609 (weiß). Bundesanstalt für Wasserbau, BAW, Karlsruhe, Germany, 5 S., 6 Anlagen.

Bijlsma, E. (2008): The Elastocoast system - A study of possible failure mechanisms. *Delft University of Technology*, Delft, The Netherlands, 159 p.

Bruun, P.; Grünback, A.R. (1977): Stability of slopeing structures in relation to surf similarity parameter - risk criteria in design. *Coastal Engineering, Elsevier*, Vol. 1, pp. 287-322.

Davidse, M.P. (2009): Experiment analysis; the relation between wave loading and resulting strain in an asphaltic concrete revetment. *Master Thesis, Delft University of Technology, Faculty of Civil Engineering, Section Hydraulic Engineering*, Delft, The Netherlands, 149 p.

EAK (2002): Empfehlungen für Küstenschutzwerke. Heide i. Holst., Germany: *Die Küste. Archiv für Forschung und Technik an der Nord- und Ostsee*, Heft 65, Boyens & Co., 589 S.

EurOtop (2007): European Overtopping Manual. Pullen, T.; Allsop, N.W.H.; Bruce, T.; Kortenhaus, A.; Schüttrumpf, H.; Van der Meer, J.W.; Kuratorium für Forschung im Küsteningenieurwesen: Die Küste, Heft 73, www.overtopping-manual.com.

Evertz, T. (2009): Verfestigung von Deckwerken mit Polyurethan - Elastomere Deckwerke im Wasserbau. *Technical University of Hamburg-Harburg*, Hamburg-Harburg, Germany, 236.

FZK (2008a): Additional proposal for model tests with *ELASTOCOAST* revetment. Forschungszentrum Küste (FZK), Hannover, Braunschweig.

FZK (2008b): Proposal for model tests with *ELASTOCOAST* revetment. Forschungszentrum Küste (FZK), Hannover, Germany.

Geisenhainer, P.; Kortenhaus, A.; Oumeraci, H. (2008): Large-scale experiments on dike breaching and breach growth. *Proceedings 31st International Conference Coastal Engineering (ICCE)*, Hamburg, Germany.

Gu, D. (2007a): Hydraulic properties of PUR-revetments compared to those of open stone asphalt revetments. *Delft University of Technology*, Delft, The Netherlands, 153 pp.

Gu, D. (2007b): Some important mechanical properties of Elastocoast for safety investigation of dikes. Delft University of Technology, Delft, The Netherlands.

Herbich, J.B. (1999): Handbook of Coastal Engineering. McGraw-Hill.

Klein Breteler, M. (2007): Validatie van GOLKLAP. Report H4134.

Kortenhaus, A.; Oumeraci, H. (2002): Probabilistische Bemessungsmethoden für Seedeiche. Berichte Leichtweiß-Institut für Wasserbau, Technische Universität Braunschweig, Nr. 877, Braunschweig, Germany, 205 S., 6 Anlagen.

Ludwigs, G. (2009): Wave loads on Elastocoast revetment in the large wave flume. *Diplomarbeit am Leichtweiß-Institut für Wasserbau, Fachbereich Bauingenieurwesen, Technische Universität Braunschweig*, Braunschweig, Germany.

Mansard, E.P.D.; Funke, E.R. (1980): The measurement of incident and reflected spectra using a least square method. *Proceedings 17th International Conference Coastal Engineering (ICCE)*, ASCE, Volume 1, Sydney, Australia, pp. 154-172.

Muttray, M. (2000): Wellenbewegung an und in einem geschütteten Wellenbrecher - Laborexperimente im Großmaßstab und theoretische Untersuchungen. Ph.D. thesis, *Dissertation, Fachbereich Bauingenieurwesen, Leichtweiß-Institut für Wasserbau, Technische Universität Braunschweig (02.10.2000)*, Braunschweig, Deutschland, 280S.

Muttray, M. (2001): Wellenbewegung an und in einem geschütteten Wellenbrecher - Laborexperimente im Großmaßstab und theoretische Untersuchungen. Braunschweig, Germany: *Mitteilungen aus dem Leichtweiß-Institut für Wasserbau der Technischen Universität Braunschweig*, Heft 148, S. 1-304.

Oumeraci, H.; Kortenhaus, A.; Allsop, N.W.H.; De Groot, M.B.; Crouch, R.S.; Vrijling, J.K.; Voortman, H.G. (2001): Probabilistic design tools for vertical breakwaters. Rotterdam, The Netherlands: Balkema, 392 p.

Oumeraci, H.; Kortenhaus, A.; Breustedt, H.; Schley, P. (2007): Hydraulic model investigations on breakwaters with a core made of geotextile sand containers. Berichte Leichtweiß-Institut für Wasserbau, Technische Universität Braunschweig, Nr. 933, Braunschweig, Germany, 71 p.

Oumeraci, H.; Kudella, M. (2004): Wave-induced pore pressure in the sandy seabed underneath a caisson breakwater. Berichte Leichtweiß-Institut für Wasserbau, Technische Universität Braunschweig, Nr. 900, Braunschweig, Germany, 119 p.

Oumeraci, H.; Kudella, M.; Staal, T. (2009a): Failure of the Elastocoast revetment during the large-scale model tests in GWK. Berichte Leichtweiß-Institut für Wasserbau, Technische Universität Braunschweig, Nr. 987, Braunschweig, Germany.

Oumeraci, H.; Kudella, M.; Staal, T. (2009b): Pre-design and preparatory works for the large-scale model tests on *ELASTOCOAST* revetment in GWK. Berichte Leichtweiß-Institut für Wasserbau, Technische Universität Braunschweig, Nr. 986, Braunschweig, Germany.

Oumeraci, H.; Muttray, M. (2001): Bemessungswellenparameter vor Strukturen mit verschiedenen Reflexionseigenschaften. Abschlussbericht DFG-Projekt, OU 1/3-3, Braunschweig, Germany, 93 S.

Oumeraci, H.; Staal, T. (2009): Testing the range and accuracy of the Massa Model M-300/95 Ultrasonic Sensor. Leichtweiss Institut for Hydromechanics and Coastal Engineering, Braunschweig, Germany.

Pilarczyk, K.W.; Klein Breteler, M.; Bezuijen, A. (1995): Wave forces and structural response of placed block revetments on inclined structures. *In: Demirbilek, Z. and Kobayashi, N. (eds.): Wave forces on inclined and vertical structures*, New York, USA, pp. 52-87.

Schüttrumpf, H. (2001): Hydrodynamische Belastung der Binnenböschung von Seedeichen durch Wellenüberlauf. Ph.D. thesis, *Dissertation, Fachbereich Bauingenieurwesen, Leichtweiß-Institut für Wasserbau, Technische Universität Braunschweig (05.02.2001)*, Braunschweig, Germany.

Seelig, W.N. (1983): Wave reflection from coastal structures. *Proceedings of Coastal Structures 1983*, American Society of Civil Engineers (ASCE), pp. 961-973.

Staal, T. (2008): Vorbemessung eines innovativen Deckwerks für den Küstenschutz. *Diplomarbeit am Leichtweiß-Institut für Wasserbau, Fachbereich Bauingenieurwesen, Technische Universität Braunschweig*, Braunschweig, Germany, 83 S., 7 Anhänge.

Stive, R.J.H. (1984): Wave impact on Uniform Steep Slopes at Approximately Prototype Scale.

USACE (2002): Coastal Engineering Manual. Engineer Manual 1110-2-1100, US Army Corps of Engineers, Washington D.C., USA (in 6 volumes).

Zanuttigh, B.; Van der Meer, J.W. (2006): Wave reflection from coastal structures. *Proceedings 30th International Conference Coastal Engineering (ICCE)*, ASCE, San Diego, USA, pp. 4337-4349.

Annex A

Locations of measuring devices

A.1 Locations of measuring devices

Tab. A.1.1: Locations of measuring devices in the x-y-z coordinate system (start of test series)

Channel		Description		X	Y	Z (separation wall=0)
1	PT 01	Pressure Transducer	Mod. A, EC top, toe	243.45	2.15	1.10
2	PT 02	Pressure Transducer		245.70	2.90	1.10
3	PT 03	Pressure Transducer		245.95	2.98	1.10
4	PT 04	Pressure Transducer		246.20	3.07	1.10
5	PT 05	Pressure Transducer	Mod. A, EC top, impact area	246.45	3.15	1.10
6	PT 06	Pressure Transducer		246.70	3.23	1.10
7	PT 07	Pressure Transducer		246.95	3.32	1.10
8	PT 08	Pressure Transducer		247.20	3.40	1.10
9	PT 09	Pressure Transducer	Mod. A, EC top, SWL	249.00	4.00	1.10
10	PT 10	Pressure Transducer	Mod. A, EC bottom, toe	243.50	2.01	1.10
11	PT 11	Pressure Transducer		246.00	2.84	1.10
12	PT 12	Pressure Transducer	Mod. A, EC bottom, impact area	246.50	3.01	1.10
13	PT 13	Pressure Transducer		247.00	3.17	1.10
14	PT 14	Pressure Transducer	Mod. A, EC bottom, SWL	249.05	3.86	1.10
15	PT 15	Pressure Transducer		246.06	2.65	1.10
16	PT 16	Pressure Transducer	Mod. A, Sand top, impact area	246.56	2.82	1.10
17	PT 17	Pressure Transducer		247.06	2.99	1.10
18	PT 18	Pressure Transducer	Mod. A, Sand bottom, toe	243.90	1.06	1.10
19	PT 19	Pressure Transducer		246.31	1.89	1.10
20	PT 20	Pressure Transducer	Mod. A, Sand bottom, impact area	246.81	2.06	1.10
21	PT 21	Pressure Transducer		247.31	2.23	1.10
22	PT 22	Pressure Transducer	Mod. A, Sand bottom, SWL	249.00	2.91	1.10
23	PT 23	Pressure Transducer		251.10	2.91	1.10
24	PT 24	Pressure Transducer	Mod. A, water table	253.60	2.91	1.10
25	PT 25	Pressure Transducer		255.60	2.91	1.10
26	PT 26	Pressure Transducer	Mod. B, EC top, toe	243.45	2.15	1.10
27	PT 27	Pressure Transducer		245.70	2.90	1.10
28	PT 28	Pressure Transducer		245.95	2.98	1.10
29	PT 29	Pressure Transducer		246.20	3.07	1.10
30	PT 30	Pressure Transducer	Mod. B, EC top, impact area	246.45	3.15	1.10
31	PT 31	Pressure Transducer		246.70	3.23	1.10
32	PT 32	Pressure Transducer		246.95	3.32	1.10
33	PT 33	Pressure Transducer		247.20	3.40	1.10
34	PT 34	Pressure Transducer	Mod. B, EC top, SWL	249.00	4.00	1.10
35	PT 35	Pressure Transducer	Mod. B, EC bottom, toe	243.50	2.01	1.10
36	PT 36	Pressure Transducer		246.00	2.84	1.10
37	PT 37	Pressure Transducer	Mod. B, EC bottom, impact area	246.50	3.01	1.10
38	PT 38	Pressure Transducer		247.00	3.17	1.10
39	PT 39	Pressure Transducer	Mod. B, EC bottom, SWL	249.05	3.86	1.10
40	PT 40	Pressure Transducer	Mod. B, Filter bottom, impact area	246.53	2.91	1.10
41	PT 41	Pressure Transducer		246.09	2.56	1.10
42	PT 42	Pressure Transducer	Mod. B, Sand top, impact area	246.59	2.72	1.10
43	PT 43	Pressure Transducer		247.09	2.89	1.10
44	PT 44	Pressure Transducer	Mod. B, Sand bottom, toe	243.93	0.96	1.10

Channel		Description		X	Y	Z (separation wall=0)
45	PT 45	Pressure Transducer	Mod. B, Sand bottom, impact area	246.35	1.79	1.10
46	PT 46	Pressure Transducer		246.85	1.96	1.10
47	PT 47	Pressure Transducer		247.35	2.13	1.10
48	PT 48	Pressure Transducer	Sand bottom, SWL	249.40	2.81	1.10
49	DT 1	Displacement Transducer	Mod. A	246.45	3.15	1.25
50	DT 2	Displacement Transducer	Mod. B	246.45	3.15	1.25
51	AT 1	Acceleration Transducer	Mod. A	246.45	3.15	1.25
52	AT 2	Acceleration Transducer	Mod. B	246.45	3.15	1.25
53	RUG 1	Wave Run up Gauge	Mod. A, toe	244.75	2.50	0.80
54	RUG 2	Wave Run up Gauge	Mod. A, crest	250.14	4.38	0.80
55	RUG 3	Wave Run up Gauge	Mod. B, toe	246.45	2.50	0.80
56	RUG 4	Wave Run up Gauge	Mod. B, crest	250.14	4.38	0.80
57	LTG 01	Layer Thickness Gauge	Mod. A, impact area, delta_d=5cm	247.05	3.35	0.00
58	LTG 02	Layer Thickness Gauge	Mod. A, slope low bottom, delta_d=1cm	250.38	4.46	0.00
59	LTG 03	Layer Thickness Gauge	Mod. A, slope low top, delta_d=2cm	250.38	4.70	0.00
60	LTG 04	Layer Thickness Gauge	Mod. A, slope high, delta_d=2cm	253.73	5.58	0.00
61	LTG 05	Layer Thickness Gauge	Mod. A, crest, delta_d=1cm	257.10	6.70	0.00
62	LTG 06	Layer Thickness Gauge	Mod. B, impact area, delta_d=5cm	247.05	3.35	0.00
63	LTG 07	Layer Thickness Gauge	Mod. B, slope low bottom, delta_d=1cm	250.38	4.46	0.00
64	LTG 08	Layer Thickness Gauge	Mod. B, slope low top, delta_d=2cm	250.38	4.70	0.00
65	LTG 09	Layer Thickness Gauge	Mod. B, slope high, delta_d=2cm	253.73	5.58	0.00
66	LTG 10	Layer Thickness Gauge	Mod. B, crest, delta_d=1cm	257.10	6.70	0.00
67	USS 1	Ultrasonic Sensor	Mod. A, slope low	250.38	4.46	1.50
68	USS 2	Ultrasonic Sensor	Mod. B, slope low	253.73	5.58	1.50
69	VT(P) 1	Velocity Transducer	Mod. A, slope low	250.38	4.56	0.45
70	VT(P) 2	Velocity Transducer	Mod. A, slope high, delta_d=2cm	253.73	5.63	0.30
71	VT(P) 3	Velocity Transducer	Mod. A, crest	257.10	6.72	0.15
72	WG 01	Wave Gauge	gauge array 1	79.05	0.00	0.60
73	WG 02	Wave Gauge		81.15	0.00	0.60
74	WG 03	Wave Gauge		84.85	0.00	0.60
75	WG 04	Wave Gauge		90.25	0.00	0.60
76	WG 05	Wave Gauge	gauge array 2	180.00	0.00	0.60
77	WG 06	Wave Gauge		182.10	0.00	0.60
78	WG	Wave Gauge		185.80	0.00	0.60

Channel		Description		X	Y	Z (separation wall=0)
	07					
79	WG 08	Wave Gauge		191.20	0.00	0.60
80	WG 09	Wave Gauge	underwater slope low	220.00	0.00	0.60
81	WG 10	Wave Gauge	underwater slope high	230.00	0.50	0.60
82	WG 11	Wave Gauge	EC low	240.00	1.00	0.60
83	WG 12	Wave Gauge	EC middle	242.70	1.90	0.60
84	WG 13	Wave Gauge	EC high	245.17	2.72	0.60
85		Paddle Stroke	Paddle stroke	0.00	0.00	-
86		Wave Gauge	WG paddle	0.05	0.00	0.00
87	Input	Wave Generator	WG	0.00	0.00	-
88	WG	Wave Gauge	(3.59)	3.59	0.00	0.00

Tab. A.1.2:　　　Locations of measuring devices in the x-y-z coordinate system (changed channels)

Channel		Description		X	Y	Z (separation wall=0)
1	PT 01	Pressure Transducer	Mod. C, EC bottom, toe	243.497	2.008	1.10
2	PT 02	Pressure Transducer		245.747	2.758	1.10
3	PT 03	Pressure Transducer		245.997	2.838	1.10
4	PT 04	Pressure Transducer		246.247	3.928	1.10
5	PT 05	Pressure Transducer	Mod. C, EC bottom, impact area	246.497	3.08	1.10
6	PT 06	Pressure Transducer		246.747	3.088	1.10
7	PT 07	Pressure Transducer		246.997	3.178	1.10
8	PT 08	Pressure Transducer		247.247	3.258	1.10
9	PT 09	Pressure Transducer	Mod. C, EC bottom, SWL	249.047	3.858	1.10
10	PT 10	Pressure Transducer	Mod. C, filter bottom, toe	243.563	1.82	1.10
11	PT 11	Pressure Transducer		246.063	2.65	1.10
12	PT 12	Pressure Transducer	Mod. C, filter bottom, impact area	246.563	2.82	1.10
13	PT 13	Pressure Transducer		247.063	2.984	1.10
14	PT 14	Pressure Transducer	Mod. C, filter bottom, SWL	249.113	3.67	1.10
15	PT 15	Pressure Transducer		246.123	2.46	1.10
16	PT 16	Pressure Transducer	Mod. C, Sand , impact area	246.623	2.63	1.10
17	PT 17	Pressure Transducer		247.123	2.795	1.10
18	PT 18	Pressure Transducer	Mod. C, Sand bottom, toe	243.90	1.06	1.10
19	PT 19	Pressure Transducer		246.31	1.89	1.10
20	PT 20	Pressure Transducer	Mod. C, Sand bottom, impact area	246.81	2.06	1.10
21	PT 21	Pressure Transducer		247.31	2.23	1.10
22	PT 22	Pressure Transducer	Mod. C, Sand bottom, SWL	249.00	2.91	1.10
23	PT 23	Pressure Transducer		251.10	2.91	1.10
24	PT 24	Pressure Transducer	Mod. C, water table	253.60	2.91	1.10
25	PT 25	Pressure Transducer		255.60	2.91	1.10
26	PT 26	Pressure Transducer	Mod. B, EC top, toe	243.45	2.15	1.10

Channel	Description			X	Y	Z (separation wall=0)
27	PT 27	Pressure Transducer		245.70	2.90	1.10
28	PT 28	Pressure Transducer		245.95	2.98	1.10
29	PT 29	Pressure Transducer		246.20	3.07	1.10
30	PT 30	Pressure Transducer	Mod. B, EC top, impact area	246.45	3.15	1.10
31	PT 31	Pressure Transducer		246.70	3.23	1.10
32	PT 32	Pressure Transducer		246.95	3.32	1.10
33	PT 33	Pressure Transducer		247.20	3.40	1.10
34	PT 34	Pressure Transducer	Mod. B, EC top, SWL	249.00	4.00	1.10
35	PT 49	Pressure Transducer	Mod. C, Sand, SWL	249.176	3.481	1.10
36	PT 36	Pressure Transducer		246.00	2.84	1.10
37	PT 37	Pressure Transducer	Mod. B, EC bottom, impact area	246.50	3.01	1.10
38	PT 38	Pressure Transducer		247.00	3.17	1.10
39	PT 39	Pressure Transducer	Mod. B, EC bottom, SWL	249.05	3.86	1.10
40	PT 40	Pressure Transducer	Mod. B, Filter bottom, impact area	246.53	2.91	1.10
41	PT 41	Pressure Transducer		246.09	2.56	1.10
42	PT 42	Pressure Transducer	Mod. B, Sand top, impact area	246.59	2.72	1.10
43	PT 43	Pressure Transducer		247.09	2.89	1.10
44	PT 44	Pressure Transducer	Mod. B, Sand bottom, toe	243.93	0.96	1.10
45	PT 45	Pressure Transducer		246.35	1.79	1.10
46	PT 46	Pressure Transducer	Mod. B, Sand bottom, impact area	246.85	1.96	1.10
47	PT 47	Pressure Transducer		247.35	2.13	1.10
48	PT 48	Pressure Transducer	Sand bottom, SWL	249.40	2.81	1.10

Annex B

List of tests performed for regular and irregular waves

B.1 Incident wave parameters and wave reflection analysis

B.1.1 Regular wave tests

Test	H_{nom} [m]	T_{nom} [s]	h [m]	H_m [m]	T_m [s]	C_r [-]	ξ_m [-]
09051301	0.2	3.0	3.40	0.22	3.00	0.339	2.67
09051302	0.2	4.0	3.40	0.19	4.00	0.621	3.77
09051303	0.2	5.0	3.40	0.21	5.00	0.682	4.59
09051401	0.2	6.0	3.40	0.18	5.93	0.734	5.78
09051402	0.2	7.0	3.40	0.22	7.00	0.782	6.24
09051403	0.2	8.0	3.40	0.17	7.90	0.860	7.94
09051404	0.6	3.0	3.40	0.65	3.00	0.127	1.55
09051405	0.6	4.0	3.60	0.68	4.01	0.292	2.02
09051406	1.0	3.0	3.60	1.04	3.00	0.183	1.22
09051501	0.6	5.0	3.70	0.64	4.95	0.487	2.57
09051502	1.0	4.0	3.70	1.14	3.92	0.161	1.53
09051503	1.3	4.0	3.70	1.40	3.92	0.143	1.38
09051504	0.6	6.0	3.90	0.65	6.00	0.581	3.1
09051505	0.6	7.0	3.90	0.54	6.93	0.665	3.91
09051801	0.6	8.0	3.90	0.55	7.98	0.695	4.49
09051802	1.3	5.0	3.90	1.37	4.90	0.155	1.75
09060501	0.2	3.0	3.40	0.22	2.99	0.332	2.65
09060502	0.2	5.0	3.40	0.20	5.00	0.678	4.66
09060503	0.2	8.0	3.40	0.17	8.00	0.863	8.05
09060504	0.6	3.0	3.40	0.66	3.00	0.091	1.54
09060505	0.6	4.0	3.60	0.69	4.00	0.289	2
09061803	0.6	5.0	3.80	0.58	4.99	0.521	2.72
09061804	0.6	6.0	3.90	0.72	6.00	0.567	2.95
09061805	0.6	7.0	3.90	0.52	6.99	0.633	4.02
09062301	0.5	7.0	3.80	0.44	7.00	0.731	4.39
09062302	0.4	8.0	3.70	0.50	7.99	0.731	4.72
09062303	0.7	3.0	3.50	0.67	3.00	0.102	1.53
09062304	0.8	3.0	3.50	0.75	3.00	0.119	1.44
09062305	0.9	3.0	3.50	0.84	3.00	0.152	1.36
09062306	1.0	3.0	3.50	0.92	3.01	0.105	1.31
09062307	0.4	3.0	3.40	0.39	3.00	0.241	1.99
09062308	0.5	3.0	3.40	0.49	3.00	0.228	1.79
09062912	1.0	5.0	3.90	1.01	5.01	0.358	2.08
09062913	1.0	6.0	4.10	0.92	6.02	0.496	2.61
09062914	1.3	6.0	4.20	1.24	6.03	0.406	2.25
09062915	1.0	7.0	4.20	1.17	7.02	0.541	2.7
09062916	1.0	8.0	4.20	0.91	8.05	0.689	3.52

—————— Failure of *Model Alternative A*

B.1.2   Irregular wave tests

Test	H_{nom} [m]	T_{nom} [s]	h [m]	H_{m0} [m]	$T_{m-1.0}$ [s]	C_r [-]	$\xi_{m-1,0}$ [-]
09060801	0.2	3.0	3.40	0.22	2.71	0.316	2.40
09060803	0.2	4.0	3.40	0.23	3.61	0.464	3.14
09060804	0.3	3.0	3.40	0.33	2.71	0.287	1.98
09060805	0.5	3.0	3.40	0.49	2.79		1.65
09060901	0.4	4.0	3.50	0.45	3.62	0.4	2.23
09060902	0.5	4.0	3.60	0.53	3.64		2.09
09060903	0.6	4.0	3.60	0.67	3.61	0.348	1.84
09060904	0.4	6.0	3.70	0.43	5.42	0.608	3.45
09061001	0.2	8.0	3.40	0.19	7.04	0.735	6.64
09061002	0.2	6.0	3.40	0.21	5.43	0.634	4.91
09061003	0.3	4.0	3.50	0.34	3.58	0.443	2.55
09061004	0.3	5.0	3.50	0.34	4.46		3.19
09061101	0.3	8.0	3.50	0.30	6.88		5.25
09061102	0.3	7.0	3.50	0.31	6.21		4.64
09061103	0.3	6.0	3.50	0.32	5.54	0.632	4.06
09061104	0.3	5.0	3.50	0.32	4.59	0.555	3.38
09061201	0.4	5.0	3.60	0.38	4.66		3.16
09061202	0.4	7.0	3.70	0.42	6.40	0.682	4.09
09061203	0.4	8.0	3.70	0.42	7.11	0.73	4.56
09061501	0.5	8.0	3.80	0.53	6.96	0.713	3.97
09061502	0.5	6.0	3.80	0.53	5.54	0.598	3.17
09061601	0.4	3.0	3.40	0.40	2.66	0.271	1.75
09061602	0.5	3.0	3.40	0.49	2.69	0.256	1.60
09061603	0.3	7.0	3.50	0.31	6.45	0.69	4.79
09061801	0.7	4.0	3.60	0.70	3.62		1.80
09061802	0.7	5.0	3.80	0.72	4.61	0.453	2.26
09061901	0.5	7.0	3.80	0.53	6.41	0.658	3.66
09061902	0.5	5.0	3.70	0.53	4.60	0.515	2.63
09061903	0.2	7.0	3.40	0.21	6.48	0.697	5.89
09062201	0.6	5.0	3.80	0.63	4.60	0.491	2.41
09062202	0.6	6.0	3.90	0.64	5.55	0.577	2.90
09062203	0.7	7.0	4.00	0.74	6.41	0.624	3.10
09062204	0.7	6.0	4.00	0.74	5.55	0.552	2.69
09062309	0.8	5.0	3.90	0.83	4.54	0.418	2.07
09062401	0.6	8.0	4.00	0.64	7.02	0.704	3.66
09062403	0.6	7.0	3.90	0.62	7.08	0.694	3.73
09062501	1.0	6.0	4.10	1.04	5.52	0.487	2.26
09062502	0.8	8.0	4.00	0.87	6.68	0.669	2.99
09062503	1.0	7.0	4.00	1.04	6.38	0.545	2.61
09062504	0.8	7.0	4.00	0.84	6.39	0.593	2.90

Test	H_nom [m]	T_nom [s]	h [m]	H_m0 [m]	T_m-1.0 [s]	C_r [-]	ξ_m-1,0 [-]
09062505	0.8	6.0	4.00	0.84	5.54	0.538	2.51
09062601	1.0	5.0	3.90	1.03	4.63	0.385	1.90
09062602	0.9	5.0	3.90	0.93	4.60	0.416	1.99
09062603	1.0	8.0	4.00	1.08	6.60	0.638	2.65
09062604	1.1	6.0	4.20	1.14	5.57	0.476	2.17
09062607	0.9	6.0	4.00	0.94	5.54	0.51	2.37
09062911	1.2	8.0	3.80	1.17	6.54	0.316	2.52

only for analysis of p_{max} layer 1

B.1.3 Solitary wave tests

Test	H_nom [m]	T_nom [s]	h [m]	H_m0 [m]	T_m-1.0 [s]	C_r [-]	ξ_m-1,0 [-]
09062605	0.5	-	4.00	-	-	-	-
09062606	1.0	-	4.00	-	-	-	-
09062903	0.25	-	4.00	-	-	-	-
09062904	0.75	-	4.00	-	-	-	-
09062905	1.2	-	4.00	-	-	-	-

B.1.4 Freak wave tests

Test	H_nom [m]	T_nom [s]	h [m]	H_m0 [m]	T_m-1.0 [s]	C_r [-]	ξ_m-1,0 [-]
09062901	1.20	-	4.00	-	-	-	-
09062902	1.20	-	4.00	-	-	-	-
09062906	1.00	-	4.00	-	-	-	-
09062907	1.00	-	4.00	-	-	-	-
09062908	0.80	-	4.00	-	-	-	-
09062909	1.40		4.00				
09062910	1.40		4.00				

Annex C

Main results of regular and irregular wave tests (Tables)

C.1 Test results all layers

C.1.1 Regular wave tests

Tab. C.1.1:   Test results for regular wave tests, Model Alternative A

Test	Config.	WT	H_{m0} [m]	$T_{m-1,0}$ [s]	h_s [m]	$\xi_{m-1,0}$ [-]	n [-]	C_r [-]	$p_{max}/\rho g H_{m0}$ [-]	$p_{2max}/\rho g H_{m0}$ [-]	$p_{3max}/\rho g H_{m0}$ [-]	$p_{4max}/\rho g H_{m0}$ [-]	$p_{5max}/\rho g H_{m0}$ [-]	z_{pmax}/H_{m0} [-]	δ	$u_{r,4}$ [kPa]	$u_{r,5}$ [kPa]	$R_{u2\%}/H_{m0}$ [-]	$R_{d2\%}/H_{m0}$ [-]
090513 01	A	RW	0.22	3.00	3.4	2.667	100	0.339	1.311	0.914	-	0.069	0.015	0.775	0.000	-	-	1.385	-0.824
090513 02	A	RW	0.19	4.00	3.4	3.774	100	0.621	1.747	1.412	-	0.149	0.032	0.873	0.060	-	-	1.845	-1.366
090513 03	A	RW	0.21	5.00	3.4	4.588	100	0.682	2.316	2.070	-	0.343	0.032	1.602	-	-	-	1.834	-1.589
090514 01	A	RW	0.18	5.93	3.4	5.781	100	0.734	2.700	2.570	-	0.411	0.044	1.809	-	-	-	2.058	-1.824
090514 02	A	RW	0.22	7.00	3.4	6.245	100	0.782	2.833	2.761	-	0.663	0.046	1.929	-	-	-	2.163	-1.670
090514 03	A	RW	0.17	7.90	3.4	7.943	100	0.860	3.384	3.369	-	0.745	0.057	1.924	-	-	-	1.818	-1.858
090514 04	A	RW	0.65	3.00	3.4	1.548	100	0.127	1.104	0.875	-	0.103	0.017	0.123	0.210	-	-	1.226	0.031
090514 05	A	RW	0.68	4.01	3.6	2.024	100	0.292	1.138	0.885	-	0.121	0.032	0.663	-	-	-	1.678	-0.034
090514 06	A	RW	1.04	3.00	3.6	1.223	100	0.183	1.221	0.848	-	0.155	0.015	0.268	0.400	-	-	0.887	0.241
090515 01	A	RW	0.64	4.95	3.7	2.574	100	0.487	1.134	0.995	-	0.311	0.037	0.982	-	-	-	1.785	-0.363
090515 02	A	RW	1.14	3.92	3.7	1.528	100	0.161	1.315	1.130	-	0.289	0.028	0.411	0.620	-	-	1.389	0.283
090515 03	A	RW	1.40	3.92	3.7	1.379	100	0.143	1.550	0.997	-	0.327	0.027	0.335	1.114	-	-	1.220	0.285
090515 04	A	RW	0.65	6.00	3.9	3.099	100	0.581	1.525	1.305	-	0.560	0.032	1.275	1.572	-	-	2.068	-0.503
090515 05	A	RW	0.54	6.93	3.9	3.910	100	0.665	2.149	1.895	-	0.711	0.049	1.690	1.665	-	-	2.148	-0.903
090518 01	A	RW	0.55	7.98	3.9	4.494	100	0.695	2.081	1.820	-	0.788	0.050	1.516	-	-	-	2.181	-1.127
090518 02	A	RW	1.37	4.90	3.9	1.745	100	0.155	1.171	0.781	-	0.217	0.022	0.732	-	-	-	-	0.323

Tab. C.1.2:   Test results for regular wave tests, Model Alternative B

Test	Config.	WT	H_{m0} [m]	$T_{m-1,0}$ [s]	h_s [m]	$\xi_{m-1,0}$ [-]	n [-]	C_r [-]	$p_{max}/\rho g H_{m0}$ [-]	$p_{2max}/\rho g H_{m0}$ [-]	$p_{3max}/\rho g H_{m0}$ [-]	$p_{4max}/\rho g H_{m0}$ [-]	$p_{5max}/\rho g H_{m0}$ [-]	z_{pmax}/H_{m0} [-]	δ	$u_{r,4}$ [kPa]	$u_{r,5}$ [kPa]	$R_{u2\%}/H_{m0}$ [-]	$R_{d2\%}/H_{m0}$ [-]
090513 01	B	RW	0.22	3.00	3.4	2.667	100	0.339	1.096	0.910	0.630	0.111	0.023	1.139	-	-	-	1.123	-0.714
090513 02	B	RW	0.19	4.00	3.4	3.774	100	0.621	1.792	1.607	1.221	0.328	0.038	1.284	-	-	-	1.771	-1.286
090513 03	B	RW	0.21	5.00	3.4	4.588	100	0.682	2.065	1.974	1.502	0.387	0.027	1.214	-	-	-	1.665	-1.515
090514 01	B	RW	0.18	5.93	3.4	5.781	100	0.734	2.653	2.478	1.969	0.436	0.050	1.371	-	-	-	1.788	-1.770
090514 02	B	RW	0.22	7.00	3.4	6.245	100	0.782	2.783	2.670	1.898	0.483	0.037	1.929	-	-	-	1.995	-1.605
090514 03	B	RW	0.17	7.90	3.4	7.943	100	0.860	3.334	3.253	2.317	0.638	0.046	2.449	-	-	-	1.701	-1.806
090514 04	B	RW	0.65	3.00	3.4	1.548	100	0.127	0.929	0.783	0.552	0.069	0.012	0.123	0.194	-	-	1.236	-0.040
090514 05	B	RW	0.68	4.01	3.6	2.024	100	0.292	1.049	0.809	0.624	0.060	0.024	0.780	-	-	-	1.694	-0.196
090514 06	B	RW	1.04	3.00	3.6	1.223	100	0.183	1.325	0.798	0.430	0.044	0.012	0.268	0.161	-	-	0.916	0.263
090515 01	B	RW	0.64	4.95	3.7	2.574	100	0.487	1.172	1.079	0.846	0.158	0.030	0.982	-	-	-	1.955	-0.532
090515 02	B	RW	1.14	3.92	3.7	1.528	100	0.161	1.166	0.903	0.570	0.089	0.022	0.481	0.257	-	-	1.445	0.353
090515 03	B	RW	1.40	3.92	3.7	1.379	100	0.143	1.597	0.852	0.100	0.121	0.021	0.335	0.484	-	-	1.284	0.412
090515 04	B	RW	0.65	6.00	3.9	3.099	100	0.581	1.485	1.421	1.140	0.298	0.027	1.275	-	-	-	2.128	-0.724
090515 05	B	RW	0.54	6.93	3.9	3.910	100	0.665	2.070	2.012	1.586	0.507	0.040	1.690	-	-	-	2.165	-1.144
090518 01	B	RW	0.55	7.98	3.9	4.494	100	0.695	2.049	1.971	1.640	0.536	0.038	1.516	-	-	-	2.224	-1.283
090518 02	B	RW	1.37	4.90	3.9	1.745	100	0.155	1.040	0.955	0.717	0.162	0.021	0.732	-	-	-	1.811	0.363
090605 01	B	RW	0.22	2.99	3.4	2.653	100	0.332	1.214	0.887	0.242	0.109	0.029	0.773	-	-	-	1.207	-0.844
090605 02	B	RW	0.20	5.00	3.4	4.663	100	0.678	2.396	1.774	0.580	0.094	0.023	1.653	-	-	-	1.788	-1.712
090605 03	B	RW	0.17	8.00	3.4	8.054	100	0.863	3.751	2.207	0.969	0.138	0.058	2.455	-	-	-	1.672	-1.852
090605 04	B	RW	0.66	3.00	3.4	1.540	100	0.091	0.920	0.654	0.118	0.058	0.013	0.380	0.017	-	-	1.198	-0.059
090605 05	B	RW	0.69	4.00	3.6	2.005	100	0.289	1.047	0.666	0.132	0.075	0.036	0.652	-	-	-	1.770	-0.114
090618 03	B	RW	0.58	4.99	3.8	2.720	50	0.521	1.335	-	0.239	0.168	0.030	1.112	-	-	-	2.026	-0.758
090618 04	B	RW	0.72	6.00	3.9	2.952	50	0.567	1.453	-	0.332	0.285	0.025	1.284	1.063	-	-	2.259	-0.515
090618 05	B	RW	0.52	6.99	3.9	4.019	50	0.633	2.276	-	0.626	0.362	0.044	1.754	-	-	-	2.597	-1.101
090623 01	B	RW	0.44	7.00	3.8	4.390	50	0.731	2.387	-	0.707	0.340	0.042	1.857	-	-	-	2.435	-1.478
090623 02	B	RW	0.50	7.99	3.7	4.723	50	0.731	2.324	-	0.646	0.360	0.038	1.612	-	-	-	2.037	-1.234
090623 03	B	RW	0.67	3.00	3.5	1.527	50	0.102	1.279	-	0.147	0.067	0.024	0.403	0.050	-	-	1.100	-0.095
090623 04	B	RW	0.75	3.00	3.5	1.439	50	0.119	1.420	-	0.136	0.057	0.014	0.358	0.039	-	-	1.043	-0.009
090623 05	B	RW	0.84	3.00	3.5	1.361	50	0.152	1.098	-	0.105	0.030	0.015	0.320	0.057	-	-	0.999	0.061
090623 06	B	RW	0.92	3.00	3.5	1.306	50	0.105	1.378	-	0.086	0.022	0.012	0.294	0.075	-	-	0.914	0.100
090623 07	B	RW	0.39	3.00	3.4	1.992	50	0.241	0.974	-	0.151	0.059	0.024	1.269	-	-	-	1.335	-0.478
090623 08	B	RW	0.49	3.00	3.4	1.789	50	0.228	1.244	-	0.119	0.061	0.018	0.512	-	-	-	1.265	-0.352
090629 12	B	RW	1.01	5.01	3.9	2.076	30	0.358	1.218	-	0.269	0.091	0.020	-	-	-	-	2.201	-0.016
090629 13	B	RW	0.92	6.01	4.1	2.605	30	0.496	1.428	-	0.437	0.232	0.031	-	-	-	-	2.230	-0.291
090629 14	B	RW	1.24	6.03	4.2	2.253	30	0.406	1.385	-	0.401	0.239	0.031	-	-	-	-	-	0.023
090629 15	B	RW	1.17	7.02	4.2	2.703	30	0.541	1.431	-	0.566	0.355	0.041	-	3.592	-	-	-	-0.127
090629 16	B	RW	0.91	8.05	4.2	3.516	30	0.689	2.001	-	0.872	0.554	0.067	-	-	-	-	2.308	-0.790

Tab. C.1.3: Test results for regular wave tests, Model Alternative C

Test	Config.	WT	H_{m0} [m]	$T_{m-1,0}$ [s]	h_s [m]	$\xi_{m-1,0}$ [-]	n [-]	C_r [-]	$p_{max}/\rho g H_{m0}$ [-]	$p_{2max}/\rho g H_{m0}$ [-]	$p_{3max}/\rho g H_{m0}$ [-]	$p_{4max}/\rho g H_{m0}$ [-]	$p_{5max}/\rho g H_{m0}$ [-]	z_{pmax}/H_{m0} [-]	δ	$u_{r,4}$ [kPa]	$u_{r,5}$ [kPa]	$R_{u2\%}/H_{m0}$ [-]	$R_{d2\%}/H_{m0}$ [-]
090605 01	C	RW	0.22	2.99	3.4	2.653	100	0.332	-	1.054	0.583	0.103	0.020	-	-	-	-	1.187	-0.811
090605 02	C	RW	0.20	5.00	3.4	4.663	100	0.678	-	0.000	0.000	0.000	0.000	-	-	-	-	1.868	-1.404
090605 03	C	RW	0.17	8.00	3.4	8.054	100	0.863	-	3.332	2.589	0.682	0.046	-	-	-	-	1.822	-1.768
090605 04	C	RW	0.66	3.00	3.4	1.540	100	0.091	-	0.910	0.581	0.069	0.015	-	-	-	-	1.113	0.017
090605 05	C	RW	0.69	4.00	3.6	2.005	100	0.289	-	0.942	0.965	0.063	0.030	-	-	-	-	1.858	-0.148
090618 03	C	RW	0.58	4.99	3.8	2.720	50	0.521	-	1.216	1.153	0.140	0.037	-	-	-	-	2.050	-0.575
090618 04	C	RW	0.72	6.00	3.9	2.952	50	0.567	-	1.302	0.799	0.191	0.031	-	0.028	-	-	2.115	-0.474
090618 05	C	RW	0.52	6.99	3.9	4.019	50	0.633	-	2.063	1.384	0.318	0.046	-	-	-	-	2.473	-1.063
090623 01	C	RW	0.44	7.00	3.8	4.390	50	0.731	-	2.236	1.513	0.330	0.045	-	-	-	-	2.370	-1.442
090623 02	C	RW	0.50	7.99	3.7	4.723	50	0.731	-	2.348	1.472	0.306	0.047	-	-	-	-	2.083	-1.238
090623 03	C	RW	0.67	3.00	3.5	1.527	50	0.102	-	1.054	0.583	0.032	0.016	-	-	-	-	1.103	-0.077
090623 04	C	RW	0.75	3.00	3.5	1.439	50	0.119	-	1.097	0.557	0.063	0.016	-	-	-	-	1.067	0.001
090623 05	C	RW	0.84	3.00	3.5	1.361	50	0.152	-	0.990	0.577	0.035	0.016	-	-	-	-	1.000	0.093
090623 06	C	RW	0.92	3.00	3.5	1.306	50	0.105	-	0.988	0.557	0.021	0.013	-	-	-	-	0.935	0.135
090623 07	C	RW	0.39	3.00	3.4	1.992	50	0.241	-	0.811	0.641	0.084	0.020	-	-	-	-	1.237	-0.523
090623 08	C	RW	0.49	3.00	3.4	1.789	50	0.228	-	0.781	0.670	0.037	0.017	-	-	-	-	1.236	-0.308
090629 12	C	RW	1.01	5.01	3.9	2.076	30	0.358	-	1.064	0.746	0.074	0.022	-	-	-	-	2.130	-0.067
090629 13	C	RW	0.92	6.01	4.1	2.605	30	0.496	-	1.370	0.814	0.182	0.031	-	-	-	-	-	-0.346
090629 14	C	RW	1.24	6.03	4.2	2.253	30	0.406	-	1.276	0.790	0.164	0.028	-	-	-	-	-	0.049
090629 15	C	RW	1.17	7.02	4.2	2.703	30	0.541	-	1.270	0.835	0.315	0.040	-	0.178	-	-	-	-0.084
090629 16	C	RW	0.91	8.05	4.2	3.516	30	0.689	-	1.778	1.222	0.493	0.065	-	-	-	-	-	-0.867

C.1.2 Irregular wave tests

Tab. C.1.4: Test results for irregular wave tests, Model Alternative B

Test	Config.	WT	H_{m0} [m]	$T_{m-1,0}$ [s]	h_s [m]	$\xi_{m-1,0}$ [-]	n [-]	C_r [-]	$p_{max}/\rho g H_{m0}$ [-]	$p_{2max}/\rho g H_{m0}$ [-]	$p_{3max}/\rho g H_{m0}$ [-]	$p_{4max}/\rho g H_{m0}$ [-]	$p_{5max}/\rho g H_{m0}$ [-]	z_{pmax}/H_{m0} [-]	δ	$u_{r,4}$ [kPa]	$u_{r,5}$ [kPa]	$R_{u2\%}/H_{m0}$ [-]	$R_{d2\%}/H_{m0}$ [-]
09060801	B	WS	0.22	2.71	3.4	2.400	1000	0.316	1.677	-	0.208	0.084	0.029	0.767	-	0.215	0.111	1.309	-0.857
09060803	B	WS	0.23	3.61	3.4	3.140	1000	0.464	2.073	-	0.458	0.089	0.025	1.442	-	0.323	0.145	1.652	-1.446
09060804	B	WS	0.33	2.71	3.4	1.979	1000	0.287	4.008	-	0.228	0.049	0.025	0.767	-	0.371	0.209	1.488	-0.676
09060805	B	WS	0.49	2.79	3.4	1.653	1000	-	5.363	-	-	-	-	0.506	-	-	-	-	-
09060901	B	WS	0.45	3.62	3.5	2.234	1000	0.400	7.458	-	0.254	0.089	0.025	0.947	-	0.438	0.254	1.943	-0.839
09060902	B	WS	0.53	3.64	3.6	2.095	1000	-	5.021	-	-	-	-	1.009	-	-	-	-	-
09060903	B	WS	0.67	3.61	3.6	1.838	1000	0.348	5.677	-	0.327	0.127	0.077	0.553	0.016	0.394	0.209	1.959	-0.592
09060904	B	WS	0.43	5.42	3.7	3.448	1000	0.608	2.477	-	0.757	0.076	0.034	1.870	-	0.440	0.141	2.503	-1.410
09061001	B	WS	0.19	7.04	3.4	6.644	1000	0.735	4.159	-	1.181	0.161	0.057	2.565	-	0.613	0.273	2.381	-2.269
09061002	B	WS	0.21	5.43	3.4	4.905	1000	0.634	3.194	-	0.861	0.113	0.043	2.352	-	0.521	0.258	2.330	-2.052
09061003	B	WS	0.34	3.58	3.5	2.553	1000	0.443	2.255	-	0.328	0.062	0.031	1.264	-	0.244	0.151	1.787	-1.011
09061004	B	WS	0.34	4.46	3.5	3.191	1000	-	2.211	-	-	-	-	1.535	-	-	-	-	-
09061101	B	WS	0.30	6.88	3.5	5.254	1000	-	3.332	-	-	-	-	2.020	-	-	-	-	-
09061102	B	WS	0.31	6.21	3.5	4.644	1000	-	3.017	-	-	-	-	1.932	-	-	-	-	-
09061103	B	WS	0.32	5.54	3.5	4.062	1000	0.632	2.564	-	0.776	0.114	0.049	1.863	-	0.514	0.229	2.307	-1.678
09061104	B	WS	0.32	4.59	3.5	3.382	1000	0.555	2.308	-	0.606	0.138	0.051	1.625	-	0.363	0.108	2.186	-1.468
09061201	B	WS	0.38	4.66	3.6	3.163	1000	-	2.288	-	-	-	-	1.856	-	-	-	-	-
09061202	B	WS	0.42	6.40	3.7	4.092	1000	0.682	2.714	-	1.032	0.484	0.052	1.885	-	0.442	0.157	2.580	-1.508
09061203	B	WS	0.42	7.11	3.7	4.563	1000	0.730	3.087	-	1.110	0.474	0.069	1.898	-	0.438	0.169	2.759	-1.492
09061501	B	WS	0.53	6.96	3.8	3.968	1000	0.713	2.646	-	1.049	0.596	0.062	1.685	-	0.441	0.248	2.730	-1.336
09061502	B	WS	0.53	5.54	3.8	3.169	1000	0.598	2.211	-	0.705	0.328	0.035	1.700	-	0.156	0.018	2.655	-1.262
09061601	B	WS	0.40	2.66	3.4	1.749	1000	0.271	4.742	-	0.184	0.052	0.018	0.423	-	0.409	0.246	1.358	-0.577
09061602	B	WS	0.49	2.69	3.4	1.600	1000	0.256	6.015	-	0.246	0.071	0.024	0.346	0.036	0.630	0.276	1.365	-0.492
09061603	B	WS	0.31	6.45	3.5	4.792	1000	0.690	3.032	-	1.038	0.263	0.048	1.912	-	0.744	0.349	2.544	-1.813
09061801	B	WS	0.70	3.62	3.6	1.799	1000	-	4.974	-	-	-	-	0.527	-	-	-	-	-
09061802	B	WS	0.72	4.61	3.8	2.260	1000	0.453	2.894	-	0.187	0.151	0.023	0.664	-	0.250	0.046	2.573	-0.832
09061901	B	WS	0.53	6.41	3.8	3.664	1000	0.658	2.520	-	0.720	0.510	0.061	1.696	-	0.169	0.090	2.762	-1.349
09061902	B	WS	0.53	4.60	3.7	2.634	1000	0.515	2.712	-	0.242	0.156	0.027	1.361	-	0.068	0.127	2.298	-1.035
09061903	B	WS	0.21	6.48	3.4	5.893	1000	0.697	3.499	-	0.772	0.188	0.103	2.386	-	0.498	0.273	2.287	-2.280
09062201	B	WS	0.63	4.60	3.8	2.411	1000	0.491	2.179	-	0.230	0.157	0.025	0.902	-	0.136	0.078	2.363	-0.942
09062202	B	WS	0.64	5.55	3.9	2.896	1000	0.577	2.029	-	0.271	0.189	0.026	1.178	-	0.196	0.022	2.586	-1.082
09062203	B	WS	0.74	6.41	4.0	3.103	1000	0.624	2.194	-	0.525	0.383	0.044	1.380	1.809	0.395	0.011	2.820	-1.057
09062204	B	WS	0.74	5.55	4.0	2.689	1000	0.552	2.198	-	0.404	0.337	0.031	1.491	-	0.301	0.096	2.679	-1.009
09062309	B	WS	0.83	4.54	3.9	2.072	1000	0.418	4.281	-	0.260	0.279	0.035	1.102	1.175	0.134	0.023	2.233	-0.740
09062401	B	WS	0.64	7.02	4.0	3.663	1000	0.704	2.615	-	0.943	0.537	0.053	1.725	-	0.380	0.037	2.708	-1.281
09062403	B	WS	0.62	7.08	3.9	3.730	500	0.694	2.431	-	0.820	0.536	0.048	1.601	1.979	0.314	0.020	2.884	-1.259
09062501	B	WS	1.04	5.52	4.1	2.261	500	0.487	2.157	-	0.396	0.056	0.009	0.918	2.470	0.194	0.009	-	-0.780
09062502	B	WS	0.87	6.68	4.0	2.990	500	0.669	2.144	-	0.724	0.421	0.050	1.269	-	0.180	0.011	-	-1.007
09062503	B	WS	1.04	6.38	4.0	2.609	500	0.545	1.772	-	0.563	0.369	0.092	0.898	-	0.449	0.008	-	-0.849
09062504	B	WS	0.84	6.39	4.0	2.901	500	0.593	2.053	-	0.604	0.510	0.044	1.306	-	0.391	0.016	2.847	-1.029
090625 05	B	WS	0.84	5.54	4.0	2.513	500	0.538	-	-	0.521	0.397	0.039	-	-	0.166	0.008	2.470	-0.902
090626 01	B	WS	1.03	4.63	3.9	1.900	500	0.385	-	-	0.375	0.345	0.054	-	-	0.446	0.063	2.140	-0.682
090626 02	B	WS	0.93	4.60	3.9	1.987	500	0.416	-	-	0.216	0.230	0.029	-	-	0.078	0.011	2.341	-0.720
090626 03	B	WS	1.08	6.60	4.0	2.651	500	0.638	-	-	0.641	0.410	0.055	-	-	0.636	0.005	-	-0.854
090626 04	B	WS	1.14	5.57	4.2	2.174	500	0.476	-	-	0.366	0.336	0.035	-	-	0.461	0.003	-	-0.759
090626 07	B	WS	0.94	5.54	4.0	2.375	500	0.510	-	-	0.221	0.218	0.021	-	-	0.160	0.031	2.650	-0.895
09062911	B	WS	1.17	6.54	3.8	2.520	500	-	-	-	-	-	-	-	-	-	-	-	-

Tab. C.1.5: Test results for irregular wave tests, Model Alternative C

Test	Config.	WT	H_{m0} [m]	$T_{m-1,0}$ [s]	h_s [m]	$\xi_{m-1,0}$ [-]	n [-]	C_r [-]	$p_{max}/\rho g H_{m0}$ [-]	$p_{2max}/\rho g H_{m0}$ [-]	$p_{3max}/\rho g H_{m0}$ [-]	$p_{4max}/\rho g H_{m0}$ [-]	$p_{5max}/\rho g H_{m0}$ [-]	z_{pmax}/H_{m0} [-]	δ	$u_{r,4}$ [kPa]	$u_{r,5}$ [kPa]	$R_{u2\%}/H_{m0}$ [-]	$R_{d2\%}/H_{m0}$ [-]
09060801	C	WS	0.22	2.71	3.4	2.400	1000	0.316	-	1.300	0.760	0.119	0.020	-	-	0.770	0.175	1.378	-0.864
09060803	C	WS	0.23	3.61	3.4	3.140	1000	0.464	-	1.792	1.188	0.214	0.032	-	-	0.350	0.251	1.795	-1.208
09060804	C	WS	0.33	2.71	3.4	1.979	1000	0.287	-	2.521	1.013	0.085	0.030	-	-	0.390	0.312	1.369	-0.671
09060805	C	WS	0.49	2.79	3.4	1.653	1000	-	-	2.170	-	-	-	-	-	-	-	-	-
09060901	C	WS	0.45	3.62	3.5	2.234	1000	0.400	-	2.276	1.316	0.185	0.029	-	-	0.437	0.408	1.829	-0.784
09060902	C	WS	0.53	3.64	3.6	2.095	1000	-	-	2.574	-	-	-	-	-	-	-	-	-
09060903	C	WS	0.67	3.61	3.6	1.838	1000	0.348	-	3.711	1.217	0.196	0.119	-	0.029	0.470	0.355	1.948	-0.575
09060904	C	WS	0.43	5.42	3.7	3.448	1000	0.608	-	2.327	1.499	0.452	0.048	-	-	0.503	0.353	2.376	-1.334
09061001	C	WS	0.19	7.04	3.4	6.644	1000	0.735	-	3.967	2.649	0.688	0.065	-	-	0.751	0.480	2.344	-2.215
09061002	C	WS	0.21	5.43	3.4	4.905	1000	0.634	-	3.069	1.879	0.419	0.044	-	-	0.727	0.412	2.159	-1.908
09061003	C	WS	0.34	3.58	3.5	2.553	1000	0.443	-	1.542	1.240	0.091	0.035	-	-	0.313	0.251	1.692	-1.009
09061004	C	WS	0.34	4.46	3.5	3.191	1000	-	-	2.038	-	-	-	-	-	-	-	-	-
09061101	C	WS	0.30	6.88	3.5	5.254	1000	-	-	3.360	-	-	-	-	-	-	-	-	-
09061102	C	WS	0.31	6.21	3.5	4.644	1000	-	-	2.966	-	-	-	-	-	-	-	-	-
09061103	C	WS	0.32	5.54	3.5	4.062	1000	0.632	-	2.563	1.680	0.450	0.049	-	-	0.665	0.481	2.097	-1.586
09061104	C	WS	0.32	4.59	3.5	3.382	1000	0.555	-	2.140	1.431	0.234	0.041	-	-	0.427	0.274	2.071	-1.325
09061201	C	WS	0.38	4.66	3.6	3.163	1000	-	-	2.277	-	-	-	-	-	-	-	-	-
09061202	C	WS	0.42	6.40	3.7	4.092	1000	0.682	-	2.731	1.921	0.551	0.059	-	-	0.501	0.338	2.627	-1.523
09061203	C	WS	0.42	7.11	3.7	4.563	1000	0.730	-	3.098	2.205	0.680	0.067	-	-	0.609	0.383	2.682	-1.498
09061501	C	WS	0.53	6.96	3.8	3.968	1000	0.713	-	2.702	2.151	0.590	0.069	-	-	0.530	0.413	2.707	-1.343
09061502	C	WS	0.53	5.54	3.8	3.169	1000	0.598	-	2.062	1.522	0.342	0.041	-	-	0.328	0.149	2.533	-1.217
09061601	C	WS	0.40	2.66	3.4	1.749	1000	0.271	-	2.946	0.721	0.124	0.027	-	-	0.414	0.376	1.287	-0.584
09061602	C	WS	0.49	2.69	3.4	1.600	1000	0.256	-	3.227	0.920	0.105	0.035	-	-	0.696	0.519	1.282	-0.463
09061603	C	WS	0.31	6.45	3.5	4.792	1000	0.690	-	3.006	2.033	0.435	0.065	-	-	0.961	0.595	2.378	-1.742
09061801	C	WS	0.70	3.62	3.6	1.799	1000	-	-	2.604	-	-	-	-	-	-	-	-	-
09061802	C	WS	0.72	4.61	3.8	2.260	1000	0.453	-	1.650	1.131	0.241	0.032	-	-	0.212	0.169	2.393	-0.793
09061901	C	WS	0.53	6.41	3.8	3.664	1000	0.658	-	2.368	1.599	0.428	0.065	-	-	0.312	0.244	2.627	-1.334
09061902	C	WS	0.53	4.60	3.7	2.634	1000	0.515	-	1.527	1.061	0.159	0.032	-	-	0.144	0.232	2.197	-1.031
09061903	C	WS	0.21	6.48	3.4	5.893	1000	0.697	-	3.263	1.097	0.181	0.026	-	-	0.566	0.423	2.278	-2.169
09062201	C	WS	0.63	4.60	3.8	2.411	1000	0.491	-	1.667	1.116	0.161	0.029	-	-	0.166	0.158	2.298	-0.900
09062202	C	WS	0.64	5.55	3.9	2.896	1000	0.577	-	1.754	1.096	0.343	0.043	-	-	0.193	0.098	2.366	-1.062
09062203	C	WS	0.74	6.41	4.0	3.103	1000	0.624	-	2.067	1.339	0.335	0.048	-	0.052	0.334	0.138	2.721	-1.024
09062204	C	WS	0.74	5.55	4.0	2.689	1000	0.552	-	1.757	1.045	0.356	0.043	-	-	0.435	0.223	2.616	-0.999
09062309	C	WS	0.83	4.54	3.9	2.072	1000	0.418	-	2.316	1.420	0.291	0.048	-	0.069	0.333	0.103	2.220	-0.719
09062401	C	WS	0.64	7.02	4.0	3.663	1000	0.704	-	2.504	1.661	0.517	0.058	-	-	0.265	0.161	2.670	-1.277
09062403	C	WS	0.62	7.08	3.9	3.730	500	0.694	-	2.377	1.552	0.512	0.063	-	0.094	0.396	0.075	2.830	-1.268
09062501	C	WS	1.04	5.52	4.1	2.261	500	0.487	-	1.588	0.728	0.344	0.038	-	0.141	0.316	-0.243	-	-0.788
09062502	C	WS	0.87	6.68	4.0	2.990	500	0.669	-	2.115	1.379	0.373	0.052	-	-	0.344	0.212	-	-1.044
09062503	C	WS	1.04	6.38	4.0	2.609	500	0.545	-	1.618	1.346	0.331	0.059	-	-	0.535	0.211	-	-0.918
09062504	C	WS	0.84	6.39	4.0	2.901	500	0.593	-	1.906	0.000	0.000	0.000	-	-	0.444	0.188	2.877	-1.058
09062505	C	WS	0.84	5.54	4.0	2.513	500	0.538	-	1.700	0.997	0.259	0.044	-	-	0.365	0.009	2.508	-0.948
09062601	C	WS	1.03	4.63	3.9	1.900	500	0.385	-	2.189	1.185	0.168	0.042	-	-	0.583	0.226	2.076	-0.708
09062602	C	WS	0.93	4.60	3.9	1.987	500	0.416	-	2.464	0.907	0.175	0.038	-	-	0.239	-0.096	2.112	-0.786
09062603	C	WS	1.08	6.60	4.0	2.651	500	0.638	-	1.885	1.811	0.413	0.222	-	-	0.916	0.387	-	-0.903
09062604	C	WS	1.14	5.57	4.2	2.174	500	0.476	-	1.748	0.464	0.118	0.014	-	-	0.612	-0.292	-	-0.811
09062607	C	WS	0.94	5.54	4.0	2.375	500	0.510	-	1.901	0.750	0.237	0.033	-	-	0.334	0.028	2.639	-0.932
09062911	C	WS	1.17	6.54	3.8	2.520	500	-	-	1.727	-	-	-	-	-	-	-	-	-

Annex D

Comparative analysis of the results for regular waves

D.1 Incident wave parameters and wave reflection analysis
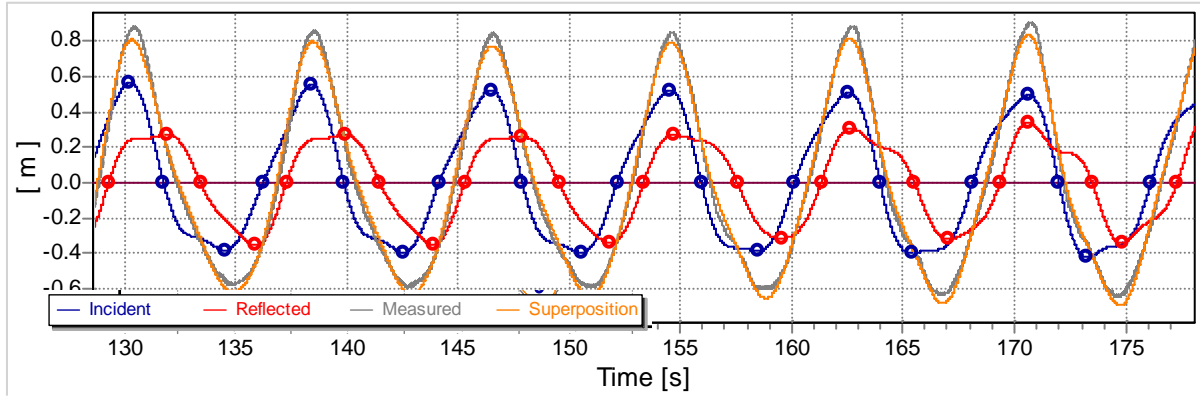

Fig. D.1.1: Time series for regular waves

The wave and reflection analysis for regular waves was performed using H_m and T_m.
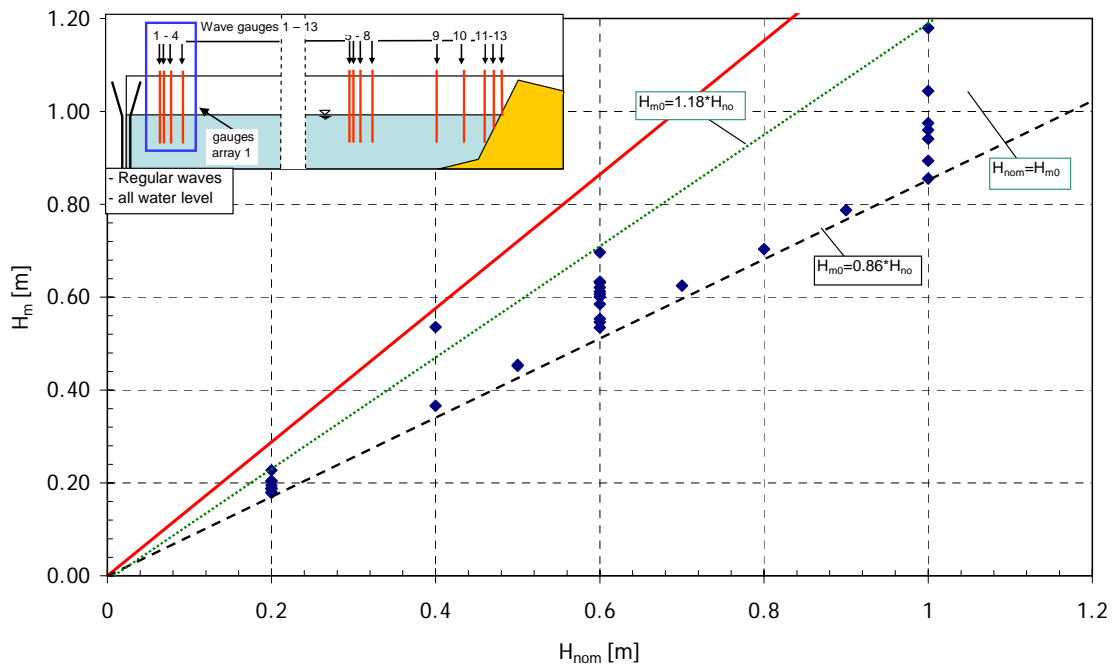

Fig. D.1.2: Comparison of incident wave height H_{m0} and nominal wave height H_{nom} for all tests with regular waves for different water levels
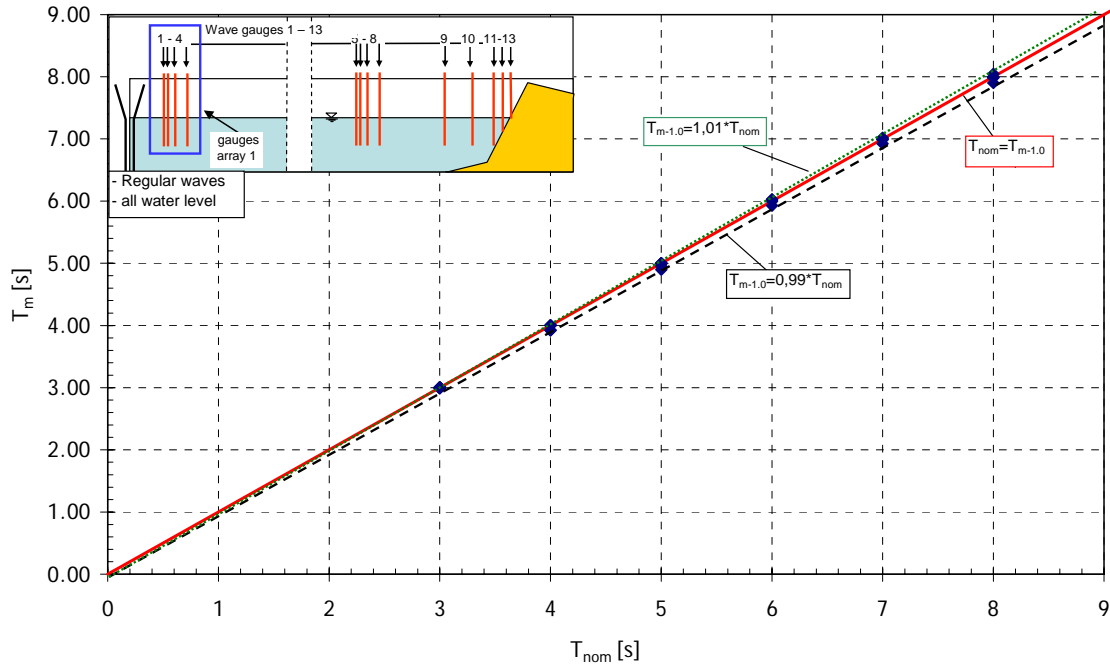
Fig. D.1.3: Comparison of $T_{m-1.0}$ and T_{nom} for all tests with for all tests with regular waves for different water levels
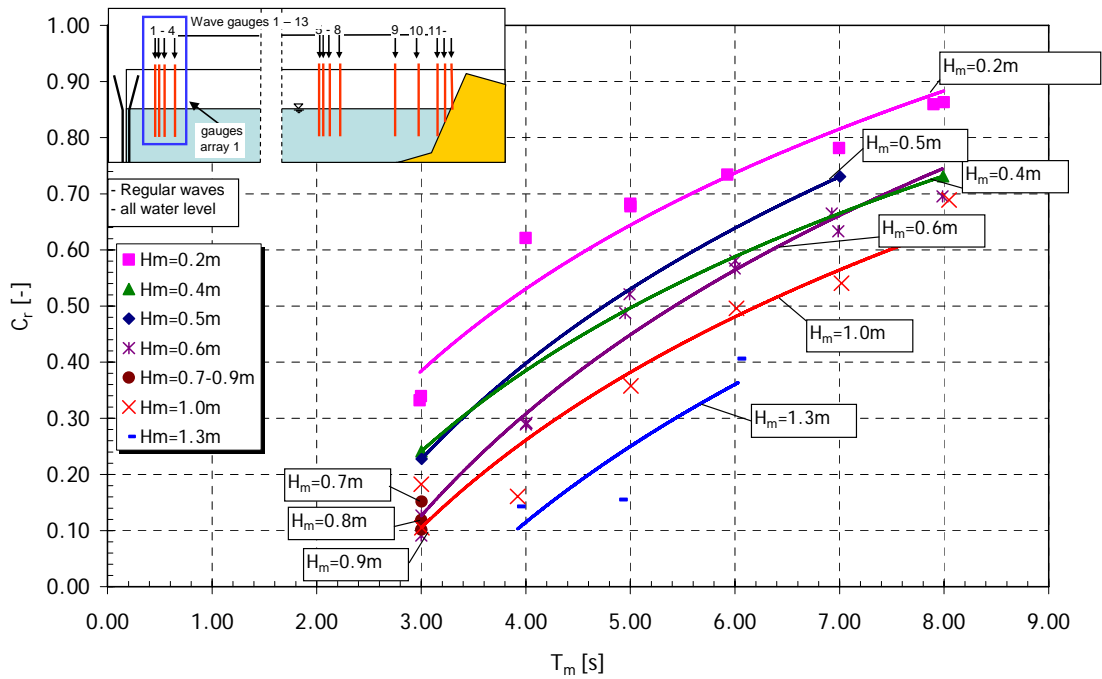
Fig. D.1.4: Reflection coefficient C_r plotted against the wave period T_m ordered by nominal wave heights H_{nom}
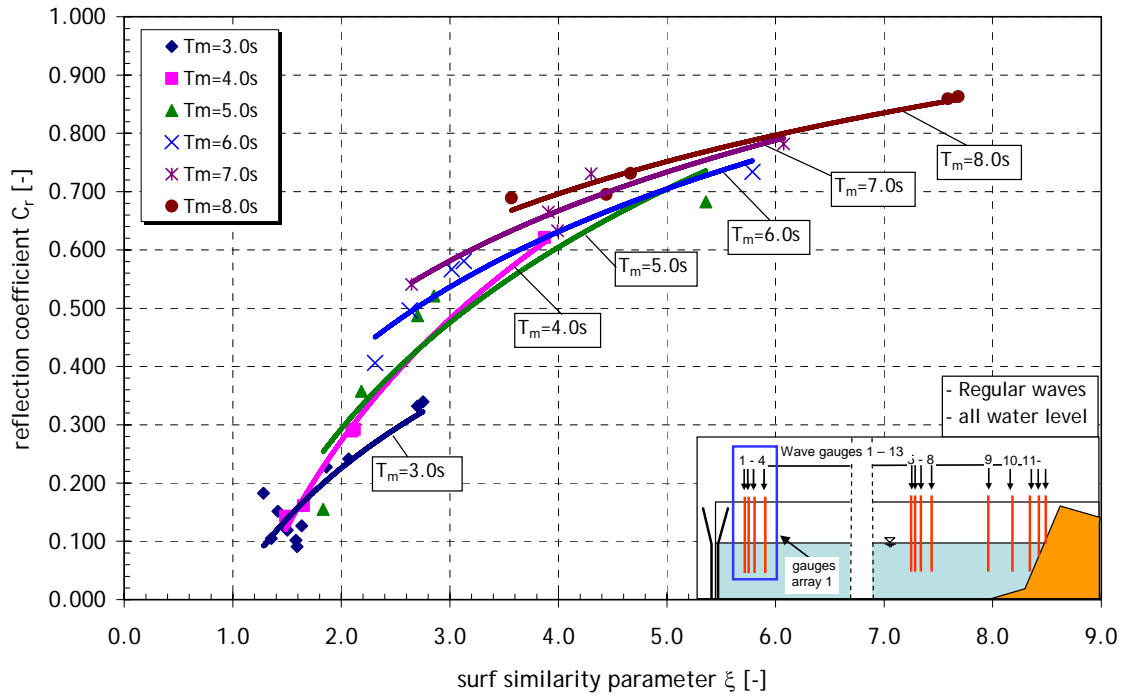
Fig. D.1.5: Reflection Coefficient C_r plotted against the Surf Similarity Parameter ξ ordered by nominal wave periods T_{nom}

D.2 Wave run-up and run-down
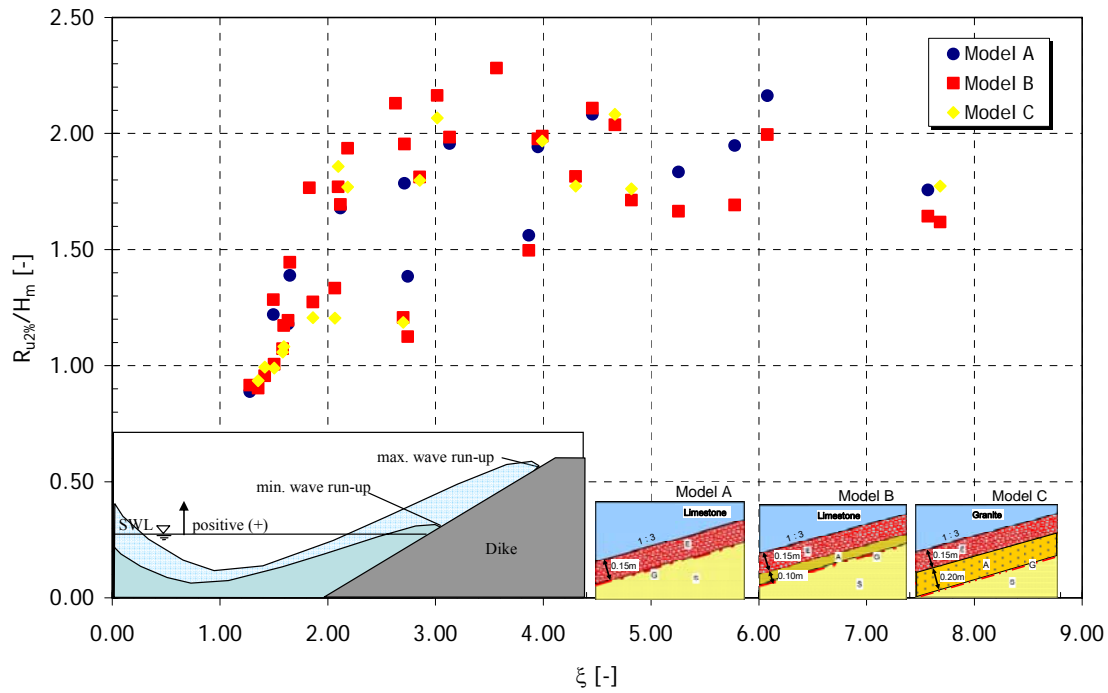
Fig. D.2.1: Wave run-up $R_{u2\%}$ for regular waves for Model Alternative A, B and C
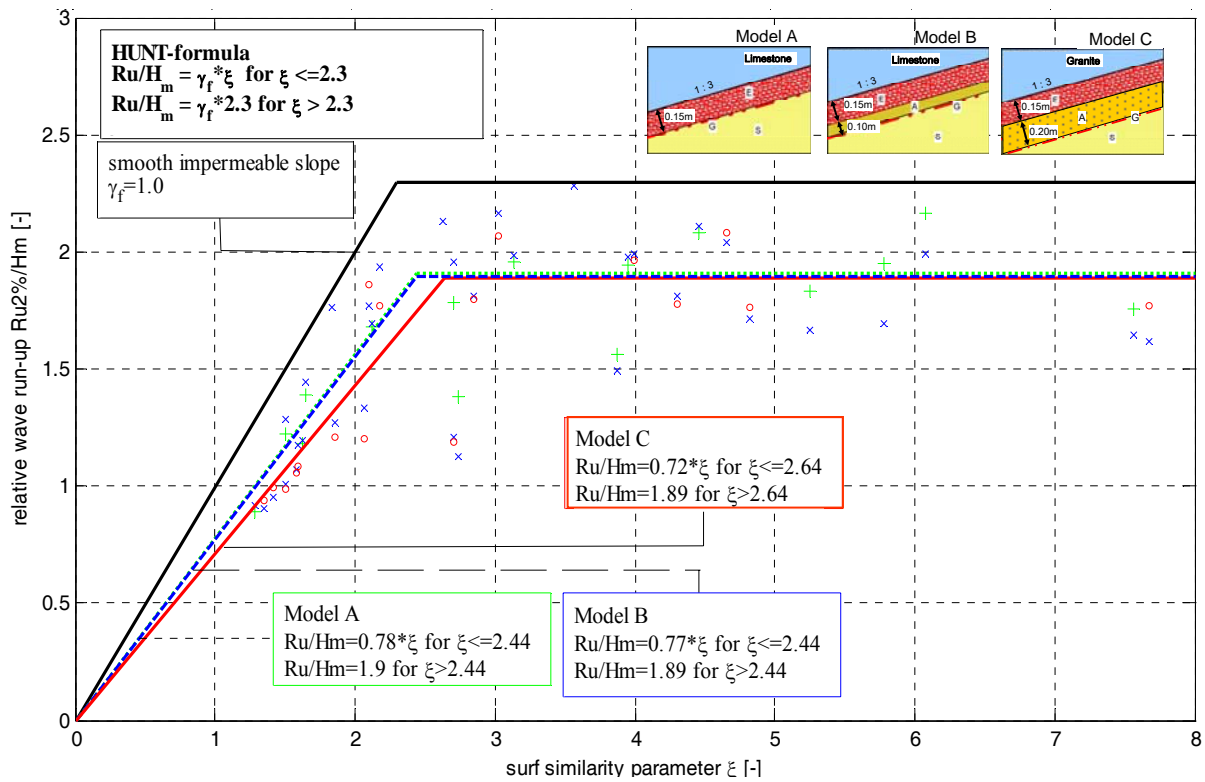
Fig. D.2.2: Wave run-up $R_{u2\%}$ for regular waves with prediction formula

Prediction formula for Wave run-up *Model Alternative A*:

$$\frac{R_u}{H_m} = 0.78 \cdot \xi \text{ for } \xi \leq 2.44$$

$$\frac{R_u}{H_m} = 1.9 \text{ for } \xi > 2.44$$

(D.2.1)

Prediction formula for Wave run-up *Model Alternative B*:

$$\frac{R_u}{H_m} = 0.77 \cdot \xi \text{ for } \xi \leq 2.44$$

$$\frac{R_u}{H_m} = 1.89 \text{ for } \xi > 2.44$$

(D.2.2)

Prediction formula for Wave run-up *Model Alternative C*:

$$\frac{R_u}{H_m} = 0.72 \cdot \xi \text{ for } \xi \leq 2.64$$

$$\frac{R_u}{H_m} = 1.89 \text{ for } \xi > 2.64$$

(D.2.3)
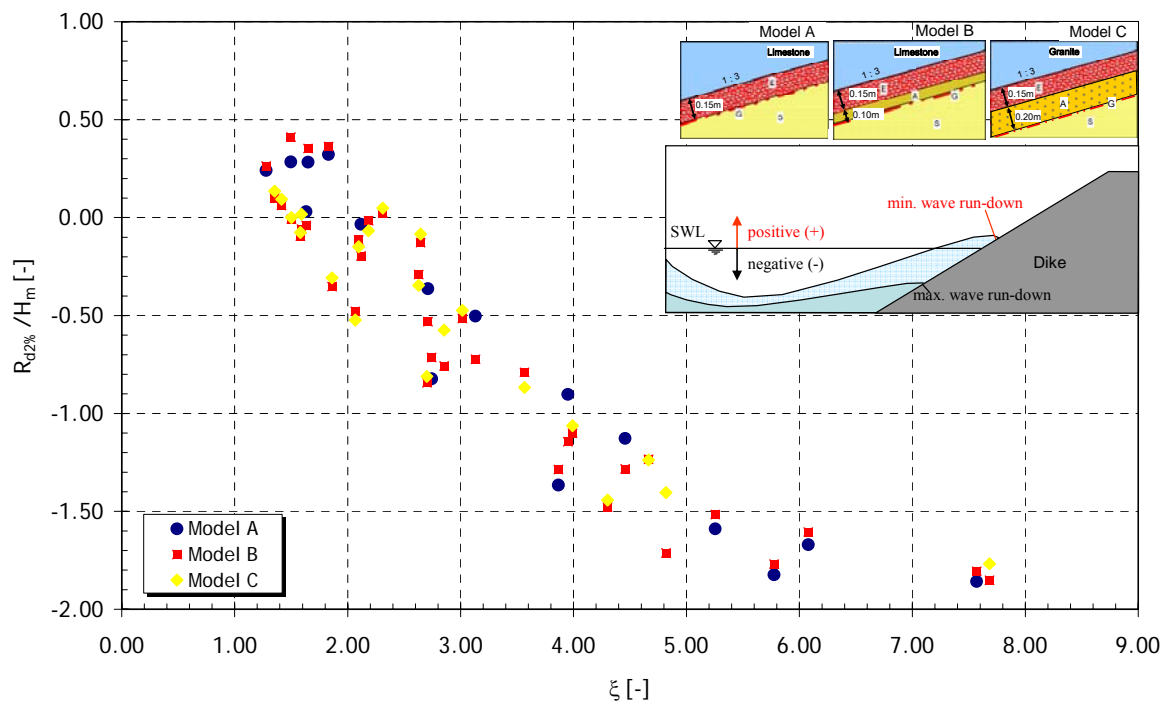
Fig. D.2.3: Wave run-down $R_{d2\%}$ for regular waves for Model Alternative A, B and C
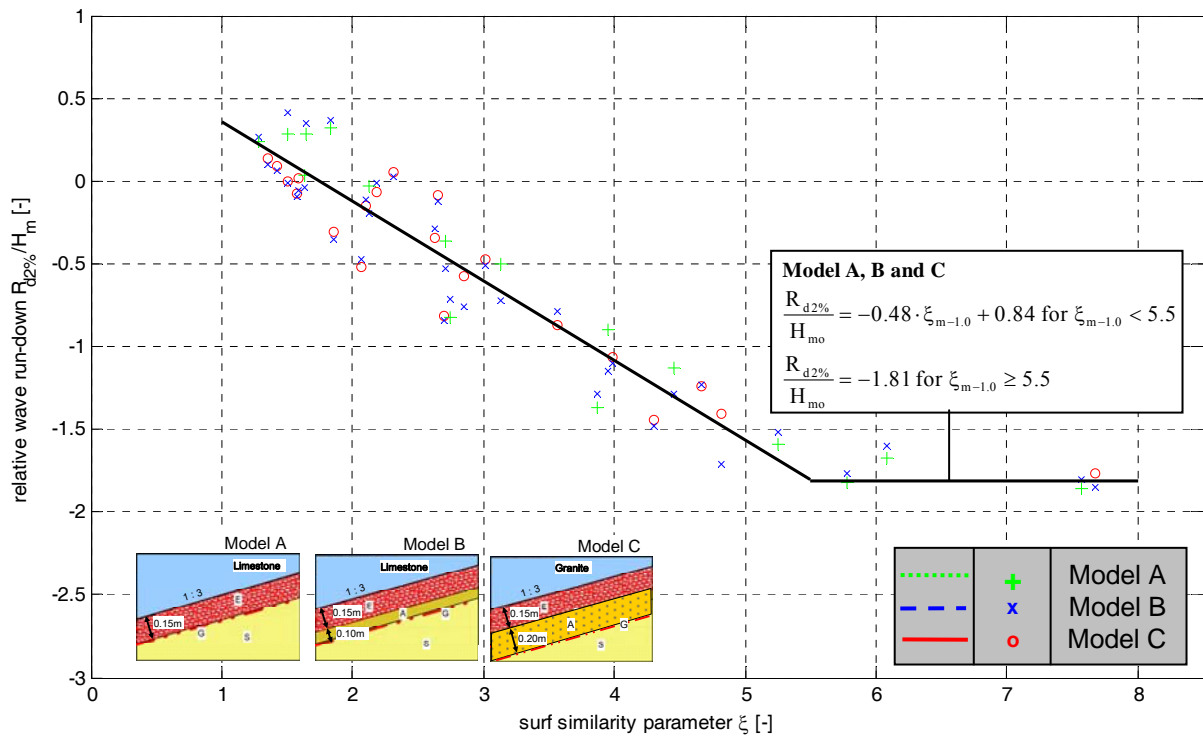
Fig. D.2.4: Wave run-down $R_{d2\%}$ for regular waves with prediction formula

Prediction formula for Wave run-down *Model Alternative A, B* and *C*:

$$\frac{R_{d2\%}}{H_m} = -0.48 \cdot \xi + 0.84 \text{ for } \xi < 5.5$$

$$\frac{R_{d2\%}}{H_m} = -1.81 \text{ for } \xi \geq 5.5$$

(D.2.4)

D.3 Wave pressure on and beneath the revetment

$$\xi = \xi_m = \frac{\tan \alpha}{\sqrt{H_m / L_0}}$$

Impact loads

Transition zone
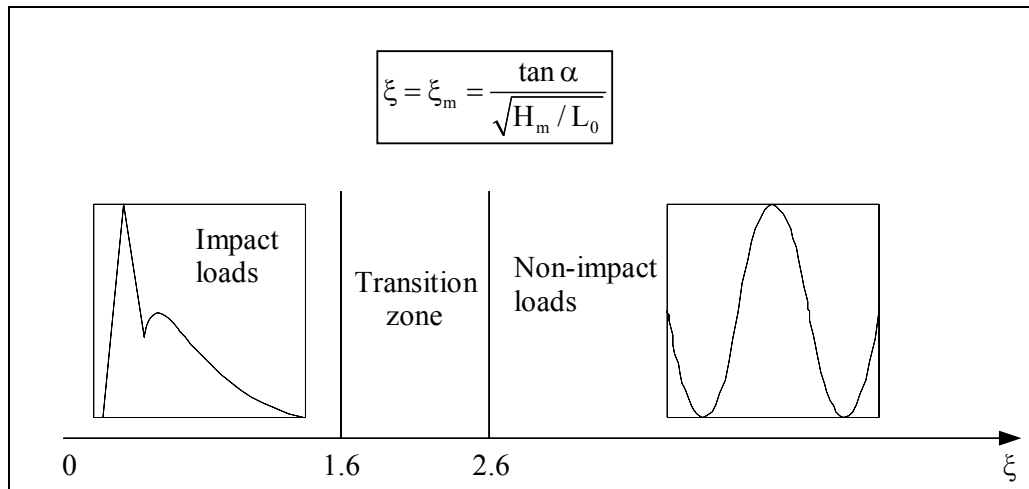
Non-impact loads

Fig. D.3.1: Wave Load Classification

D.3.1 Wave pressure on the revetment

$$\xi_m = \frac{\tan \alpha}{\sqrt{H_m / L_0}}$$

with
H_m = deep water wave height [m]
L_0 = deep water wave length related to wave period T_m [m]
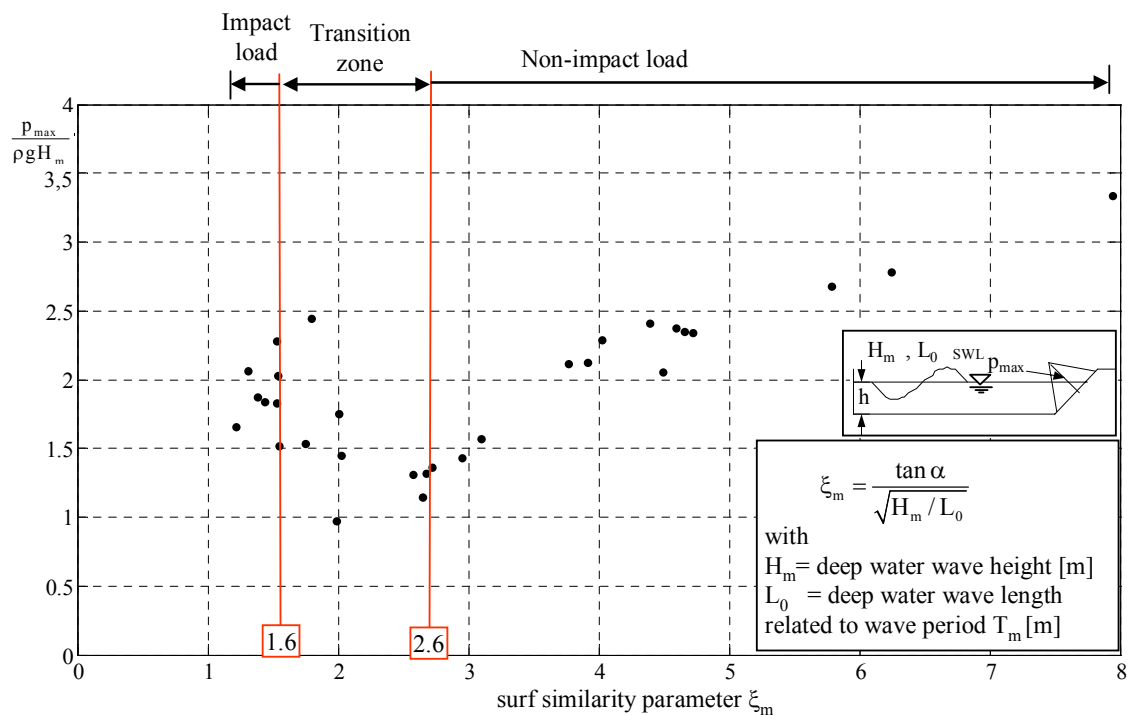
Fig. D.3.2: Maximum pressure $p_{max,N}/\rho g H_m$ on the revetment against the surf similarity parameter ξ_m for regular wave tests

D.3.1.1 Impact load and Transition Zone

Prediction formulae for the impact pressure $p_{max}/\rho g H_m$ on the revetment:

$$\frac{p_{max}}{\rho \cdot g \cdot H_m} = 2.0$$

$$\sigma' = 12.24\%$$

(D.3.1)

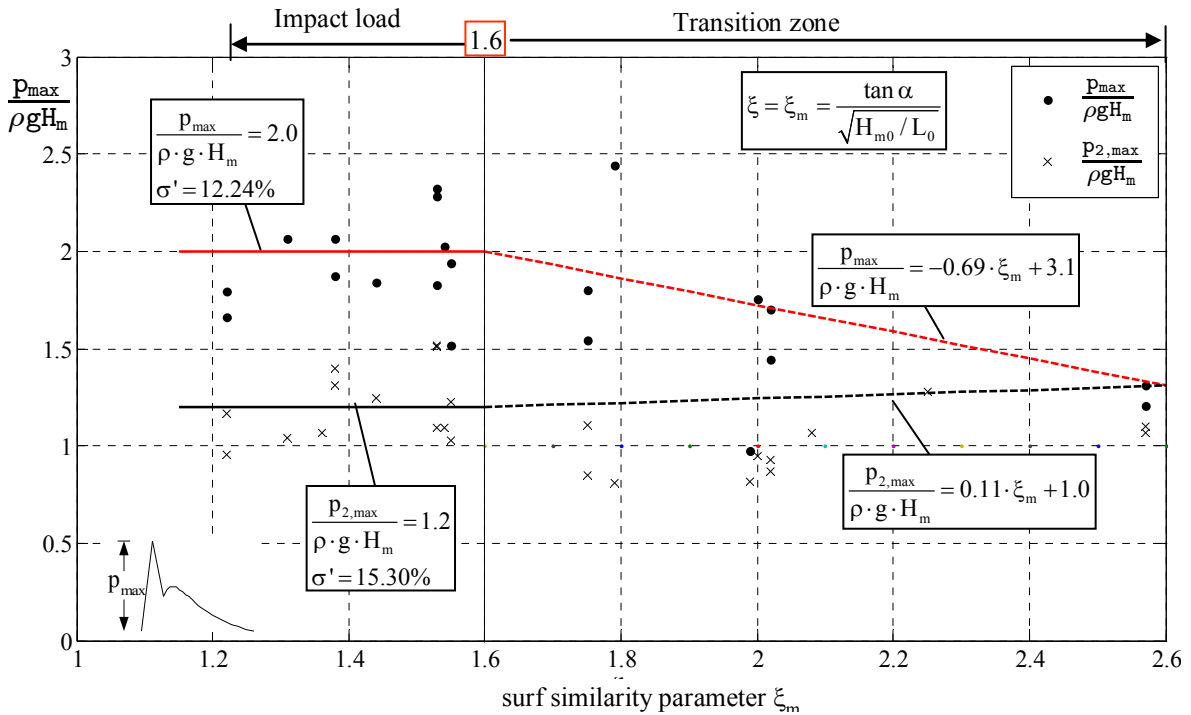$$\frac{p_{max}}{\rho \cdot g \cdot H_m} = -0.69 \cdot \xi_m + 3.1 \quad \text{for } 1.6 < \xi < 2.6$$

(D.3.2)
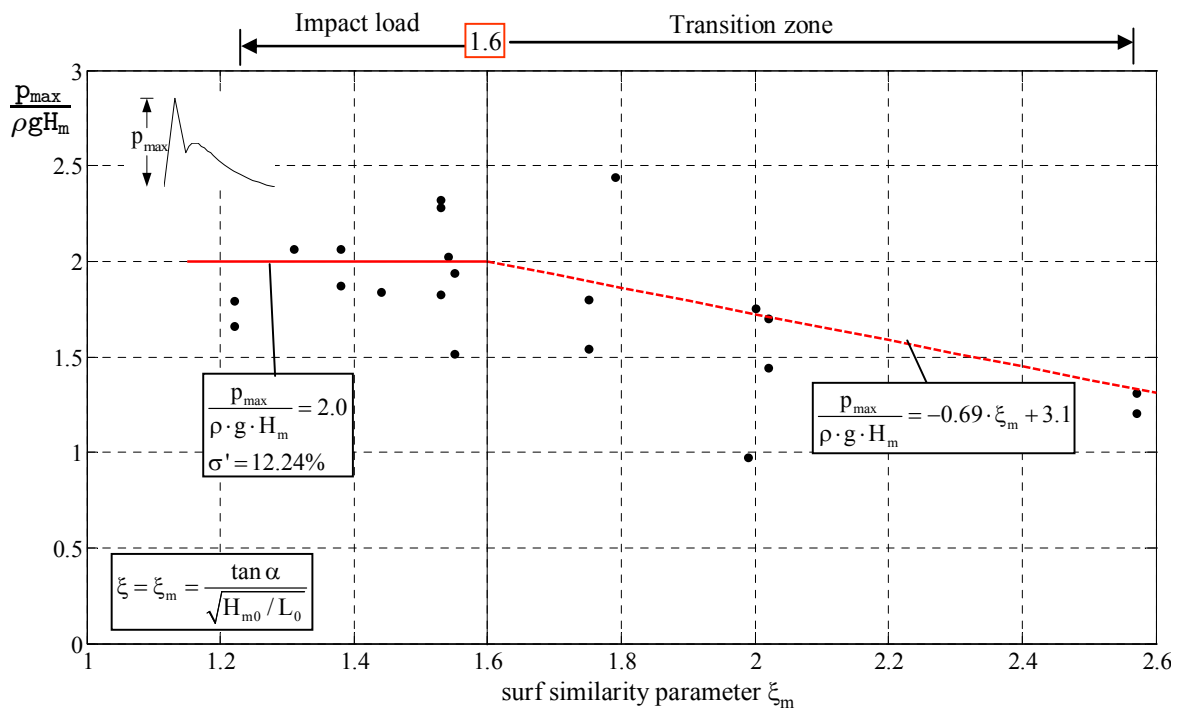
Fig. D.3.3: Formulae for the impact pressure $p_{max}/\rho g H_m$ on the revetment against the surf similarity parameter ξ_m for regular wave tests

D.3.1.2 Non-impact Load

Prediction formulae for the quasi-static load $p_{stat}/\rho g H_m$ on the revetment:

$$\frac{p_{stat}}{\rho \cdot g \cdot H_m} = 0.5 \cdot \xi_m \quad \text{for } \xi_m < 4.8$$

$$\sigma' = 14.25\%$$

(D.3.3)

and

$$\frac{p_{stat}}{\rho \cdot g \cdot H_m} = 0.35 \cdot \xi_m + 0.68 \quad \text{for } \xi_m > 4.8$$

(D.3.4)
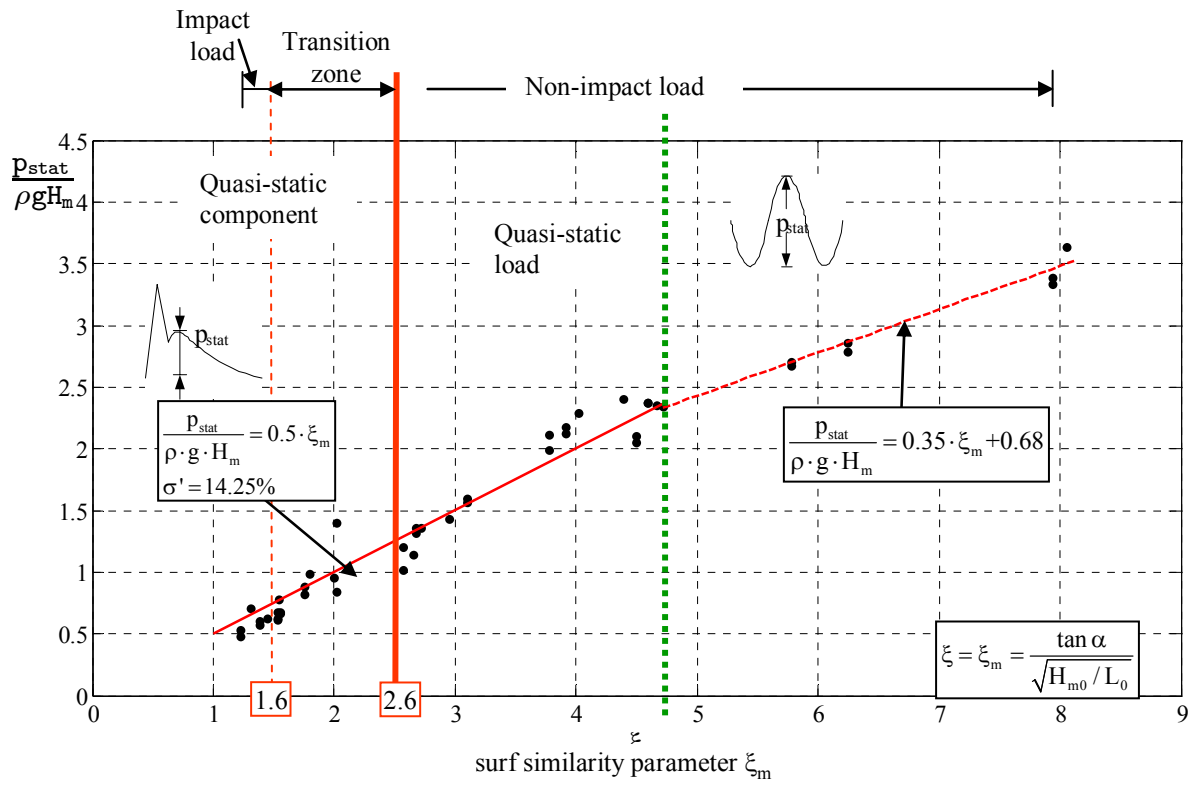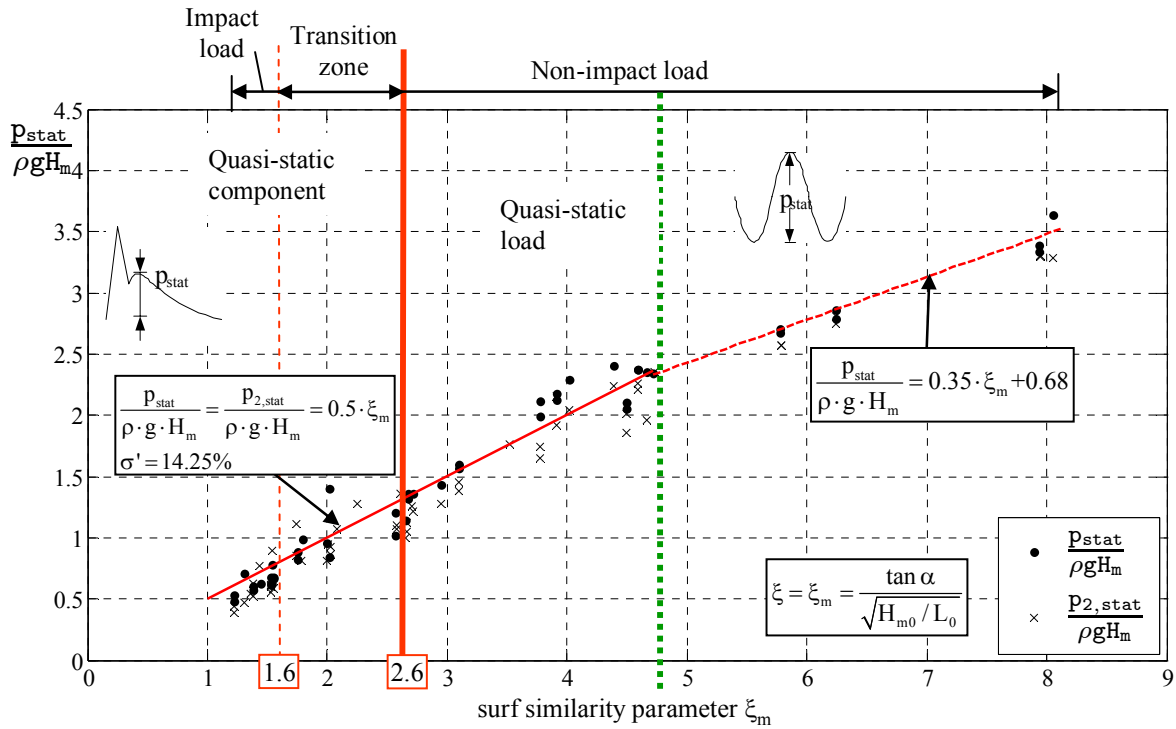
Fig. D.3.4: Formulae for the quasi-static load $p_{stat}/\rho g H_m$ on the revetment against the surf similarity parameter ξ_m for regular wave tests

D.3.2 Wave pressure beneath the revetment
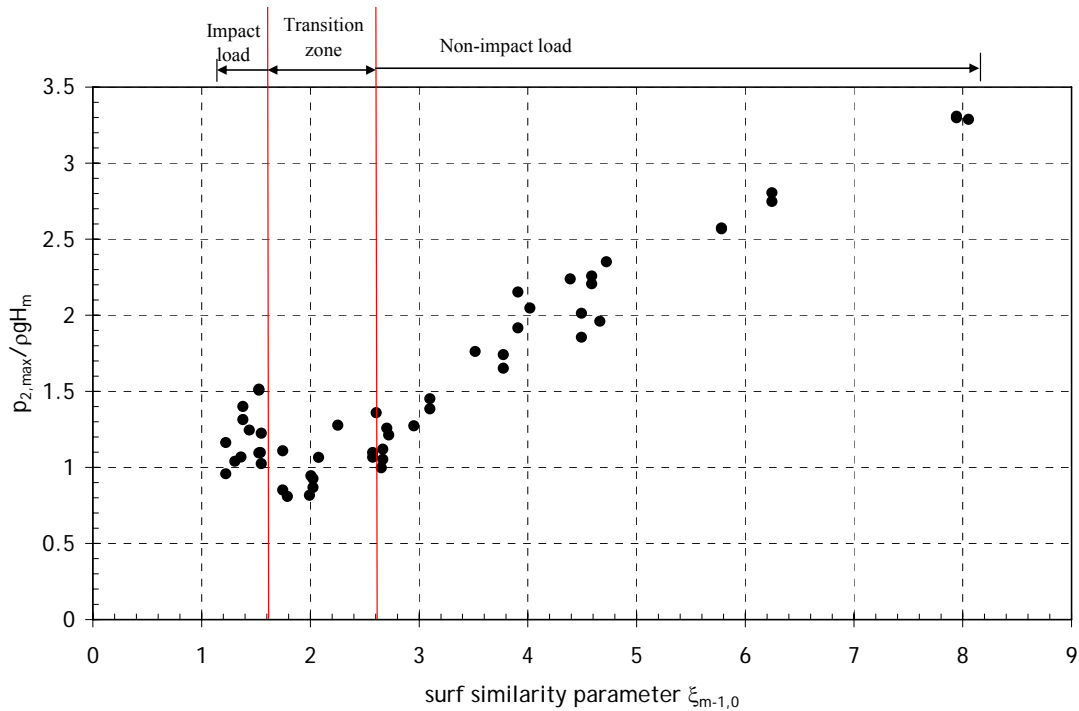
D.3.2.1 Impact load and Transition Zone

Prediction formulae for the impact pressure $p_{max}/\rho g H_m$ beneath the revetment:

$$\frac{p_{2,max}}{\rho \cdot g \cdot H_m} = 0.6 \cdot \frac{p_{max}}{\rho \cdot g \cdot H_m} = 1.2 \quad \text{for } \xi < 1.6$$
$$\sigma' = 15.30\%$$

(D.3.5)

and:

$$\frac{p_{2,max}}{\rho \cdot g \cdot H_m} = 0.11 \cdot \xi_m + 1.0 \quad \text{for } 1.6 < \xi < 2.6$$

(D.3.6)

Fig. D.3.5: Formulae for the impact pressure $p_{max}/\rho g H_m$ on and beneath the revetment against the surf similarity parameter ξ_m for regular w

D.3.2.2 Non-impact Load

Prediction formulae for the quasi-static load $p_{stat}/\rho g H_m$ beneath the revetment:

$$\frac{p_{stat}}{\rho \cdot g \cdot H_m} = \frac{p_{2,stat}}{\rho \cdot g \cdot H_m} = 0.5 \cdot \xi_m \quad \text{for } \xi_m < 4.8$$

$$\sigma' = 14.25\%$$

(D.3.7)

and

$$\frac{p_{stat}}{\rho \cdot g \cdot H_m} = \frac{p_{2,stat}}{\rho \cdot g \cdot H_m} = 0.35 \cdot \xi_m + 0.68 \quad \text{for } \xi_m > 4.8$$

(D.3.8)

Fig. D.3.6: Formulae for the quasi-static load $p_{stat}/\rho g H_m$ on and beneath the revetment against the surf similarity parameter ξ_m for regular wave tests

D.3.3 Location of peak pressure on and just beneath the revetment
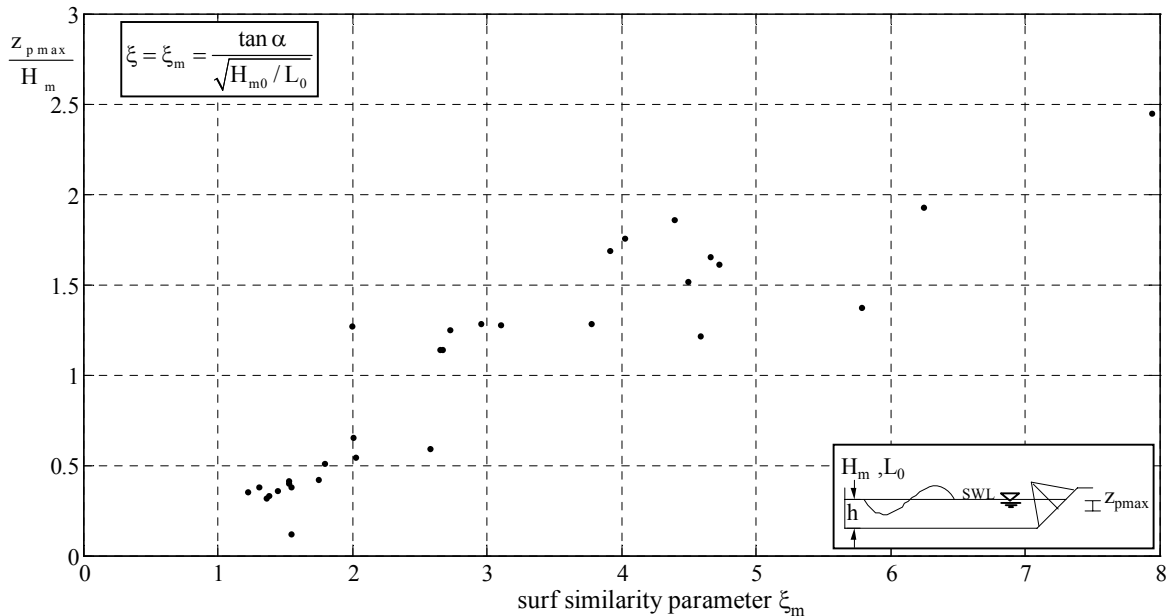
Fig. D.3.7: Location of the maximum pressure on the revetment z_{pmax}/H_m against the surf similarity parameter ξ_m for regular wave tests

D.3.3.1.1 Schüttrumpf's approach

$$\frac{z_{p\,max}}{H_{m0}} = 0.8 + 0.6 \cdot \tan(\xi - 2.1) \tag{D.3.9}$$

On the *ELASTOCOAST* revetment:

$$\frac{z_{p\,max}}{H_{m0}} = 1.15 \cdot \left[0.8 + 0.6 \cdot \tan(\xi - 2.1)\right] \tag{D.3.10}$$
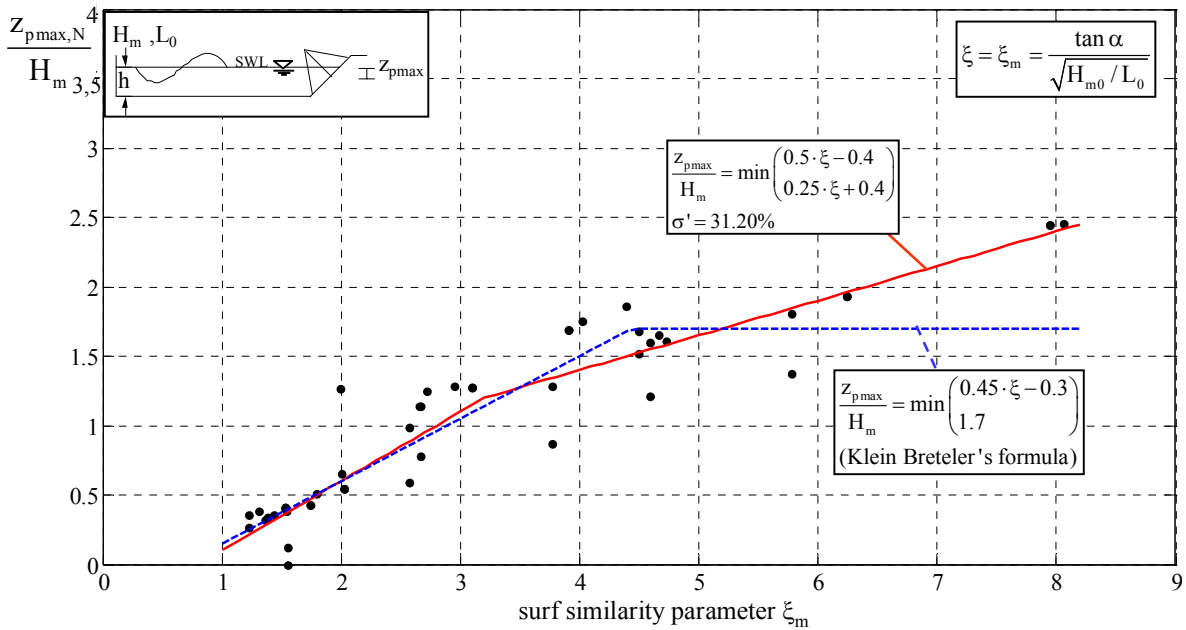
$$\sigma' = 33.69\%$$
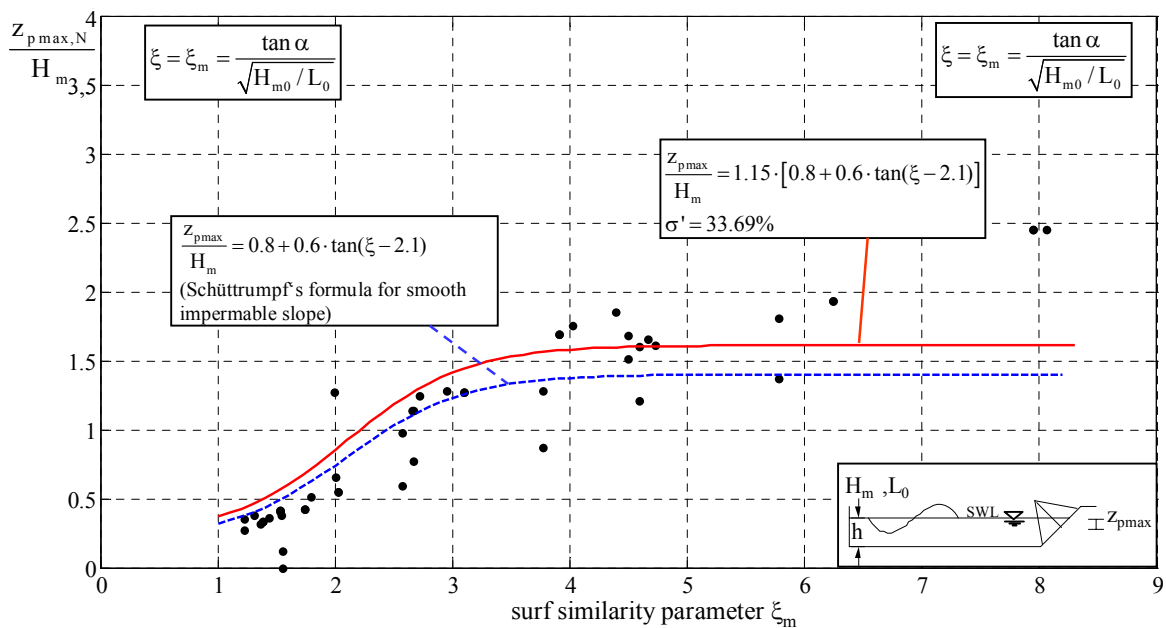
Fig. D.3.8: Prediction formula for the peak pressure location of the peak pressure on the revetment z_{pmax}/H_m against the surf similarity parameter ξ_m using Schüttrumpf's approach

Beneath the *ELASTOCOAST* revetment:

$$\frac{z_{p\,max}}{H_m} = 1.6 \cdot \left[0.8 + 0.6 \cdot \tan(\xi - 2.1)\right] \tag{D.3.11}$$
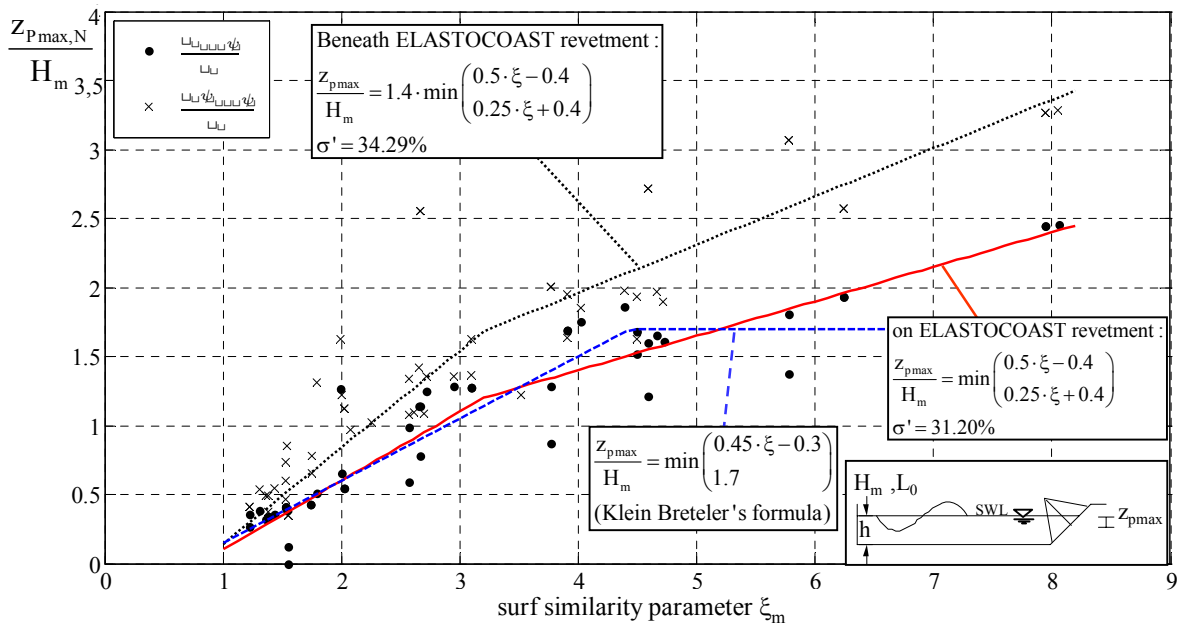
$$\sigma' = 32.94\%$$
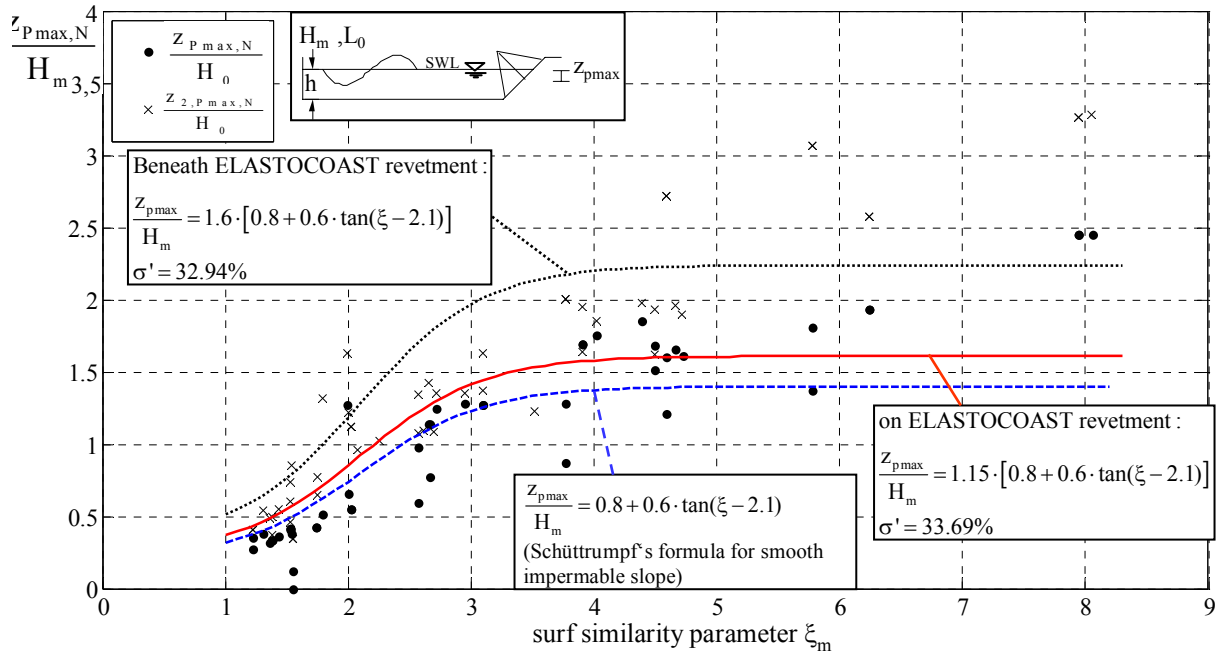
Fig. D.3.9: Prediction formula for the peak pressure location of the peak pressure on and beneath the revetment z_{pmax}/H_m against the surf similarity parameter ξ_m using Schüttrumpf's approach

D.3.3.1.2 Klein Breteler's approach

$$\frac{z_{p\,max}}{H_{m0}} = \min\begin{pmatrix} 0.45 \cdot \xi - 0.3 \\ 1.7 \end{pmatrix} \qquad (D.3.12)$$

On the *ELASTOCOAST* revetment:

$$\frac{z_{p\,max}}{H_m} = \min\begin{pmatrix} 0.5 \cdot \xi - 0.4 \\ 0.25 \cdot \xi + 0.4 \end{pmatrix} \qquad (D.3.13)$$

$$\sigma' = 31.20\%$$

Fig. D.3.10: Prediction formula for the peak pressure location of the peak pressure on the revetment z_{pmax}/H_m against the surf similarity parameter ξ_m using Klein Breteler's approach

Beneath the *ELASTOCOAST* revetment:

$$\frac{z_{pmax}}{H_m} = 1.4 \cdot \min\begin{pmatrix} 0.5 \cdot \xi - 0.4 \\ 0.25 \cdot \xi + 0.4 \end{pmatrix}$$

$$\sigma' = 34.29\%$$

(D.3.14)

Fig. D.3.11: Prediction formula for the peak pressure location of the peak pressure on and beneath the revetment z_{pmax}/H_m against the surf similarity parameter ξ_m using Klein Breteler's approach

D.3.4 Pressure distribution on and just beneath the revetment

D.3.4.1 Impact load and Transition Zone
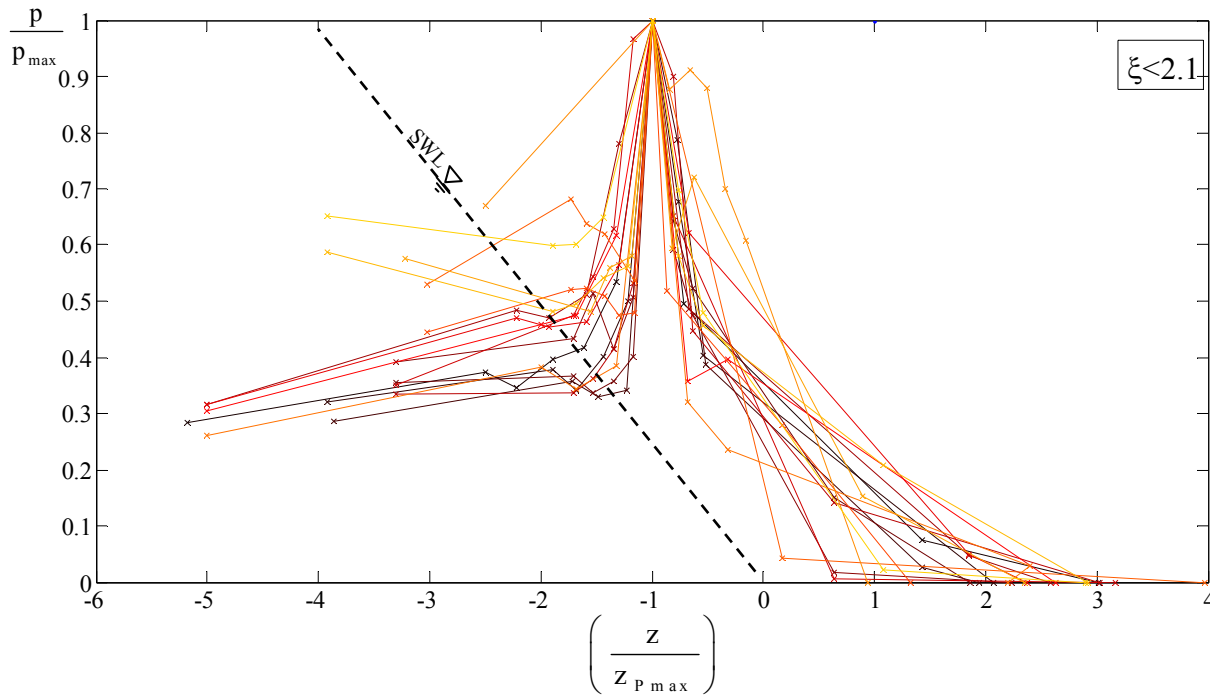
Fig. D.3.12: Spatial pressure distribution on the revetment for impact load and transition zone (regular waves)
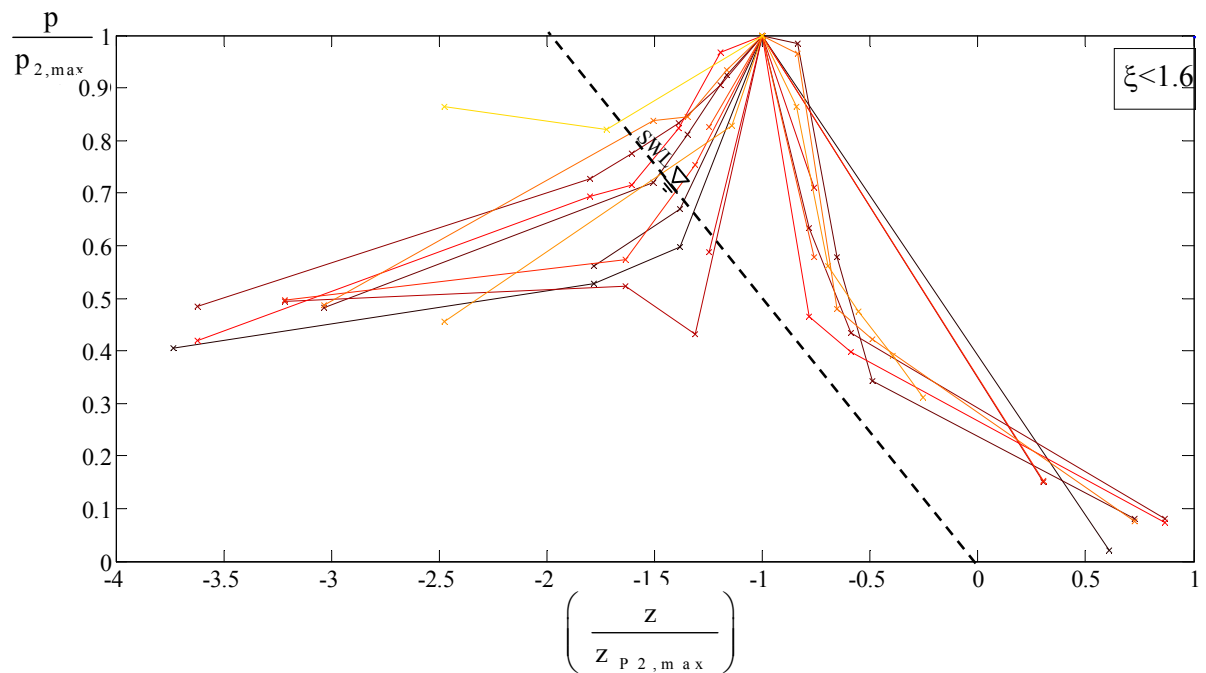
Fig. D.3.13: Spatial pressure distribution beneath the revetment for impact load and transition zone (regular waves)
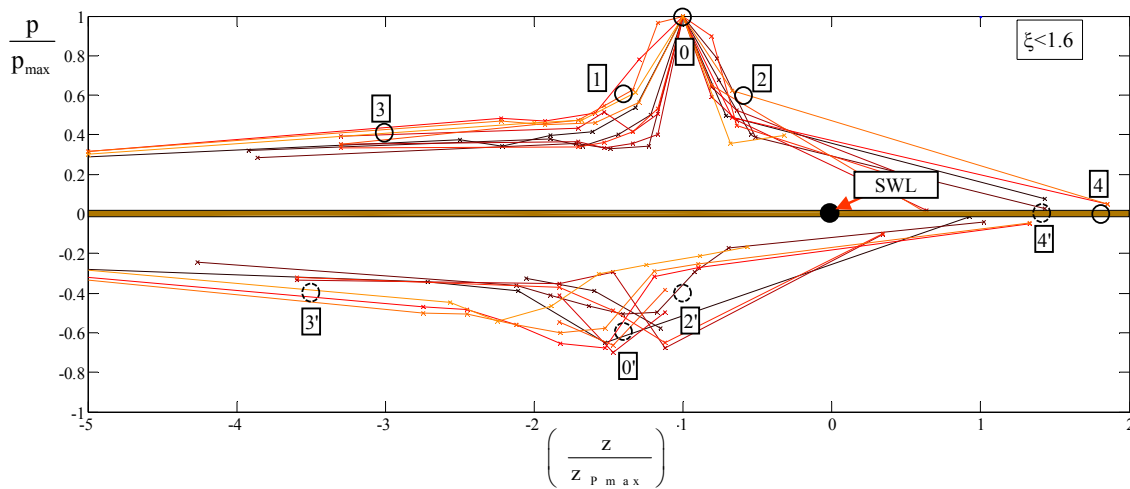
Fig. D.3.14: Pressure distribution on and beneath the revetment for impact load ($\xi<1.6$)

Pressure distribution <u>on</u> the revetment for impact load:

$$\text{Point 0}: \quad \frac{p_0}{p_{max}} = 1.0 \quad \text{with} \quad \frac{z_0}{z_{pmax}} = 1.0 \tag{D.3.15}$$

$$\text{Point 1}: \quad \frac{p_1}{p_{max}} = 0.6 \quad \text{with} \quad \frac{z_1}{z_{pmax}} = -1.4 \tag{D.3.16}$$

$$\text{Point 2}: \quad \frac{p_2}{p_{max}} = 0.6 \quad \text{with} \quad \frac{z_2}{z_{pmax}} = -0.4 \tag{D.3.17}$$

$$\text{Point 3}: \quad \frac{p_3}{p_{max}} = 0.4 \quad \text{with} \quad \frac{z_3}{z_{pmax}} = -3.0 \tag{D.3.18}$$

$$\text{Point 4}: \quad \frac{p_4}{p_{max}} = 0.0 \quad \text{with} \quad \frac{z_4}{z_{pmax}} = \frac{R_{u2\%}}{z_{pmax}} \tag{D.3.19}$$

Pressure distribution <u>beneath</u> the revetment for impact load:

$$\text{Point 0'}: \quad \frac{p_0{}'}{p_{max}} = 0.6 \quad \text{with} \quad \frac{z_0{}'}{p_{max}} = -1.4 \tag{D.3.20}$$

$$\text{Point 2'}: \quad \frac{p_2{}'}{p_{max}} = 0.4 \quad \text{with} \quad \frac{z_2{}'}{p_{max}} = -1.0 \tag{D.3.21}$$

$$\text{Point 3'}: \quad \frac{p_3{}'}{p_{max}} = 0.4 \quad \text{with} \quad \frac{z_3{}'}{p_{max}} = -3.4 \tag{D.3.22}$$

$$\text{Point 4'}: \quad \frac{p_4{}'}{p_{max}} = 0.0 \quad \text{with} \quad \frac{z_4{}'}{p_{max}} = -\frac{R_{u2\%}}{z_{pmax}} - 0.4 \tag{D.3.23}$$
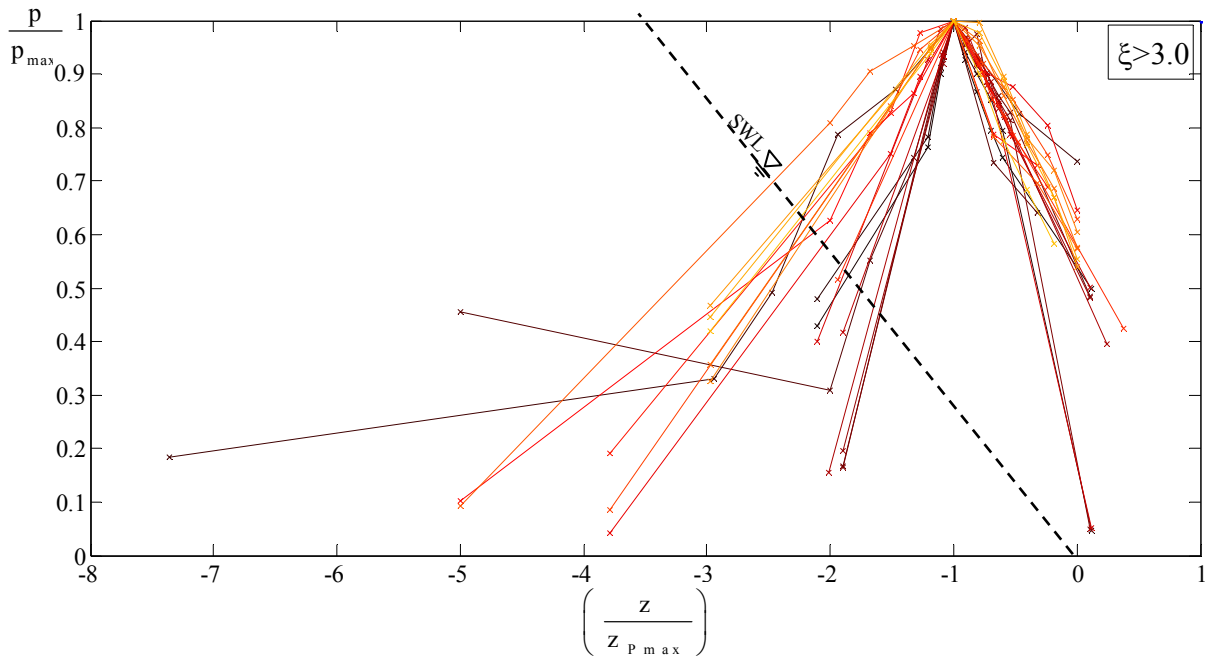
D.3.4.2 Non-impact Load

Fig. D.3.15: Spatial pressure distribution on the revetment for $\xi_{m-1,0}>3.0$ for non-impact load (regular waves)
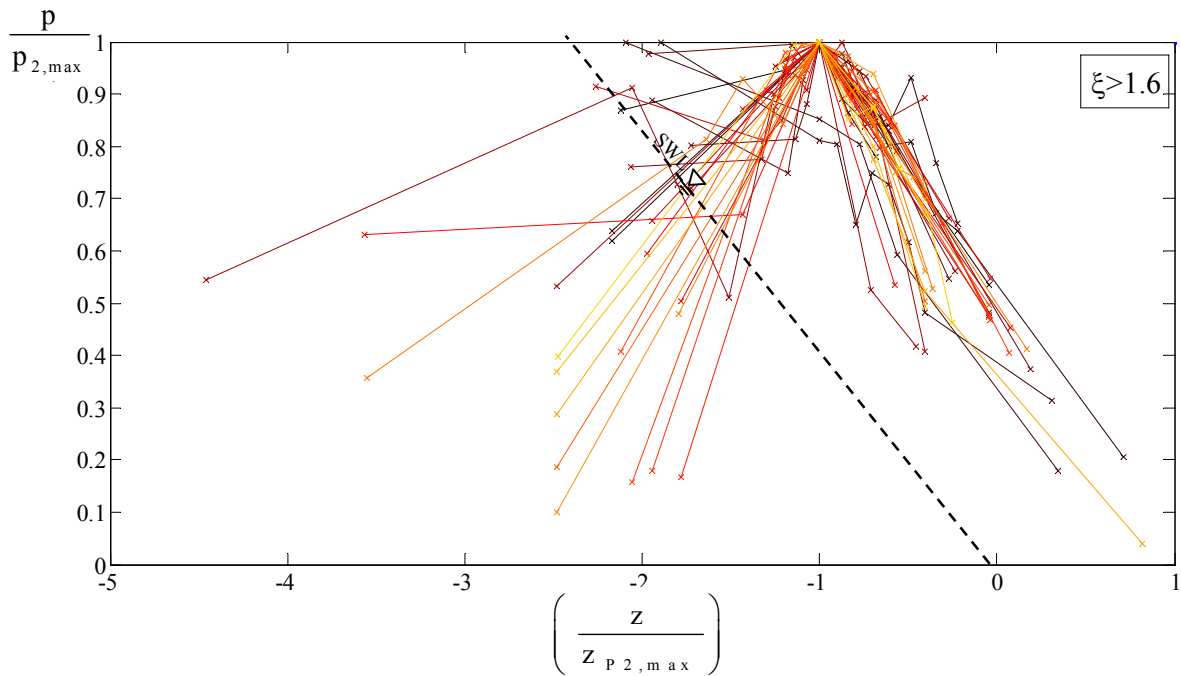

Fig. D.3.16: Spatial pressure distribution beneath the revetment for $\xi_{m-1,0}>3.0$ for non-impact load (regular waves)
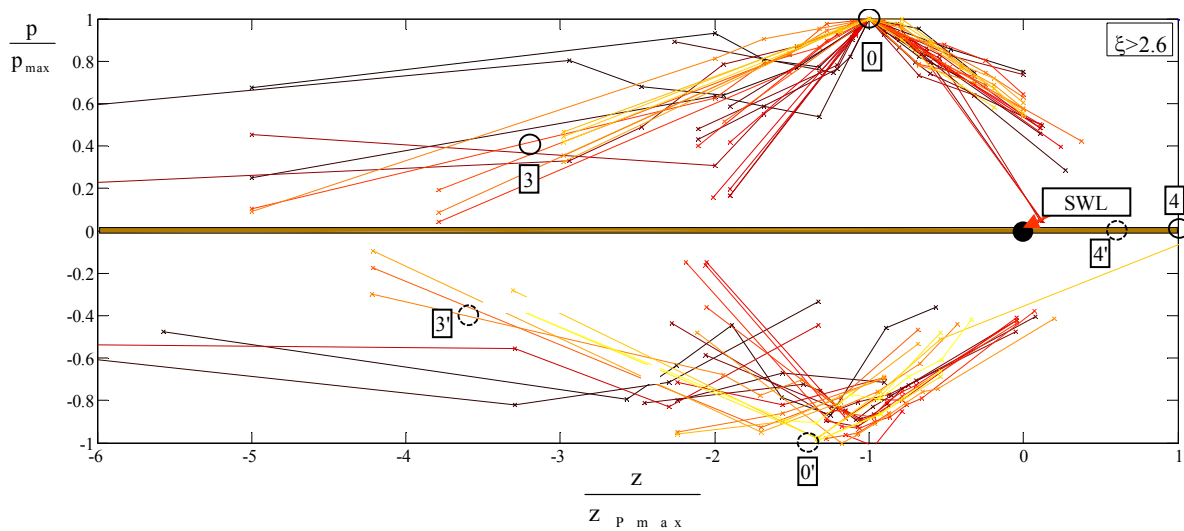
Fig. D.3.17: Pressure distribution on and beneath the revetment for non-impact load ($\xi > 2.6$)

Pressure distribution <u>on</u> the revetment for non-impact load:

$$\text{Point } 0: \quad \frac{p_0}{p_{stat}} = 1.0 \quad \text{with} \quad \frac{z_0}{z_{pmax}} = 1.0 \tag{D.3.24}$$

$$\text{Point } 3: \quad \frac{p_3}{p_{stat}} = 0.4 \quad \text{with} \quad \frac{z_3}{z_{pmax}} = -3.2 \tag{D.3.25}$$

$$\text{Point } 4: \quad \frac{p_4}{p_{stat}} = 0.0 \quad \text{with} \quad \frac{z_4}{z_{pmax}} = \frac{R_{u2\%}}{z_{pmax}} \tag{D.3.26}$$

Pressure distribution <u>beneath</u> the revetment for non-impact load:

$$\text{Point } 0': \quad \frac{p_0{}'}{p_{stat}} = 1.0 \quad \text{with} \quad \frac{z_0{}'}{z_{pmax}} = -1.4 \tag{D.3.27}$$

$$\text{Point } 3': \quad \frac{p_3{}'}{p_{stat}} = 0.4 \quad \text{with} \quad \frac{z_3{}'}{z_{pmax}} = -3.6 \tag{D.3.28}$$

$$\text{Point } 4': \quad \frac{p_4{}'}{p_{stat}} = 0.0 \quad \text{with} \quad \frac{z_4{}'}{z_{pmax}} = -\frac{R_{u2\%}}{z_{pmax}} - 0.2 \tag{D.3.29}$$

Annex E

Negative transient pore pressure in the sand core beneath the revetment

E "Negative" transient pore pressure

In Section 6.1.2 the total transient pore pressure including both "positive" and "negative" components have been analyzed. However, as shown in chapter 8 (see Fig 8.10) for the analysis of the stability of the sand core beneath the revetment against soil liquefaction, rather the "negative" pressure component, which represents an "uplift", is needed. Therefore, the analysis of the transient pore pressure should also be performed for this purpose; i.e. prediction formulae for the "negative" transient pore pressure should also be derived.

As shown in Section 6.1.1 all pore pressures recorded within the sand core beneath the revetment are of quasi-static nature for the entire range of tested surf similarity parameters ($\xi_{m-1,0} = 1.6 - 6.6$), i.e. irrespective of the loading case considered on the revetment (impact and non-impact load). Therefore, there is no need to discriminate between impact and non-impact load for the analysis of the "negative" transient pore pressure and for the derivation of the associated prediction formulae.

E.1 Definitions, pre-processing and preliminary analysis

In the same way as in Section 6.1.2 for all three locations B, C and D (see Fig 6.11 and Fig 6.10) the maximum pore pressure recorded at the upper boundary of the sand core (layer 3) beneath the revetment represents the initial pore pressure, and thus a reference in terms of both time and magnitude for the associated pore pressures recorded at the same locations B, C and D in layer 4 and layer 5 (see Fig. E.1.1). As shown in Fig. E.1.1 exemplarily for Model C and location C, the reference "negative" transient pore pressure $u_{0,max}$ at time $t_{u0,max}$ corresponds to the peak value $u_{t,C,layer3}$ recorded by PT12 in Layer 3 while $u_{t,C,layer4}$ and $u_{t,C,layer5}$ are the "negative" transient pore pressure recorded at the same time $t_{u,max}$ by PT16 in layer 4 and PT20 in layer5, respectively.
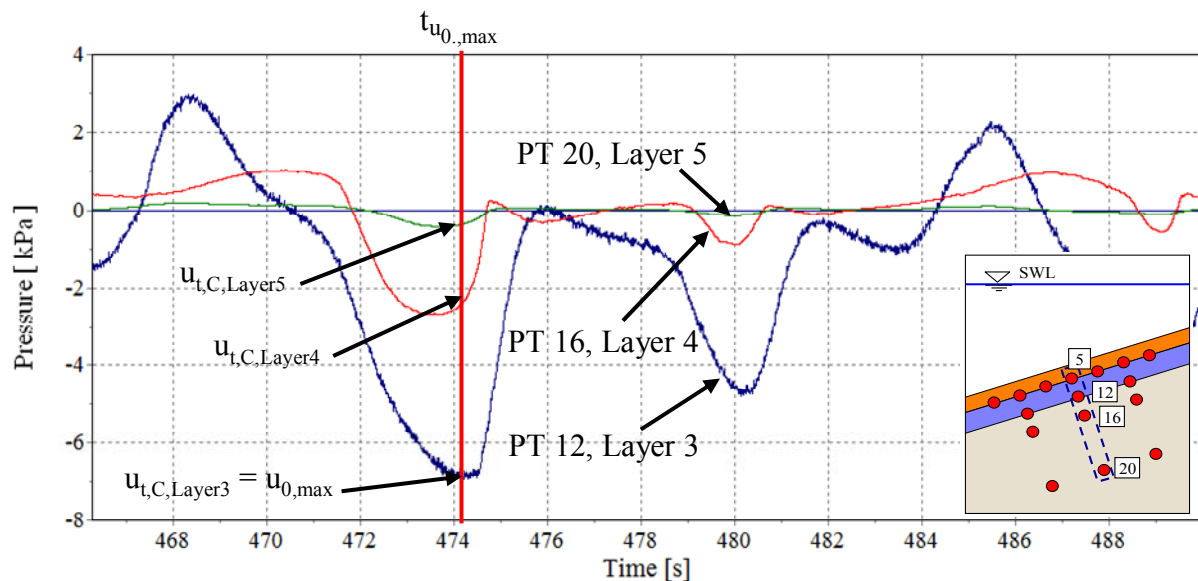

Fig. E.1.1: Definition sketch for simultaneous "negative" transient pore pressure at layers 3,4 and 5 (exemplarily at Location C for Model C)

The pressure recorded at the three locations B, C and D are analyzed event by event. For each of these three locations the negative transient pore pressure recorded simultaneously at layers 3, 4 and 5 are considered for both Models B and C. The event-based analysis and the consideration of the negative transient pressures occurring at the same time in layers 3, 4 and 5 for each location B, C and D is necessary because the difference $u_0 - u_{t,layeri}$ is relevant for the analysis of the stability against transient soil liquefaction (see Chapter 8 and Fig 8.10). Using the pressure head associated with the incident wave height H_{m0} the pressure difference $u_0 - u_{t,layer\ i}$ is made dimensionless:

$$\Delta \bar{u} = \frac{u_0 - u_{t,layer\ i}}{\rho g H_{m0}} \tag{E.1.1}$$

For both Models B and C, $\Delta \bar{u}$ is plotted against surf similarity parameter $\xi_{m-1,0}$ as shown exemplarily for location B in Fig. E.1.2a for layer 4 and in Fig. E.1.2b for layer 5 which both indicate that there is aclearly defined upper boundary of the function $\Delta \bar{u} = f(\xi_{m-1,0})$ which can be assumed to be similar for both Models B and C. Since the upper bound is relevant for the analysis of the stability against transient soil liquefaction, the analysis of all data should proceed accordingly; i.e. a relationship $\Delta \bar{u} = f(\xi_{m-1,0})$ describing an upper limit has to be determined. Given the considerable number of data sets resulting from several combinations between Models (B and C), locations (B, C and D) and layers 4 and 5 meaningful simplifications have to be introduced. For this purpose, the effect of the location (B, C or D) and the effect of the Model (B or C) on the relative pressure difference should first be examined.
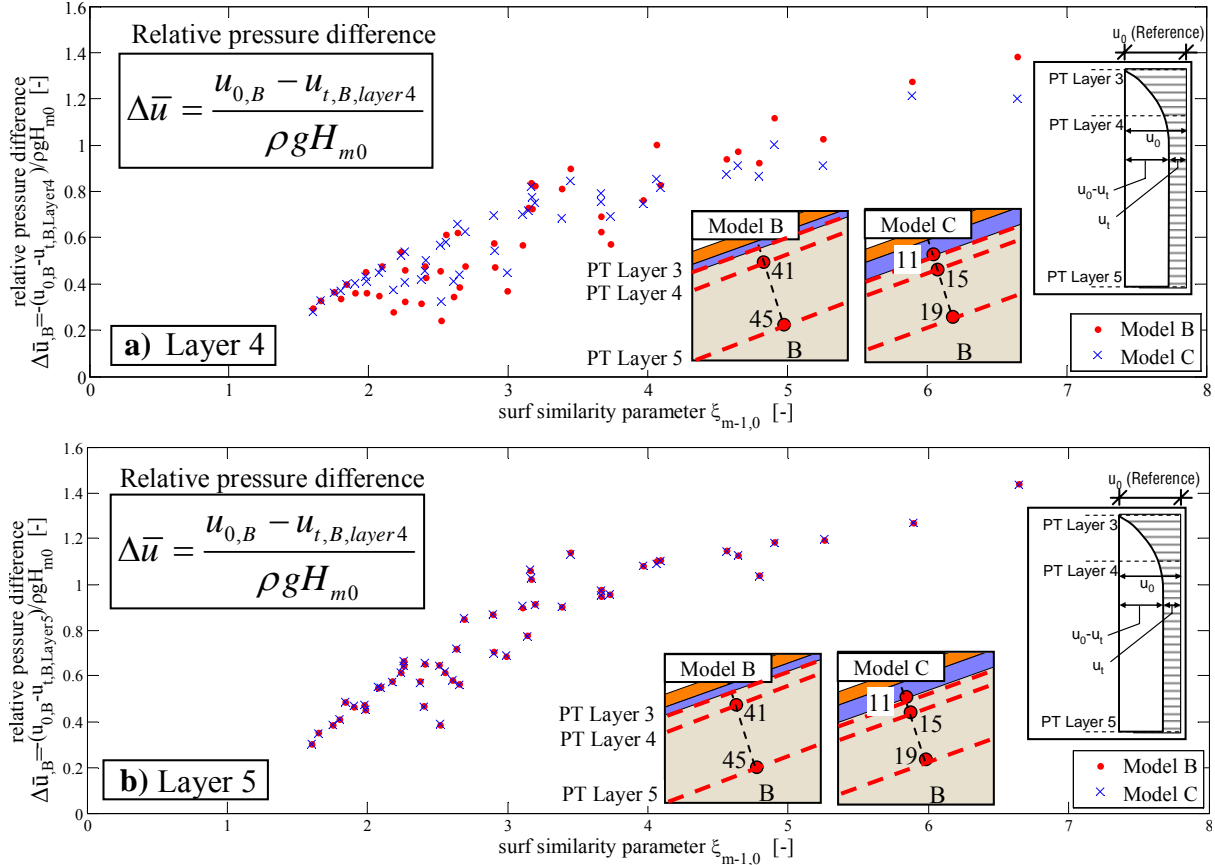

Fig. E.1.2: Relative pressure difference $\Delta \bar{u}_B$ vs surf similarity parameter at Location B for both Models B and C

The effect of the locations (B, C or D) on relative pressure difference Δū is shown exemplarily for Model B and layer 4 in Fig. E.1.3, indicating that the smallest Δū-values are clearly obtained at the highest location D. On the other hand it also indicates that for lower surf similarity parameters the highest Δū-values may occur at both locations B and C, while for higher surf similarity parameters the highest Δū-values rather occur at location B.
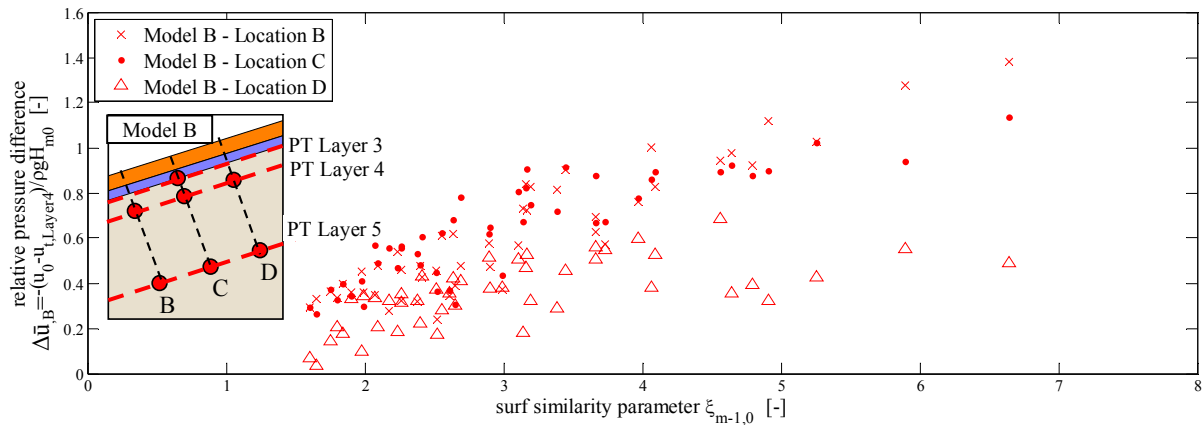

Fig. E.1.3:Effect of location on relative pressure difference Δū for Model B, Layer 4

The effect of the model alternative (B or C) on relative pressure difference Δū is shown exemplarily for layer 4 and all locations B, C and D in Fig. E.1.4. As expected, the fitted curve for Model B provides slightly larger Δū -values than Model C - especially for higher surf similarity parameters.
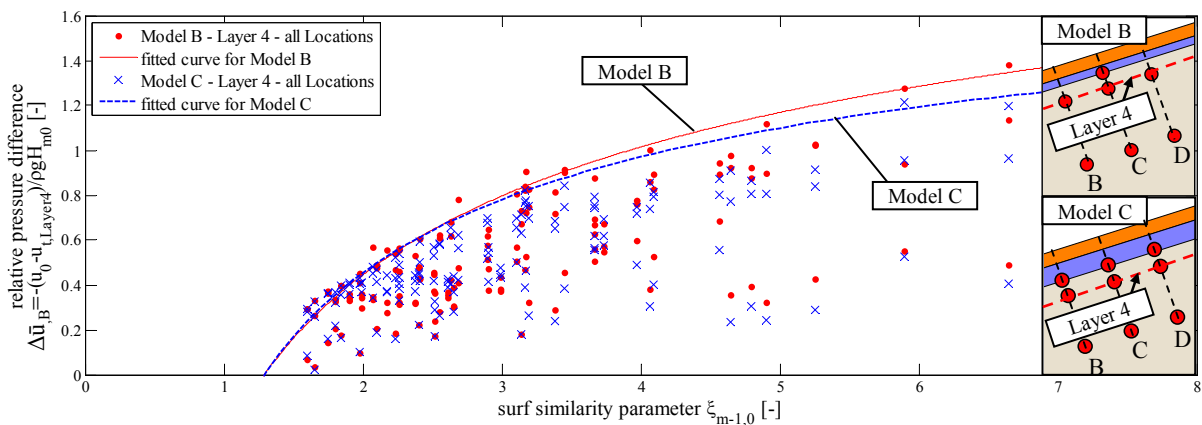

Fig. E.1.4:Effect of model alternative on relative pressure differences at Layer 4 for all locations B, C and D

E.2 Tentative prediction formulae for relative pore pressure difference

Based on the preliminary analysis in Fig Fig. E.1.2 - Fig. E.1.4 and due to the high complexity and the significant amount of work associated with the event-based analysis of all data sets as well as to the time constraint within the framework of this study, it is reasonable from the point of view of engineering practice to provide prediction formulae which are the safe side. Therefore, the data sets for both Models B and C and all locations B, C and D are merged together to determine a predicition forumulae for the relative pressure difference at layer 4 and layer 5.

At layer 4 the following upper envelope is obtained (Fig. E.2.1):

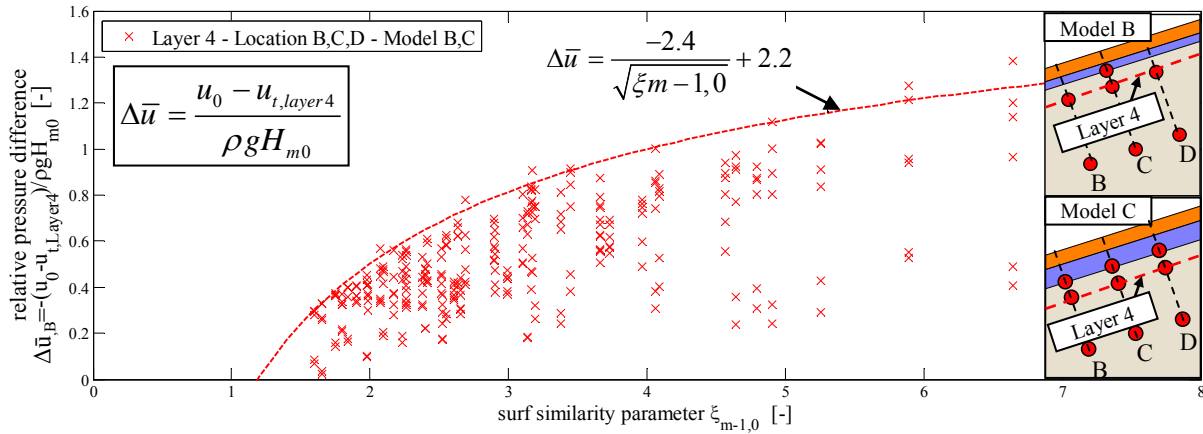$$\frac{u_0 - u_{t,layer4}}{\rho g H_{m0}} = \frac{-2.4}{\sqrt{\xi m - 1,0}} + 2.2 \qquad \text{(E.2.1)}$$

Fig. E.2.1: Relative pressure difference at layer 4

At layer 5 the upper envelope can approximately be obtained by multiplying Δū at layer 4 (Eq. E.2.1) with a factor 1.1 only (Fig. E.2.2):

$$\frac{u_0 - u_{t,layer5}}{\rho g H_{m0}} = 1.1 \cdot \left(\frac{-2.4}{\sqrt{\xi m - 1,0}} + 2.2 \right) \qquad \text{(E.2.2)}$$
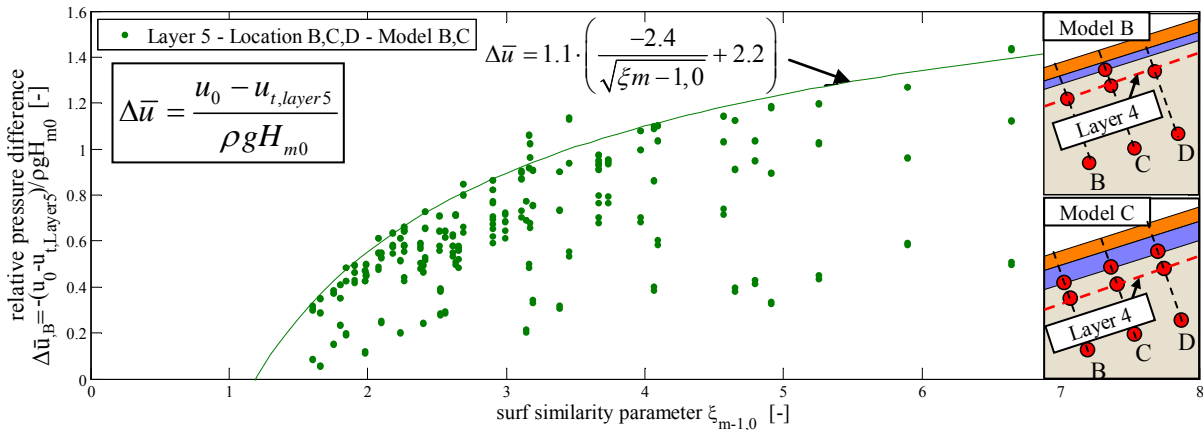

Fig. E.2.2: Relative pressure difference at layer 5

Plotting in Fig. E.2.3 both upper envelopes which described by Eqs. (E.2.1) and (E.2.2) for layer 4 and 5, respectively and recalling that (see Fig 6.1):

   (i)   pressure u_0 represents the reference value of the negative transient pressure at the upper boundary of the sand core (layer 3) beneath the revetment (see Fig 8.10),
   (ii)   Layer 3 and layer 4 are separated by a sand thickness of only 0.20 m while layer 3 and layer 5 are separated by a sand thickness of 0.80 m for Model B and 0.60m for Model C (see Fig 6.1 b,c),

it is obvious from Fig. E.2.3 that the uplift pressure gradient between layer 3 and layer 4 is much higher than the uplift pressure gradient between layer 4 and layer 5. Considering that the initial effective vertical stress due to the weight of the sand core increases linearly with depth z (see Eq. 8.2), it is obvious that the soil liquefaction potential due to wave-induced transient pore pressure is much higher just beneath the revetment (e.g. between layer 3 and 4) than at deeper locations (e.g. between layer 4 and 5). This explains the results in chapter 8, showing that soil liquefaction indeed occurred between layer 3 and 4, thus causing the collapse of Model A.
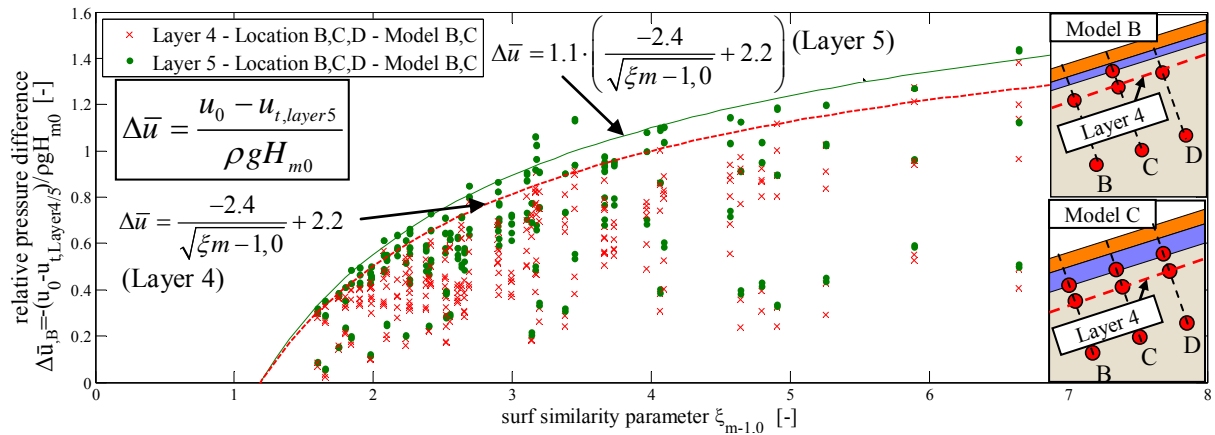

Fig. E.2.3: Relative pressure difference at Layers 4 and 5